

Technical Report Documentation Page

1. Report No. FHWA/TX-16/0-6785-1	2. Government Accession No.	3. Recipient's Catalog No.	
4. Title and Subtitle Extending Use of Steel-Laminated Elastomeric Bearings to Higher Demand Applications		5. Report Date October 2015; Published June 2016	6. Performing Organization Code
7. Author(s) Belivanis, K., Han, L., Sun, C., Helwig, T., Engelhardt, M., Tassoulas, J., Williamson, E.		8. Performing Organization Report No. 0-6785-1	
9. Performing Organization Name and Address Center for Transportation Research The University of Texas at Austin 1616 Guadalupe Street, Suite 4.202 Austin, TX 78701		10. Work Unit No. (TRAIS)	11. Contract or Grant No. 0-6785
12. Sponsoring Agency Name and Address Texas Department of Transportation Research and Technology Implementation Office P.O. Box 5080 Austin, TX 78763-5080		13. Type of Report and Period Covered Technical Report 9/01/2012–8/31/2015	14. Sponsoring Agency Code
15. Supplementary Notes Project performed in cooperation with the Texas Department of Transportation and the Federal Highway Administration.			
16. Abstract: Elastomeric bearings have historically been used on bridges with short to moderate spans. The resulting demand on the bearings is usually not very severe in terms of the necessary support reaction or the deformational requirements. The bearings have historically showed good behavior and as a result, there is a strong desire to use the bearings on higher demand applications with larger support reactions and more significant deformational requirements. Although longer span concrete bridges may be candidates for these higher demand applications, many steel girder systems such as tub girder systems are also good candidates for these applications. The necessary translational and rotational demands for these bridges are significant and the support reactions are much larger than bridges that have typically utilized elastomeric bearings. TxDOT has utilized the bearings on some steel tub girders and although many of these bearings have behaved well, isolated bearings have shown significant distress in a relatively short period of time. Although in recent years, TxDOT has successfully used elastomeric pads in steel bridge applications, no full size tests on the large bearings have been conducted to demonstrate the ability of the bearings to satisfy the long-term performance requirements. In the absence of these tests, it is not clear if manufacturers have the ability to consistently produce bearings for high demand applications. The research outlined in this proposal consists of laboratory testing, field monitoring, and parametric computational modeling that will provide the supporting data so that elastomeric bearings can be confidently used in the wide range of bridge applications throughout the state of Texas. The use of elastomeric bearings in steel bridge applications will result in systems that are easier to fabricate, erect, and maintain while also improving the long-term bridge behavior.			
17. Key Words Bearing pad, Elastomeric Bearing		18. Distribution Statement No restrictions	
19. Security Classif. (of report) Unclassified	20. Security Classif. (of this page) Unclassified	21. No. of pages 184	22. Price

Form DOT F 1700.7 (8-72) Reproduction of completed page authorized



THE UNIVERSITY OF TEXAS AT AUSTIN
CENTER FOR TRANSPORTATION RESEARCH

Extending Use of Steel-Laminated Elastomeric Bearings to Higher Demand Applications

Konstantinos Victor Belivanis

Liwei Han

Cong Sun

Todd Helwig

Michael Engelhardt

John Tassoulas

Eric Williamson

CTR Technical Report:

0-6785-1

Report Date:

October 2015

Project:

0-6785

Project Title:

Extending Use of Elastomeric Bearings to Higher Demand Applications

Sponsoring Agency:

Texas Department of Transportation

Performing Agency:

Center for Transportation Research at The University of Texas at Austin

Project performed in cooperation with the Texas Department of Transportation and the Federal Highway Administration.

Center for Transportation Research
The University of Texas at Austin
1616 Guadalupe St, Suite 4.202
Austin, TX 78701

<http://ctr.utexas.edu/>

Disclaimers

Author's Disclaimer: The contents of this report reflect the views of the authors, who are responsible for the facts and the accuracy of the data presented herein. The contents do not necessarily reflect the official view or policies of the Federal Highway Administration or the Texas Department of Transportation (TxDOT). This report does not constitute a standard, specification, or regulation.

Patent Disclaimer: There was no invention or discovery conceived or first actually reduced to practice in the course of or under this contract, including any art, method, process, machine manufacture, design or composition of matter, or any new useful improvement thereof, or any variety of plant, which is or may be patentable under the patent laws of the United States of America or any foreign country.

Engineering Disclaimer

NOT INTENDED FOR CONSTRUCTION, BIDDING, OR PERMIT PURPOSES.

Project Engineer: Todd Helwig
Professional Engineer License State and Number: Texas No. 94280
P. E. Designation: Research Supervisor

Acknowledgments

The authors would like to express their appreciation to the Director and the Members of the Project Committee. Specifically, thanks to Darrin Jensen for active collaboration and meeting organization, crucial to conveying the updates and feedback from the research team to the TxDOT Project Committee and vice versa. Also special thanks to Tim Bradberry for his help in clarifying the current TxDOT bearing design practice, the information on bridges that qualify for higher demand applications, and constructive comments and thoughts throughout the project time. Last but not least, the research team would like to acknowledge the contribution of Jeff Cotham for the significant information and experience transmitted over the course of the project.

Table of Contents

CHAPTER 1 : INTRODUCTION	1
CHAPTER 2 : LITERATURE REVIEW	5
2.1 General Description.....	5
2.1.1 Purpose of bearings.....	5
2.1.2 Types of bearings.....	5
2.1.3 Unreinforced elastomeric bearings	6
2.1.4 Fiber reinforced elastomeric bearings.....	6
2.1.5 Steel reinforced elastomeric bearings	7
2.1.6 Advantages of steel reinforced elastomeric bearings.....	7
2.1.7 Shortcomings of steel reinforced elastomeric bearings	7
2.2 Properties.....	7
2.2.1 Shape factor	8
2.2.2 Steel reinforcement	8
2.2.3 Effective elastomer thickness	8
2.2.4 Shear modulus/hardness.....	9
2.2.5 Bulk modulus.....	9
2.3 Failure Modes.....	9
2.3.1 Compression	9
2.3.2 Shear	11
2.3.3 Rotation.....	12
2.3.4 Stability	13
2.3.5 Slippage.....	13
2.4 Historical Development of Code Provisions	14
2.4.1 Performance of elastomeric bearings - NCHRP 298	14
2.4.2 Low temperature behavior and acceptance criteria for elastomeric bridge bearings - NCHRP 325	14
2.4.3 Elastomeric bridge bearings: recommended test methods - NCHRP 449	14
2.4.4 Rotation limits for elastomeric bearings - NCHRP 596	15
2.4.5 Current design approaches.....	15

CHAPTER 3 : FIELD MONITORING OF STEEL TUB GIRDER BRIDGE WITH ELASTOMERIC BEARINGS	19
3.1 Bridge Instrumentation.....	19
3.1.1 Instrumentation overview	20
3.1.2 Installation.....	26
3.1.3 Data acquisition program.....	27
3.2 Interpretation of Instrumentation Results	28
3.2.1 Methodology	28
3.2.2 Data correction for translational movement measurements.....	28
3.2.3 Data extrapolation.....	29
3.3 Field Instrumentation Results Summary and Observations	30
3.3.1 Temperature monitoring	30
3.3.2 Translations.....	32
3.3.3 Rotations	34
3.3.4 Slipping	38
3.4 Field Instrumentation Conclusions.....	40
CHAPTER 4 : DESCRIPTION OF THE EXPERIMENTAL PROGRAM	43
4.1 Introduction – Purpose of Experimental Program.....	43
4.2 Material Testing	43
4.2.1 Specimen preparation.....	43
4.2.2 Testing procedure.....	50
4.2.3 Low temperature testing	51
4.3 Full Scale Bearing Tests	54
4.3.1 Full scale compression testing	55
4.3.2 Full scale shear testing	58
4.3.3 Full scale rotational testing	64
4.4 Summary	67
CHAPTER 5 : RESULTS OF THE EXPERIMENTAL PROGRAM.....	69
5.1 Introduction	69
5.2 Material Test Results	69
5.3 Full Scale Compression Test Results	74
5.3.1 Stiffness results	74
5.3.2 Test observations	78

5.4	Full Scale Shear Test Results	79
5.4.1	Stiffness results	79
5.4.2	Directional stiffness results.....	82
5.4.3	Test observations	84
5.5	Full Scale Rotational Test Results.....	87
5.5.1	Combined compression and rotation results	87
5.5.2	Test observations	89
5.6	Summary	89
CHAPTER 6 : FINITE ELEMENT ANALYSIS MODELING OF ELASTOMERIC BEARINGS	91	
6.1	Introduction	91
6.2	Material Model	91
6.2.1	Material coefficients	91
6.2.2	Bulk modulus.....	93
6.3	Finite Element Modeling.....	95
6.3.1	Numerical scheme.....	95
6.3.2	FEA model.....	96
6.3.3	Mesh.....	99
6.4	FEA Results.....	103
6.4.1	Compression modeling	103
6.4.2	Shear modeling	105
6.4.3	Rotation modeling.....	108
6.5	Summary	112
CHAPTER 7 : PARAMETRIC FE STUDY OF ELASTOMER LAYER	113	
7.1	Introduction	113
7.2	FE Model.....	114
7.3	Compression Study.....	116
7.4	Rotation Study	126
7.5	Superposition Study	135
7.5.1	Compression and shear	135
7.5.2	Compression, rotation, and shear.....	136

7.6 Summary	139
CHAPTER 8 : INVESTIGATION OF DISTRESSED BEARINGS	141
8.1 Problem Description.....	141
8.2 Methods	143
8.3 Measurements.....	145
8.4 Summary	149
CHAPTER 9 : CONCLUSIONS.....	151
CHAPTER 10 : DESIGN METHODOLOGY AND EXAMPLES.....	153
10.1 Rubber Design Properties and Bearing Design Parameters	153
10.1.1 Rubber stiffness/strength	153
10.1.2 Temperature dependent stiffness	153
10.1.3 Design parameters.....	154
10.2 Design Approach.....	154
10.2.1 Limitations of current (TxDOT) design methodology.....	154
10.2.2 AASHTO/ EN-1337 design methodology	155
10.2.3 Alteration proposal of current AASHTO LRFD design provision and TxDOT design practice.....	155
10.3 Design Procedure (Code Language).....	156
10.4 Design Flowchart	159
10.5 Design Examples.....	159
10.5.1 Bearing 1	160
10.5.2 Bearing 2	161
10.5.3 Bearing 3	163
REFERENCES.....	165

List of Figures

Figure 1.1: A typical elastomeric bearing and one used for higher demand application.....	2
Figure 2.1: Bulging effect for different reinforcement layouts for the same axial load P	6
Figure 2.2: Bearing (a) without and (b) with rollover at the edge	8
Figure 2.3: Compression failure due to (a) tension debonding and (b) fractured steel plates	10
Figure 2.4: Delamination due to cyclic shear loading	12
Figure 2.5: Bearing deformation for applied moment (a) with and (b) without lift-off	13
Figure 2.6: Shear strain at the steel-elastomer interface due to (a) axial load, (b) shear load, (c) rotation.....	16
Figure 3.1: IH-35 N & US-290 E direct connector.....	19
Figure 3.2: Typical instrumentation at each support location.....	20
Figure 3.3: Measured displacements at each support location	20
Figure 3.4: Trace box with 0.5 in. x 0.5 in. grid	21
Figure 3.5: Inclinometer installation.....	22
Figure 3.6: String potentiometers in service	22
Figure 3.7: Linear pot location.....	23
Figure 3.8: Detailed schematic of the assembly	24
Figure 3.9: Linear pots in service	24
Figure 3.10: Layout of the wireless DAQ network inside the bridge	25
Figure 3.11: Cables from east girder entering the west girder through a hole provided for drainage.....	27
Figure 3.12: Instrumentation in the exterior of the bridge using a bucket truck	27
Figure 3.13: GUI of the real-time bridge monitoring program.....	28
Figure 3.14 : Movements of the bearing relative to the string potentiometer position.....	29
Figure 3.15 : Actual and extrapolated measurements from string potentiometers	30
Figure 3.16: Ambient and Girder Temperatures for 07/31/2013-08/03/2013	31
Figure 3.17: Ambient and Girder Temperatures for 1/14/2014 - 1/18/2014	31
Figure 3.18: Longitudinal displacement measures time history of a week.....	32
Figure 3.19: Transverse displacement measures time history of week	32
Figure 3.20: Different deformation patterns for different periods of the year.....	33

Figure 3.21: Range of displacements in the longitudinal and transverse directions for each bent.....	34
Figure 3.22: X axis rotation of east tub girder at bend 2 – 28 days.....	35
Figure 3.23: Y axis rotation of east tub girder at bend 2 – 28 days.....	35
Figure 3.24: Torsional rotation measured at bent 1	36
Figure 3.25: FFT output (Frequency spectrum).....	37
Figure 3.26: Calculated torsional rotation at bent 1 due to thermal load.....	37
Figure 3.27: Temperature time history	38
Figure 3.28: Observed slipping between the bearing and girder sole plate (Ambient Temperature at time of picture - 61 °F)	39
Figure 3.29: Lateral (radial) movement of bridge observed at expansion joint from bridge deck: a) shift observed in lane striping, b) shift observed in bridge rail.....	40
Figure 4.1: Dimensions of the shear test specimen (Unit: inches)	44
Figure 4.2: Sections of the elastomeric bearings	45
Figure 4.3: Process of shear test specimens acquisition	46
Figure 4.4: Bearing cutting process	47
Figure 4.5: Acquisition of the rubber strips (Bearing S)	48
Figure 4.6: Separation of the rubber strips (Bearing XL)	48
Figure 4.7: Preparing DST specimens from bearing strips	49
Figure 4.8: Typical DST specimens under different shear test steps.....	49
Figure 4.9: Shear modulus test on specimens with different lengths	50
Figure 4.10: Geometry of the specimen for low temperature test (units: inches).....	51
Figure 4.11: Low temperature testing setup	52
Figure 4.12: Specimens being placed inside the testing chamber at the testing temperature	53
Figure 4.13: Loading control system for DST under low temperature	54
Figure 4.14: Schematic plan view of the self-reacting test setup with important parts	56
Figure 4.15: Actual test setup and linear potentiometer location	56
Figure 4.16: Bearing tested in compression.....	57
Figure 4.17: Schematic of the test setup	58
Figure 4.18: Schematic of the self-reacting shear frame	59
Figure 4.19: Combined axial and shear test setup at FSEL	59
Figure 4.20: Bearing tested in shear	60
Figure 4.21: Shear stiffness definition	61

Figure 4.22: Bearings on supports before being placed in the shear test setup	62
Figure 4.23: Clamped configuration entering the test setup	62
Figure 4.24: Test setup with engaged bearings.....	63
Figure 4.25: Testing protocol.....	64
Figure 4.26: Modification to the shear test setup for rotation.....	65
Figure 4.27: Compression-induced rotation at a bearing.....	66
Figure 4.28: Increased local shear deformations noticeable at the compression side of the bearing.....	66
Figure 5.1: Region of the rubber layers shown in Figure 5.2	69
Figure 5.2: Shear modulus results of bearings with different dimensions (Units: psi).....	70
Figure 5.3: Two sections on the elastomeric bearing	71
Figure 5.4: Shear modulus contour of two sections inside the bearing XL (Units: psi).....	72
Figure 5.5: Average shear moduli from different bearings (Units: psi)	73
Figure 5.6: Standard deviation of the shear moduli from different bearings (Units: psi).....	73
Figure 5.7: Load-deflection curves for large (L) bearings under compression	75
Figure 5.8: Load-deflection curves for medium (M) bearings under compression	75
Figure 5.9: Load-deflection curves for small (S) bearings under compression.....	76
Figure 5.10: Axial stiffness values for large (L) bearings	77
Figure 5.11: Axial stiffness values for medium (M) bearings	77
Figure 5.12: Axial stiffness values for small (S) bearings.....	78
Figure 5.13: Uniform layer thickness along the bearing length (a), and non-uniform layer thickness along the bearing length (b)	79
Figure 5.14: Force - displacement curves of the small bearing at different axial loads (S)	80
Figure 5.15: Calculated shear stiffness at different axial loads (S)	81
Figure 5.16: Test-Material stiffness correlation (S).....	81
Figure 5.17: Force-Displacement curves (M).....	82
Figure 5.18: Effect of shear direction on shear stiffness (L)	83
Figure 5.19: Effect of shear direction (normalized) on shear stiffness (L).....	83
Figure 5.20: Effect of shear direction on shear stiffness (M)	84
Figure 5.21: Effect of shear direction (normalized) on shear stiffness (M).....	84
Figure 5.22: Bearing M under 1.5 ksi axial load and 75% shear strain.....	85
Figure 5.23: Rollover effect on bearing S.....	85
Figure 5.24: Bearing L under 2.0 ksi axial load and 100% shear strain.....	86

Figure 5.25: Buckled bearing M	86
Figure 5.26: Combined compression and rotation test data (Bearing L – $\theta=0.5^\circ$)	87
Figure 5.27: Lift-off during combined compression and rotation test.....	88
Figure 5.28: Bearing L under combined compression and rotation ($\theta=1.5^\circ$)	88
Figure 5.29: Combined compression and rotation test data and FEA prediction (Bearing L – $\theta=1.5^\circ$)	89
Figure 6.1: Regularized Coulomb friction model	96
Figure 6.2: Finite element model for elastomeric bearing.....	97
Figure 6.3: Schematic diagram for compression modeling	97
Figure 6.4: Schematic diagram for shear modeling	98
Figure 6.5: Schematic diagram for rotation modeling	98
Figure 6.6: Mesh sensitivity study on number of element layers per elastomer layer.....	100
Figure 6.7: Mesh sensitivity study on global mesh size	100
Figure 6.8: 3D view of mesh for Bearing S	101
Figure 6.9: 2D sectional view of mesh for Bearing S.....	101
Figure 6.10: 3D view of mesh for Bearing M.....	101
Figure 6.11: 2D sectional view of mesh for Bearing M	102
Figure 6.12: 3D view of mesh for Bearing L.....	102
Figure 6.13: 2D sectional view of mesh for Bearing L.....	102
Figure 6.14: 2D sectional view of deformed mesh for Bearing S under axial load.....	103
Figure 6.15: 2D sectional view of deformed mesh for Bearing M under axial load	103
Figure 6.16: 2D sectional view of deformed mesh for Bearing L under axial load	103
Figure 6.17: Force vs deflection curves for Bearing S under axial load.....	104
Figure 6.18: Force vs deflection curves for Bearing M under axial load	104
Figure 6.19: Force vs deflection curves for Bearing L under axial load	105
Figure 6.20: 2D sectional view of deformed mesh for Bearing S in shear	106
Figure 6.21:2D sectional view of deformed mesh for Bearing M in shear.....	106
Figure 6.22: 2D sectional view of deformed mesh for Bearing L in shear.....	106
Figure 6.23: Lateral force vs displacement curves for Bearing S in shear	107
Figure 6.24: Lateral force vs displacement curves for Bearing M in shear	107
Figure 6.25: Lateral force vs displacement curves for Bearing L in shear	108
Figure 6.26: Contact status contour for bearing in partial contact.....	109
Figure 6.27: 2D sectional view of deformed mesh in partial contact in rotation modeling	109

Figure 6.28: Contact status contour for bearing in complete contact	110
Figure 6.29: Sectional view of deformed mesh in complete contact in rotational modeling	110
Figure 6.30: Force vs deflection curves for Bearing M in rotational modeling ($\theta=1.5^\circ$)	111
Figure 6.31: Force vs deflection curves for Bearing L in rotational modeling ($\theta=0.5^\circ$)	111
Figure 6.32: Force vs deflection curves for Bearing L in rotational modeling ($\theta=1.5^\circ$)	112
Figure 7.1: Mesh of elastomer layer S	114
Figure 7.2: Sign convention for elastomer layer.....	115
Figure 7.3: Deformed mesh of layer S under axial load of 1GS.....	116
Figure 7.4: Contour of shear strain γ_{xy} for layer S under axial load of 2GS.....	117
Figure 7.5: Contour of shear strain γ_{yz} for layer S under axial load of 2GS.....	117
Figure 7.6: γ_{xy} profile along longitudinal axis for bearing S under axial load of 2GS	118
Figure 7.7: γ_{xy} profiles along longitudinal axis for bearing S under various levels of axial load.....	118
Figure 7.8: γ_{yz} profiles along transverse axis for bearing S under various levels of axial load.....	119
Figure 7.9: Extrapolated γ_{xy} profiles along longitudinal axis for bearing S	119
Figure 7.10: Extrapolated γ_{xy} profiles along longitudinal axis for bearing M	120
Figure 7.11: Extrapolated γ_{xy} profiles along longitudinal axis for bearing L	120
Figure 7.12: Extrapolated γ_{xy} profiles along longitudinal axis for bearing XL	121
Figure 7.13: Shear strain γ_{xy} vs normalized axial load αa for layer S with $K = 450\text{ksi}$	122
Figure 7.14: Da values for layer S in longitudinal direction	122
Figure 7.15: Da values for layer M in longitudinal direction.....	123
Figure 7.16: Da values for layer L in longitudinal direction.....	123
Figure 7.17: Da values for layer XL in longitudinal direction	124
Figure 7.18: Da values for layer S in Transverse direction.....	124
Figure 7.19: Da values for layer M in Transverse direction.....	125
Figure 7.20: Da values for layer L in Transverse direction.....	125
Figure 7.21: Da values for layer XL in Transverse direction	126
Figure 7.22: Deformed mesh of bearing S under normalized rotation of $\alpha r = 4$	127
Figure 7.23: Contour of shear strain γ_{xy} for bearing S under normalized rotation of $\alpha r =$ 8	128
Figure 7.24: γ_{xy} profile along longitudinal axis for Bearing S under normalized rotation of $\alpha r = 8$	129

Figure 7.25: γ_{xy} profiles along longitudinal axis for Bearing S under various levels of normalized rotation	129
Figure 7.26: Extrapolated γ_{xy} profiles along longitudinal axis for bearing S	130
Figure 7.27: Extrapolated γ_{xy} profiles along longitudinal axis for bearing M	130
Figure 7.28: Extrapolated γ_{xy} profiles along longitudinal axis for bearing L	131
Figure 7.29: Extrapolated γ_{xy} profiles along longitudinal axis for bearing XL	131
Figure 7.30: Shear strain γ_{xy} vs normalized rotation αr for bearing S with $K = 450\text{ksi}$	132
Figure 7.31: Dr values for bearing S	133
Figure 7.32: Dr values for bearing M	133
Figure 7.33: Dr values for bearing L	134
Figure 7.34: Dr values for bearing XL	134
Figure 7.35: Shear strain profiles along the longitudinal axis for step 1 & step 2	136
Figure 7.36: Profile of superposition ratios	136
Figure 7.37: Shear strain profiles along the longitudinal axis for step 1 & step 2	137
Figure 7.38: Profile of superposition ratios for step 2	137
Figure 7.39: Shear strain profiles along the longitudinal axis for step 2 & step 3	138
Figure 7.40: Profile of superposition ratio for step 3	138
Figure 8.1: Plan of IH-35 NB & US-290 EB direct connector	141
Figure 8.2: Distressed bearing for girder 1, bent 4	142
Figure 8.3: Distressed bearing for girder 1, bent 4	142
Figure 8.4: Bearing with damage for girder 1, bent 5	143
Figure 8.5: Sign conventions of a bearing	143
Figure 8.6: Digital level on the steel sole plate	144
Figure 8.7: Digital level on the concrete surface	144
Figure 8.8: Measuring with inside caliper	145
Figure 8.9: Maximum angle of rotation imposed on bearings for girder 1	147
Figure 8.10: Maximum angle of rotation imposed on bearings for girder 2	147
Figure 8.11: Max shear strain on bearings for girder 1 under DL and rotation	149
Figure 8.12: Max shear strain on bearings for girder 2 under DL and rotation	149
Figure 10.1: Typical shear stress-strain curves for service shear deformations (orange) and failure (blue)	153
Figure 10.2: Stress-strain curves for rubber for rubber at various temperatures	154
Figure 10.3: Proposed bearing design flowchart	159

List of Tables

Table 2.1: AASHTO Limits for Method A.....	16
Table 2.2: Shear strain components at the steel-elastomer interface	16
Table 3.1: Power consumption for each group of devices.....	26
Table 3.2: Maximum and minimum recorded temperatures for Austin (Source: Utah Climate Center).....	31
Table 3.3: Ranges of rotation variation.....	38
Table 4.1: Conditioning time for DST specimen (2”X2”X0.5”) before the low temperature test.....	53
Table 4.2: Test matrix of bearings tested in compression	57
Table 4.3: Test matrix of bearings tested in shear	60
Table 4.4: Matrix of conducted tests.....	61
Table 4.5: Test matrix of bearings tested in rotation	67
Table 5.1: Summary of the measured shear modulus values from bearing tests.....	74
Table 5.2: Material-scale and full-scale shear stiffness comparison	80
Table 6.1: Measured lateral stiffness of bearings in full scale testing.....	92
Table 6.2: Calcuated C1 values	93
Table 6.3: Calculated apparent bulk modulus for all bearings	95
Table 6.4: Summary of Loads.....	99
Table 6.5: Summary of bearing dimensions	99
Table 6.6: Summary of numerical and experimental results	105
Table 6.7: Summary of numerical and experimental results	108
Table 6.8: Summary of loads for rotation modeling.....	109
Table 7.1: Summary of elastomer layers	115
Table 7.2: Summary of axial loads	116
Table 7.3: Summary of normalized rotation deformation	127
Table 8.1: Bearing dimensions per location	141
Table 8.2: Measurements of angles	146
Table 8.3: Maximum shear strain γ_r due to static rotation	148
Table 8.4: Maximum shear strain γ_a due to dead load.....	148
Table 10.1: Summary of design values.....	160

CHAPTER 1: INTRODUCTION

The two primary structural materials that are used in bridge construction are concrete and steel. While there is a wide array of different structural systems that may be used in bridges, the most commonly used system is a girder bridge in which flexural members are used to span a desired area or obstacle. A girder system is typically divided into a superstructure, which consists of the girders, bridge deck and rail, and a substructure, which consists of the piers, abutments and other foundation elements. A bridge bearing is generally provided as the critical link between the superstructure and the substructure. The key role of the bearing is to resist the girder reactions while also accommodating the necessary rotational and translational deformations that occur at the bridge support due to the applied loading and changes in the thermal conditions in the bridge environment.

Historically, the selection of a suitable bearing for a specific bridge has often been made as a function of the geometry and even the primary structural material that is used in the bridge. Girder bridges are categorized as either a concrete girder or steel girder system depending on the structural material comprising the girders. Concrete girder systems have often employed elastomeric bearings that consist of an elastomer (rubber) medium with embedded steel plates. Steel girder systems, on the other hand, often are supported on more expensive bearings due to deformational demand and reaction magnitude that are a function of the geometries for which the steel girder systems are commonly employed.

Steel girders are often used for moderate to long-span bridges. In many applications, steel bridges may include skewed supports and/or horizontally curved geometry. The long spans coupled with potential support skew and curved geometry result in significant demands on the bearings at the supports to accommodate rotations and complex bridge movements from both environmental loads and daily truck traffic. The longer span applications also often result in larger support reactions that the bearings must accommodate compared to the reactions in shorter concrete girder systems.

Historically, many steel bridge systems made use of pot bearings to accommodate the rotational and translational demands that occur from dead load and vehicular use as well as changes in the thermal conditions that the bridge experiences throughout its life. While pot bearings are relatively expensive to fabricate, past studies sponsored by TxDOT (0-5040) have shown that these bearings may not perform well with regard to accommodating translations of the bridge superstructure relative to the substructure elements. In many cases, significant restraint against thermal deformation can occur in pot bearings. In addition, the materials as well as the sliding surfaces associated with other bearing types have proven to degrade with time and as a result frequent inspection and/or replacement may be required.

Elastomeric bearing pads that are routinely used in concrete bridge systems potentially provide a more reliable means of accommodating translations with improved economy. However, these bearings are not used in many higher demand applications because the current TxDOT design specifications possess rotational limitations that restrict their use. A recent study (NCHRP 596) revealed that stress limits and provisions restricting liftoff that previously governed the design of large bearings may in fact be unnecessary. Design provisions in AASHTO are divided into two potential Design methods referred to as 1) Method A, and 2) Method B. This NCHRP work led to revisions to both the Method A and Method B design procedures in the AASHTO LRFD Bridge Design Specifications. However, the studies have focused primarily on bearings for use in short-to-moderate span systems commonly used in

traditional concrete girder bridge applications. The bearings used for higher demand applications have larger vertical reactions and more significant translational and rotational demands. Higher demand applications for bearings will often require much larger bearings compared to traditional applications. For example, Figure 1 shows a traditional bearing that has been used in conventional applications (such as concrete girder systems) alongside a much larger bearing that might be used in a higher demand application. There are questions about the variations in the material properties of the much larger bearings compared to traditional bearings. Variations in the vulcanizing temperature during manufacturing that are likely to occur with the larger bearings may lead to significant changes in the fundamental material properties of the bearing and the impact of these variations on the bearing behavior are not clear.



Figure 1.1: A typical elastomeric bearing and one used for higher demand application

Although elastomeric bearings have been used in some higher demand applications in recent years, no published tests on large bearings have been conducted to demonstrate the ability of the bearings to satisfy their long-term performance requirements. In the absence of these tests, it is unclear if manufacturers have the ability to consistently produce bearings for high demand applications. To investigate the variations the material properties and the impact on the bearing behavior, TxDOT funded Project 0-6785, the results of which are outlined in this report.

The technical objectives of TxDOT Project 0-6785 include:

- To extend the study of elastomeric bearing shape factors to cover geometries that would be used in high demand situations in Texas bridges where pot and disk bearings have traditionally been used.
- To assess the impact of new AASHTO LRFD Method A and Method B bearing design recommendations on bearings that would be used in typical Texas bridge designs.
- To develop and propose modifications to the design methodology where appropriate.

- To develop robust design examples to serve as a model for future TxDOT bearing designs.

The results of this research investigation provide supporting data so that elastomeric bearings can be confidently used in a wide range of bridge applications. The use of elastomeric bearings in higher demand applications such as those found in longer span steel bridge systems should result in systems that are easier to fabricate, erect, and maintain while also improving the long term bridge behavior. Although a significant focus of the study has been dedicated to steel bridge systems, the results are equally applicable to higher demand concrete bridge applications as well.

The following major tasks, each of which is addressed in this report, were included in TxDOT Project 0-6785:

1. Background studies and literature review
2. Field monitoring of existing Texas bridges and large elastomeric bearings
3. Materials testing
4. Development of test setup for full scale tests
5. Full Scale Compression Testing
6. Full Scale Shear Testing
7. Full Scale Rotational Testing
8. Parametric Finite Element Modeling
9. Design Methodology and Examples

During the field monitoring carried out in Task 2 of the study, distressed bearings were found on the IH-35 NB & US-290 EB Bridge. The outcome of an investigation into the cause of the distress is reported in Chapter 8.

The information presented in this report includes the primary findings of the study. Additional information and details can be found in the three PhD dissertations that have resulted from this research investigation.

CHAPTER 2: LITERATURE REVIEW

2.1 General Description

Elastomeric bearings have been widely used in both prestressed concrete and steel bridge girder systems; however, most of the systems that use elastomeric bearings have relatively short spans and small total lengths. Bridges with larger spans and longer total bridge lengths often are subjected to bearing reactions, thermal movements, and rotations that are outside of the range for which elastomeric bearings have traditionally been used. However, for economical and practical reasons there is a strong motivation to extend the use of the bearings to *higher demand applications* besides those for which they have traditionally been utilized. To extend the use of bearings to these *higher demand applications*, a clear understanding of the basic behavior of the bearings is necessary. In addition, knowledge of the typical testing methods for the bearings is very important for the development of laboratory testing plans and evaluation of design limitations. This chapter provides a summary of the fundamental behavior of the elastomer material and elastomeric bearings as well as an overview of previously completed research and the evolution of design guidelines.

2.1.1 PURPOSE OF BEARINGS

Elastomeric bearings have been widely adopted in the bridge industry because the bearings are able to efficiently and economically achieve the vertical, rotational, and longitudinal support conditions that are idealized as the roller or pin supports that are assumed in basic structural analysis. In addition, the bearings do not have many of the issues that traditional roller and rocker bearings have with corrosion, freezing, and fatigue. Another advantage of elastomeric bearings compared to traditional bearings is the ability to accommodate small fabrication errors either in the superstructure or the substructure (Roeder and Stanton 1983) without inducing significant forces into the system.

2.1.2 TYPES OF BEARINGS

Rubber is practically an incompressible material with a Poisson's Ratio, ν , of approximately 0.5. Although the rubber has a relatively low modulus of elasticity ($E \approx 300$ psi), there is very little change in volume under applied loads. As a result, when rubber is loaded in compression, it bulges in order to maintain its volume. Although the generic term "rubber" is frequently associated with bearings, most modern bearings are made from an elastomer which is a polymer comprised of either natural or synthetic rubber. One of the most commonly used synthetic rubbers is neoprene, which exhibits many of the same properties as natural rubber but can offer better performance in many applications. Although the behavior of an elastomeric bearing depends highly on the material properties of the rubber used for its fabrication, most elastomeric bearings for structural applications are reinforced with steel plates to improve the behavior of the bearings. The performance of a bearing can be significantly affected by the type, amount, and layout of the reinforcement. The purpose of the reinforcement is to provide significant in-plane stiffness while also restraining the effects of bulging. For example, the mitigating effect of steel shims is shown in Figure 2.1.

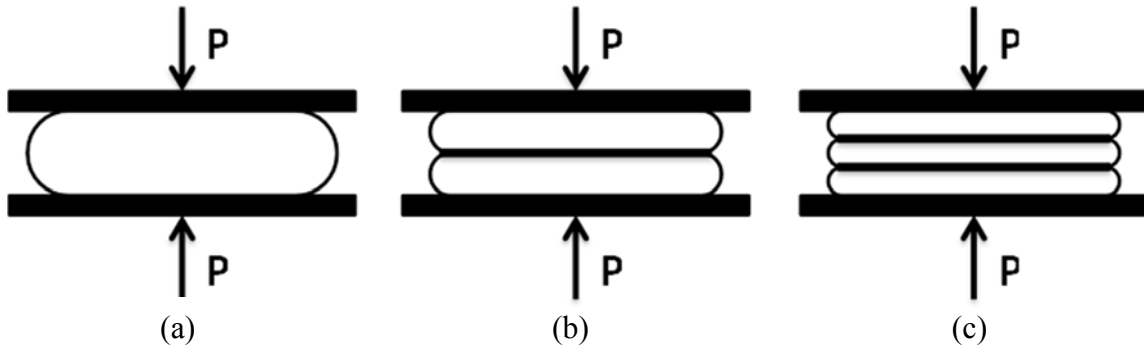


Figure 2.1: Bulging effect for different reinforcement layouts for the same axial load P

2.1.3 UNREINFORCED ELASTOMERIC BEARINGS

Unreinforced elastomeric bearings do not have internal reinforcement. As depicted in Figure 2.1a, a single large bulge is created when the bearing is subjected to axial compression. The only restraint in this case is provided by the loading surface and is dependent on the coefficient of friction between the rubber and the load surface, which can be highly variable. If adequate shear restraint does not exist between the bearing and loading surface, slippage (Bakirzis and Lindley 1970) occurs, which affects the shear demands on the bearing. In addition, without proper restraint, slipping between the bearing and loading surface can lead to the bearing “walking” from cyclic loading, in which case the bearing translates relative to the girder or foundation element. Walking of the bearing can lead to localized overstress in the bearing itself or damage to the girder due to a lack of support.

2.1.4 FIBER REINFORCED ELASTOMERIC BEARINGS

One type of reinforcement used in elastomeric bearing applications is fibers of woven cotton or fiberglass. The end product is a macroscopically homogenous, series of elastomer and fiber layers that can be molded into large pieces and cut according to the dimensions determined by the designer. The bearing is laterally stiff and may require the use of Polytetrafluoroethylene (PTFE - Teflon) sliders to accommodate the horizontal displacement demands. The force needed to overcome the static friction increases as the vertical reaction in the bearing increases and pier flexure becomes the primary mechanism of accommodating horizontal movement (Chen 2008). The role of pier flexure in cases with sliding bearings can be understood by considering the frictional forces that must be overcome for sliding to take place between the beam and the bearing. The coefficient of friction of PTFE is approximately 5%. Therefore if a bridge has a million pound reaction, a friction force of approximately 50,000 lbs. must be overcome for sliding to take place. For typical length bridge piers, a 50,000 lb. shear force can lead to relatively large deformations that may accommodate much of the necessary thermal movement. The pier design may need to include consideration of the effects of this movement. For guided disk or pot bearings, the force necessary to slide can be further magnified by misaligned guides. TxDOT project 0-5040 (Chen et. al, 2009) showed that because of frictional forces necessary to slide, the bridge often does not thermally “breath” about the fixed pier, which is often the focal point of the lateral guides in horizontally curved bridges. As a result, the guides are often misaligned and much larger forces can develop before sliding occurs.

2.1.5 STEEL REINFORCED ELASTOMERIC BEARINGS

The shear deformational characteristics of rubber limit its load carry capacity as the thickness of the elastomer increases. As depicted in Figure 2.1, steel laminates are typically used to control bulging in the elastomer. The steel shims produce independent layers of the elastomer, which therefore results in shearing of the individual layers relative to each other through the depth of the bearing. The end product is a series of alternating layers of steel and elastomer that results in a vertically stiff and horizontally flexible bearing, which accommodates the bridge movements without inducing significant horizontal loads to the substructure. An elastomer cover is included on the outside of the steel plates to ensure protection from the environment.

2.1.6 ADVANTAGES OF STEEL REINFORCED ELASTOMERIC BEARINGS

Steel reinforced elastomeric bearings have many potential advantages compared to other types of bearings, including the following:

- Steel reinforced elastomeric bearings can provide flexibility in the longitudinal and lateral direction of the bridge girders while still maintaining the necessary stiffness in the vertical direction to safely support the large girder reactions.
- The horizontal stiffness remains relatively constant over the design life as opposed to PTFE surfaces, where debris or other corrosive action on the sliding surfaces can increase the frictional resistance over time.
- Steel reinforced elastomeric bearings allow for short-term over-rotations with relatively low probability of damage (Roeder and Stanton 1996).
- Steel reinforced elastomeric bearings are an economically efficient alternative for accommodating bridge movements due to temperature and vehicular use both from an initial installation perspective and also from a maintenance perspective.

There are many advantages of using elastomeric bearings and which make potentially extending the use of the bearings to *higher demand applications* particularly attractive.

2.1.7 SHORTCOMINGS OF STEEL REINFORCED ELASTOMERIC BEARINGS

Although the previous section discussed the advantages of elastomeric bearings, there are also potential shortcomings to using steel-reinforced elastomeric bearing design:

- Steel reinforced elastomeric bearings may be limited to supporting lower vertical loads than their design alternatives.
- The rotational limits of steel reinforced elastomeric bearings are lower than the rotational capacities of many other types of bearings.

2.2 Properties

The engineering properties of the materials used in bridge bearings must be established before the engineer of record can design a bearing. The applicable properties are discussed in this section. In the following subsections the key criteria are presented along with a brief discussion on their impact on the behavior of a bearing.

2.2.1 SHAPE FACTOR

The shape factor of one elastomer layer of a reinforced bearing is a scalar measure defined as the ratio of the loaded area to the area free to bulge. A more dense reinforcement layout leads to an increased shape factor. Although the translational stiffness of the bearing is essentially unaffected, the use of large shape factors leads to bearings with higher axial and rotational stiffness due to the bulging restraint. If the bearing does not have a uniform reinforcement layout, the shape factor of the bearing is defined as the largest shape factor of the individual layers. For a bearing with a uniform reinforcement layout the shape factor is defined as:

$$S = \frac{L \cdot W}{2 \cdot t \cdot (L + W)},$$

where:

L = the length of the bearing parallel to the span of the bridge,

W = the width of the bearing perpendicular to the span of the bridge,

and t = the thickness of an individual elastomer layer of the bearing.

2.2.2 STEEL REINFORCEMENT

As previously mentioned, the main role of the steel reinforcement is to provide axial stiffness to the bearing by restricting bulging. As a result, in-plane tensile stresses are developed in the steel layer when the bearing is in compression. Therefore, the steel reinforcement must be designed to sustain these tensile stresses. However, the plate thickness that is typically required for sustaining the vertical loads will usually be less than the practical thickness required for fabrication purposes.

2.2.3 EFFECTIVE ELASTOMER THICKNESS

A steel reinforced elastomeric bearing consists of layers of steel and elastomer. As mentioned previously, the elastomer is the material that accommodates the horizontal thermal movements. A poorly detailed bearing may experience rollover as depicted in Figure 2.2b. The minimum effective elastomer thickness is twice the value of the design shear deformation to avoid rollover at the edges of the bearing, thereby resulting in a deformed shape as depicted in Figure 2.2a.

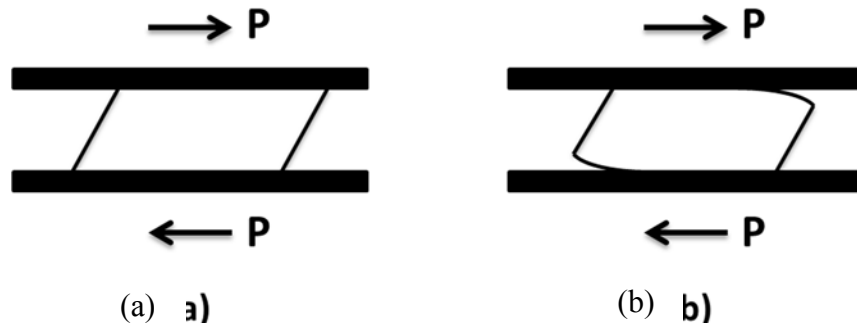


Figure 2.2: Bearing (a) without and (b) with rollover at the edge

2.2.4 SHEAR MODULUS/HARDNESS

Steel reinforced elastomeric bearings are advantageous because of their relatively small horizontal stiffness compared to the axial stiffness. As a result, the bearings resist vertical deformation while allowing translational deformations in the horizontal direction through shearing of the elastomer. Therefore, the most important property taken into consideration when designing the bearing is the shear modulus of the elastomer.

The shear modulus of the elastomer at 73°F is typically used for design. Traditionally, the Shore A durometer hardness has been specified for characterizing the shear modulus. However, numerous studies (Stanton, Roeder et al. 2008, AASHTO 2012) have reported that the relationship between hardness and shear modulus can vary significantly. To account for this variability, AASHTO assigns a range of values for a given Shore A hardness value and directs the engineer to design for the least favorable value for each design check. A higher durometer value generally indicates a stiffer elastomer.

2.2.4.1 Temperature dependence of shear modulus

The elastomer shear modulus value range, being the most important material property for the design of an elastomeric bearing, should be evaluated for the design life of the bearing. However, the elastomer shear modulus is heavily dependent on the temperature (Yura 2002). If not accounted for the variation of the shear modulus with temperature (the material becomes stiffer at lower temperatures) can result in slip of the bearing as the frictional force between the bearing and the superstructure is overcome. Slipping in the opposite direction requires the friction to be overcome again; however, this is less likely to happen due to the softer material properties at higher temperatures. As a result slip between the bridge bearings and the superstructure is more likely a one directional, low-temperature driven, cumulative phenomenon. Although some slip may occur as the bridge expands, the value of the slip is likely to be smaller than the slip that occurs as the bridge contracts.

2.2.5 BULK MODULUS

The bulk modulus represents the resistance of a material to volumetric change when subjected to hydrostatic pressure loading. The bulk modulus is volumetric-strain dependent and as a result is important to be characterized for the volumetric strain range of interest. The bulk modulus is often measured by means of a confined pressure test (Peng, Shimbori et al. 1994). Although usually treated as incompressible, elastomers tend to be slightly compressible. The small amount of compressibility can significantly affect bearing properties of interest at high levels of confinement.

2.3 Failure Modes

A bearing experiences various types of loads throughout the design life. This can lead to a number of modes in which the structure can fail. The most common modes that should be considered in bearing design are described in the following subsections.

2.3.1 COMPRESSION

There are two possible failure modes of a steel-reinforced elastomeric bearing subjected to compression. The first mode consists of debonding of the elastomer at the edge of the

reinforcement layer. This has effectively no impact to the capacity of the bearing. However, it can be an initiation point for delaminations to propagate at the reinforcement surface, reducing the effectiveness of the reinforcing and increasing the area that is free to bulge (Figure 2.3a). The second compression failure consists of the yielding and potentially fracturing the steel reinforcement as depicted in Figure 2.3b. This type of failure is less frequent as the failure load required can be up to 10 times the design value.

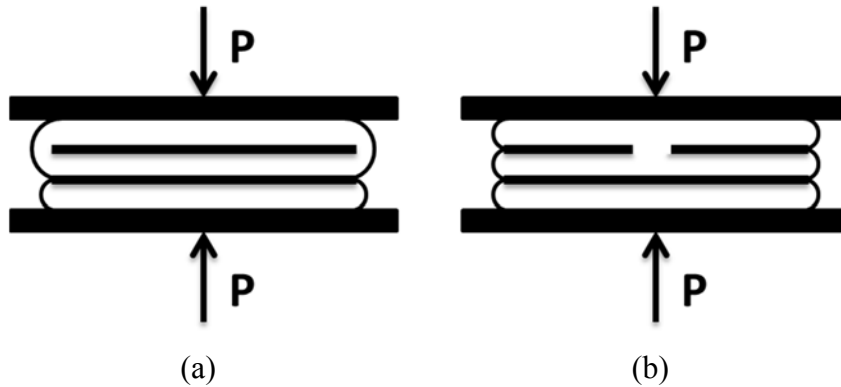


Figure 2.3: Compression failure due to (a) tension debonding and (b) fractured steel plates

2.3.1.2 Vertical stiffness of steel reinforced elastomeric bearings

The vertical stiffness of elastomeric bearings is an extremely important property of the bearing considering both pure compression from the girder reaction as well as for accommodating the necessary girder rotation. The vertical stiffness becomes particularly important for *higher demand applications* such as steel tub girder systems where lift-off between the girder and the bearing can be a concern. Lift-off is defined as the phenomenon where separation occurs between the girder and the top of the bearing under rotation, decreasing the area over which the compression is resisted. In addition, the axial stiffness of the bearing is important in calculating the relative deflection across an expansion joint, as expansion joints are sensitive to relative deflections (Roeder, Stanton et al. 1989).

The behavior of a steel-laminated bearing in compression can be simulated as the behavior of stacked bonded rubber blocks, assuming that the steel laminates are axially rigid relative to the rubber. Early work (Gent and Lindley 1959) was conducted assuming linear elastic behavior for rubber and accounting for incompressibility, resulting in the proposed apparent Young's modulus, E'_a , for the bonded rubber block given by

$$\frac{1}{E'_a} = \frac{1}{E_a} + \frac{1}{E_b},$$

where E_a is the apparent Young's modulus of the equivalent bonded incompressible rubber block, E_b is the modulus of bulk compression, and E_a is given by

$$E_a = \frac{4}{3} E(1 + S^2),$$

where E is the Young's modulus of the rubber, often replaced (Muhr and Thomas 1989) by $3G$, where G is the shear modulus of the rubber, and S is the aspect ratio, equal to the ratio of the loaded area over the area that is free to bulge. The above equations were developed for infinitely long strips of bonded rubber and have reasonable agreement with experimental data for low levels of stress.

Subsequent research (Gent and Meinecke 1970) developed analytical expressions for rubber blocks of any cross-section. Specifically, for rectangular sections the published solution for E_a is given by

$$E_a = 3G \left[\frac{4}{3} - \frac{2(lw + 4t^2)}{3(l^2 + 8t^2 + w^2)} + \frac{1}{3} \left(\frac{w^2}{l^2} \right) \left(1 - \frac{192w}{\pi^5 l} \sum_{n=1,3,5,\dots}^{\infty} \frac{1}{n^5} \tanh \left(\frac{n\pi l}{2w} \right) \right) \right],$$

where l is the length of the block, w is the width of the rubber block, and t is the thickness of the rubber block. More recent research (Yeoh, Pinter et al. 2002) has developed an analogous expression relaxing the assumption of incompressibility in the elastomer. The corresponding value of E_a is given by

$$E_a = 3G \left[\frac{4}{3} - \frac{2(lw + 4t^2)}{3(l^2 + 8t^2 + w^2)} + \frac{8}{t^2} \sum_{n=1,3,5,\dots}^{\infty} \frac{4wl}{n^2 \pi^2 \lambda_n^2} - \frac{8w}{n^2 \pi^2 \lambda_n^2} \tanh \left(\frac{\lambda_n l}{2} \right) \right],$$

where

$$\lambda_n^2 = \frac{n^2 \pi^2}{w^2} + \frac{12G}{t^2 E_b}.$$

The expressions presented above were developed for linear elastic material and are in good agreement for unfilled rubbers. However, filled rubber expresses nonlinearities in behavior at lower values of deformation and loads leading to a divergence of experimental results and predictions of the above equations. Filled rubber is rubber with added particles, such as carbon black, that modify the properties of the rubber, mitigate aging effects, and reduce the consumption of binder materials. Researchers (Muhr and Thomas 1989) have tried to reduce this divergence by providing a relationship that accounts for the material nonlinearities (strain-dependent shear modulus, $G_{\bar{\gamma}}$) based on the average shear strain in the layer, $\bar{\gamma}$, weighted for energy density. The proposed expression for the apparent compression modulus, $E_{c(ec)}$, is

$$E_{c(ec)} = 3G_{\bar{\gamma}}(1 + 2S^2),$$

where

$$\bar{\gamma} = \sqrt{3(1 + 2S^2)} \cdot e_c.$$

AASHTO (AASHTO 2012) specifies the compressive strain of each layer, e_c , as

$$e_c = \frac{\sigma_c}{4.8 \cdot G \cdot S^2}.$$

The above expression was adopted from previous research (Stanton, Roeder et al. 2008), acknowledging the fact that this simplified expression is prone to inaccuracies.

More recent research of bonded cylindrical discs (Anderson, Mott et al. 2004, Qiao and Lu 2014) proves the high sensitivity of the vertical stiffness on Poisson's ratio (v) for values of v close to 0.5 and large shape factors (larger than 10). This fact combined with the fact that for neoprene rubber (elastomer under consideration in this study) the values of v can range from 0.499 to 0.4999 (Holownia 1980) justifies the difficulty of finding an expression valid for the calculation of vertical stiffness of an elastomeric bearing. The complexity is further aggravated when accounting for the significant sensitivity of the measurement of v at low volumetric strains considering difficulties of fitting the testing sample into the testing device (Peng, Shimbori et al. 1994).

2.3.2 SHEAR

A steel-reinforced elastomeric bearing is expected to experience significant shear deformations during its design life, mainly due to thermal expansion and contraction of the

superstructure. Other loadings that can result in significant horizontal movements of the superstructure are earthquake, wind, and even traffic loads.

2.3.2.1 Cyclic Shearing

Cyclic shear deformation of a bearing can cause the creation and propagation of cracks at the interface between the reinforcement layer and the elastomer. Cracks are initiated at locations where tension debonding has occurred or the vulcanizing process was not completely successful. As the cracks propagate the tensile stresses at the steel shims are relieved, allowing adjacent layers of elastomer to bulge as one. This failure mode is illustrated in Figure 2.4.

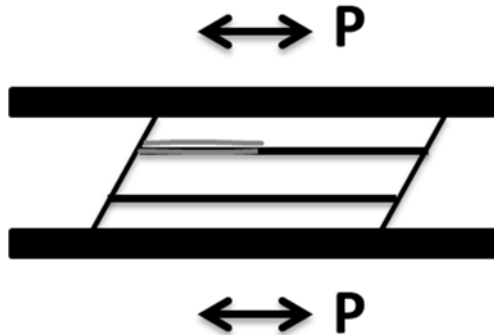


Figure 2.4: Delamination due to cyclic shear loading

2.3.2.2 Slipping

Knowledge of the bearing stiffness in each direction is important so that slipping is avoided. Slipping occurs when the force developed at the bearing-girder interface (or the bearing to substructure interface) due to the shearing of the bearing exceeds the static friction. The bearing shear stiffness ($K_{bearing}$) is dependent only on the plan area ($A=LB$), the total rubber thickness (H_{tot}), and the average rubber material shear modulus (G) as can be seen in:

$$K_{bearing} = \frac{G \cdot L \cdot B}{H_{tot}}.$$

In *higher demand applications*, i.e. curved box girders, it has been observed that the shearing of the bearing due to temperature effects on the bridge superstructure does not happen consistently in one direction throughout the year. The shearing direction is dependent on the bridge curvature but also the direction of the solar radiation, enabling predominantly longitudinal or transverse movements. Initial research conducted numerically (Nguyen and Tassoulas 2010) showed insignificant variability on the bearing shear stiffness for different shearing directions, although a reduction of the maximum shear strain was observed. However, no experimental data exists to validate or contradict these conclusions.

2.3.3 ROTATION

The rotational and axial demands on the bearing are often interrelated since both demands tend to increase when span lengths are increased. However, the design requirements for increased axial and rotational demands are often contradictory. To accommodate the high axial load, an axially stiff bearing is required. However, in order to prevent lift-off (Figure 2.5a) a

flexible bearing is required. While lift-off of the bearing on its own does not constitute a failure, the ramifications of lift-off can affect the axial performance since the vertical reaction must be resisted by a smaller area of the bearing, and thus, local compressive failure can initiate as a result of lift-off.

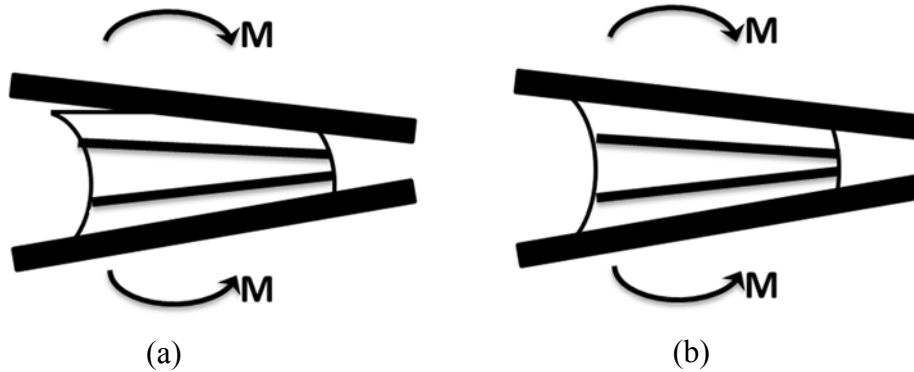


Figure 2.5: Bearing deformation for applied moment (a) with and (b) without lift-off

Past AASHTO provisions did not allow lift-off, and, as a result, the structural engineer had to find the balance between accommodating both the axial load and the rotational demands. Based upon research conducted by Stanton et al. (Stanton, Roeder et al. 2008) that showed that the effect of lift-off, if accounted in the design considerations, does not cause detrimental effects to the bearing, partial lift-off is allowed in the current version of AASHTO.

2.3.4 STABILITY

The shear modulus of an elastomeric bearing decreases with increasing axial load (Gent 1964, Stanton, Scroggins et al. 1990, Weisman and Warn 2012). The degradation in the stiffness makes instability in the bearing a potential concern. The buckling capacity decreases as the shear strains are increased, however, the thickness of the rubber layer is believed to have a greater influence than the shape factor in this effect (Buckle, Nagarajaiah et al. 2002). Tests associated with previous research were conducted at lower axial stress levels and shape factors up to approximately 15 were investigated. In addition, the bearing pads that were tested were significantly smaller than pads that would fit the characterization for *higher demand applications*. Because of stability concerns AASHTO does not allow exceeding half the buckling stresses.

2.3.5 SLIPPAGE

Another common failure mode is the slippage (walking out) of the bearing when it is not attached via a sole plate to the superstructure or via mechanical devices to the pier (McDonald, Heymsfield et al. 2000, Nims and Parvin 2000, Heymsfield, McDonald et al. 2001). In some cases, stability limits conflict with the limits imposed to prevent slippage. In such a case, occasional bearing slippage is preferred as no detrimental consequences have been reported as long as the slippage occurs between the bearing and the beam and not the bearing-pier interface (Bradberry, Cotham et al. 2005). However, in such a case, the sole plate must be designed to account for the relative displacement of the bearing.

2.4 Historical Development of Code Provisions

This portion of the literature review focuses on the historical development of design procedures for steel-reinforced elastomeric bearings. Although research on bearings has been conducted all over the world, design provisions in AASHTO (AASHTO 2012) are mainly a result of research funded by the National Cooperative Highway Research Program (NCHRP).

2.4.1 PERFORMANCE OF ELASTOMERIC BEARINGS - NCHRP 298

NCHRP 298 (Roeder, Stanton et al. 1987) presented the results on the investigation of the behavior of steel-reinforced elastomeric bearings under room and low temperatures. The study also focused on the behavior under compressive, shear, rotations, and combined loading, as well as investigating the limits for stability and fatigue.

The low temperature effect on the shear modulus of the elastomer was found to be noticeable and significant below 32 degrees Fahrenheit. In addition to the instantaneous stiffening of the elastomer, the shear modulus was found to continue to increase when the elastomer was exposed for longer periods to temperatures below 32 degrees Fahrenheit. This effect is called crystallization and was further investigated in subsequent research studies (Roeder, Stanton et al. 1989).

The investigation on the compressive and rotational behavior led to limits in the compressive stress of 1600 psi and the no-lift-off provision for the girder rotation. Furthermore, during this study, the 50% shear strain limit due to the shearing of the bearing (provision still existing today) was imposed as a result of observations of rollover during the tests. Rollover was believed to create a potential tearing failure in the elastomer, which would likely increase under repeated loading.

The reduction of the bearing shear stiffness with increasing load was also reported in this study, with no limit established or mathematical model presented. However, the difficulties in calculating the axial stiffness of a multi-layer steel-reinforced elastomeric bearing were identified.

2.4.2 LOW TEMPERATURE BEHAVIOR AND ACCEPTANCE CRITERIA FOR ELASTOMERIC BRIDGE BEARINGS - NCHRP 325

During this study (Roeder, Stanton et al. 1989) the behavior of natural rubber and neoprene steel-reinforced elastomeric bearings was investigated. The major outcome was that, although both materials experienced a shear modulus stiffening effect, the effect was more prominent for neoprene bearings for the same room temperature shear modulus. Moreover, the crystallization effect was extensively studied leading to a limit of the ratio of the shear modulus at cold temperature to the shear modulus at room temperature to a value less than four for both natural rubber and neoprene compounds. The phenomenon of relaxation was also investigated during this research study; however, subsequent research (English, Klingner et al. 1994) showed that relaxation tests do not represent realistic bridge behavior. Finally, acceptable fabrication tolerances were reduced.

2.4.3 ELASTOMERIC BRIDGE BEARINGS: RECOMMENDED TEST METHODS - NCHRP 449

NCHRP 449 (Yura, Kumar et al. 2001) investigated the test methods that should be used for evaluating steel-reinforced elastomeric bearings, proposed test methods to be used for material acceptance, and set limiting criteria. The researchers proposed the elimination of the

following previously required tests: Shore A Hardness, shear resistance, ozone resistance, and compression set. Also, aging tests were determined to be irrelevant for bearing sizes and shape factors utilized in civil engineering applications.

In addition to the elimination of certain tests for steel-reinforced elastomeric bearings, NCHRP 449 proposed an inclined shear test as a method to measure the shear stiffness of the bearings. The test involved inclined plates inducing shear in a bearing under compression. The inclined compression test provides a unique comparison of axial load vs. shear strain. Due to the fact that in the current study the effect of axial load on the shear stiffness for bearings that generally would be classified as higher demand applications needed to be investigated, this test method was not considered.

The detrimental effect of misalignment of steel laminates on the performance of elastomeric bearings was also investigated. The conclusions were that the horizontal misalignment of the laminates has less impact on the performance of the bearing than does variations in the rubber layer thickness or rotational misalignments. Lastly, the need for a better understanding of the temperature dependent interaction between the bridge superstructure and the elastomeric bearing was indicated, especially for the case of low-temperature stiffening including crystallization.

2.4.4 ROTATION LIMITS FOR ELASTOMERIC BEARINGS - NCHRP 596

NCHRP 596 (Stanton, Roeder et al. 2008) focused on the study of the rotational response of steel-reinforced elastomeric bearings. The study included static and cyclic tests for the evaluation of stiffness and failure limit states. It also involved finite element simulations.

Experimental results confirmed the existence of reserve capacity even after debonding of the elastomer from the steel laminates. This led to the conclusion of no unique definition of failure; however, it was observed that this phenomenon can expedite the propagation of delamination due to cyclic shearing. Experiments also proved the ability of steel-laminated bearings to carry axial loads up to 10 times greater than their design values and addressed a need for improvement of the manufacturing quality.

The finite element portion of the study indicated that stiffer compounds performed better for comparable loads. This improvement was markedly evident for bearing with higher shape factors. Furthermore, the difficulties for matching compressive stiffness were further confirmed and the need of investigating the effect of the aspect ratio on the axial and rotational performance of a bearing was indicated. Lastly, a proposal was made to relax the no-lift-off provision.

2.4.5 CURRENT DESIGN APPROACHES

Although some U.S. states, including Texas, follow their own design approaches and methodologies, all methodologies are generally based on AASHTO (AASHTO 2012) provisions for elastomeric bearings. The current AASHTO provisions allow the designer to choose between two methods, “Method A” and “Method B”, for proportioning the bearing and are described in the following subsections.

2.4.5.1 Method A

Relatively to Method B, Method A produces inherently more conservative designs as a result of the stress limits associated with it. The implicit rotational and stability limits are met as a result of the geometrical constraints imposed by this method. Specifically the method provisions are presented in Table 2.1.

Table 2.1: AASHTO Limits for Method A

Geometric limit	Compressive stress limit	Rotation limit	Shear deformation limit	Stability limit
$\frac{S_i^2}{n} < 22$	$\sigma_s < 1.25GS_i$ & $\sigma_s < 1.25 \text{ ksi}$	Implicitly accounted for	$\Delta_s < \frac{h_{rt}}{2}$	$h_{rt} < \frac{L}{3}, \frac{W}{3}, \text{ & } \frac{D}{4}$

In the table above, σ_s is the average compressive stress from applicable service load combinations, S_i the shape factor of an internal elastomer layer, n the number of internal layers, G the shear modulus of the elastomer, Δ_s the maximum shear deformation of the elastomer from applicable service load combinations, and h_{rt} the total elastomer thickness. L and W are the plan dimensions of a rectangular bearing and D is the diameter of a circular bearing.

2.4.5.2 Method B

Method B adopts a total shear strain approach, namely the explicit summation of the shear strain components at the steel-elastomer interface coupled with an amplification factor on cyclic components. Cyclic components include shear strains caused by traffic, earthquakes, and other transient loads. Thermal shear strains may not be counted as cyclic due to their low strain rates. The shear strain components corresponding to a specific deformation mode are depicted in Figure 2.6.

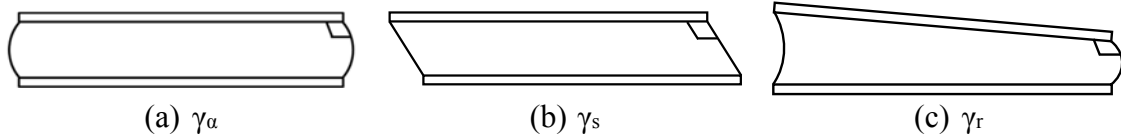


Figure 2.6: Shear strain at the steel-elastomer interface due to (a) axial load, (b) shear load, (c) rotation

The limit ($\gamma_{cap}=5.0$) for the total shear strain as a summation of the static values and the amplification of the cyclic components is not representative of the ultimate strain the material can withstand. Rather, it is an empirical limit, reflecting monotonic and cyclic test data (Stanton, Roeder et al. 2008) and is currently adopted by AASHTO (AASHTO 2012) and the European code (EN1337-3 2005). The shear strains due to each deformation mode are calculated according to equations summarized in Table 2.2.

Table 2.2: Shear strain components at the steel-elastomer interface

Bearing geometry	γ_a	γ_s	γ_r
Rectangular	$1.4 \left(\frac{\sigma_s}{GS_i} \right)$	$\frac{\Delta_s}{h_{rt}}$	$0.5 \left(\frac{L}{h_{ri}} \right)^2 \frac{\theta_s}{n}$
Circular	$1.0 \left(\frac{\sigma_s}{GS_i} \right)$	$\frac{\Delta_s}{h_{rt}}$	$.375 \left(\frac{D}{h_{ri}} \right)^2 \frac{\theta_s}{n}$

In the table above, h_{ri} is the thickness of an internal elastomer layer and θ_s the maximum service limit state rotation angle.

In addition to the total shear strain limits, Method B accounts for stability as a failure mode of the bearings. As a result, the design of taller bearings with reduced shear forces is permitted. The checks associated with stability include the comparison of two geometry-related factors A and B . The equations for those factors are as follows:

$$A = \frac{1.92 \frac{h_{rt}}{L}}{\sqrt{1 + \frac{2.0L}{W}}}$$

$$B = \frac{2.67}{(S_i + 2.0) \left(1 + \frac{L}{4.0L} \right)}$$

and the following condition should be satisfied: $2A \leq B$.

If the former condition is not satisfied the capacities should be compared to the average compressive stress. In the case of bridges where the deck is free to translate horizontally the following expression should be satisfied:

$$\sigma_s \leq \frac{GS_i}{2A - B}$$

If the bridge deck is fixed against horizontal translation the following expression should be satisfied:

$$\sigma_s \leq \frac{GS_i}{A - B}$$

For the purposes of this study, the first expression is used since the case of elastomeric bearings that are also used to accommodate horizontal translations will be addressed.

AASHTO also provides expressions for checking the thickness of the steel reinforcement against yielding and fatigue. However, for constructability purposes, particularly for bearings designed for higher demand applications the thickness will always be larger than the minimum specified by AASHTO, which also includes expressions for the axial deflections.

CHAPTER 3: FIELD MONITORING OF STEEL TUB GIRDER BRIDGE WITH ELASTOMERIC BEARINGS

3.1 Bridge Instrumentation

The primary applications for the elastomeric bearings have historically been in short to medium span bridges with relatively moderate magnitudes of bridge reactions and deformation demand. However, the researchers on this study are aware of two bridge projects in Central Texas where elastomeric bearings have been used in higher demand applications. The researchers choose one of these bridges for extended monitoring to gain a measure of the bearing performance as well as the demand on the bearing throughout an annual thermal cycle. The bridge selected for field monitoring was a direct connector between IH-35 N & US-290 E in North Austin as shown in Figure 3.1. This bridge was one of the first bridges where the elastomeric bearings were used in a “higher demand application.” Although the majority of the bearings are behaving as expected, a few of the bearings are showing some minor damage, and one bearing had much more extensive damage. The damage to the bearings was documented in reports from the routine maintenance inspections.



Figure 3.1: IH-35 N & US-290 E direct connector

As shown in Figure 3.1, the bridge consists of twin trapezoidal box girders to form the horizontally curved direct connector. An attractive feature to this bridge for the field monitoring was the ability to access the box girders on the south end of the bridge using a simple extension ladder. In addition, this bridge is in close proximity to Ferguson Structural Engineering Laboratory (FSEL), which minimized travel in cases where potential problems may have occurred with the instrumentation. The proximity of the bridge to FSEL proved important since a number of visits were necessary throughout the year as the wireless system needed manual restarts and battery changes.

3.1.1 INSTRUMENTATION OVERVIEW

The primary goal of the field instrumentation was to gain a measure of the movements of the girders at the bearing locations. A number of different sensors were therefore used to capture these movements: linear potentiometers, inclinometers, and mechanical devices that recorded a displacement trace of the support translations. Figure 3.2 illustrates the layout of the linear potentiometers installed, and Figure 3.3 shows the measured deformations acquired at each support location.

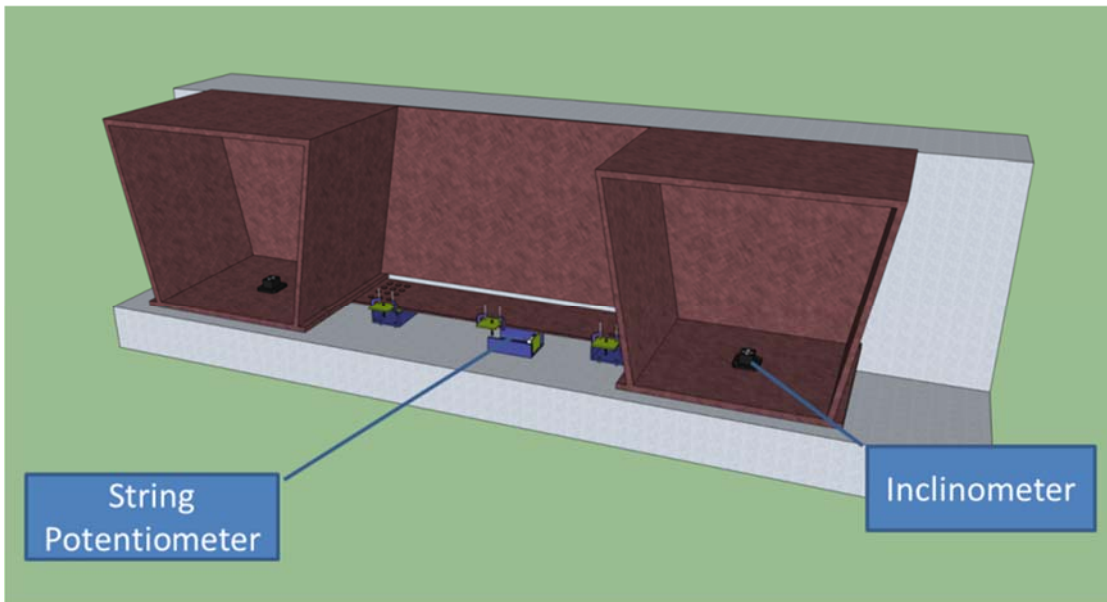


Figure 3.2: Typical instrumentation at each support location

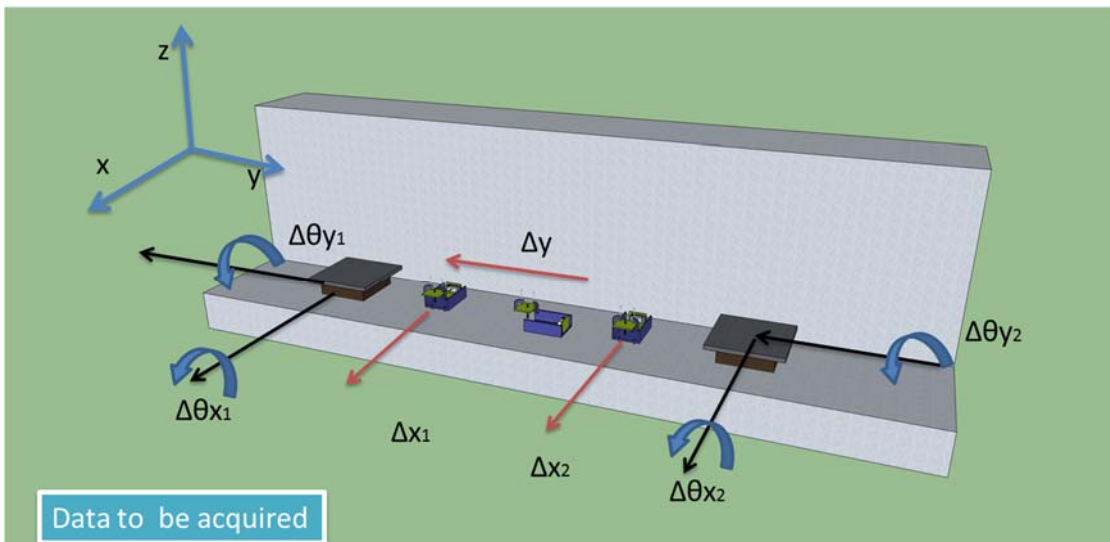


Figure 3.3: Measured displacements at each support location

3.1.1.1 Trace Devices

To validate the results obtained from the wireless data acquisition system (DAQ), mechanical trace devices were placed at each bearing location. These devices were developed on Project 0-5040 (Chen et al. 2009). The devices consisted of containers with a layer of microcrystalline wax as shown in Figure 3.4. The containers were attached to the abutments and pier caps with an adhesive adjacent to the bearing locations. A stylus attached to the bottom flange was inserted into the wax trace box that was fastened to the pier. The stylus moves with bridge as the girders expand and contract due to changes in the thermal environment. The movement therefore leaves a trace in the wax that provides a measure of the magnitude and direction of the movement of the girders relative to the pier cap. Since these movements are accounted for by the elastomeric bearing, the devices provide a mechanical measurement of the extreme demand on the bearings throughout the year. All trace devices were placed at an ambient temperature within the range of 63-67 °F. A 0.5 in. × 0.5 in. grid was drawn, and the initial point of submersion was always the 0, 0 point. Because the abutment on the South end of the bridge could be reached with a ladder, those trace devices were accessible by the researchers without the need of a special aerial lift, which allowed frequent comparisons between the mechanical and electrical measurements to make sure proper data was being recorded.. Comparisons of the trace devices and the electronic readings on the other piers were not possible without a boom lift or bucket truck.

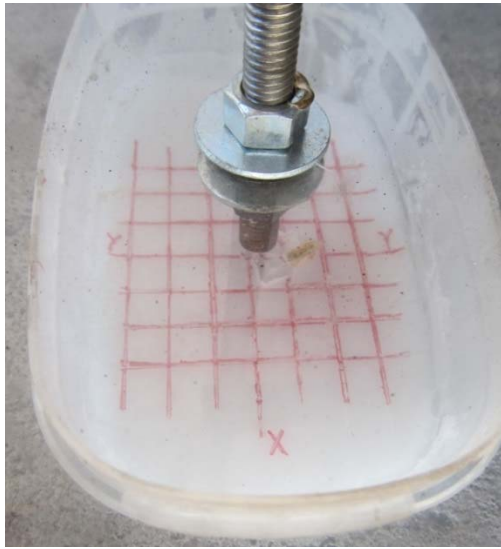


Figure 3.4: Trace box with 0.5 in. x 0.5 in. grid

3.1.1.2 Inclinometers

Inclinometers are linear displacement voltage transducers (LVDTs) used to measure rotation. In this study, a total of eight Rieker RDD-13 inclinometers were utilized. These sensors were chosen due to their high accuracy, their dual axis of rotation capacity, and their temperature compensation over the range of temperatures expected in the box girders of the instrumented bridge. The inclinometers were attached to steel angles that were connected to the bottom flange of the box girder at each bearing location using an epoxy adhesive as shown in Figure 3.5, which shows the inclinometer installed between two bearing stiffeners at a plate diaphragm inside one of the box girders.



Figure 3.5: Inclinometer installation

3.1.1.3 String Potentiometers

String potentiometers were used to electronically measure the displacement of the girders at the bearing locations relative to the piers. In this study, a total of twelve UniMeasure P510 string potentiometers were utilized. These particular potentiometers were chosen due to their temperature compensation and resistance to weather, which was an important feature since the sensors were placed in the relatively harsh environment on tops of the piers. The potentiometers were connected to a steel mounting angle that was attached to the pier cap or abutment using an epoxy adhesive. The individual potentiometers were oriented to capture either the transverse or horizontal movement of the diaphragms that frame between the two girders. The movements of the diaphragms relative to the pier cap or abutment provides a direct measure of the girder movement. An illustration of an installed string potentiometer can be seen in Figure 3.6.



Figure 3.6: String potentiometers in service

3.1.1.4 Linear Potentiometers

Displacements at the end of the curved tub girder due to the thermal movement of the bridge were further investigated by additional linear displacement sensors. As is shown in Figure 3.7, the linear displacement sensors (linear pots) were installed at the center of the bottom flange of the tub girders. The displacements along the transverse and longitudinal directions are captured by the linear pots. Furthermore, the sensors served as verification of the data obtained from the string potentiometers.

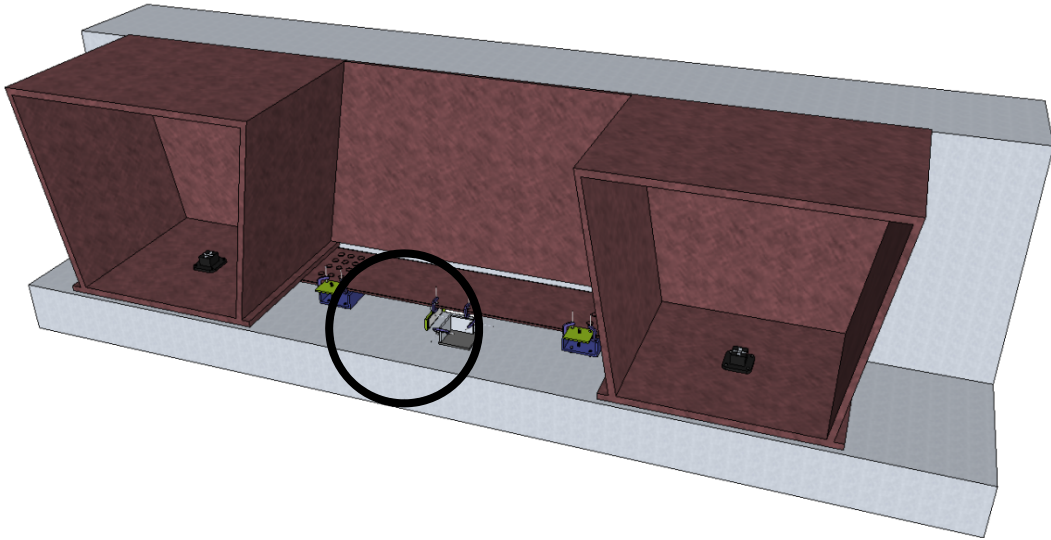


Figure 3.7: Linear pot location

Steel stands were fabricated to support the linear pots. Details are shown in Figure 3.8 and Figure 3.9. Two linear pots were clamped to a steel angle that is attached to the top of the bridge pier. Another steel angle was clamped at the bottom flange of the tub girder. The two linear pots are oriented so as to capture the displacements along the longitudinal and transverse directions. Teflon was utilized to reduce the friction between the tips of the linear pots and the steel plates. In Figure 3.8, the plates (shaded green) follow the bridge movement. The linear pots fixed to the bridge piers captured this movement.

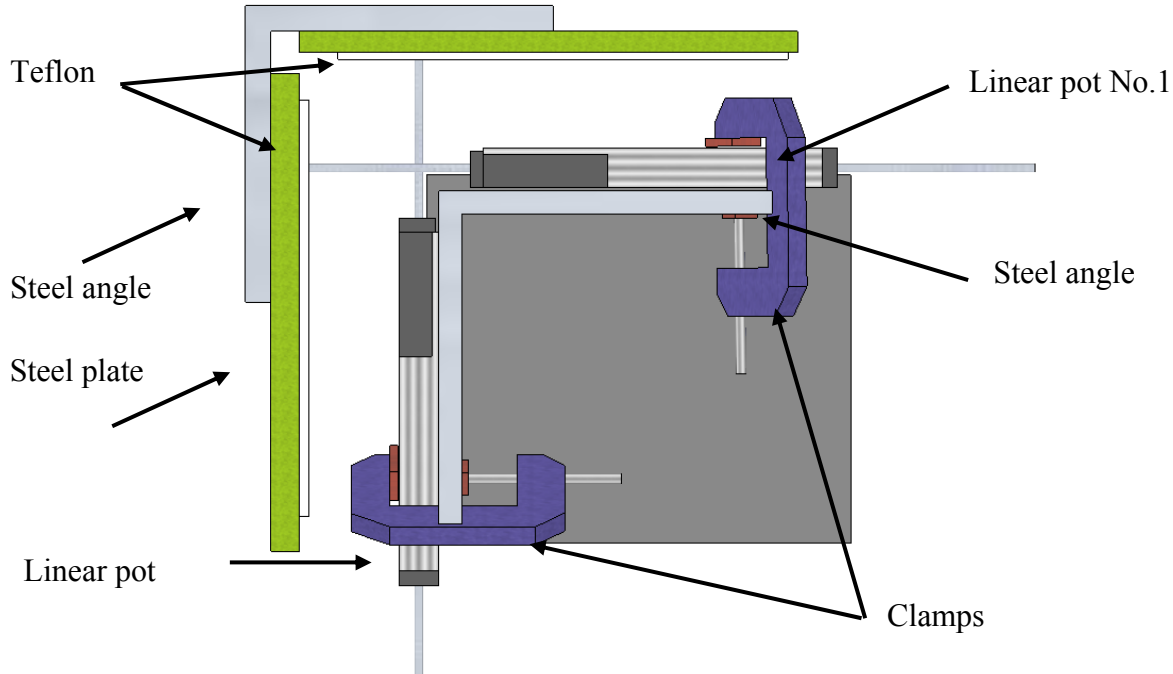


Figure 3.8: Detailed schematic of the assembly



Figure 3.9: Linear pots in service

3.1.1.5 Thermocouples

Thermocouples were installed in the second span of the west girder at the web and bottom flange locations. The main purpose of the thermocouples was to measure the ambient temperature as well as the temperature differential at a given cross-section for a more precise calibration of the finite element models so as to model the full bridge and predict the movements at the support locations.

3.1.1.6 Nodes, Gateway and Cellular Modem

The electronic displacement sensors and thermocouples provide an analog output voltage. This voltage was captured by wireless nodes placed at the support locations and transferred wirelessly to a gateway installed close to the bridge access port. The gateway was programmed

to transform the voltage readings to engineering units of interest (translations and rotations) and stored the data acquired on the built-in hard drive. The data was backed-up periodically at the FSEL server through a cellular modem placed in the bridge and connected to the DAQ system. Another use of the cellular modem was to provide researchers the ability to monitor real-time the instrument recordings and the battery status of the system. A schematic of the data transfer for the wireless network that was used on the bridge is shown in Figure 3.10. The wireless nodes can be configured to serve as either an “end node” or a “router node.” End nodes obtain readings from the sensors and transfer the data to a router node. Router nodes can obtain readings from sensors as well as data from other nodes. The router nodes then transfer the data to other router nodes or to the gateway.

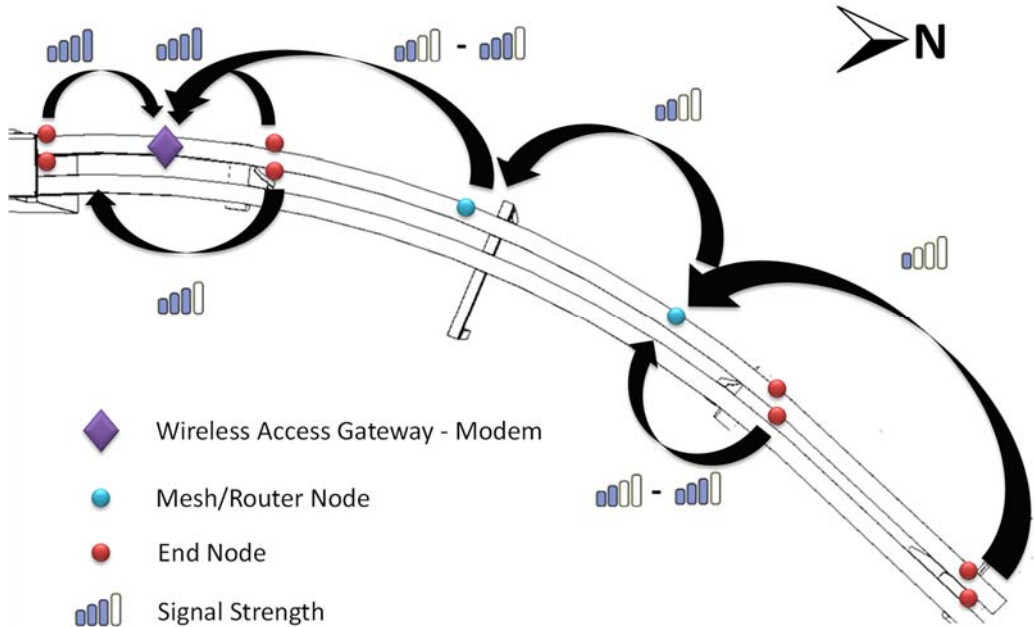


Figure 3.10: Layout of the wireless DAQ network inside the bridge

In Figure 3.10, the red nodes represent the end nodes, while the blue nodes represent mesh/router nodes. The research team tried to limit the use of router nodes as they increase the power consumption of the system and can be potential sources of data loss. All the acquired data was collected at the gateway (purple diamond) where it was stored and transmitted to the cellular network with the help of a cellular modem.

3.1.1.7 Powering the System

The field instrumentation system was powered with the use of a solar panel and rechargeable batteries. The power consumption was measured to ensure that the installed system provided a sustainable solution. The power consumption for each of the groups of devices used in the field monitoring study is presented in Table 3.1.

Table 3.1: Power consumption for each group of devices

Device	Number	Current (mA)	Voltage (V)	Group Power Consumption (W)
Wireless Access	1	610	12	7.32
WSN nodes	10	16	12	1.92
Inclinometers	8	20	12	1.92
String Potentiometers	12	25	12	3.6
Total				14.76

The solar panel installed at the abutment of the bridge has a nominal output power of 85W. Based on previous FSEL research, a good estimate of the output power that is charging the battery is approximately half of the nominal output power of the solar panel. As a result, the system will draw three times less energy than the energy produced and stored in a set of five batteries of 80Ah each. This configuration was chosen to account for cloudy days and the winter period, when the sun exposure is significantly reduced compared to summertime.

3.1.2 INSTALLATION

The installation of the instrumentation was completed in multiple phases due to the need of a bucket truck that was provided by TxDOT. The bucket truck was necessary to access many of the piers and also to feed wiring from the exterior of the girders to the interior of the box girders. The first phase of the instrumentation involved the installation of the inclinometers in the east girder. The second phase of the instrumentation included the transfer of the cables from the east girder to the west girder (Figure 3.11) and the installation of the trace devices and inclinometers at each support location (Figure 3.12). The last phase included the installation of the inclinometers in the west girder and the setup of the data acquisition system.



Figure 3.11: Cables from east girder entering the west girder through a hole provided for drainage



Figure 3.12: Instrumentation in the exterior of the bridge using a bucket truck

3.1.3 DATA ACQUISITION PROGRAM

The program that was developed for data acquisition from all the devices had a sampling rate of 1 Hz and a rolling average of the last four readings. This solution was chosen as a balance

between optimum power consumption without changing the solar panel already installed. The rolling average was utilized for minimizing the data loss due to network congestion. Although the program and device configuration performed well, effort was put into optimizing the program and configuration to provide a reliable and sustainable structural health monitoring system. An illustration of the graphical user interface (GUI) of the program developed is shown in Figure 3.13.

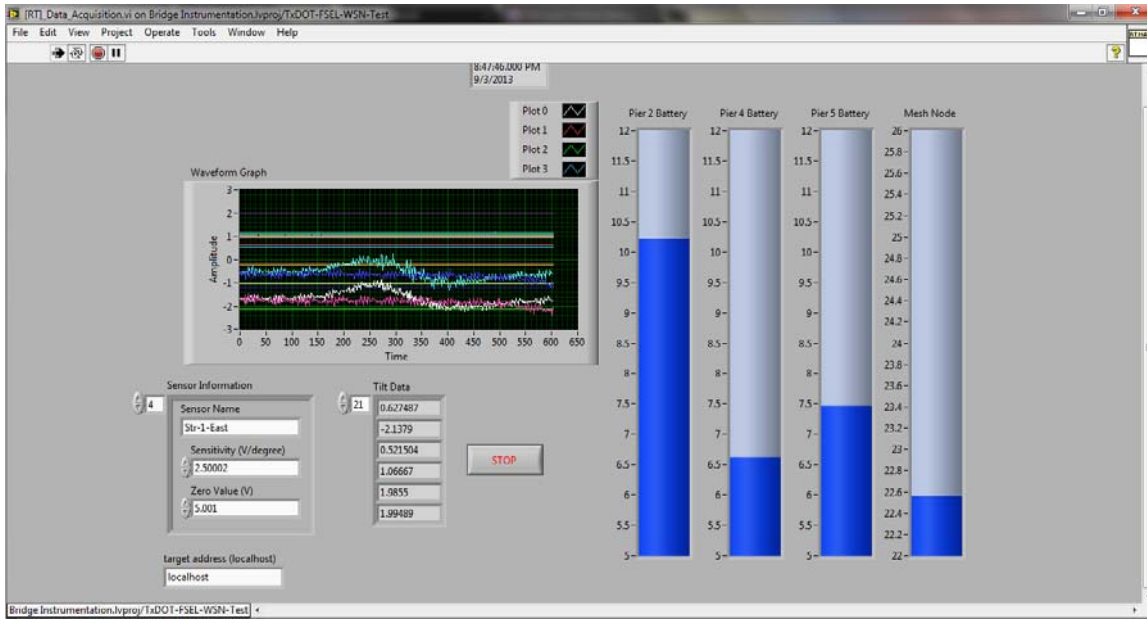


Figure 3.13: GUI of the real-time bridge monitoring program

3.2 Interpretation of Instrumentation Results

3.2.1 METHODOLOGY

The raw data from the instrumentation measurements were downloaded periodically and processed by codes developed in the commercially available mathematical software MATLAB. These programs refine the raw data with mathematical algorithms and extrapolate the actual movement at the center of each elastomeric bearing.

3.2.2 DATA CORRECTION FOR TRANSLATIONAL MOVEMENT MEASUREMENTS

Data correction for translational measurements may be required when the measured translational movements of an object are not oriented directly along the measuring axis of the sensor. For example, the box girders experienced movements in both the longitudinal and transverse direction. As a result, the string potentiometer readings often include a measure of the movements in both the longitudinal and transverse directions. If the box girders were to only move in either the longitudinal or transverse direction, the measurement from the string potentiometer would be the actual translation. However, since the box girder actually translated in both the longitudinal and transverse direction, each actual translation was different from the raw string potentiometer measurements because the cable extension of a string potentiometer is affected by a translation perpendicular to the axis of measurement.

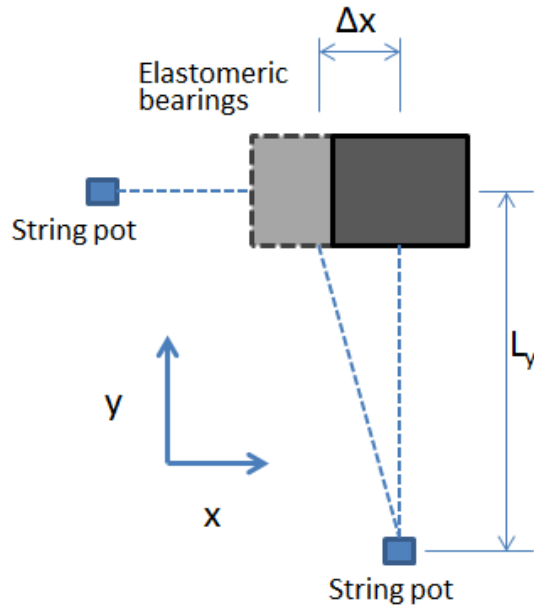


Figure 3.14 : Movements of the bearing relative to the string potentiometer position.

This effect is demonstrated in Figure 3.14 that shows the behavior of two string pots that are oriented to capture movements in the x and y directions. Considering the pot oriented to measure displacements in the y -direction, bearing movement in only the x -direction results in a measurement from the y -direction potentiometer. This “apparent” movement leads to the discrepancy between the actual translations and the measured value. The relation between actual translations and string potentiometer measurements is expressed in following equations.

$$\begin{cases} (\Delta x + L_x)^2 + (\Delta y)^2 = (\delta x + L_x)^2 \\ (\Delta y + L_y)^2 + (\Delta x)^2 = (\delta y + L_y)^2 \end{cases}$$

where Δx , Δy are the actual translations, δx , δy are the string potentiometer measurements. The non-linear equations above were solved in MATLAB by the trust-region-dogleg method.

3.2.3 DATA EXTRAPOLATION

The field instrumentation was not able to directly record the translations of each bearing because the string potentiometers could not be installed at the geometric center of the elastomeric bearings. The actual movements of each bearing were extrapolated in terms of their spatial locations with regard to the devices.

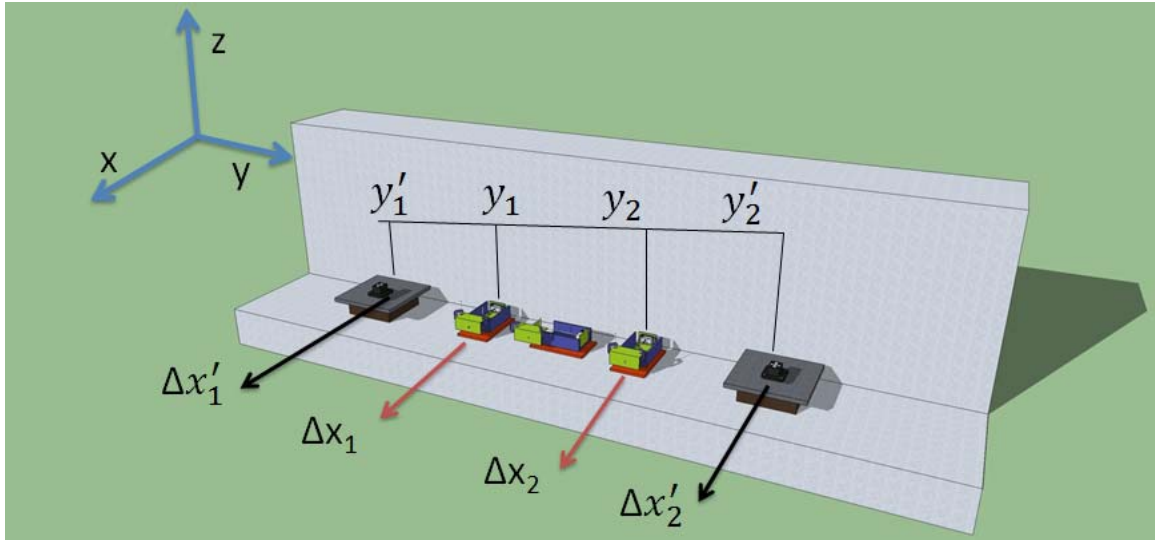


Figure 3.15 : Actual and extrapolated measurements from string potentiometers

As presented in Figure 3.15, Δx_1 and Δx_2 are the measured translational movements in the x -direction, and $\Delta x'_1$ and $\Delta x'_2$ are the translational movements of the elastomeric bearings in the x -direction at the center point to be determined. The values y'_1 , y'_2 , y_1 and y_2 represent the location in y -direction. It was assumed that the trapezoidal box girder is rigid at the transverse section as the girder is stiffened by a steel plate diaphragm at this location. Therefore, the movements of the elastomeric bearings in x -direction are extrapolated based on the assumption of linear distribution along the y direction:

$$\begin{cases} \Delta x'_1 = \Delta x_1 + \frac{y'_1 - y_1}{y_2 - y_1} (\Delta x_2 - \Delta x_1) \\ \Delta x'_2 = \Delta x_2 + \frac{y'_2 - y_2}{y_2 - y_1} (\Delta x_2 - \Delta x_1) \end{cases}$$

3.3 Field Instrumentation Results Summary and Observations

3.3.1 TEMPERATURE MONITORING

The period of monitoring of the bridge was more than one year. Representative data of girder temperature measurements and ambient air temperature records during both winter and summer are presented in Figure 3.16 and Figure 3.17. The temperatures experienced by the girder are higher than the ambient air temperature, by a margin of up to 40°F in the summer. Subsequently, it confirms the theory that the thermal response of the bridge is highly contingent on changes in the weather environment in both the heating and cooling phases. This could be less of a concern in a bridge with several girders because the majority of the spans are not exposed to direct solar radiation. However, in twin-girder systems the significance of the deformation of one girder can be substantial.

Table 3.2 presents the maximum and minimum ambient temperatures for the period of monitoring, as well as the 10, 20, and 50-year respective values for the area. The range of the ambient air temperature fluctuation for 50 years is 108°F. Considering the 40°F temperature

difference between the girder and air, the range of girder temperature fluctuation was estimated to be 148°F over a 50 year time scale, which considerably exceeds the design value of 120°F.

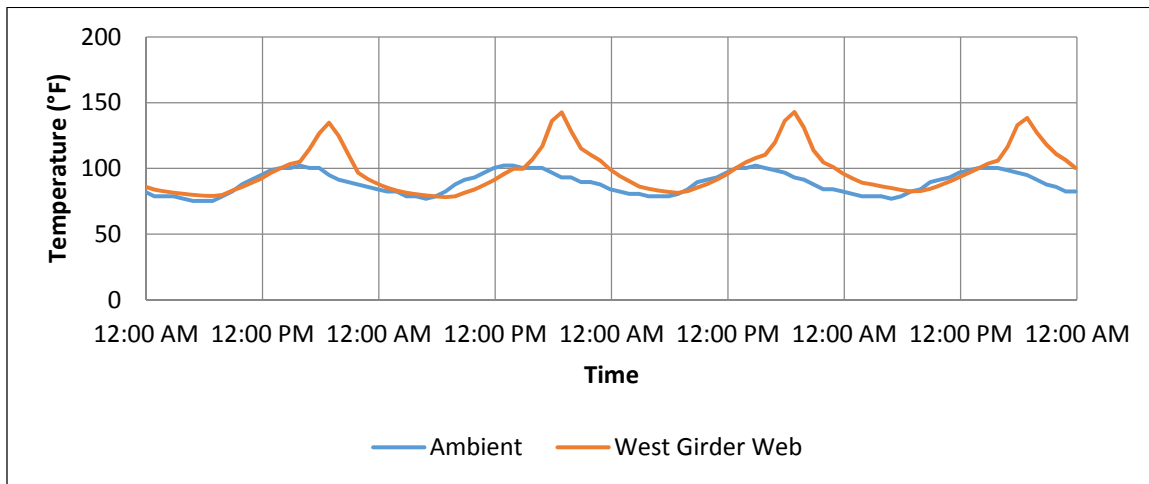


Figure 3.16: Ambient and Girder Temperatures for 07/31/2013-08/03/2013

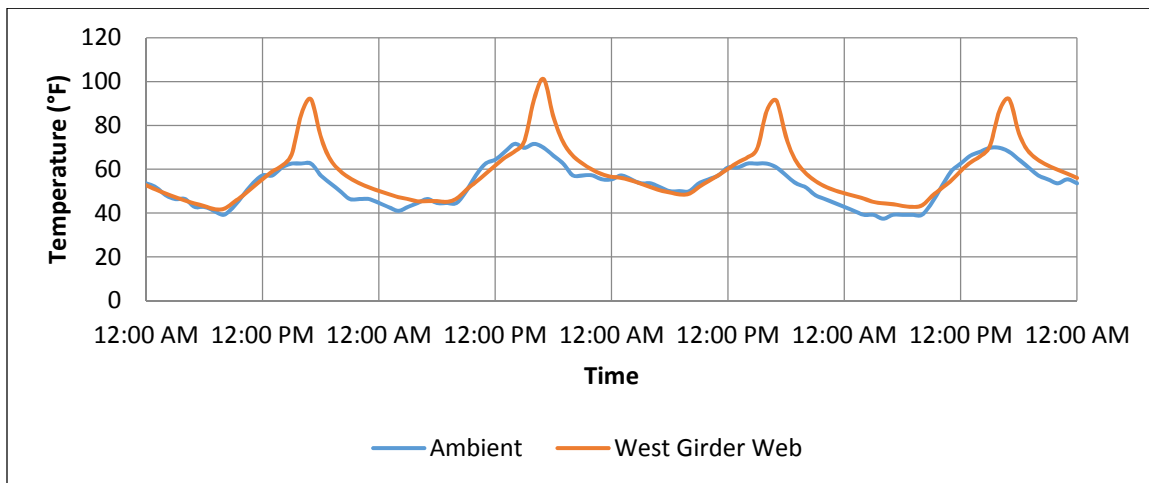


Figure 3.17: Ambient and Girder Temperatures for 1/14/2014 - 1/18/2014

Table 3.2: Maximum and minimum recorded temperatures for Austin (Source: Utah Climate Center)

Period	Ambient Temperature	
	Maximum (°F)	Minimum (°F)
1 year	108	22.2
10 years	111.2	8.6
20 years	111.9	8.6
50 years	111.9	3.9

3.3.2 TRANSLATIONS

3.3.2.1 Displacements Monitoring

Figure 3.18 and Figure 3.19 present the time-history of the representative data of both longitudinal and transverse displacement measurements between 08/01/2013 and 08/07/2013, respectively.

The data from the field monitoring reveals that the solar azimuth plays an important role in the thermal response of the bridge. Figure 3.20 shows the trace of daily thermal cycles of the bridge movement at bent 2, synthetized from the longitudinal and transverse displacement measurements. The data shows that the daily thermal cycles significantly differ from each other and are dependent on the time of the year. This effect can be attributed to the difference in the angle of incidence of the solar radiation on the structure.

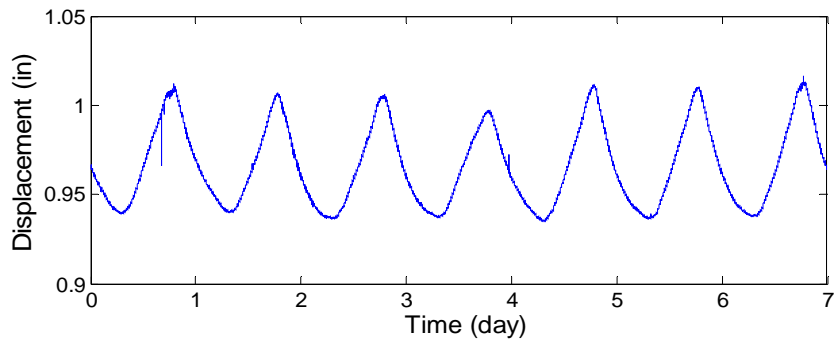


Figure 3.18: Longitudinal displacement measures time history of a week

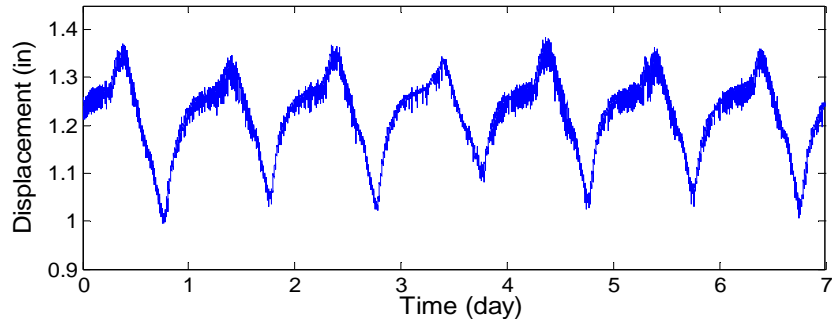


Figure 3.19: Transverse displacement measures time history of week

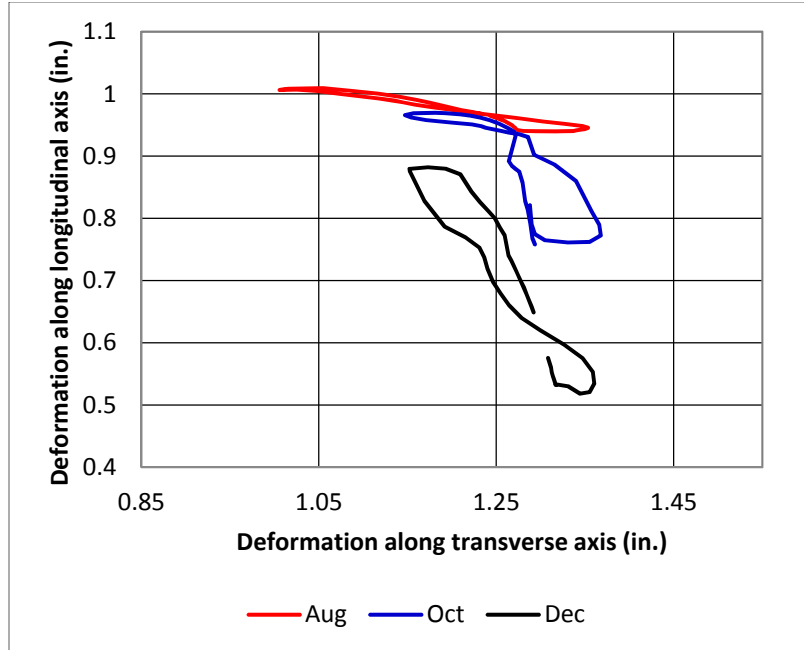


Figure 3.20: Different deformation patterns for different periods of the year

3.3.2.2 Summary of Translational Movements

One of the goals of the field monitoring was to capture the translational demand on the bearings through an annual thermal cycle. Figure 3.21 illustrates the measured and design range of displacements at each bent for a temperature difference of 120 °F. As can be seen, the actual longitudinal demands are reasonably close to the design values for the exterior bents (Bents 1 and 5). For the interior bents, the design values over-predict the measured values by as much as 400%. The cause of this difference is likely similar to behavior observed in previous studies on the thermal performance of steel bridges (Chen et al., 2009) in which the shear forces that develop between the girders and the bearings result in deformations from the bents. The first support of the bridge is a rigid abutment and as a result the shear that develops between the bearing and the support results in immeasurable deformation in the substructure. Bents 2 and 4 support only the steel box girders and therefore the support reaction is in a single direction and likely results in flexing of the pier. Bent 5 serves as the support for two bridges, the steel box girder unit and a prestressed concrete girder bridge. Because the two different bridges are able to deform relative to one another, the shears that develop between the bearings are in opposite directions, therefore reducing the deformation in the supporting pier. It can also be seen that the design values for the transverse translations differ from the measured displacements in all bents except from bent 4, where the center of the arc segment of the direct connector is. This can raise concerns over the assumptions made for the thermal analysis of the bridge, especially assumptions made about the support conditions.

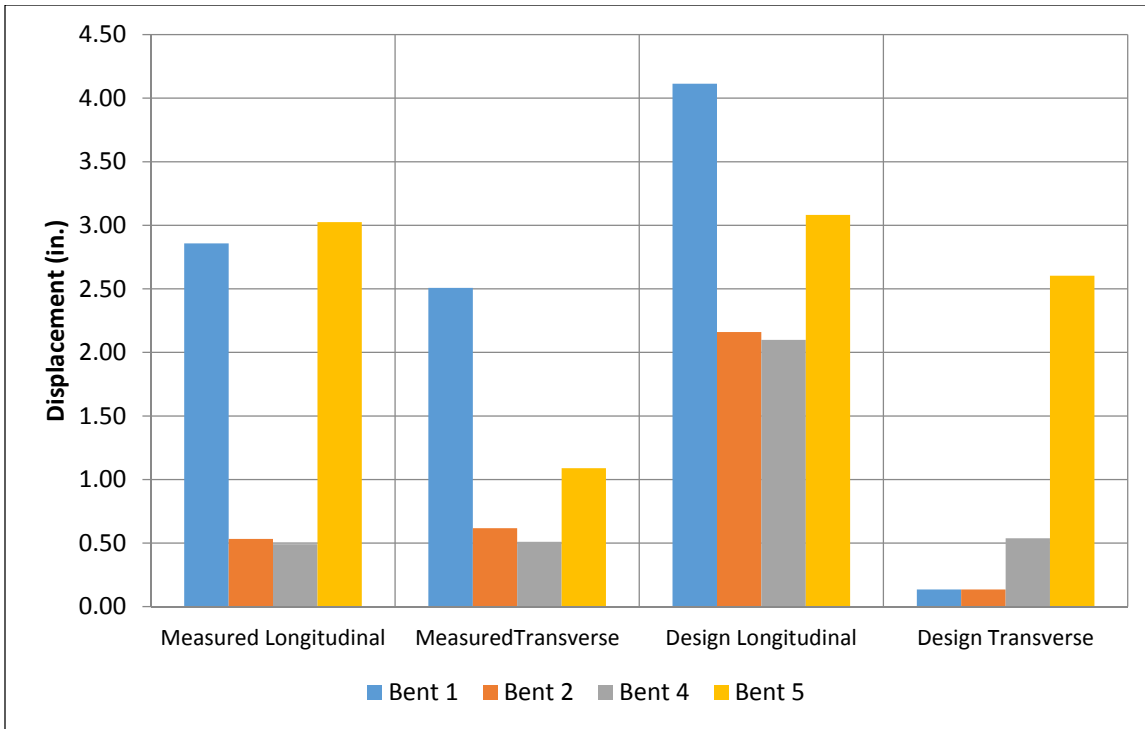


Figure 3.21: Range of displacements in the longitudinal and transverse directions for each bent

3.3.3 ROTATIONS

The biaxial rotations at each girder were also collected by inclinometers. Representative data of biaxial rotations time history at bent 2 between August 1st and August 28th are presented from Figure 3.22 to Figure 3.23.

The instrumentation measurements of the bridge movement (both translations and rotations) are in fact the combined effect of relatively long-term thermal loads and transient traffic loads. The rotation measurements show that the structural response of the bridge due the vehicular traffic significantly exceeds those induced by thermal loads, forming a sharp contrast to the translational measurements for which the structural response due to the traffic are minor compared with the thermal effects. To gain a better understanding of the behavior of bridge movements, the structural response due to the thermal effect and traffic loads needs to be isolated.

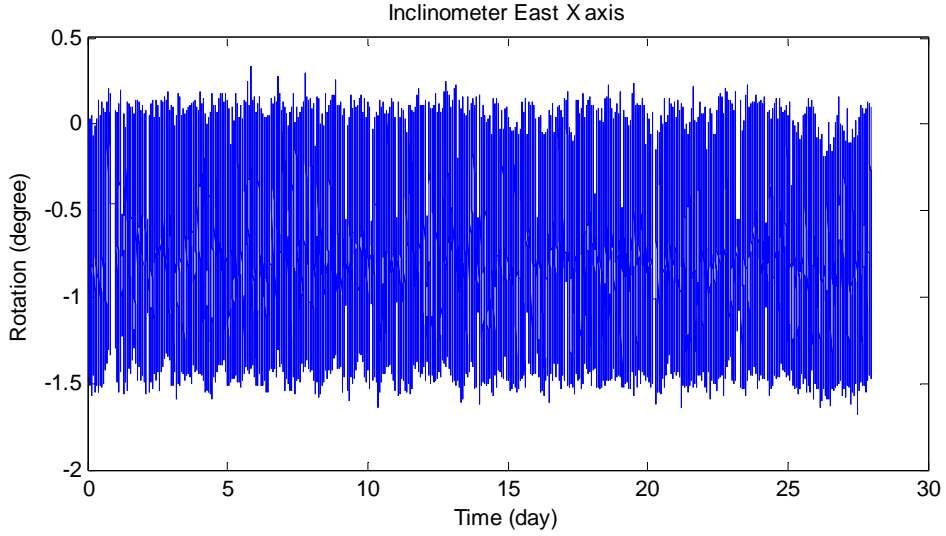


Figure 3.22: X axis rotation of east tub girder at bend 2 – 28 days

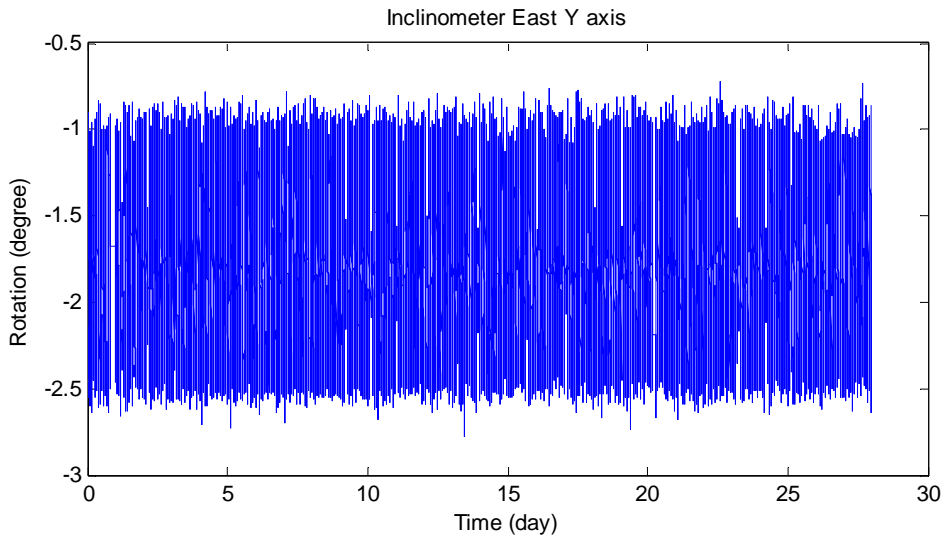


Figure 3.23: Y axis rotation of east tub girder at bend 2 – 28 days

3.3.3.2 Time-Frequency Analysis

A time-frequency analysis approach was adopted in this study to separate the rotational effects of the different loads. The primary characteristic of the structural response of the bridge structure subject to traffic loads is a relatively short duration due to the transient nature of vehicular traffic. The thermal effects on the bridge structure, conversely, last over a much longer period of time. Therefore, the structural response due to the traffic has an appearance that is similar in form to high-frequency “noise,” while the thermal effect is similar to the low frequency “signal” in the time domain. Therefore, mapping the measurement records from the time domain to the frequency domain will help decompose all values into components of different frequencies, hence the high frequency “noise” can be separated from the low frequency

“signal” with ease. A type of discrete Fourier transform algorithm, the Fast Fourier Transform (FFT), is used in this study providing fast and efficient results for data processing.

3.3.3.3 Filtering Example

Figure 3.24 presents the girder twist measurements at bent 1(abutment) between 03/13/2013 and 03/19/2013. As mentioned in the previous section, the measurements include combined effects of thermal and dynamic response. Fast Fourier Transform analysis is first performed to map the data from the time domain to the frequency domain.

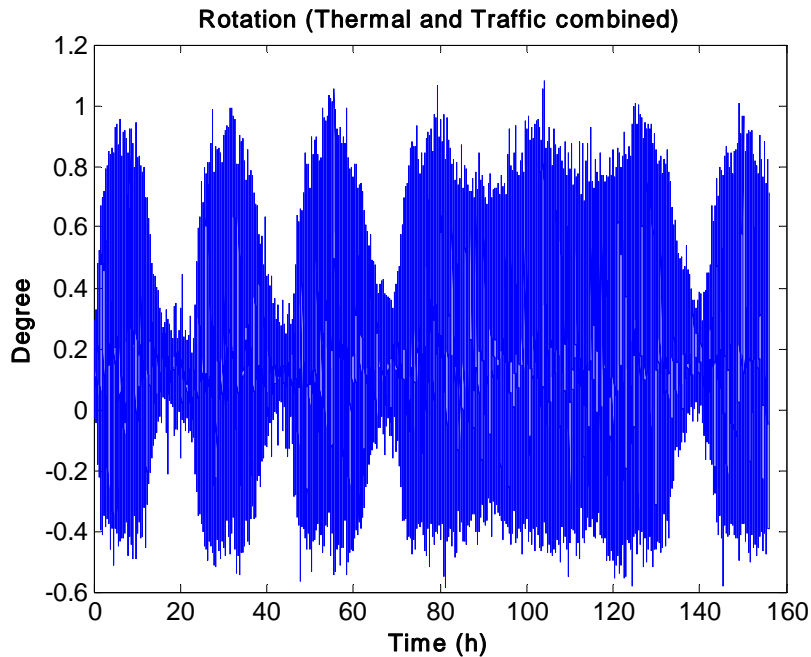


Figure 3.24: Torsional rotation measured at bent 1

Figure 3.25 presents the norm of the data after they have been mapped. They are complex numbers and are symmetric on the frequency domain by the nature of Fourier Transformation. The two ends of the frequency spectrum represent the low frequency components of the data, whereas the interior of the spectrum stands for the high frequency components of the data. Hence, it was possible to separate the low frequency signal, which is the torsional rotation due to the thermal effect, from the high frequency “noise,” which is mainly the torsional rotation due to the traffic loads, by removing the interior high frequency components from the spectrum. The data can then be mapped from the frequency domain back to the time domain using Inverse Fast Fourier Transform Algorithm (IFFT). Finally the torsional rotation time-history was obtained due to solely the thermal effects, as shown in Figure 3.26.

The calculated thermal response time history in Figure 3.26 exhibits a visually observable pattern of fluctuation as a function of time of day that is synchronized with the temperature time history as presented in Figure 3.27.

The range of calculated torsional rotation due to the thermal effect is 0.1497 degree, which is significantly lower the range of variation of the total torsional rotation, 1.0814 degrees during this period of time, as expected.

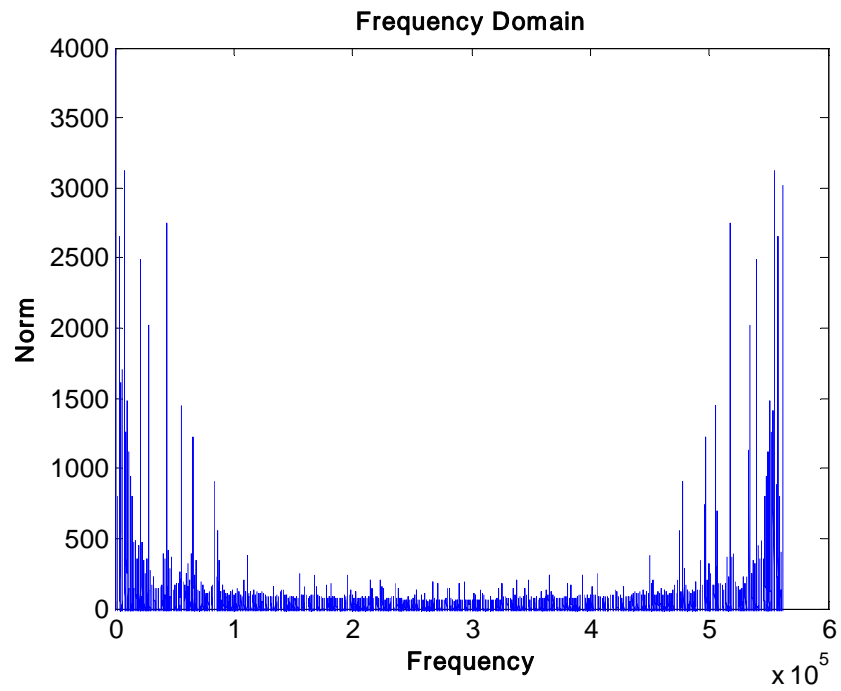


Figure 3.25: FFT output (Frequency spectrum)

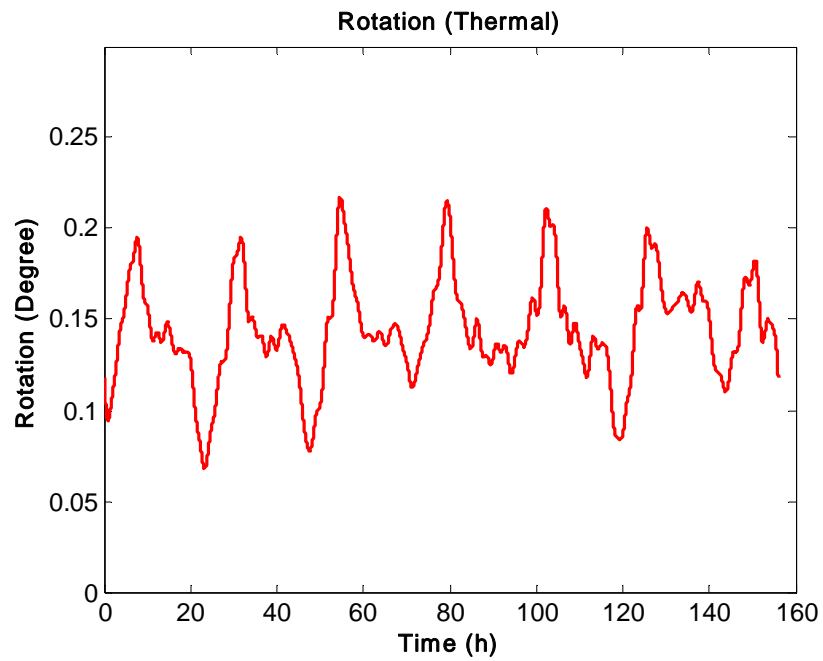


Figure 3.26: Calculated torsional rotation at bent 1 due to thermal load

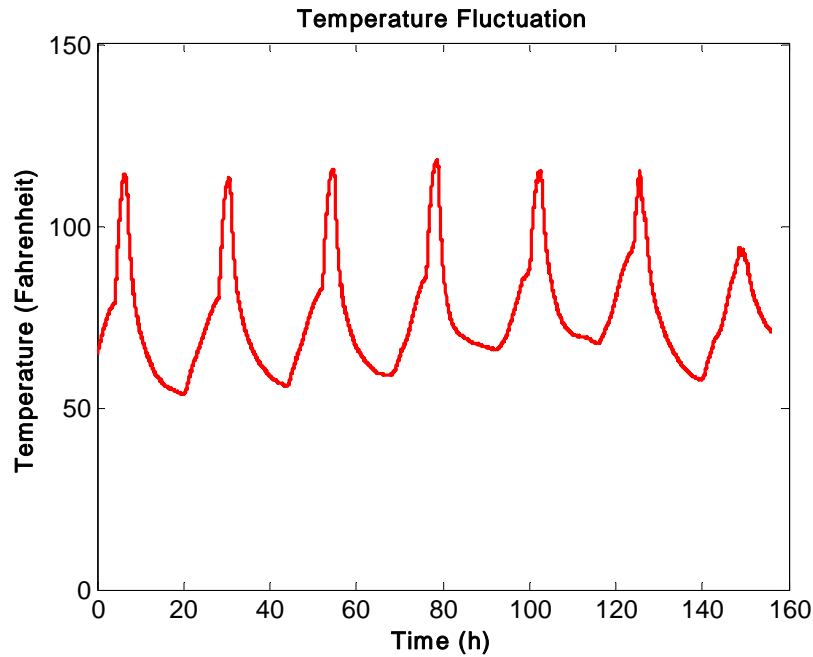


Figure 3.27: Temperature time history

3.3.3.4 Summary of Rotational Measurements

The time-frequency analysis of the torsional rotation measurements confirmed the postulation from the research team that the dynamic structural response due to the vehicular traffic is the predominant effect in variations of the torsional rotation. Table 3.3 presents the ranges of torsional rotation variation at each bent from the instrumentation measurements.

Table 3.3: Ranges of rotation variation

Measurement	Bent1	Bent2	Bent4	Bent5
X axis Rotation (°) (East Girder)	1.66	1.85	0.60	1.52
X axis Rotation (°) (West Girder)	1.59	1.84	0.35	1.71
Y axis Rotation (°) (East Girder)	1.96	2.08	0.95	1.68
Y axis Rotation (°) (West Girder)	1.83	2.02	0.84	1.86

3.3.4 SLIPPING

During the installation of the instrumentation for the field monitoring studies, discolorations around the bearing to girder surface clearly showed that slip had occurred between the bearings and girder flanges. Researchers attempted to identify the cause for the slipping as well as obtaining a measure of the magnitude of the slip.

In general, slipping occurs when the force developed at the girder-bearing interface exceeds the friction force. This phenomenon can be observed when:

- The friction coefficient is low
- The vertical reaction is low
- The elastomer stiffness is significant

In the case of the instrumented bridge, it was found that the last two parameters played an important role on the observed slipping. After reviewing the bridge design, it was found that the design vertical reactions for bent 5 were relatively low, resulting in a compressive stress of approximately 140 psi. This value is sufficiently low so that the friction force can be overcome with a temperature difference of approximately 50 °F assuming an elastomer stiffness of 100 psi and a coefficient of friction of 0.3. However, the variation of the stiffness of the elastomer as a function of the ambient temperature, as well as the impact of aging effects on the stiffness of the elastomer need to be accounted for to improve the understanding of the observed behavior. In general, the stiffness of the elastomer likely increases with decreasing temperature and increasing age. While assessing the impact of the age of the elastomer was not likely practical on this project, investigating the effect of temperature is something that was investigated in the laboratory.



Figure 3.28: Observed slipping between the bearing and girder sole plate (Ambient Temperature at time of picture - 61 °F)

In the bearing shown in Figure 3.28, discoloration in the form of an elastomer skid trace on the steel sole plate indicates that slipping has occurred. Also, highlighted in the red box is the location of the bearing that has lost contact with the sole plate of the girder. The slipping of the bridge girders on the bearing has led to the entire bridge displacing laterally (radially) as demonstrated by the pictures taken from the bridge deck in Figure 3.29. The figure shows pictures taken from the bridge deck of the shift observed in the traffic lane stripping as well as the lateral translation observed in the bridge rail. The measured value of the shift was more than 2.5 inches. Such a measurement was not possible to be taken at the bearing-sole plate interface as the surface corrosion of the weathering steel tended to gradually eliminate older slip traces. The slip traces were apparent at both bearing locations of Bent 5. As a result, it can be said that slip, is a cold-temperature-driven phenomenon, non-recoverable, and cumulative as the bridge experiences new temperature lows over its design life.

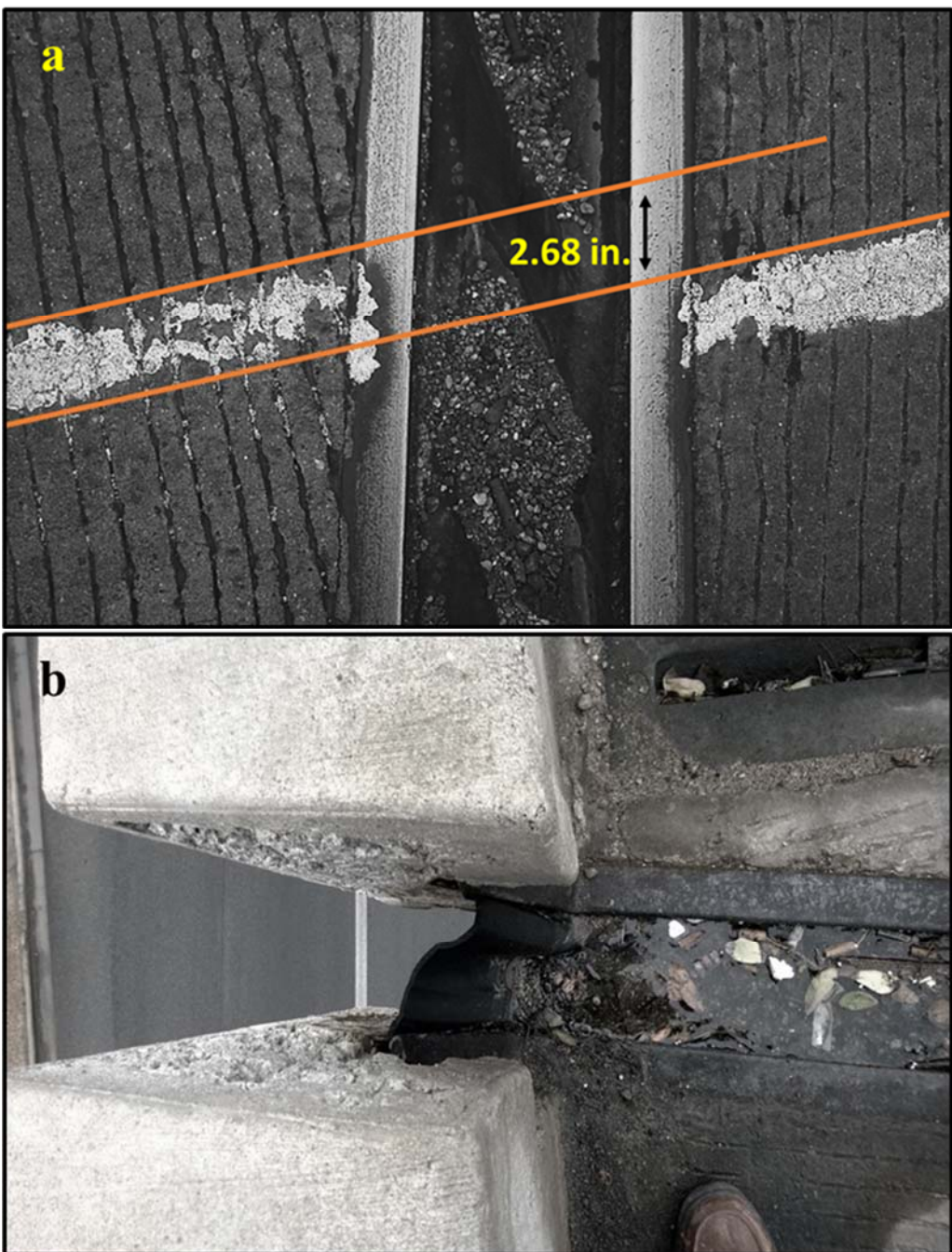


*Figure 3.29: Lateral (radial) movement of bridge observed at expansion joint from bridge deck:
a) shift observed in lane striping, b) shift observed in bridge rail*

3.4 Field Instrumentation Conclusions

This section provides a summary of the conclusions drawn from observations and measurements of the field monitoring studies.

- Effects of solar radiation obviously have a significant role in the thermal behavior of the bridge. Based upon field measurements of the ambient and local girder

temperature as well as historic ambient air temperature records in the Austin area, the estimated range of bridge temperatures may be as high as 148°F over a 50 year return period, which is higher than the design value of 120°F. The researchers will look into the previous measurements from Chen et al. (2009) to improve this estimate.

- The measured longitudinal displacements are reasonably close to the design values at the exterior bents. However, considerable differences between those values were observed at the interior bents. It is also found that the transverse displacement at bent 1(abutment) was under-predicted. Based upon the field observations, additional considerations from past studies to improve the understanding of the thermal behavior of the bridges will be investigated.
- The observed slipping at bent 5 may have occurred due to the relatively low vertical reaction causing a reduced friction force at the bearing. This friction may be more prone to be overcome with the daily thermal cycle that the bridge experiences.
- Time-frequency analyses of the torsional rotation measurements reveal that thermally induced rotations are insignificant compared to vehicular traffic induced rotations. It is therefore less of a concern than the dynamic response of the bridge.

CHAPTER 4: DESCRIPTION OF THE EXPERIMENTAL PROGRAM

4.1 Introduction – Purpose of Experimental Program

In order to gain a better understand of the rubber and steel-elastomer composite layered behavior and performance a thorough experimental program was developed and conducted. In addition, measurements of the basic material properties were necessary as well as the determination of the respective material coefficients, which are essential input for subsequent finite element studies. Furthermore, establishing the fundamental limits as needed for effective bearing design was necessary. For this reason, both small scale material tests on the elastomer as well as full scale steel-laminated elastomeric bearings were tested in the deformational modes of interest.

4.2 Material Testing

The materials tests served a number of purposes. One of the concerns with utilizing larger elastomeric bearings is the potential for increased variations in the material properties across the bearing. Since the primary property of interest in the bearings is the shear behavior, the primary test that is of interest focuses on measuring the shear behavior of the elastomer. In order to obtain the properties from finished bearings, shear tests were conducted with test specimens obtained directly from the bearings. Traditionally, the method of testing that has been used to measure the shear properties is the Quad Shear Test (QST) in which four blocks of the elastomer are bonded to pull plates that are then used to measure the properties. While the QST method is well defined and has long been used in such tests, it requires extensive preparation and does not necessarily reflect the behavior of the elastomer taken directly from the bearing. Instead of using this traditional method, a more efficient method was developed, providing an improved technique of obtaining the shear properties throughout the bearing. The new method is referred to as the Dual Shear Test (DST) and is discussed in more detail in Sun (2015). Extensive comparisons were made between the DST and QST testing methods to ensure that the newly developed method provided meaningful measurements of the desired properties. The DST method agreed very well with the QST method, providing good measurements of the desired data, while improving the efficiency and accuracy of the desired measurements. The DST shear testing methodology made use of the pre-existing bond between the rubber and the steel shims, thereby accelerating the testing process. In addition, due to the method of progressive testing of the elastomer across a strip of the bearing, the DST method provides better resolution of the property variations across the bearing compared to the QST method. The shear test results provided essential information on the shear behavior of the elastomer, which provided required information for the finite element parametric studies.

4.2.1 SPECIMEN PREPARATION

The specimens for the shear modulus tests were prepared with geometries dictated by the dimensions of the bearings. The dual shear test (DST) specimens were obtained by cutting the bearings symmetrically and assuming symmetric distribution of properties throughout the bearing. This DST testing method provided higher efficiency in the specimen preparation than the traditional QST method, which involves bonding of rubber to steel with the use of adhesives. Nevertheless, the acquisition of the DST specimens still required careful planning to ensure that

the specimens would provide representative data for all of the elastomer layers. This section outlines the DST specimen preparation from four different bearing geometries.

Due to the different layer thicknesses of the elastomeric bearings, shear test specimens with two different sets of dimensions were prepared. The length of each elastomer cube is required to be four times the thickness as per ASTM D4014. As shown in Figure 4.1, dimensions of the specimens are dependent on the geometry of the bearing, especially the thickness of the internal elastomer layers. Hence, bearings with a higher length-to-thickness ratio produce more specimens and more detailed information about material property variation can be obtained. The specimen on top, which has 0.375 inch elastomer layer, is obtained from a small bearing matching the geometry that has most frequently been used for prestressed concrete girder bridges. All the other bearings yielded 2"x2"x1/2" elastomer layer DST specimens.

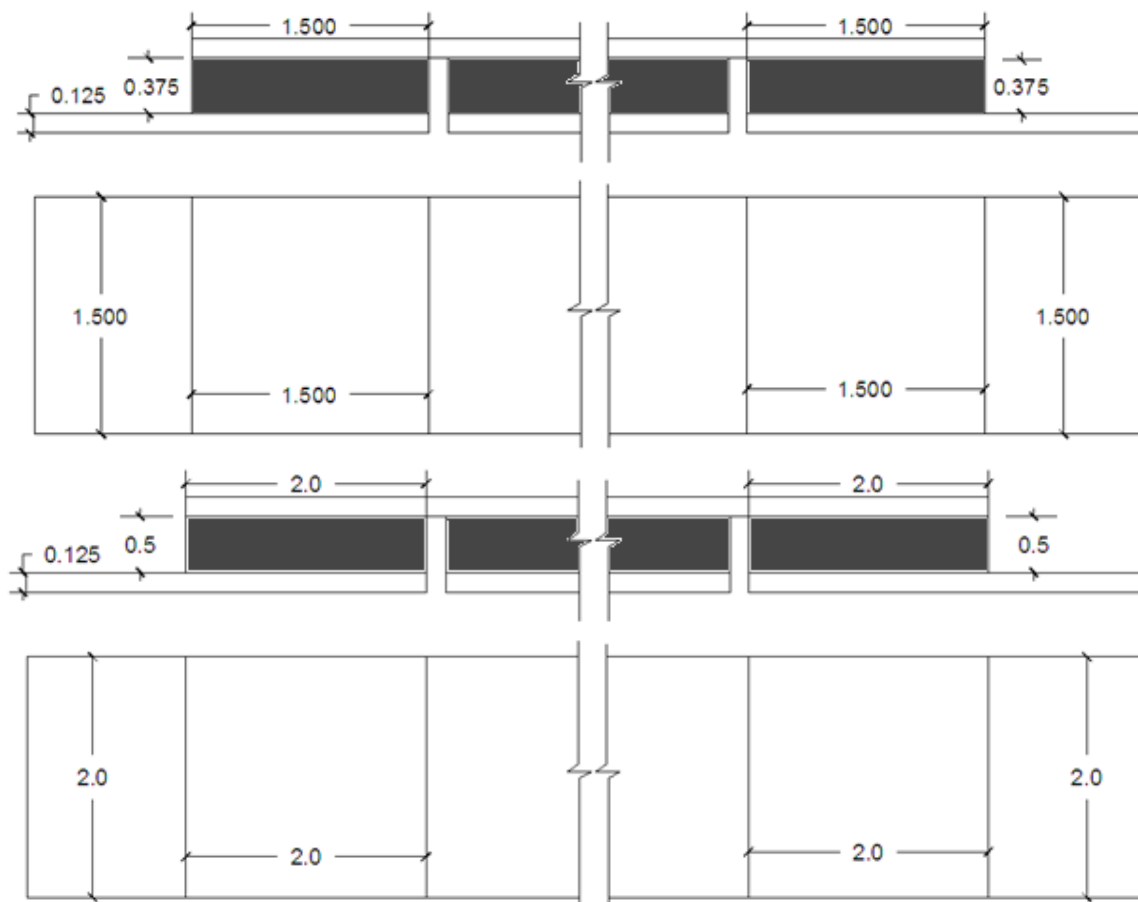


Figure 4.1: Dimensions of the shear test specimen (Unit: inches)

The labeling of the four different bearings is illustrated in the following figures. For the small, medium, and large bearings, the DST tests were conducted over all of the internal rubber layers. For the extra-large bearing, the shear test was done on the material selected at the edge and the middle to characterize the variation of the material property from the exterior to interior of a bearing. Cut sections are shown in the following figures.

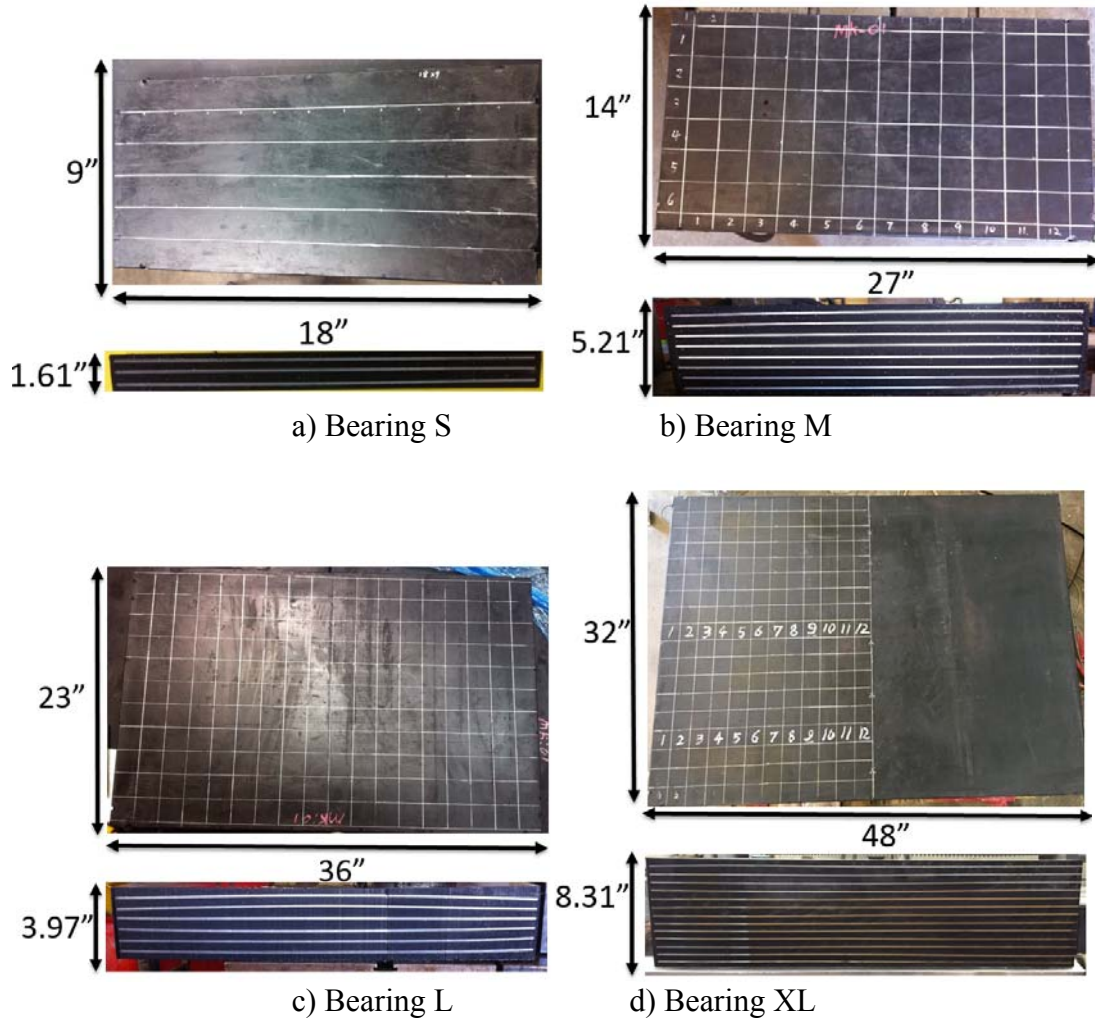


Figure 4.2: Sections of the elastomeric bearings

In order to obtain the material property variation of the bearings, the shear tests needed to involve as much rubber material as possible. However, since the elastomeric bearings are different in dimensions, the specimen acquisition was different for each bearing. Therefore, different cutting plans were carried out according to the specific bearings. The number of the rubber cubes is associated with the accuracy of the variation. However, since the DST specimen directly used the elastomer between two steel shims, the shims were used as pull plates in the test. Therefore, the bond between the elastomer and the shims are maintained in the tests. Since the tests focused on the elastomer and two adjacent shims, not all of the elastomer could be tested. However, by assuming symmetry in the elastomer properties throughout the bearing, specimens for each layer could be obtained from different regions of the bearings. With this technique, the material properties were obtained from every elastomer layer.

The testing strips were acquired as shown in Figure 4.3, and each strip yielded several specimens depending on the length of the strip. Each testing strip included two layers of steel shim and one layer of elastomer material. Since the strip evaluated the shear modulus of the rubber blocks at both ends at the same time, the strip needed to cover the material cubes that were symmetric to the centerline of the bearing. In this study, as assumed based on the

preliminary hardness test results, the material properties are investigated symmetrically about the bearing's longitudinal and transverse axes.

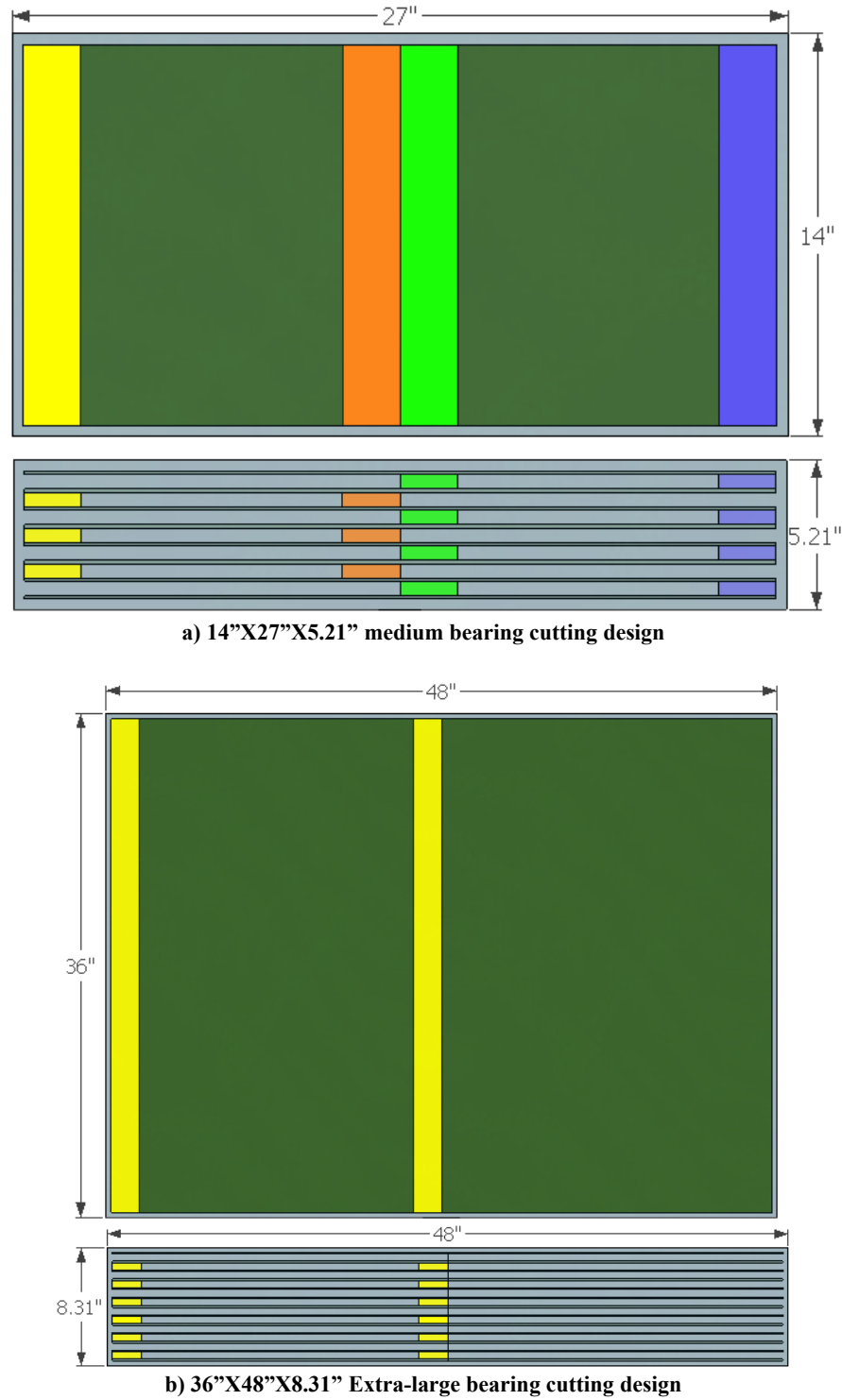


Figure 4.3: Process of shear test specimens acquisition

The cutting design shown in Figure 4.3 depicts the primary cuts on the elastomer layers where the steel and the elastomer material needed to be separated. As the DST specimens make use of the pre-existing bonding effect between the steel shims and the rubber material, the aspect dimensions of the rubber cubes depend on the thickness of the rubber layers. Also, the total length of each cut included an even number of the elastomer cubes so that the DST specimens were tested symmetrically.

The bearing cutting process is depicted in Figure 4.4. The saw blade went across the bearing from one edge to another. Except for the small bearing, all the cuts on the other bearings were made across the width. The distance between adjacent cuts equals the length of the elastomer cube. In the end, the initial bearing cutting sliced a full sized bearing into groups of rubber strips as shown in Figure 4.5.



Figure 4.4: Bearing cutting process

In Figure 4.4, two cutting methods are shown. Most small size bearings could be cut either by band saw or vertical saw, as shown in the picture on the left. However, the extra-large bearing could not be cut on either saw. Therefore, cuts on the extra-large bearing were made using a water jet cutting technique. The water jet cutting was carried out at a commercial machine shop. Due to the relatively high cost of cutting, specimens were taken from a strip on one edge and a strip at the middle of the bearing. For all the different size bearings that were tested, the bearing produced an even number of rubber strips shown in Figure 4.5. Each bearing strip included the steel shims as well as rubber layers, which generated a DST specimen after being separated.



Figure 4.5: Acquisition of the rubber strips (Bearing S)

The specimens were finalized by separating the steel shims and the rubber shown in Figure 4.6. The cuts were made throughout the bearing strips. The rubber layers which were attached with two steel shims were reserved as DST specimens. This cutting method did not significantly affect the original stress state between the rubber and steel within the bearing. Therefore, the bonding effect from the vulcanization during the manufacture could be maintained.

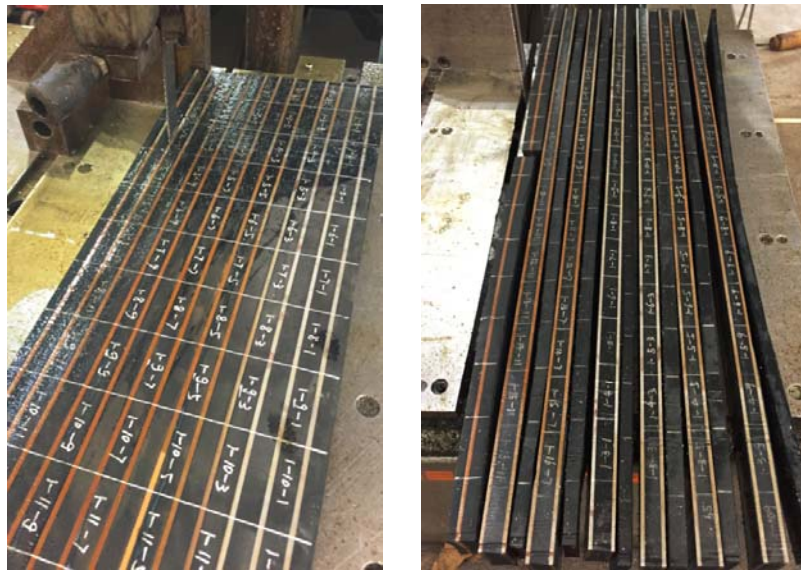


Figure 4.6: Separation of the rubber strips (Bearing XL)

When the first group of specimens was obtained, the other specimens were progressively fabricated by cutting the rubber cubes at both ends after being tested. The final fabrication step of these specimens is shown in Figure 4.7. The picture on the left shows a group of newly fabricated DST specimens. The picture on the right shows the rubber cubes cut off the specimens after they were tested. During the fabrication process DST specimens with different lengths were produced. DST specimens with different lengths during the preparation process for the shear test are shown in Figure 4.8.



Figure 4.7: Preparing DST specimens from bearing strips

In the following figures, the rubber strips were marked every 2" along the longitudinal direction. With this test method, the 10-inch long DST specimen in the picture was able to produce five pairs of shear moduli. To begin the testing procedure, one of the shims was cut near the end of the specimen and the elastomer was stripped off. This formed the gripping region of the pull plate. A cut was then made in the gripped shim to form two specimens at the end of the bearing strip that was tested. After the test was completed, the tested elastomer at the end of the strip was removed creating the gripping region for the next test. The gripped shim was then cut to again form the next pair of elastomer cubes were to be tested. As the test continued, the specimen was cut until the last two rubber cubes were left with the steel shims.



Figure 4.8: Typical DST specimens under different shear test steps

As shown in Figure 4.8, the bearing strip was shortened as more rubber cubes were tested. By making use of the steel shims and bonding effect inside the bearing, the pre-existing stress was properly conserved. The shear properties measured represented the average of the two blocks at the end of the strip. As a result, the material properties inside the bearing were acquired from the edge to the center consecutively. This was a significant contribution to the investigating techniques of the finished bearings. The evaluation process of the variability of the material property inside bearings, due to their aging and vulcanization process, was significantly accelerated. When the outer two blocks were tested, the two adjacent blocks would be tested. In this way, a full strip of the bearing specimen was progressively tested from the edge to the middle of the bearing, thereby providing a measure of the variation of the properties across the bearing. .

4.2.2 TESTING PROCEDURE

The shear test was conducted in a 22-kip capacity MTS test machine as shown in Figure 4.9. Because the capacity of the testing machine was much higher than the forces that were to be applied to the specimens, there were concerns about the accuracy of the load measurements. A 500 lb. capacity load cell was therefore added to the test setup to provided higher resolution readings of the applied forces. The loading rate was maintained as 0.05 shear strain per second. Similar to the traditional quad shear testing methodology from ASTM D4014, each specimen experienced six loading cycles until the loading curves were firmly repeatable. The maximum loading strain was 50%, which was considered large enough to reflect the variation of shear modulus inside the bearings. The shear moduli were calculated based on the slope between the 0.2 and 0.4 shear strain. This calculation method reflected the average shear stiffness of the material even under higher shear strains.

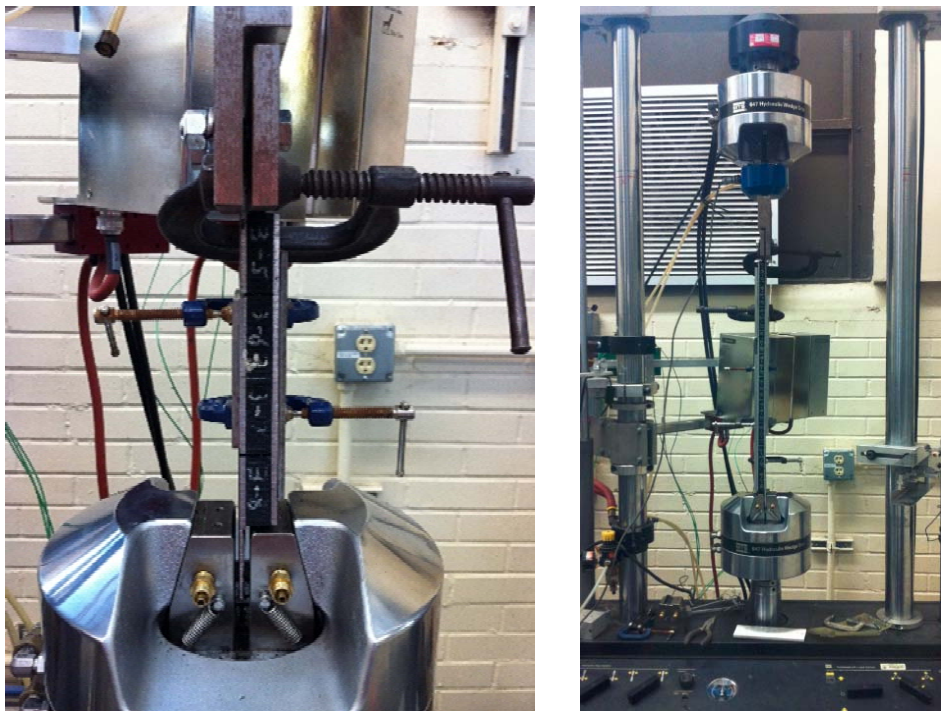


Figure 4.9: Shear modulus test on specimens with different lengths

4.2.3 LOW TEMPERATURE TESTING

While much of the tests on the variation of material properties throughout the different sized bearing were carried out at “room temperature” which was around 72 degrees F, additional tests were carried out at colder temperatures to. With the low temperature test results, the property variation within full-size elastomeric bearings due to the temperature change can be predicted through a typical thermal response analysis. Thus, the behavior of the full-size bearings under low temperatures can be characterized by updating the material properties in the finite element models, instead of testing the whole bearings in an environmental chamber.

4.2.3.1 Test setup

The dimensions of the specimens were obtained from the elastomeric bearing made of 50 IHRD rubber material. In order to better guarantee the consistency of the test specimens in hardness, all the DST specimens were selected from the middle of the inner rubber layers where the hardness was close to 50 IRHD. The geometry of the specimen in the low temperature tests is shown in Figure 4.10.

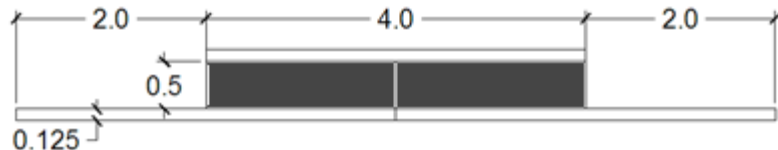


Figure 4.10: Geometry of the specimen for low temperature test (units: inches)

Low temperature tests were conducted with dual shear test specimens in a closed cold chamber. The testing setup is shown in Figure 4.11. It consists of a typical hydraulic Instron testing machine and a sealed cold chamber. Liquid nitrogen was used to lower the temperature inside the test chamber. An ATS temperature control system was used to monitor and control the amount and speed of the nitrogen going into the chamber, therefore accurately monitoring and maintaining the temperature during a test. Tests were carried out to determine the amount of time that was necessary for the specimen temperature to stabilize in the testing chamber.

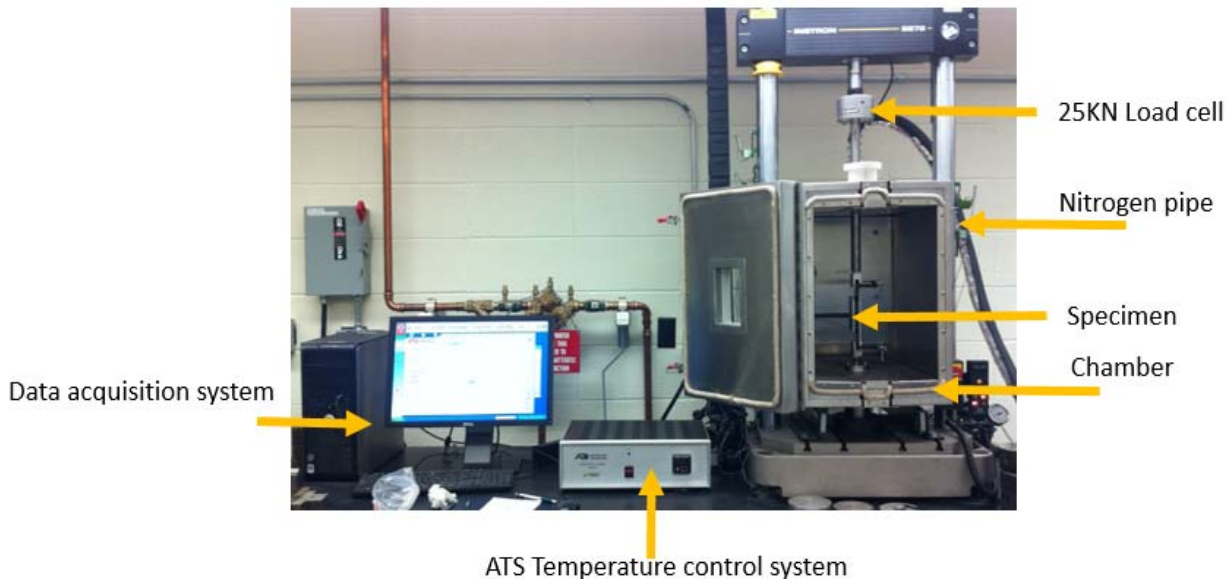


Figure 4.11: Low temperature testing setup

As rubber is a poor conductor of heat, it takes much longer for the rubber to experience temperature change than steel. Therefore, during the low temperature test it was very important to accurately control the temperature inside the rubber material to guarantee accurate test results. However, it was difficult to monitor the temperature inside the elastomer while keeping the specimen's mechanical behavior undisturbed. There is very little literature concerning the techniques to maintain temperature equilibrium during a test especially for a shear test in a closed chamber. Because no extra thermocouple could be installed inside the sealed chamber or inserted into the specimen to monitor the inner temperature during a test, a special temperature monitoring technique was proposed with the help of finite element simulation. A thermal analysis of the specimen was carried out to provide detailed temperature distribution of the specimen when the specimens are conditioned under different low temperatures before the shear test. The variation of the temperature contour inside the specimen served as a tool to identify when the thermal equilibrium was reached. As a result, the conditioning time that was required for a low temperature test was determined by the thermal analytical results. When the temperature inside the elastomer was stabilized and was equal to the conditioning temperature, the specimen reaches thermal equilibrium and was ready for a shear test under this specific temperature. The conditioning time based on the analysis is listed in the table below.

Table 4.1: Conditioning time for DST specimen (2"X2"X0.5") before the low temperature test

Centigrade (°C)	Fahrenheit (°F)	Conditioning time (Seconds)
20	70	1698
15	60	1746
10	50	1798
5	40	1829
0	32	1958
-5	23	2164
-10	14	2528
-15	5	2932
-20	-4	3690

4.2.3.2 Test methodology

In the low temperature test, the dual shear test methodology was adopted to reduce the effort in the specimen fabrication. Thus, the low temperature testing procedure primarily followed the procedure of the dual shear test conducted under room temperature. Before the test, the chamber was pre-cooled by the liquid nitrogen. After the temperature reached the testing temperature, the specimens were placed inside the chamber under the testing temperature as shown in Figure 4.12. When the time of thermal equilibrium was reached, the specimen was installed on the gripping system. Loading started once the temperature inside the chamber was again stable.



Figure 4.12: Specimens being placed inside the testing chamber at the testing temperature

Similar to the DST method under room temperatures, the cyclic loading was also applied in the procedure of the low temperature test until the shear curves were fully stabilized and repeatable. The control mode during the test was set to be displacement control.

The low temperature shear tests were also affected by the same factors that affected the shear tests under room temperature. These factors include the maximum loading strain, the loading rate, and the shear modulus calculation method. In order to have the testing results

comparable to those results from the room temperature test, the same testing procedure and calculation method was applied to the low temperature test in this material study.

In the low temperature tests, the loading rate was maintained as 0.05 shear strain/second. Maximum loading strain was 0.5 shear strain for the investigation of the shear modulus. In the low temperature test setup, the data acquisition system also controlled the loading procedure. The GUI of the loading control software is shown in Figure 4.13. Similar to the GUI of the normal MTS test machine, the relative displacement and the ramp rate respectively controlled the maximum loading strain and the loading rate.

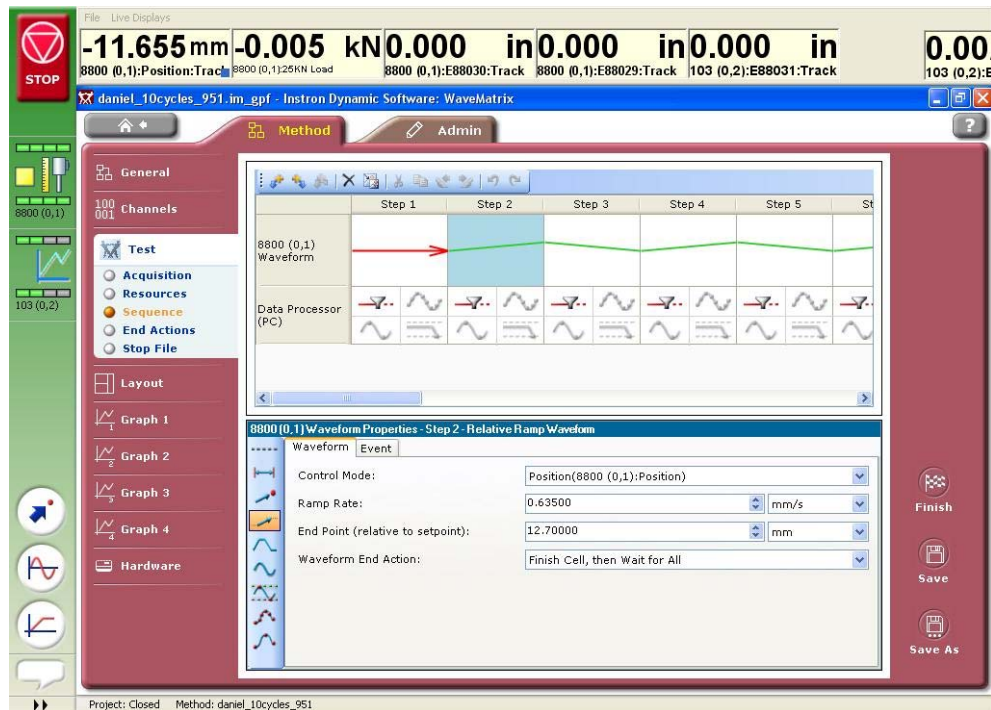


Figure 4.13: Loading control system for DST under low temperature

The number of loading cycles that were needed to have repeatable shear curves was first investigated in the pilot tests. In the investigation, all the specimens under different temperatures experienced twenty loading and unloading cycles. Results indicated that the shear curves generally stabilized after six cycles, which was similar to the shear tests under room temperature. NCHRP 449 and AASHTO specify the test procedure and the shear modulus calculation methods for the instantaneous low temperature shear test on full size bearings. However, both the calculation and the test method were different than those under room temperatures, which made the low temperature test results not comparable to the results under room temperature. As a result, the shear test procedure as well as the calculation method in this research project remained consistent to compare the test results under the low and regular temperatures.

4.3 Full Scale Bearing Tests

The full scale bearing testing portion of this study consisted of the testing of bearings that would qualify for *higher demand applications* in all their modes of deformation (compression, shear, and rotation).

4.3.1 FULL SCALE COMPRESSION TESTING

This section is dedicated to the description of the test setup and testing protocol that was followed for the testing of bearings in compression. The purpose of the compression tests was to evaluate the axial stiffness of those bearings, as literature suggested a potential discrepancy may exist between the calculated and measured axial stiffness, attributed to unknown reasons. Another purpose of the compression tests was to evaluate the current design limits for axial stress on bearings, as the previous research has focused on bearings with smaller plan areas.

4.3.1.1 Test Setup

For this portion of the research investigation, a uniaxial self-reacting testing frame was developed for the experimental testing of full scale bearings. A schematic of the test-setup is shown in Figure 4.14. The test frame was capable of applying 4,000 kips in compression, a capacity dictated by the capacity of the two hydraulic actuators that were used to apply the compression. The load was transferred from the actuators to the bearing through a stiff transfer beam. To avoid non-parallel movement of the self-reacting frame, restraining beams were placed on top and bottom of the system, as can be seen in Figure 4.15. To avoid the creation of a load path through the restraining beam, the connections were made through slotted holes, and Teflon (Polytetrafluoroethylene – PTFE) sheets placed in the interface. To validate that there were no differential movements, two linear potentiometers were placed at each side of the transfer beam to monitor displacements. The axial deformation of the bearing was taken as the average of the two recorded values.

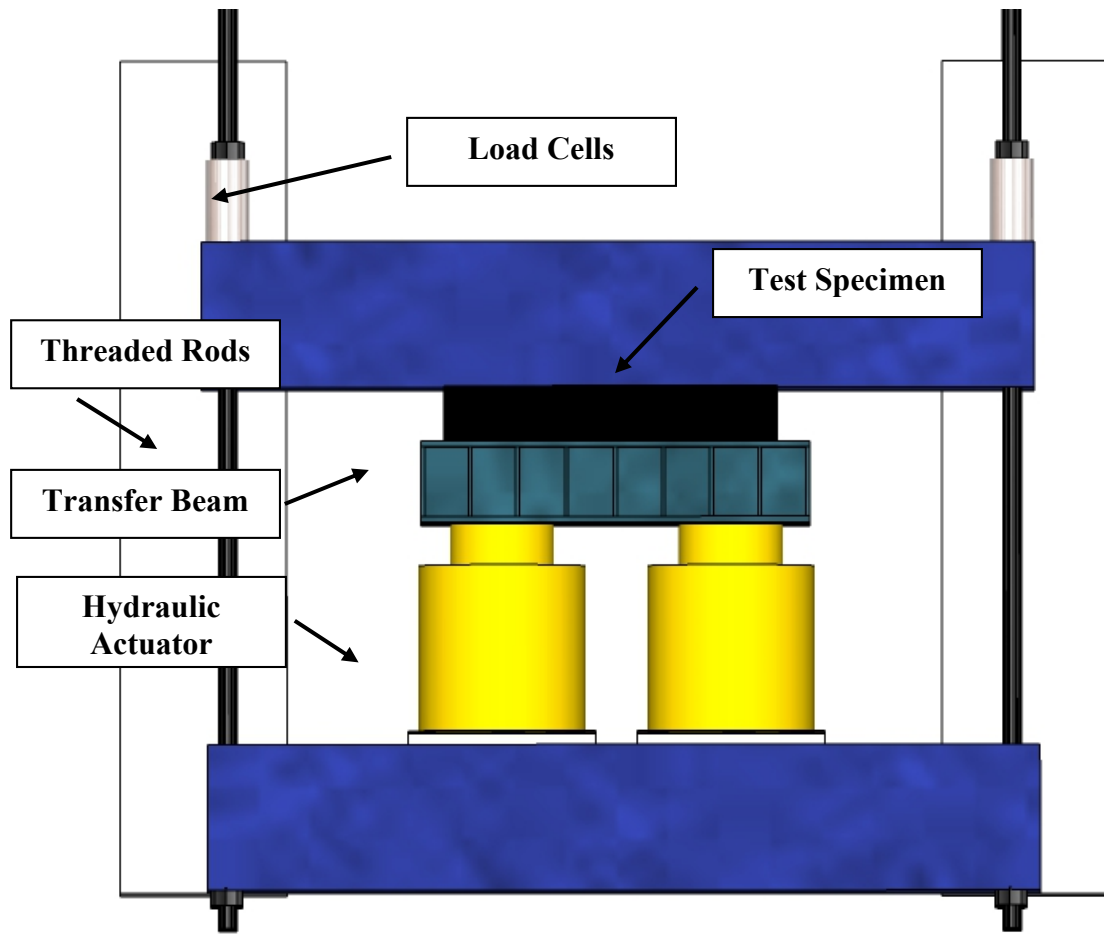


Figure 4.14: Schematic plan view of the self-reacting test setup with important parts



Figure 4.15: Actual test setup and linear potentiometer location

4.3.1.2 Test matrix and testing protocol

Similar to the material tests, each bearing was cycled to the target load six times. The reported stiffness is the value of the slope of the linear regression line of the loading portion of the sixth cycle. Each cycle duration was approximately 10 minutes. The dimensions and material properties of the bearings that were tested are listed in Table 4.2.

Table 4.2: Test matrix of bearings tested in compression

Bearing Pad	Width (in.)	Length (in.)	No. of "t"	Layer Thickness "t" (in.)	Cover (in.)	Total Height (in.)	Shear Modulus (psi)	Number of Tests
XL	24	36	12	0.5	0.375	8.31	98	2
L	36	23	5	0.5	0.375	3.97	94	3
M	27	14	7	0.5	0.375	5.21	98	4
S	18	9	2	0.375	0.25	1.61	93	4

Each test specimen was labeled with bearing pad type letter (XL-L-M-S), followed by the mode that the specimen was tested (in this report only compression – C – is reported) and a number signifying the test number (e.g. the first large bearing compression test was labeled L-C-1).

As part of this research project, the bearing performance of a range of bearing sizes under large stress levels that exceed typical design values was a major interest so as to evaluate the bearing behavior for use in *higher demand applications*. A bearing in compression under such levels is shown in Figure 4.16. Under large stress levels, the locations of the shims can be identified as the elastomer bulges between the shims.



Figure 4.16: Bearing tested in compression

4.3.2 FULL SCALE SHEAR TESTING

This section is dedicated to the description of the setup and testing protocol that was followed for the bearing shear tests. The purpose of these tests was to evaluate the shear stiffness in different directions and under various axial loads. In addition, the slip performance and the effect of rollover were assessed as well as the potential of buckling was investigated.

4.3.2.1 Test setup

The test setup developed for the experiments provided for the ability of shearing larger bearings at higher levels of axial stress. Figure 4.17 illustrates the setup, which consisted of two perpendicularly placed self-reacting frames. As with the compression-only tests outlined in the last section, the horizontal frame is responsible for applying the axial load. The vertical frame was added to the setup so as to apply a shearing deformation to the bearing. As can be seen in Figure 4.18, in order to achieve the self-reacting ability of such a frame, two bearings were sheared simultaneously. In addition, for better representation of actual conditions and for the slip tests, two concrete blocks simulating the pier cap were added in the shearing plate without disturbing the symmetry of the self-reacting system.

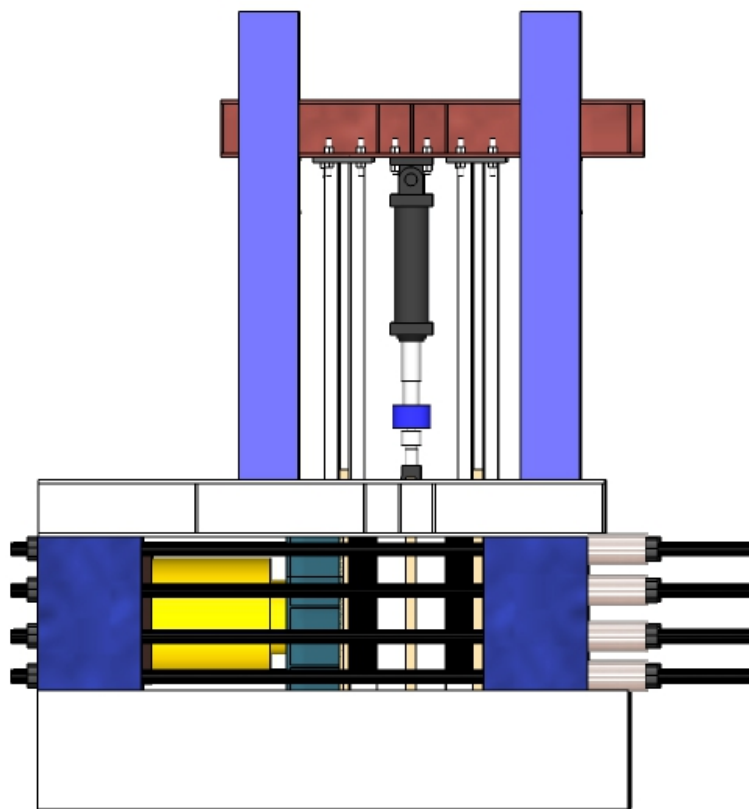


Figure 4.17: Schematic of the test setup

This setup permitted the measurement of the shear stiffness of the bearings in different shearing directions, evaluating the impact of the axial pressure on the shear stiffness, investigate the magnitude of the friction coefficient, and investigate if the 50% shear strain is a reasonable

limit for rollover. Figure 4.19 depicts the test setup as constructed at FSEL and Figure 4.20 illustrates a bearing subjected to shearing deformation. The rollover phenomenon can be seen at the top left and bottom right edges.

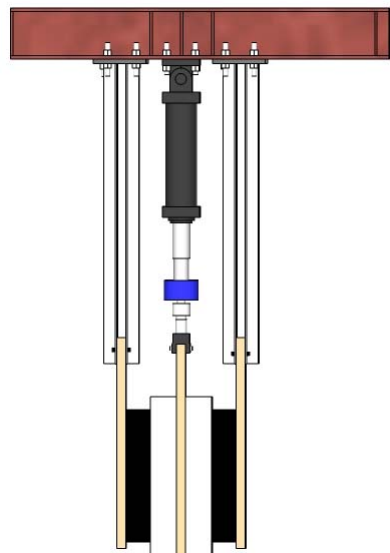


Figure 4.18: Schematic of the self-reacting shear frame



Figure 4.19: Combined axial and shear test setup at FSEL



Figure 4.20: Bearing tested in shear

4.3.2.2 Test matrix and testing protocol

As stated previously, the main purpose of this part of the study was to evaluate the shear stiffness properties of the bearings, to validate the material tests results, to obtain a better understanding of the behavior under various axial loads, and to feed the FEA portion of this study. In addition, the rollover occurrence was visually assessed. Table 4.3 presents the main variables of the tested bearings as well as the naming scheme used for them and Table 4.4 summarizes the conducted tests for each specimen. It is worth noting that tests associated with 50% of the maximum allowable axial load with current TxDOT design procedure and 100% shear strain were not conducted in the initial portion of the study to minimize the risks of instabilities caused by eccentricities in axial load induced in the system by differential slipping.

Table 4.3: Test matrix of bearings tested in shear

Bearing Pad	Width (in.)	Length (in.)	Layer Thickness "t" (in.)	Total Height (in.)	Shape Factor	Aspect Ratio
S	18	9	0.375	1.61	8	2
M	27	14	0.5	5.21	9.22	1.93
L	36	23	0.5	3.97	14.03	1.57

Table 4.4: Matrix of conducted tests

Shear Strain Level		50% Shear Strain			75% Shear Strain			100% Shear Strain		
		S	M	L	S	M	L	S	M	L
Axial Stress Level	0.5 ksi	✓	✓	✓	✓	✓	✓	✗	✗	✗
	0.8 ksi	✓	✓	✓	✓	✓	✓	✓	✓	✓
	1.0 ksi	✓	✓	✓	✓	✓	✓	✓	✓	✓
	1.5 ksi	✓	✓	✓	✓	✓	✓	✓	✓	✓
	2.0 ksi	✓	✓	✓	✓	✓	✓	✓	✓	✓

In order to define the shear stiffness of the bearing the procedure followed was consistent with the procedure specified in the material-level portion of this study. Specifically, the shear stiffness was defined as the slope of the line determined by points in the stress (τ) - shear strain (γ) curve associated with the 0.2 and 0.4 elastomer shear strain, which is illustrated in Figure 4.21.

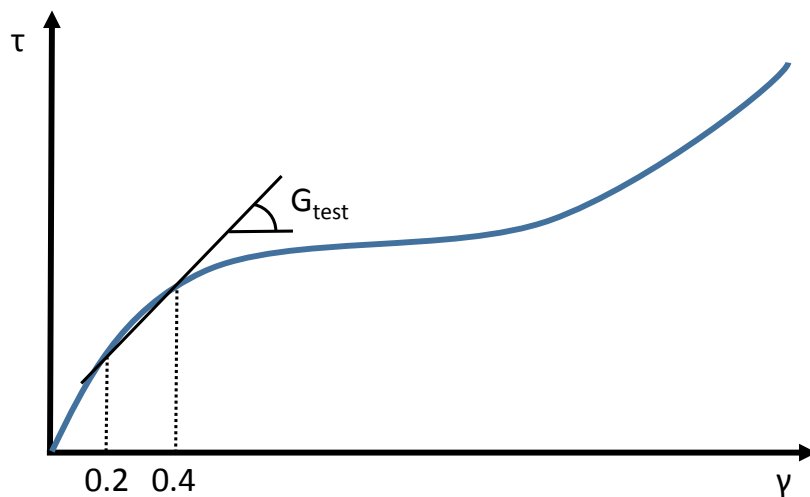


Figure 4.21: Shear stiffness definition

Because the location of the bearings was not accessible by the laboratory crane due to vertical constraints (beams holding the shear self-reacting system in place), a procedure for placing and engaging the specimens was developed. Consequently, the bearings were initially placed on the supports as shown in Figure 4.22, which were fabricated to ensure the bearing placement at a location concentric with the location of the applied load and the bearing placement at the expected angle. Subsequently, the test setup was moved at the bearing support location and the outside plates were clamped, creating a sandwich structure that did not allow the bearing to fall when the shear test setup was placed in its designated position. The clamped configuration is depicted in Figure 4.23. Finally an initial axial load of 20 kips was applied to ensure that the bearings did not slide from gravity effects prior to testing. Once the system was

under compression, the clamps were removed. The pre-testing configuration is shown in Figure 4.24.



Figure 4.22: Bearings on supports before being placed in the shear test setup



Figure 4.23: Clamped configuration entering the test setup



Figure 4.24: Test setup with engaged bearings

The testing protocol consisted of two parts that were followed throughout the study. After reaching a target axial load each bearing was sheared five times to the desired shear strain. The duration of each cycle was approximately one minute. At the end of the fifth cycle the axial load was increased to the next desired level and the cyclic shear loading was repeated. The process was repeated until the maximum target axial load was reached. After the process was completed, the axial load was dropped to the clamping load of 20 kips. The bearing was left in place overnight to release the stresses that had developed due to the inherent rubber hysteretic behavior and the testing was resumed the following day under the same protocol for a different maximum shear strain. The maximum axial load and maximum shear strain applied in this testing phase, 2 ksi axial pressure and 100% shear strain respectively. However, after the completion of the testing protocol, higher axial loads and shear strains were applied in an effort to evaluate the failure limits for the bearings, without damaging the test setup. A graphical representation of the protocol followed is illustrated in Figure 4.25.

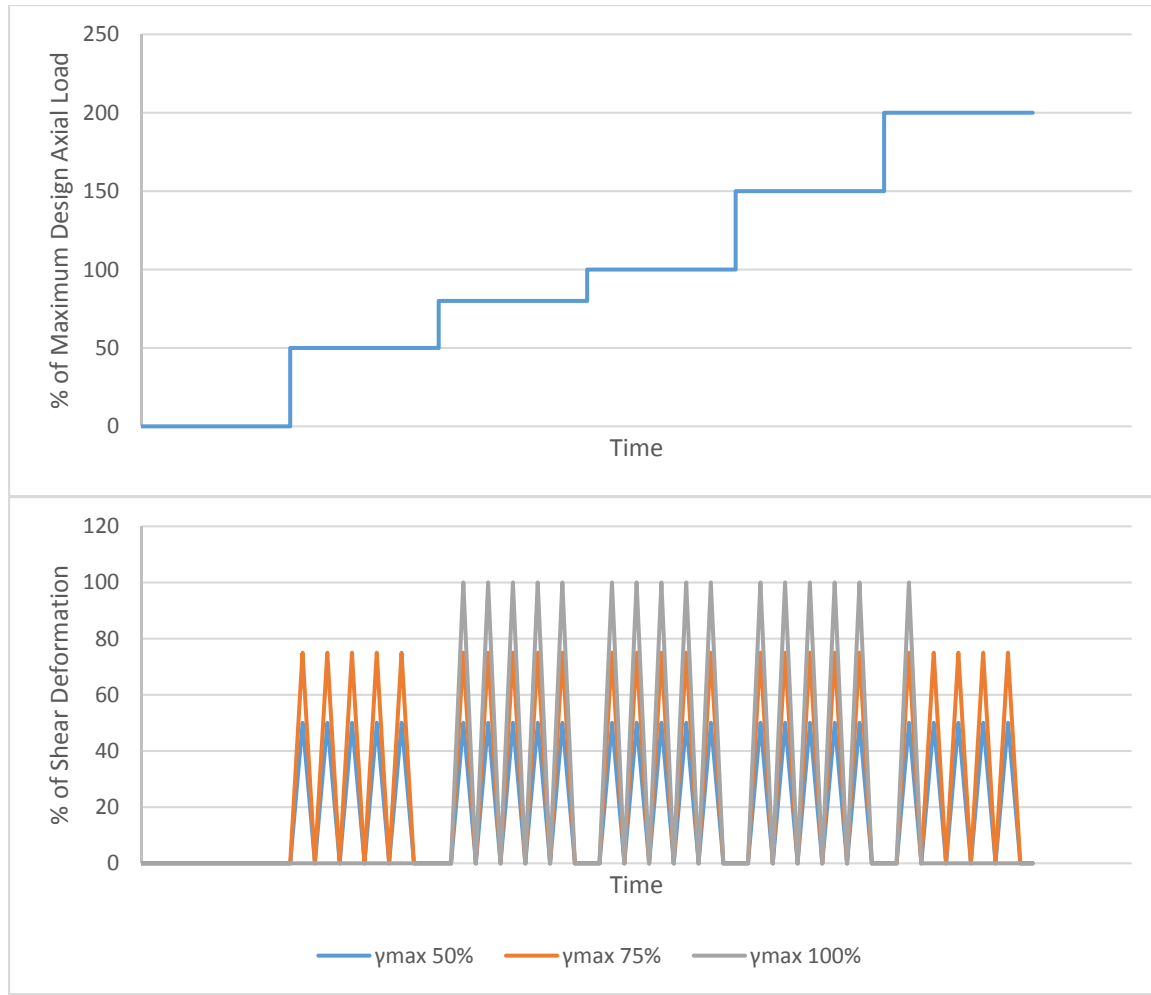


Figure 4.25: Testing protocol

4.3.3 FULL SCALE ROTATIONAL TESTING

This section describes the test setup and testing protocol that was followed for evaluating the rotational behavior of the bearings. The purpose of these tests was to evaluate the rotational stiffness and strength of the bearing and investigate the effects of the lift-off phenomenon.

4.3.3.1 Test setup

An extensive review of the literature did not provide any information of previous setups capable of accommodating compression, shear, and rotation for elastomeric bearings with the load and displacement requirements necessary for bearings in higher demand applications. Stanton et al.(Stanton, Roeder et al. 2008) did make use of a setup capable of compression, shear, and rotations; however, that setup was limited in capacity to accommodate and test conventional size bearings. Such a setup was found to be impractical to accommodate bearings classified for higher demand applications.

The approach taken in this study was to make use of the test setup used in the compression and shear portion of the investigation. This setup made use of a self-reacting system that consisted of two actuators to apply axial compression and two actuators to apply the shearing deformation. Although several potential setups capable of utilizing an external load

source to impose rotations on the bearing system were considered, such a setup was not practical due to concerns with the potential stability of the self-reacting frame. Instead of externally applying the rotation, the decision was made to evaluate the performance of the bearings at fixed magnitudes of the rotation. The rotations were achieved with the use of tapered shims that resulted in inclined loading surfaces. In order to achieve the desired angles of rotations in the range of 0.5 to 2 degrees (0.009 to 0.0349 radians) the inclined surfaces were created by attaching machined aluminum shims at the plates of the shear self-reacting system, as depicted in Figure 4.26.

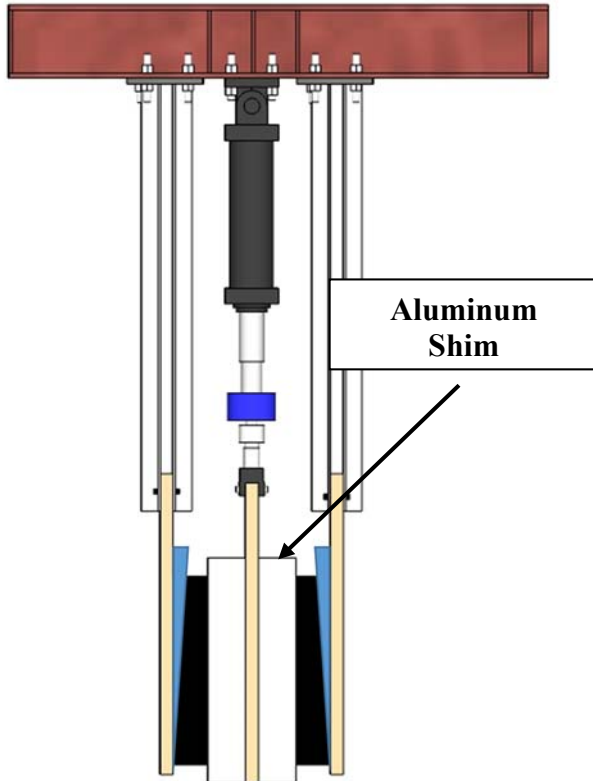


Figure 4.26: Modification to the shear test setup for rotation

There were three primary objectives for the rotational tests. The first objective was to assess the rotational stiffness and strength of the bearing as a function of the axial load/stress. The second objective focused on the lift-off phenomenon for bearings that classify for higher demand applications. Lift-off is permitted by AASHTO in the design of elastomeric bearings; however, those provisions reflect conclusions from research conducted in significantly smaller bearings. The final objective of the rotational tests was the creation of benchmarks for FEA studies for use in validating the models in this mode of deformation and producing failure identification methodologies.

In curved bridges shearing of the bearing as well as the rotation of the girders occurs in two perpendicular directions. In the case of lift-off, when shearing and lift-off occur in two perpendicular directions, the shearing will typically occur over a localized region of the bearing which will often result in torsion in the bearing. The setup that was developed allows this phenomenon to also be experimentally investigated.

4.3.3.2 Test matrix and testing protocol

After the bearings were inserted in the test setup, axial load was applied using the two actuators with a capacity of 2 million lbs. each. Because the axial loads were applied to the bearings through the angled shims, the resulting deformations on the bearings is combined axial compression at a fixed rotation as shown in Figure 4.27. Figure 4.28 depicts the expected high shear strains at the compression side of the bearing.

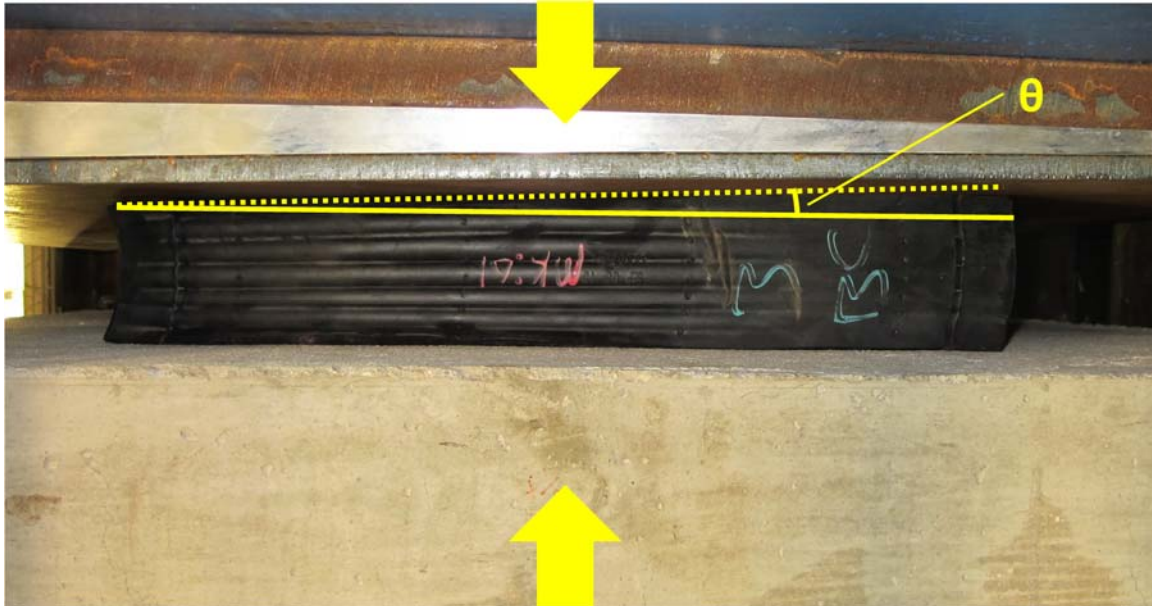


Figure 4.27: Compression-induced rotation at a bearing



Figure 4.28: Increased local shear deformations noticeable at the compression side of the bearing

Due to geometrical constraints caused by the size of the test setup, smaller size bearings were not tested in rotation. Table 4.5 presents the main variables of the tested bearings. The test protocol consisted of axially loading the bearings and measuring the shim deflection.

Table 4.5: Test matrix of bearings tested in rotation

Bearing Pad	Width (in.)	Length (in.)	Layer Thickness "t" (in.)	Total Height (in.)	Shape Factor	Aspect Ratio
M	27	14	0.5	5.21	9.22	1.93
L	36	23	0.5	3.97	14.03	1.57

4.4 Summary

This chapter provided an overview of the experimental program that included both material tests as well as full scale testing of the bearings. The purpose of the laboratory experiments is to establish a better understanding of potential variations of the material properties of the elastomer throughout bearings as well as the ability to assess the accuracy of the total shear strain approach to be applied in bearing design. Results obtained from the experimental program are described in the following chapters.

CHAPTER 5: RESULTS OF THE EXPERIMENTAL PROGRAM

5.1 Introduction

This chapter focuses on the results obtained from the material studies and the full scale tests. An overview of the data obtained is presented and the reasoning behind the rationale of the proposed design for elastomeric bearings is described.

5.2 Material Test Results

Since the material shear tests were conducted symmetrically with respect to the centerlines of the bearing, the test results on one quarter of each layer sufficed to show the shear moduli over the whole layer. These two quarters of rubber layers are depicted in Figure 5.1. The width and the length of each square equals to half of the total width and the total length of the bearing. Typical results of the dual shear tests (DST) on the bearing with different dimensions are shown in Figure 5.2 through the contours of the shear moduli over different layers. Each figure represents one quarter of the whole rubber layer between the steel shims.

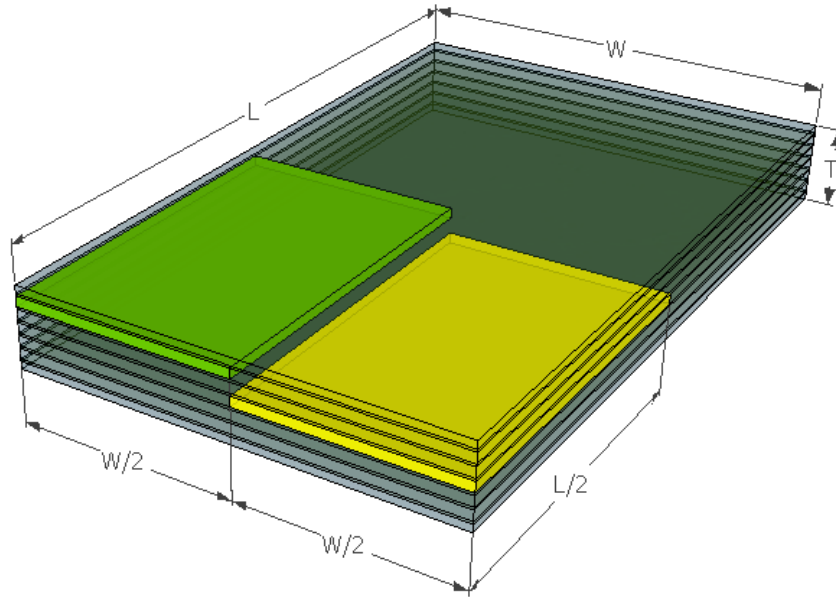
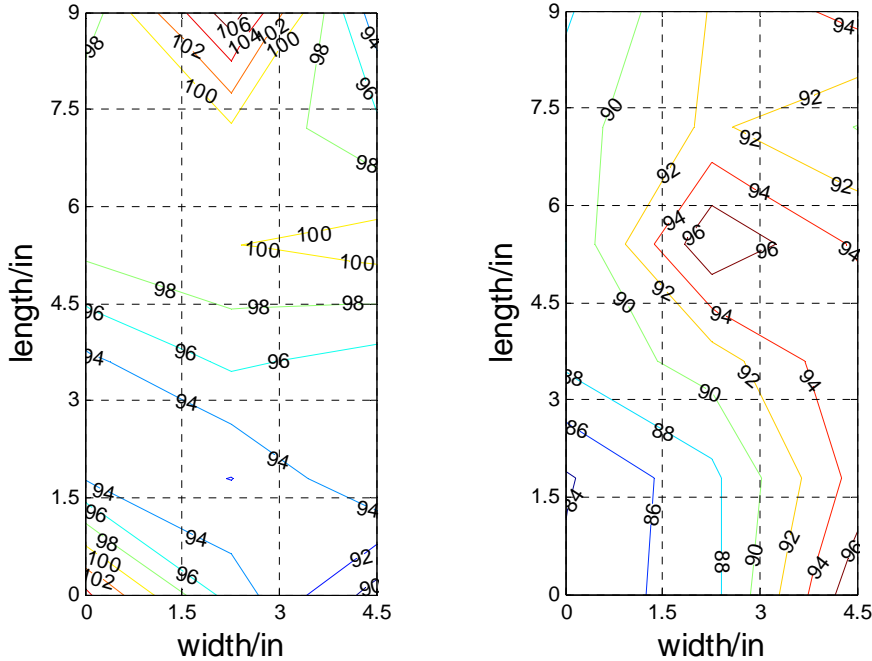
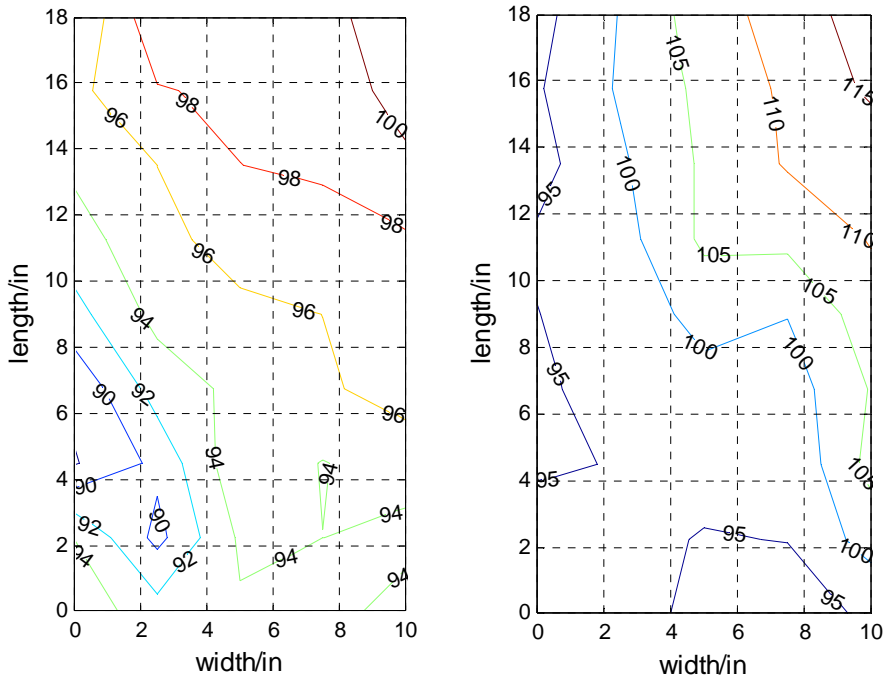


Figure 5.1: Region of the rubber layers shown in Figure 5.2



a) Shear modulus variation contour on two layers in the small bearing



b) Shear modulus variation on outer (left) and central layers (right) in the large bearing

Figure 5.2: Shear modulus results of bearings with different dimensions (Units: psi)

The test results from the small, medium, and large bearings clearly demonstrate a variation of the shear modulus inside the newly produced elastomeric bearings. Higher shear moduli were measured at the center of the bearing. This validates previous findings that higher hardness values are observed at the center of the bearing. However, there was no evident variability in the shear modulus on the surface layer. Therefore, it can be concluded that the

typical material property distribution can only be found in the central rubber layer or the rubber strips obtained along the centerlines.

For thick bearings, contour plots of the sections through the thickness can better illustrate the variation across different rubber layers. The two sections selected are shown in Figure 5.3. One section was located at the edge close to the surface to investigate the test results in the outer material of the bearing. The other one was at the section along the centerline, which reflected the shear modulus in the center.

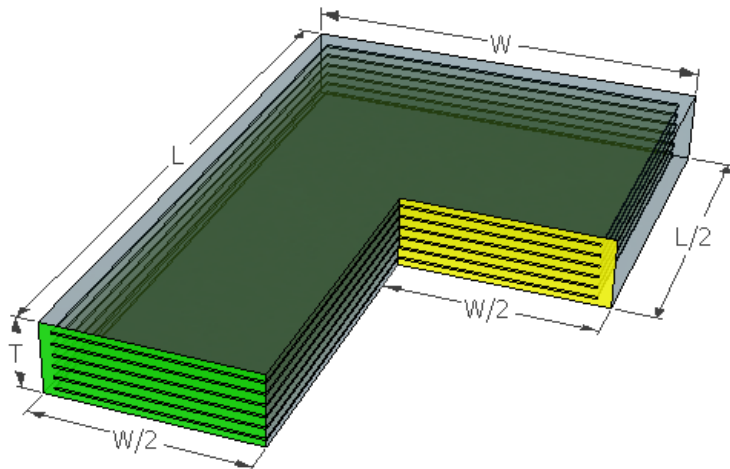


Figure 5.3: Two sections on the elastomeric bearing

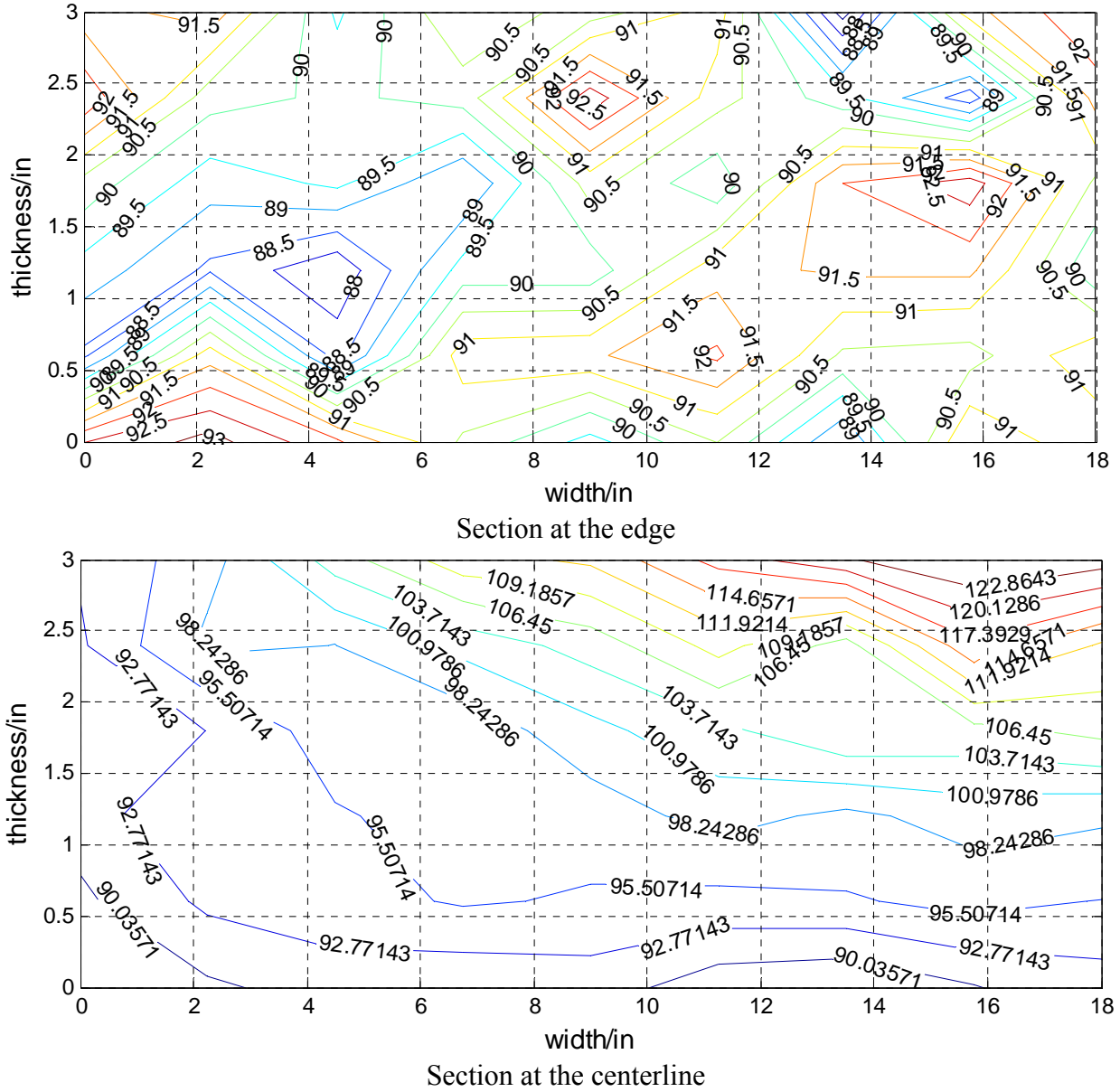


Figure 5.4: Shear modulus contour of two sections inside the bearing XL (Units: psi)

As can be seen in Figure 5.4, the shear modulus variation is more prominent in the central cross-section. The contour lines at the center were almost parallel to the rubber layers. This can be attributed to the fact that the heating during vulcanization is applied at the top and bottom of the bearing. This phenomenon further verifies the conclusion that material from molded specimens for material testing cannot properly represent the actual bearing material properties.

The average and standard deviation of the shear moduli on both sections from different bearings are shown in Figure 5.5 and Figure 5.6. The average values reflect the general shear stiffness of the rubber material. The standard deviation is utilized to evaluate the variability of the shear modulus over the selected section. Among all the bearings, the average values from the center region were higher than those from the outer portions. Although the average shear moduli on the surface of the different bearings were very close to each other, the internal values showed greater variability. For the small bearing, the average value difference is not quite obvious

between the interior and exterior. However, this difference was very obvious for the medium, large, and extra-large bearings. Furthermore, the difference of the shear moduli from the edge to the center in the medium and the extra-large bearings are larger than the others.

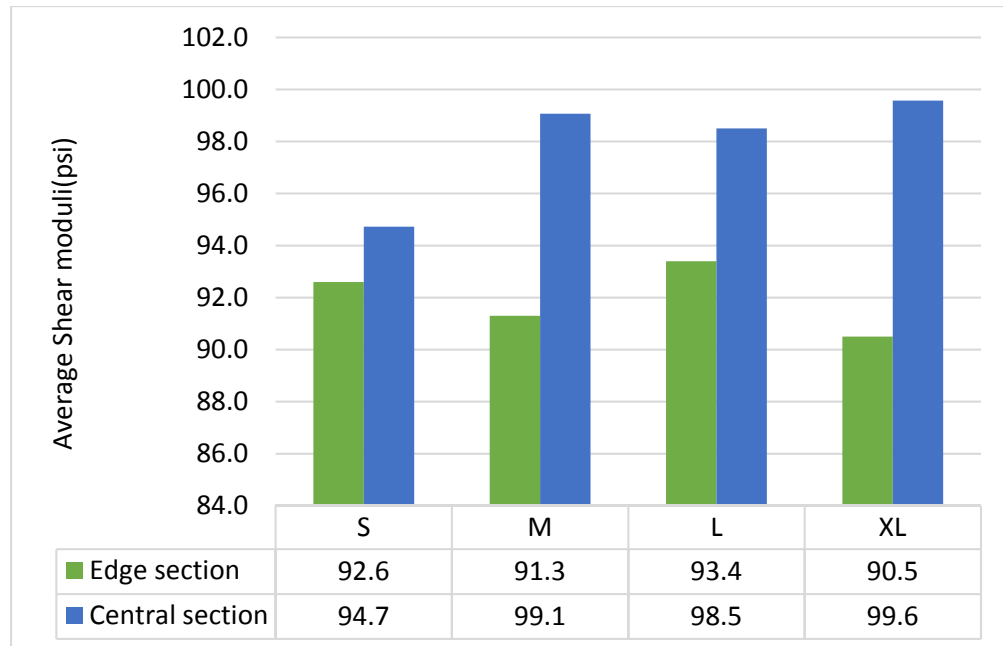


Figure 5.5: Average shear moduli from different bearings (Units: psi)

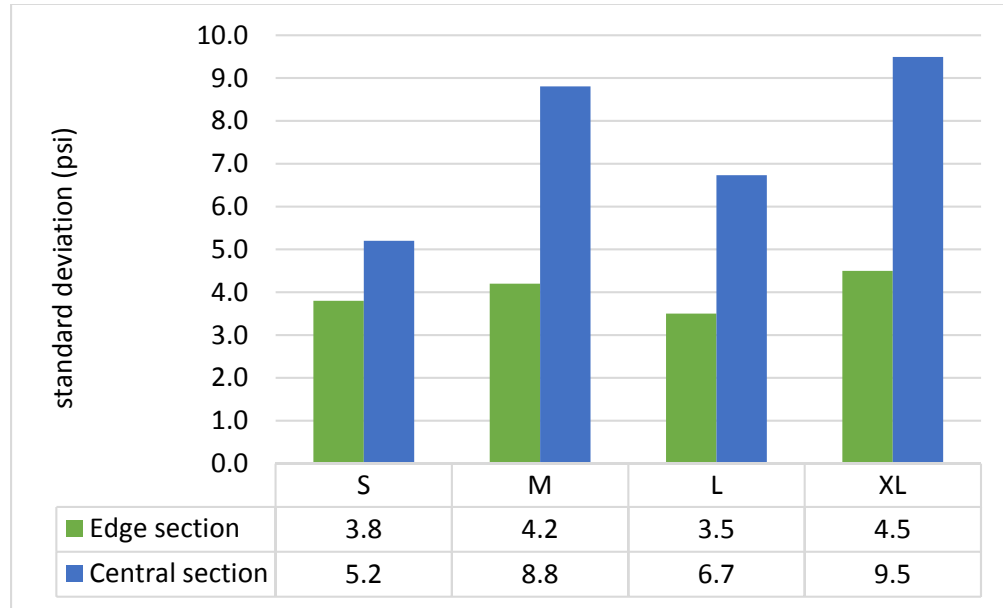


Figure 5.6: Standard deviation of the shear moduli from different bearings (Units: psi)

The variation in properties inside the smallest bearing was less obvious than in the other bearings while the variation on the surface was virtually the same. A larger variability in the shear modulus was observed inside the bearings with more rubber layers or larger total thickness. This phenomenon was a result of the uneven vulcanization and temperature exposure. The

thermal conductivity of the rubber material is only 0.1% of the steel. Thus, the heat transfer rate within the bearing is limited to a small value due to the low variability in the rubber material. As it takes much longer for the heat to transfer from the surface within the thicker bearings, the internal rubber is constantly cured under high temperature, leading to higher shear modulus values. Since this uneven curing result is not noticeable and unavoidable based on the current manufacturing techniques, the new testing methodology recommended in this study can serve as quality control. The shear test results from the bearings are summarized in Table 5.1. The values are calculated from all the material tests of the bearing. These data also demonstrate that the shear modulus variation is more obvious for the thicker bearings.

Table 5.1: Summary of the measured shear modulus values from bearing tests

Shear modulus/psi	Bearing S	Bearing M	Bearing L	Bearing XL
Minimum	83.73	80.64	86.84	87.30
Maximum	107.17	115.48	117.54	125.6
Average	93.98	96.83	97.51	95.04
Standard deviation	5.26	7.95	5.36	8.14

5.3 Full Scale Compression Test Results

5.3.1 STIFFNESS RESULTS

This section provides the stiffness results of the tested specimens in comparison with predictions using the AASHTO expressions as well as the concurrent finite element studies that were conducted as part of this study. Figure 5.7-Figure 5.9 illustrate the load-deflection curves of the specimens in comparison with the AASHTO predictions. The naming protocol for the experimental curves shown herein consists of two letters and a number. The first letter refers to the bearing size, (L) for the larger, (M) for the medium, and (S) for the small bearings referred in the Table 4.2. The second letter corresponds to the deformation mode of interest, (C) for compression, (S) for shear, and the number is a counter of the tests on identical specified bearing geometries.

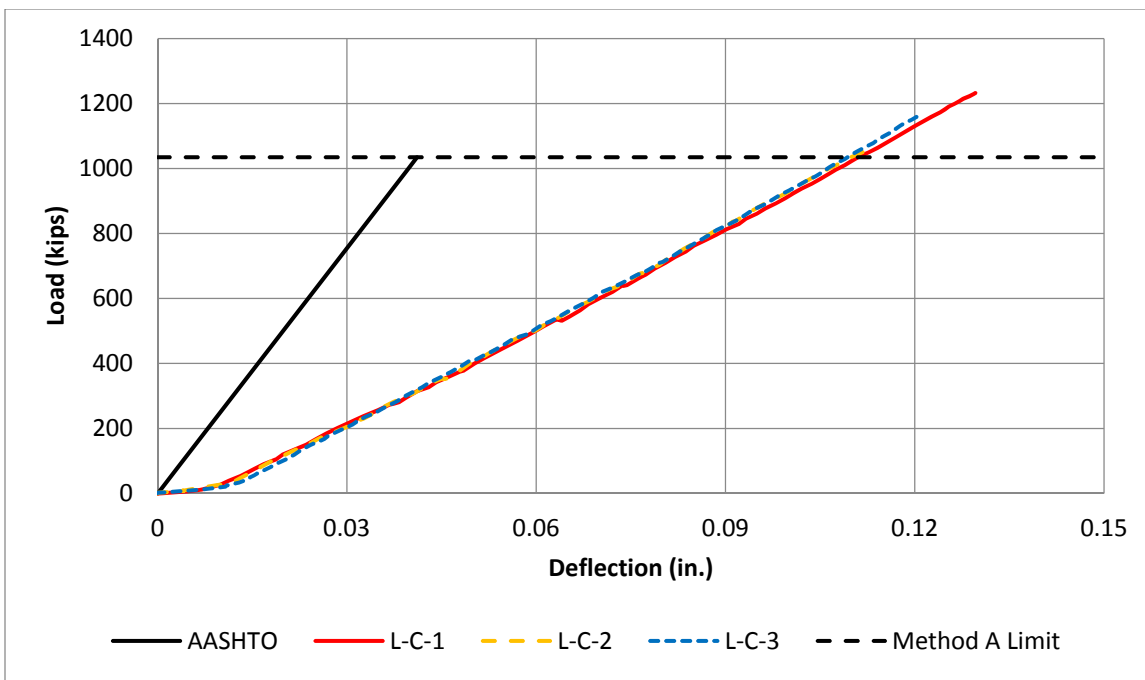


Figure 5.7: Load-deflection curves for large (L) bearings under compression

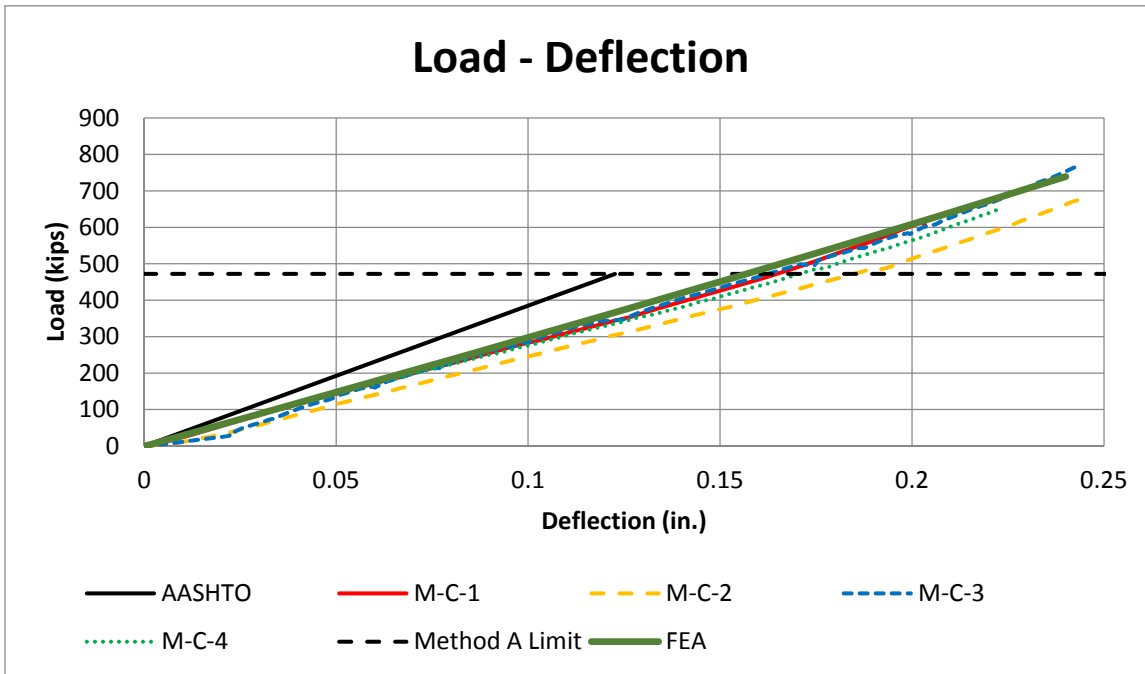


Figure 5.8: Load-deflection curves for medium (M) bearings under compression

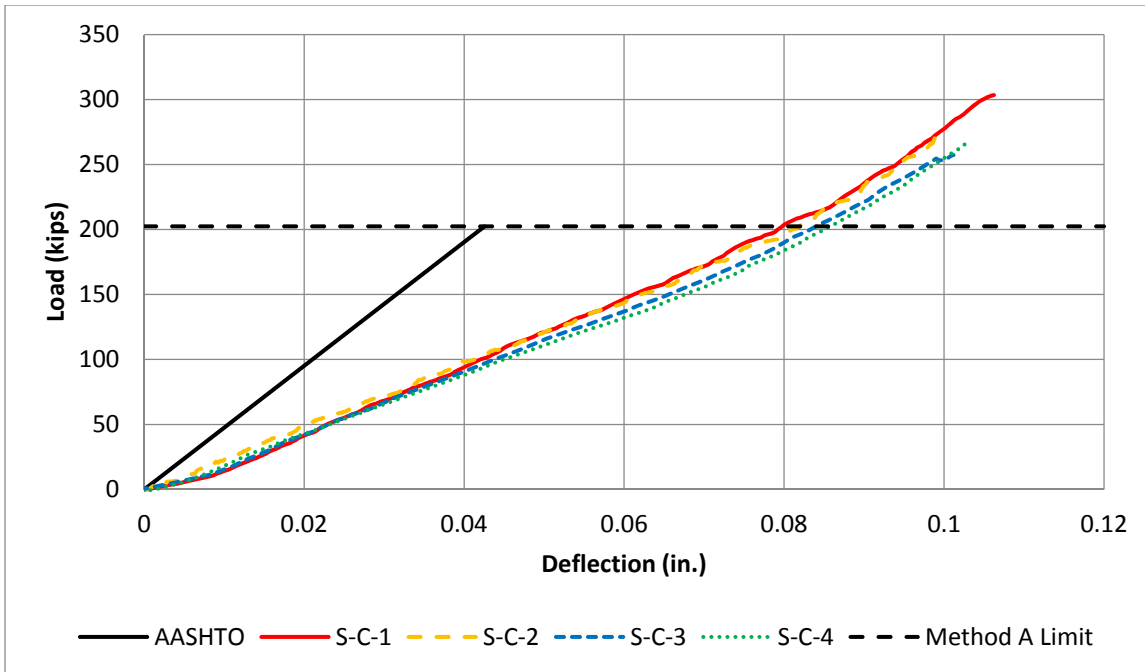


Figure 5.9: Load-deflection curves for small (S) bearings under compression

The graphs of the test results show that there is very little variation in the response of a bearing to axial loading for bearings of the same dimensions and properties, suggesting limited variability in the material properties. However, the discrepancy between the experimental results and AASHTO or FEA predictions suggest that there might be parameters affecting the axial stiffness in a way that is not captured by current knowledge.

It also can be seen that AASHTO significantly overestimates the axial stiffness of all bearings tested in this study. This can be a result of the inherent approximations of simplified equations provided, as well as the assumption of perfect bond of the rubber to the contact surface. In order to quantify the differences in stiffness, the results are presented in terms of axial stiffness using a linear regression of the test results. Figure 5.10-Figure 5.12 depict the tested and calculated stiffness values.

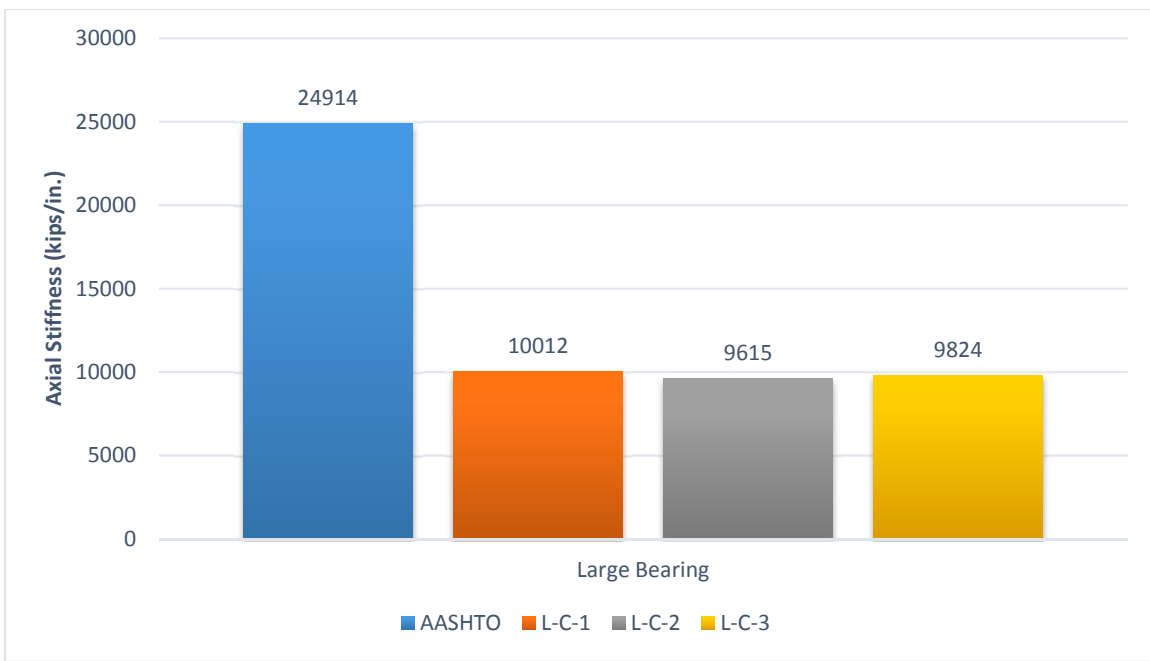


Figure 5.10: Axial stiffness values for large (L) bearings

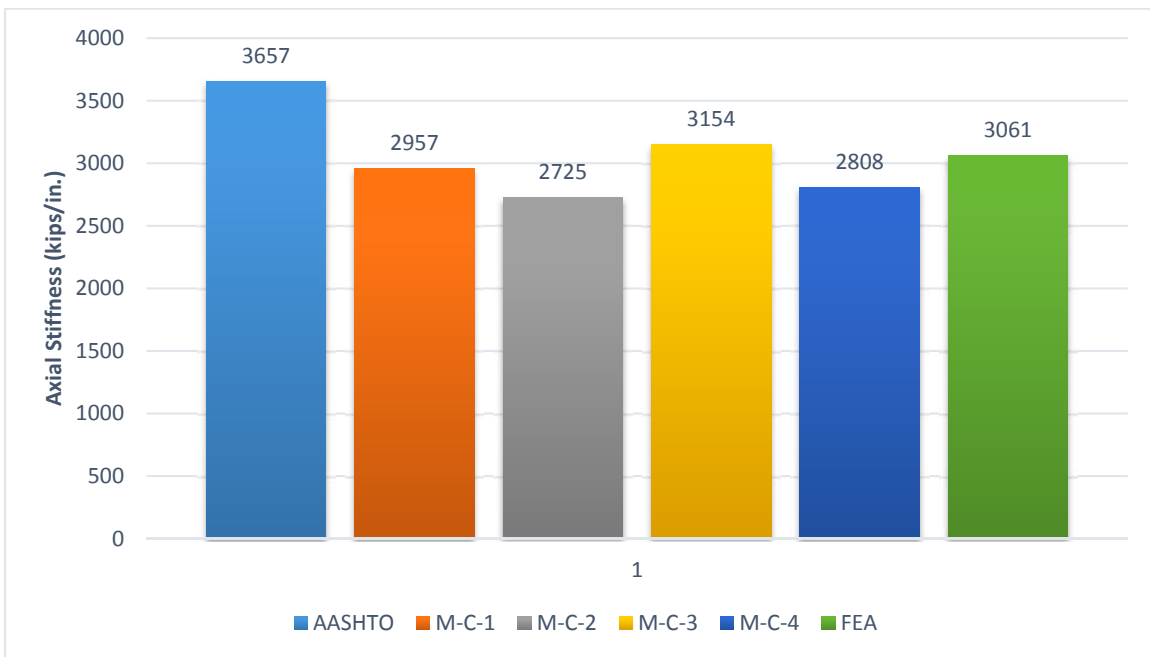


Figure 5.11: Axial stiffness values for medium (M) bearings

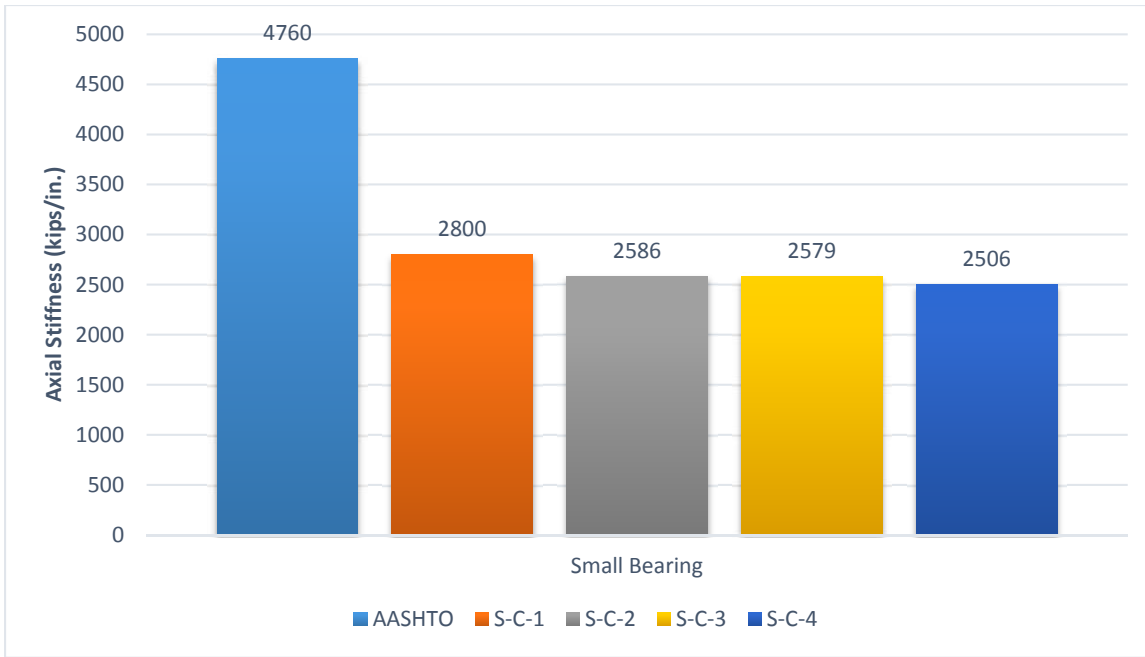


Figure 5.12: Axial stiffness values for small (S) bearings

As can be seen, there is no clear over-prediction relation that can be directly related to the plan area or the shape factor of the bearing. However, the comparison of the FEA results with the medium sized bearing provides a good indication that the results can be predicted in a relatively accurate way for all the cases.

5.3.2 TEST OBSERVATIONS

The primary focus of this phase of the study was to measure the axial stiffness of bearings with a relatively wide range of geometries. The compression testing provided a good means of inspecting the location of the steel laminates close to the surface of the bearing by observing where the bulging occurs. The results indicate that the steel laminates were placed at the locations specified for the finished product, though one bearing had a layer thickness that was not uniform along its length, creating a differential bulging in this area. Figure 5.13a-b depicts the observed bulging for the two different cases. Consequently, the relative misalignment of the steel shims does not seem to affect the axial stiffness.

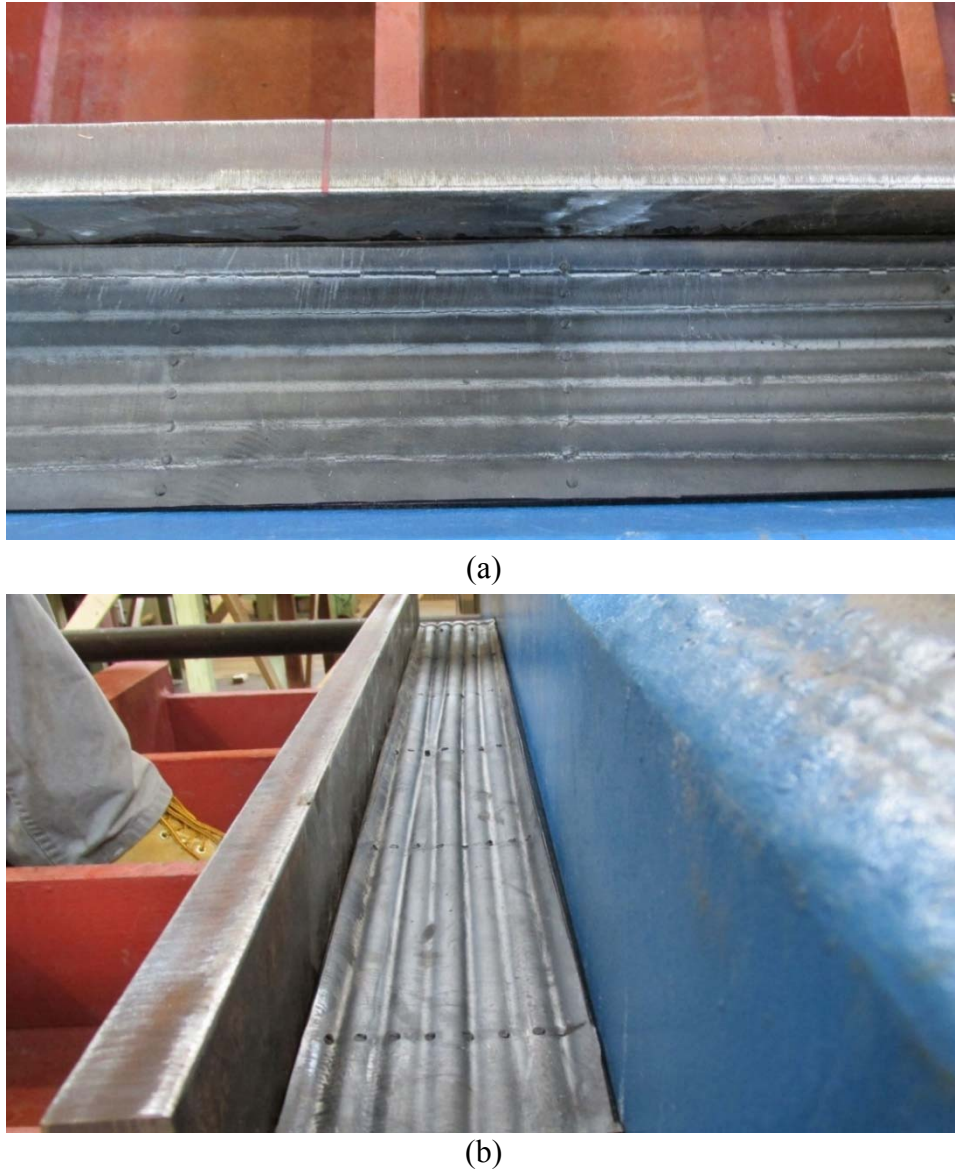


Figure 5.13: Uniform layer thickness along the bearing length (a), and non-uniform layer thickness along the bearing length (b)

5.4 Full Scale Shear Test Results

5.4.1 STIFFNESS RESULTS

This section focuses on representative data obtained from the tests conducted. The first series of tests were carried out on Bearing S. Figure 5.14 shows the force-displacement (equivalent to stress-strain) curves for the 50% shear strain series under varying axial loads on the small bearing. Similar curves were generated for the other bearing sizes. As can be seen all curves overlap, suggesting that the shear stiffness is not dependent on the axial pressure applied for this elastomeric bearing geometry, for the axial pressure levels of interest. To better illustrate the results, the shear stiffness for each case was calculated according to the procedure described

in previous sections and is shown in Figure 5.15. As can be seen, the variability of the shear stiffness is minimal, which can be reflected in the coefficient of variation (CV) of 0.015.

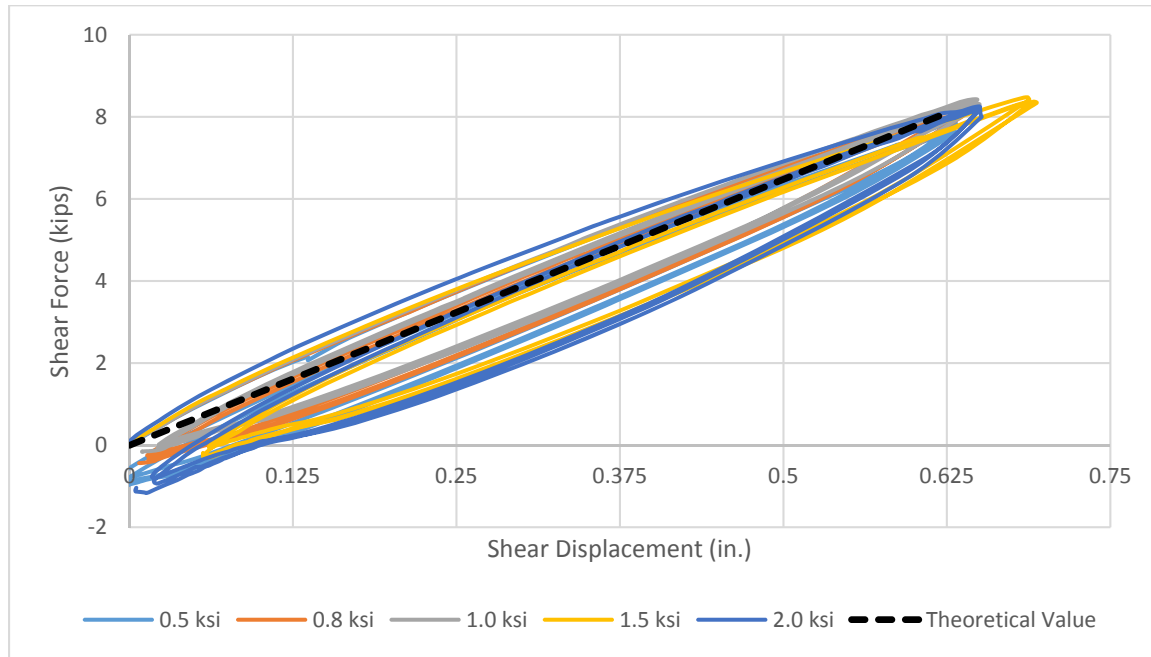


Figure 5.14: Force - displacement curves of the small bearing at different axial loads (S)

Figure 5.16 illustrates the force-displacement curves of the bearing together with the idealized linear curves corresponding to the average, maximum, and minimum shear stiffness obtained from the material level tests and the idealized linear result obtained from the full scale tests for bearing S. As can be seen, the overall shear stiffness behavior could accurately be determined from the material level testing. Table 5.2 summarizes the differences in shear stiffness in terms of calculated shear modulus.

Table 5.2: Material-scale and full-scale shear stiffness comparison

	Average shear modulus - material (psi)	Average shear modulus - full scale (psi)	% Difference
Bearing S	93.98	98.00	4.28
Bearing M	96.83	94.24	-2.67
Bearing L	97.51	101.15	3.73

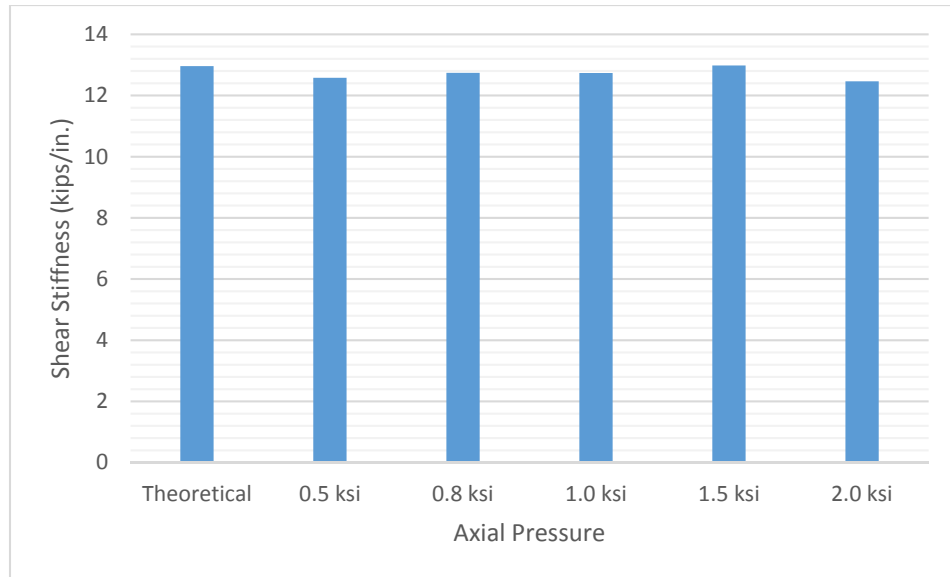


Figure 5.15: Calculated shear stiffness at different axial loads (S)

Although bearing S showed no variability in shear stiffness at tested axial stress levels, that was not the case for bearing M. Figure 5.17 shows the force displacement curves at various axial stress levels. As can be seen, there is a decrease in shear stiffness with increasing axial stress. This is a sign that the bearing is prone to buckling at either higher axial stress levels or larger shear deformations (increased shear deformations reduce the effective plan area and thus increasing the effective axial stress).

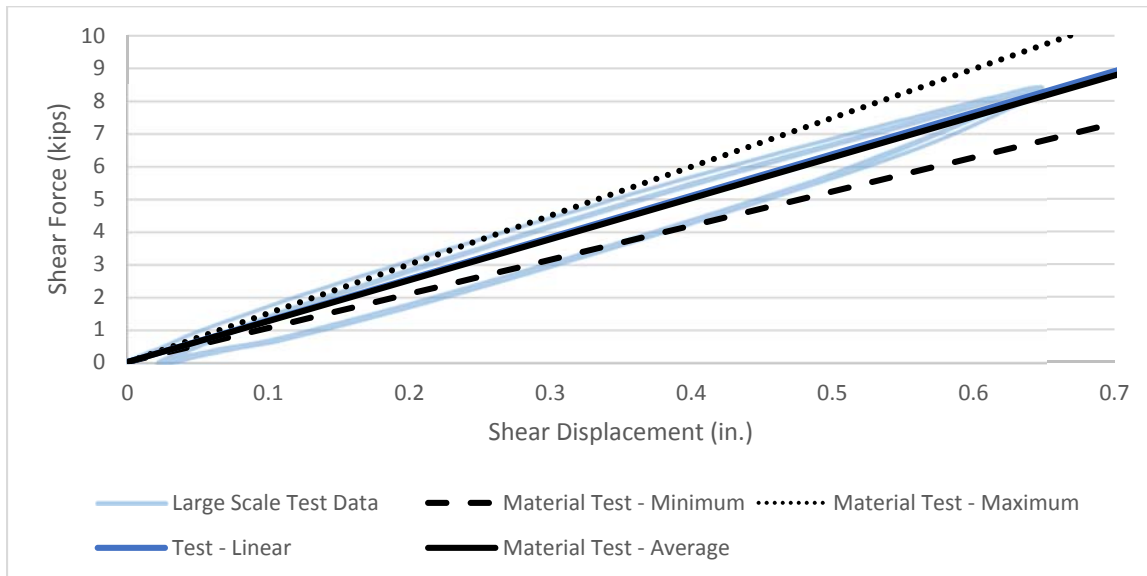


Figure 5.16: Test-Material stiffness correlation (S)

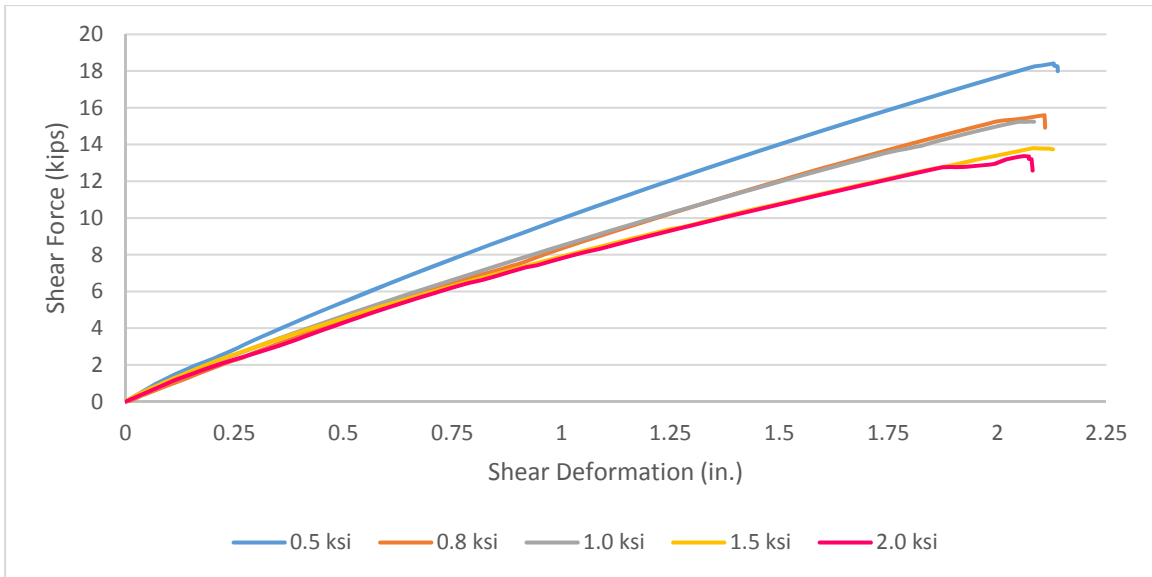


Figure 5.17: Force-Displacement curves (M)

5.4.2 DIRECTIONAL STIFFNESS RESULTS

Bearings used in higher demand applications are more likely to be used in bridges with skewed supports and/or horizontal curvature. In these applications, the bearings will likely experience shearing deformations in more than one direction. Although this issue has been investigated numerically, no experimental results backing numerical findings existed prior to this study. As can be seen in Figure 5.18 the numerical model predicted almost no impact of the shearing direction on the shear stiffness for the large bearing, a fact that was confirmed with experiments conducted at FSEL. For comparison reasons the theoretical stiffness value is also illustrated. In order to better illustrate the change in shear stiffness with respect to the shear direction, normalized results as shown in Figure 5.19.

Data discrepancy between numerical predictions and measured values can be attributed to various parameters such as the stiffness calculation method, instrumentation errors, and test setup errors. Bearing L could not be assessed for a shear angle of 90° due to geometric constraints of the test setup.

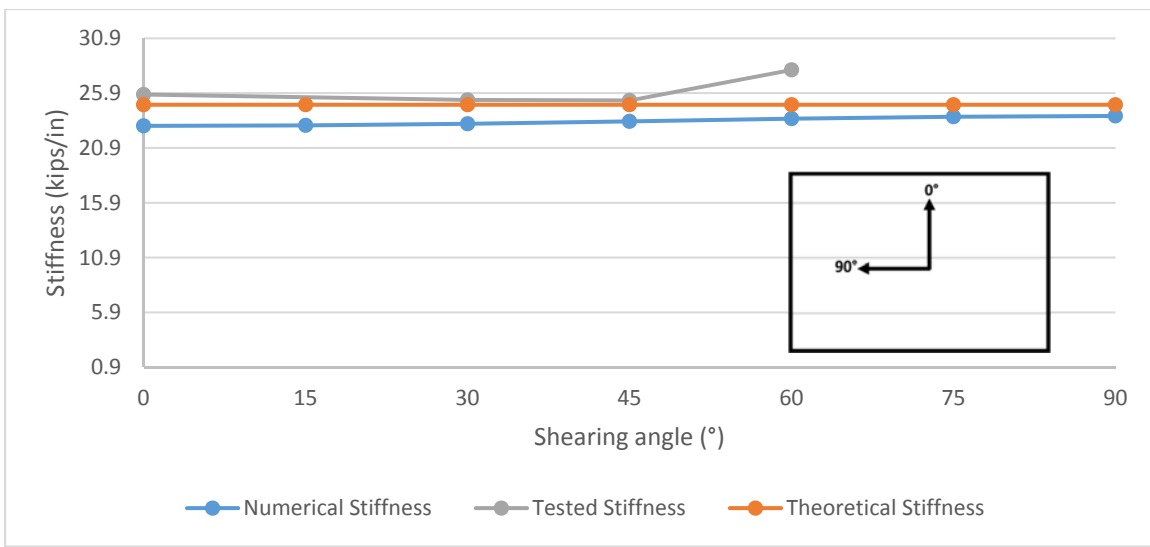


Figure 5.18: Effect of shear direction on shear stiffness (L)

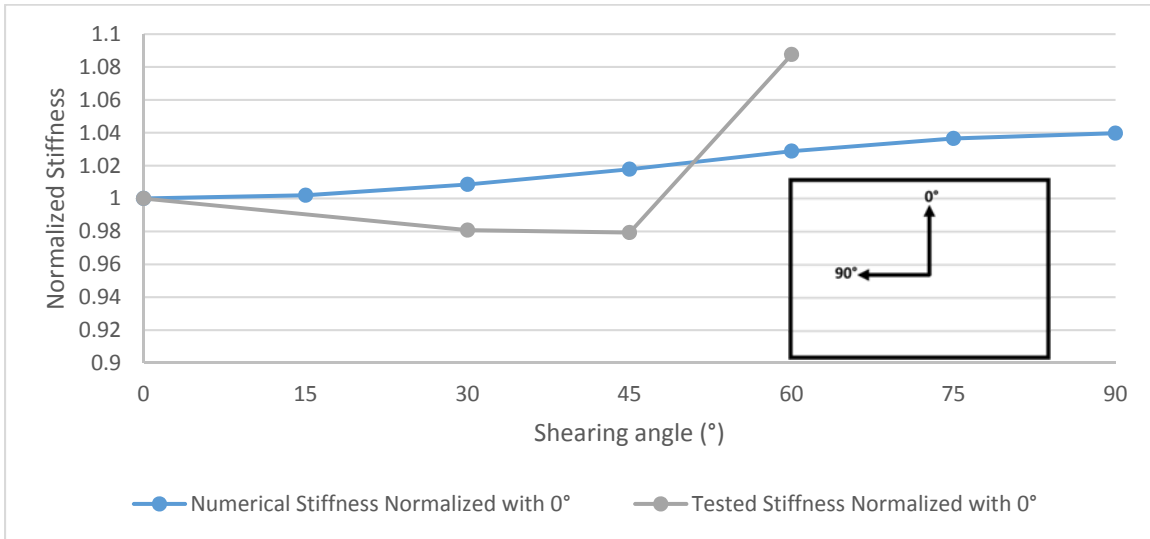


Figure 5.19: Effect of shear direction (normalized) on shear stiffness (L)

Although the findings were consistent with previous numerical studies, this research study expanded the tests to higher shape factors and aspect ratios. As a result bearing M was also tested for assessing the effects of shear directionality. As illustrated in Figure 5.20 and Figure 5.21 for bearing M, and for an axial pressure of 1200 psi the shear stiffness increases with a tendency to approach the theoretical solution as the shearing direction approaches 90°. In this case, although conservative and safe to be neglected from a slipping standpoint, the change in shear stiffness with respect to the shear direction is not negligible, reaching approximately 45%. It can also be seen that for the specific axial stress level, the prediction of the shear stiffness by means of FEA is underestimating the measured values.

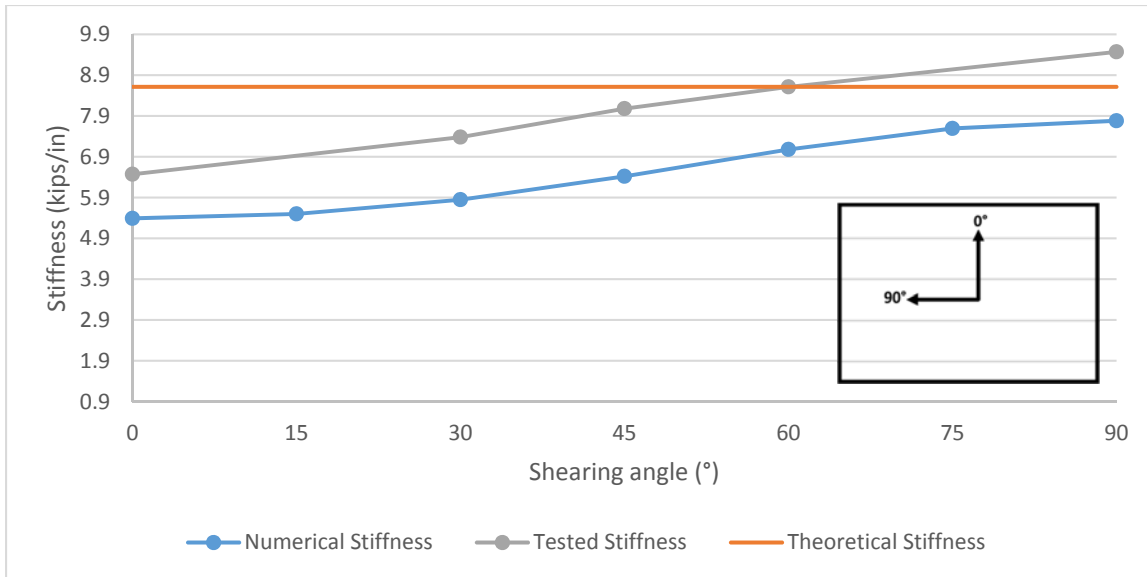


Figure 5.20: Effect of shear direction on shear stiffness (M)

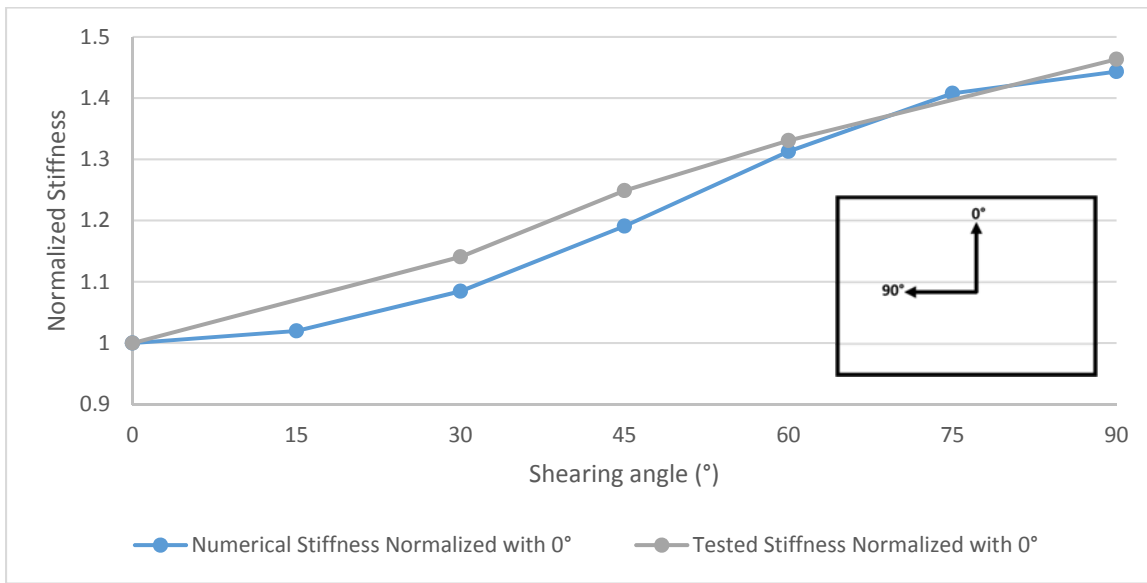


Figure 5.21: Effect of shear direction (normalized) on shear stiffness (M)

5.4.3 TEST OBSERVATIONS

For bearings M the combination of 1.5 ksi axial pressure and 75% shear strain, the bearing showed no excessive bulging or rollover as can be seen in Figure 5.22. The phenomenon of rollover (Figure 5.23) is defined as the loss of contact of portion of the bearing surface due to the bearing shearing. A similar phenomenon was noticed in bearing L (Figure 5.24). The disadvantages of the rollover effect are that it reduces the effective area of the bearing, making it more prone to buckling, and increases the potential of bending the edge of the steel laminates inside the bearing. As a result, high stresses and strains concentrate in that region and are associated with a high potential of distress initiation. It is worth noting that the bearings were inspected after all tests and there were no visible signs of distress in any of the bearings.



Figure 5.22: Bearing M under 1.5 ksi axial load and 75% shear strain



Figure 5.23: Rollover effect on bearing S



Figure 5.24: Bearing L under 2.0 ksi axial load and 100% shear strain

Finally, as design recommendations will be the final outcome of this study and stability is one of the failure modes a designer must consider, bearing M was pushed to the point of instability. Due to the larger thickness, bearing M was the bearing most prone to buckling. The bearing was tested to 2.0 ksi axial and the target shear strain was placed at 100%. Despite the fact that the target shear strain was reached the bearing is considered to have failed as the loss of axial stiffness (buckling) led to excessive axial deformations, resulting in damage to the shear test setup. In order to avoid any further damage in the shear test setup the axial load was immediately decreased, allowing for pictures only at the unloading phase. Bearing M can still be seen in the buckled configuration in Figure 5.25. It can be noticed that the excessive axial load caused the top layer of the elastomer to “flow” out at the edges. This phenomenon is less prominent at the concrete-elastomer interface due to increased friction at this location.



Figure 5.25: Buckled bearing M

5.5 Full Scale Rotational Test Results

5.5.1 COMBINED COMPRESSION AND ROTATION RESULTS

This section provides representative data from tests conducted and describes the main conclusions that were drawn from this portion of the study. As previously discussed, the purpose of this test series was to evaluate the consequences of lift-off, evaluate the validity of the total shear strain method for calculating the strength limits of a bearing, and use this test as means of validating the FEA portion of the study.

Figure 5.26 shows representative data from a combined compression and rotation test. Regarding the lift-off phenomenon, as expected, the absence of contact between the steel plate and the bearing only happened at lower axial loads, as depicted in Figure 5.27. As a result the test data chart (Figure 5.26) can be divided in two portions, the lift-off portion associated with lower loads, and the full contact portion where the plate is in contact with the total area of the bearing and the measured stiffness is identical to the axial stiffness measured in prior portions of this study.

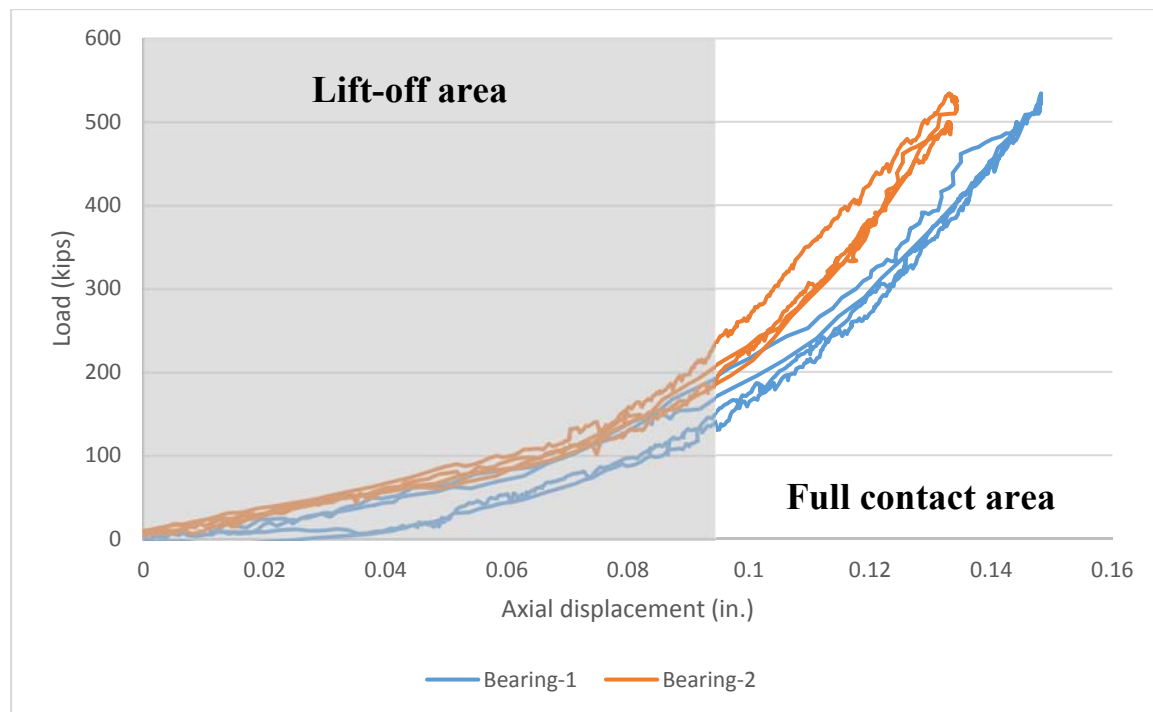


Figure 5.26: Combined compression and rotation test data (Bearing $L - \theta=0.5^\circ$)

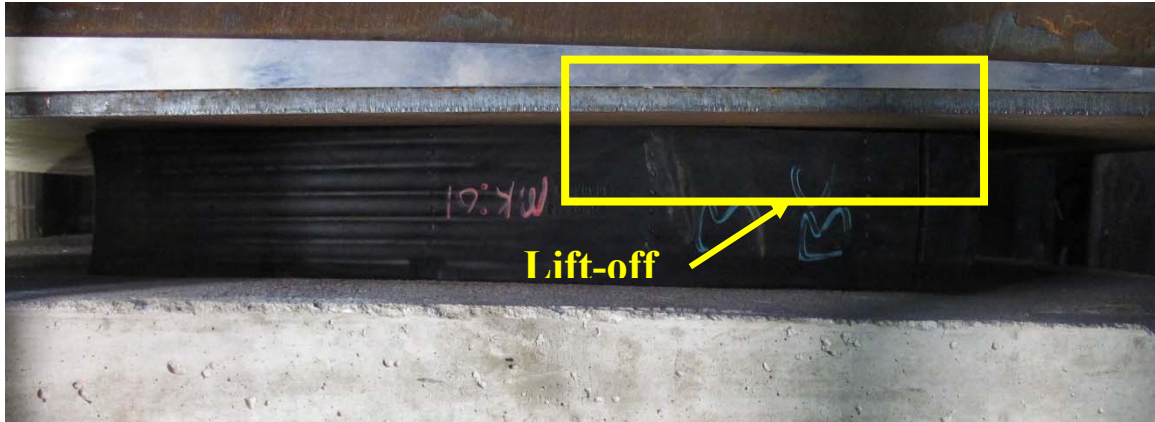


Figure 5.27: Lift-off during combined compression and rotation test

In order to evaluate the strength of the bearing, combined compression and rotation tests were conducted at higher axial loads and with larger imposed rotations. According to AASHTO LRFD, imposing a rotation of 1.5° on bearing L should fail as a total shear strain of 5.5 would be reached. However, as can be seen in Figure 5.28, bearing L was able to sustain the aforementioned rotation in addition to a compressive axial load of 800 kips, leading to a total shear strain of approximately 7.0.



Figure 5.28: Bearing L under combined compression and rotation ($\theta=1.5^\circ$)

Finally, as one of the purposes of this portion of the study was to validate the FEA models developed for this research project, test data was compared with FEA predictions. As illustrated in Figure 5.29, FEA predicts the loading curves reasonably well. The error between tests and prediction can be attributed to inherent test setup asymmetries, leading to the compression of the one bearing slightly earlier than the other. This fact inevitably offsets the two curves, plotted here without any correction. It is obvious to the reader that upon this offset correction, good correlation would be achieved. . As a result, it can be said that FEA provide accurate predictions of the bearing behavior.

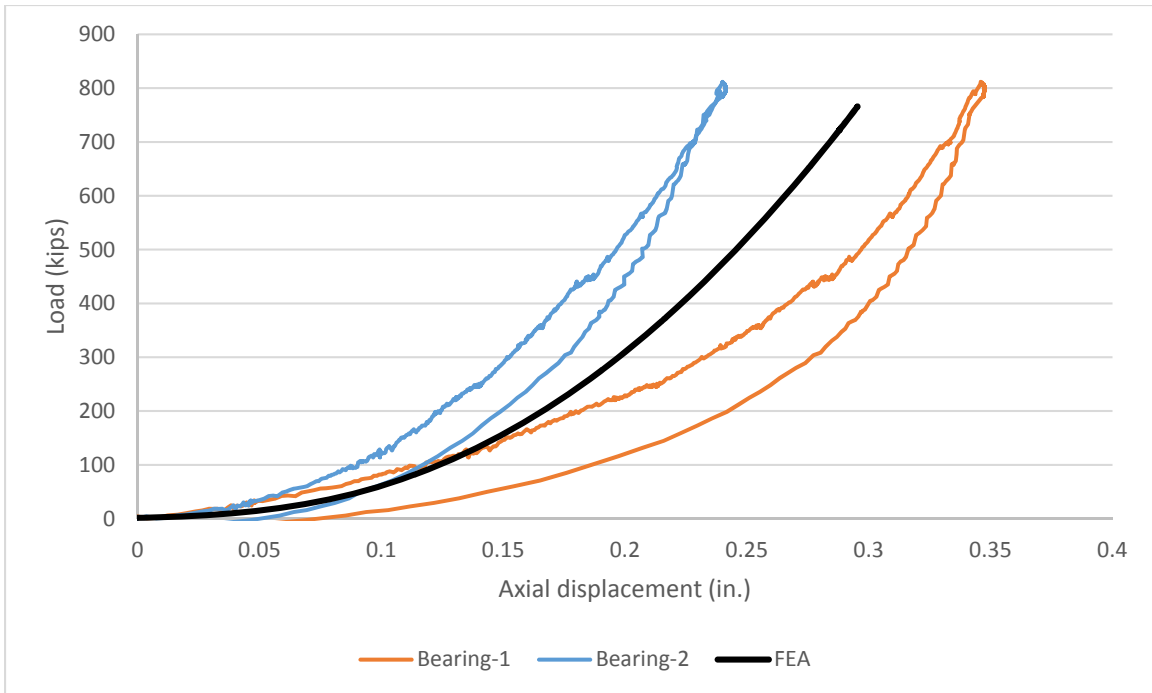


Figure 5.29: Combined compression and rotation test data and FEA prediction (Bearing L – $\theta=1.5^\circ$)

5.5.2 TEST OBSERVATIONS

No failure was noticed after the application of the maximum service load under both rotation cases despite the large shear strains at the end of the bearing as illustrated in Figure 5.28.

5.6 Summary

An overview of the experimental results was provided in this chapter. The findings are presented from the standpoint of the current design approaches assessment for the use of bridges considered as higher demand applications.

From the material experiments conducted in this study two main results can be drawn. The first is that the magnitude of material property variation in larger bearings, although existent and more prominent than in smaller bearing, should not be a concern for the designer and should not be a reason for disqualifying this bearing alternative. The second is that as neoprene rubber becomes stiffer in lower temperatures, slipping is a non-recoverable, low-temperature-driven phenomenon that should be explicitly designed for.

From the full-scale experiments conducted in this research project there were four major outcomes.

- It has been shown that AASHTO Method A and Method B design procedures produce safe bearing designs for what could be considered as higher demand applications, with Method A producing larger, uneconomic bearings.
- It has been found that equations predicting the axial deflections of bearings are not necessarily accurate for bearings qualifying for higher demand applications (high shape factors, large plan areas).

- Lift-off is a phenomenon associated with lower axial loads and thus not an issue when observed rotations are not exceeding the ones observed.
- Buckling of elastomeric bearings for non-seismic applications can also be an issue as taller bearings are needed to accommodate large temperature bridge movements; however, this issue is successfully addressed by current AASHTO design approaches.

All findings from the experimental portion of this study were used to validate the finite element simulations for model calibration and prediction comparison purposes.

CHAPTER 6: FINITE ELEMENT ANALYSIS MODELING OF ELASTOMERIC BEARINGS

6.1 Introduction

Three-dimensional Finite Element Analyses (FEA) provide an economical means to predict the structural behavior and to validate the experimental results for research purposes. Important internal quantities such as stress and strain can be sought with ease where they are difficult to be measured in the full scale testing.

This chapter presents the results of finite element modeling of elastomeric bearings under compression, shear, and rotational deformations. The numerical results were analyzed and validated by the experimental measurements.

The validity of finite element analyses of elastomeric bearings with higher shape factors are commonly compromised by an observed significant discrepancy between calculated and measured axial stiffness due to material uncertainties. An analytical model that obtains material coefficients necessary for FE modeling is first developed, prior to the finite element modeling.

6.2 Material Model

In contrast to the material linear elasticity of the steel, determining the material parameters required for characterizing the constitutive relation for the elastomer is much less explicit yet essential to the successful modeling of elastomer materials due to their complex nature of high material non-linearity. A commonly used hyperelastic material model for elastomers is adopted for finite element modeling in this study, requiring material coefficients, which include polynomial energy density function coefficients and bulk modulus, to be obtained prior to the modeling.

In general practice, the material coefficients for finite element modeling are usually obtained from the previous literature or testing results of material specimen manufactured with the same batch of elastomeric bearings through specifically designed approaches, e.g. quad and dual shear tests and cylinder bulk modulus test.

However, the specimen used for material testing, is not in a stress state that is completely the same to those in the bearing. Furthermore, material coefficients calibrated from the material testing of specimens are not representative of the material property variation and uncertainty within the bearing. Though these values could provide reasonable predictions of the global behavior of elastomeric bearings through FE modeling in certain deformational cases, they would likely perform poorly in others. An analytical model is hence developed allowing material coefficients from the global measurements of force and deformation to be obtained from the full scale testing. Putting these coefficients back into the FE model, more valid numerical results that agree with the global force-deformation experimental measurements are obtained, allowing the investigation of the behavior of the elastomeric bearing under various type of deformation to be performed with confidence.

6.2.1 MATERIAL COEFFICIENTS

The hyperelastic model of elastomers is characterized by the strain energy density function. The primary goal is to determine the polynomial coefficients of the energy function by full scale shear testing. Assuming an elastomer layer ($L \times W \times D = a \times b \times t$) perfectly

bonded at the top and bottom is subjected to a vertical force P and horizontal force H , and consequent uniform simple shear deformation of γ , the deformation gradient \mathbf{F} can be expressed as :

$$\mathbf{F} = \begin{bmatrix} 1 & \gamma & 0 \\ 0 & 1 & 0 \\ 0 & 0 & 1 \end{bmatrix}$$

Then the right Cauchy-Green deformation tensors \mathbf{C} are:

$$\mathbf{C} = \mathbf{F}^T \mathbf{F} = \begin{bmatrix} 1 & \gamma & 0 \\ \gamma & 1 + \gamma^2 & 0 \\ 0 & 0 & 1 \end{bmatrix}$$

The strain invariants of the right Cauchy-Green tensor are expressed as follows:

$$I_1 = I_2 = 3 + \gamma^2$$

$$I_3 = 1$$

The total potential energy of the system is given by:

$$\Pi = \int W(I_1, I_2, I_3) d\Omega - H\Delta$$

Provided that the body is in static equilibrium, the variation of the total potential energy should be zero:

$$\delta\Pi = \int \frac{\partial W}{\partial I_i} \frac{\partial I_i}{\partial \gamma} \delta\gamma d\Omega - \frac{\partial(Ht\gamma)}{\partial \gamma} \delta\gamma = 0$$

For Neo-Hookean material model, we substitute $W = C_1(I_1 - 3)$ into equation above:

$$C_1(2\gamma)(abt) - Ht = 0$$

The horizontal force is therefore can be expressed as:

$$H = 2C_1(ab)\gamma$$

From the full scale testing, we have the measured lateral stiffness values:

Table 6.1: Measured lateral stiffness of bearings in full scale testing

Bearing	Width W (in.)	Length L (in.)	Effective Width W _{eff} (in.)	Effective Length (in.) L _{eff} (in)	Average shear modulus - full scale (psi)
S	18	9	17.25	8.25	98.00
M	27	14	26	13	94.24
L	36	23	35	22	101.15

The C_1 can be calculated from the measured average shear modulus and bearing geometry:

$$C_1 = \frac{1}{2} \frac{LW}{L_{eff}W_{eff}} G$$

The calculated C_1 values are tabulated as followings:

Table 6.2: Calculated C1 values

Bearing	C ₁ (psi)
S	53.4
M	51.2
L	53.4

6.2.2 BULK MODULUS

The elastomer is nearly an incompressible material. Its bulk modulus is an essential parameter to the behavior of elastomeric bearings under compression and rotation.

Gent and Lindley (Gent and Lindley 1959) first derived a simplified equation to calculate the compression modulus of an elastomer layer, commonly known as the “pressure method”, which gives

$$E_c = E(A_a + B_a S^2)$$

Where $E \approx 3G$ for nearly incompressible material. This equation assumes that that elastomer layer is completely incompressible, and that the top and bottom surfaces of the bearing are perfectly bonded.

For an infinite strip (plane strain), Gent and Lindley give

$$A_a = \frac{4}{3}, B_a = \frac{4}{3}$$

In the past decades, many other researchers extended this work based on Gent and Lindley’s formulation. TX-DOT research Report 1304-3 (Muscarella and Yura 1995) suggest following values:

$$A_a = 1, B_a = 2k$$

Where $k = 0.75$ for a rectangular pad with a hardness of 50.

As the contribution of the term A_a is usually insignificant, AASHTO LRFD Bridge Design Specifications (AASHTO 2012) adopt the values

$$A_a = 0, B_a = 1.6$$

The material incompressibility is a reasonable assumption for elastomer units with low shape factors; however, the effect of bulk compression should be considered for those with high shape factors, e.g. very thin elastomer layers. The assumption of incompressibility for relatively high shape factors will lead to the overestimation of axial stiffness (Koh and Lim 2001). To take into account the effect of bulk compression, Gent and Lindley proposed a modification for prediction of the apparent compression modulus of an elastomer unit can be represented by

$$\frac{1}{E_A} = \frac{1}{E_c} + \frac{1}{K}$$

Where E_A and K denote the respective apparent compression modulus and bulk moduli.

This modification is currently included in Eurocode (EN1337-3 2005), but not in the AASHTO LRFD. Alternatively, based on the research work of NCHRP Report 596 (Stanton, Roeder et al. 2008), the B_a value that accounts for the effect of bulk compression since 2010 version AASHTO LRFD code is as follows:

$$A_a = 0$$

$$B_a = (2.31 - 1.86\lambda) + (-0.90 + 0.96\lambda) \left[1 - \min \left(\frac{L}{W}, \frac{W}{L} \right) \right]^2$$

$$\lambda = S_i \sqrt{\frac{3G}{K}}$$

Where S_i denote the shape factor of the elastomer layer

Elastomer layers and elastomeric bearings in compression have been under study analytically, computationally and experimentally for decades. Some additional pressure analytical models have also been developed by researchers. Bulk moduli that are experimentally obtained from material testing, such as cylinder bulk modulus tests, are used for the analytical and computational (FEA) models. Predictions of these analytical models have been found to share a remarkable agreement with the computational results (Qiao and Lu 2014). However, it has been widely reported that the analytical and computational models tend to overestimate the axial stiffness (compression modulus) for the elastomer units with high shape factors, in comparison with experimental measurements, to the extent that the validity of analytical and FEA models are cast doubt upon. Over-predictions of the axial stiffness up to 200% over the experimental measurements have been observed in many cases. The cause for this is still not entirely clear but believed to be attributed to uncertainties in the bulk modulus (Anderson, Mott et al. 2004).

This discrepancy poses a significant challenge for finite element modeling of elastomeric bearings, implying that the calculated global axial deformation, and ensuing pressure and strain distribution within the bearing may be considerably different from their actual behaviors, under the same level of axial loads. Therefore, the selection of bulk modulus is vital to the validity of the FE models. Therefore, an important aspect of accurate modeling is to find an appropriate apparent bulk modulus value for the bearing, which represents the bulk modulus uncertainty of the whole bearing and reflects its actual behavior under loads. Identifying an accurate representation of the bulk modulus is important for gaining an understanding of the internal behavior of bearings with high shape factors under compression deformations through numerical study with convincing results. The global measurements of axial force and deflection are then used to find the apparent bulk modulus for the succeeding finite element modeling.

Assuming an elastomeric bearing has n layers, the thickness of each layer might not be the same as surface layers are usually thinner.

For each layer

$$\begin{aligned}\frac{1}{E_{A,i}} &= \frac{1}{E_{C,i}} + \frac{1}{K_A} \\ \varepsilon_i &= \frac{F_N}{E_{A,i}A} \\ d_i &= \varepsilon_i t_i\end{aligned}$$

Where t_i and d_i are thickness and deflection of a specific layer.

The total deflection of all elastomer layers d can be obtained as follows:

$$d_T = \sum d_i$$

The axial stiffness is then given by:

$$K_N = \frac{F_N}{d_T}$$

Substituting the measured axial stiffness of the elastomeric bearings from full scale test results and their geometric parameters into above equations, the apparent bulk moduli can be solved using iterative techniques. The calculated apparent bulk moduli are listed in Table 6.3.

Table 6.3: Calculated apparent bulk modulus for all bearings

Bearing Pad	Axial stiffness (kips/in.)	Apparent Bulk Modulus (psi)
S	2617	45,020
M	2911	103,900
L	9817	65,700

6.3 Finite Element Modeling

The mathematical model of the elastomeric bearing is governed by a set of Partial Differential Equations that characterize the kinematics, constitutive relations, and equilibrium. These PDEs are solved numerically on a three-dimensional model with given boundary conditions, in the general purpose FEA program ANSYS V14. The modeling details are discussed in the following sections.

6.3.1 NUMERICAL SCHEME

In the FE Model, the elastomer and steel were discretized with the 3D 8-node solid element, SOLID 185. This element supports a variety of material models including linear elasticity, plasticity, and hyperelasticity. Its mixed formulation capacity allows the simulation of nearly-incompressible hyperelastic materials. It has eight corner nodes and one optional pressure node.

Steel shims were modeled using a linear elastic material, which is reasonable since the shims generally remain in the elastic range under the design loads. Past laboratory tests have shown that the fracture of steel shims does not typically occur until loads reach approximately ten times the typical design load.

The nearly incompressible material formulation for the elastomer is essentially a constrained variation problem. The goal of the study is the determination of the mixed displacement and pressure fields in a domain that is subjected to external boundary values and internal compressibility constraints. The principle of virtual work states that if a body is in static equilibrium, the sum of virtual work done by external and internal forces is zero by virtual displacement. The internal virtual work is augmented by a pressure-like Lagrange multiplier to implement the incompressible constraint.

$$\delta \int W d\Omega + \int \left(\frac{P - \bar{P}}{K} \right) \cdot \delta \bar{P} d\Omega - \int b \cdot \delta u d\Omega - \int t \cdot \delta u d\Gamma = 0$$

δ : The variational operator

W : Strain energy density function

P : Hydrostatic pressure from material law $P = -Ke_V$

\bar{P} : Pressure degree of freedom

KK : Bulk modulus

Bb : Body force

Tt : Surface traction

TARGET 170/CONTACT 173 3D linear surface contact elements were implemented for the contact analysis. Regularized Coulomb friction models were used to characterize the interaction of the contact surface at the tangential surface. The tangent motion is zero, i.e. “Sticking,” if the surface traction does not exceed a critical value, which is proportional to the normal contact pressure. Beyond that value, “slipping,” i.e. relative movement at the interface, will occur.

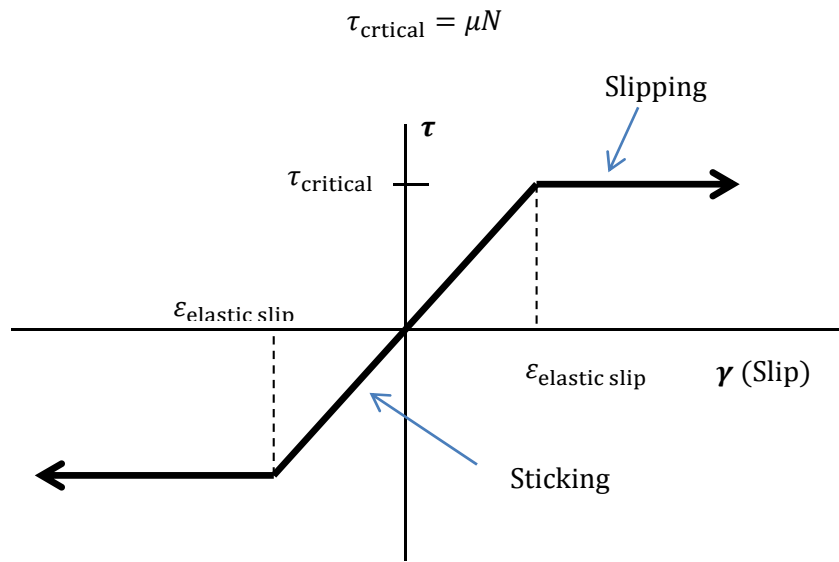


Figure 6.1: Regularized Coulomb friction model

The discontinuity between the two states: sticking and slipping creates numerical difficulties in convergence. Therefore regularized Coulomb friction that allows “elastic slip” was introduced by augmented Lagrange formulation to alleviate this problem. A constant value of 0.3 was given for all analyses.

6.3.2 FEA MODEL

The Finite element model was developed in ANSYS consisting of one elastomeric bearing and two rigid blocks above and beneath the bearing, as illustrated in Figure 6.2. The top block represents the steel sole plate connected to the superstructure, while the bottom block represents the abutment/pier.

Contact elements were used at the interface of the elastomeric bearings and the abutment/sole plates. TARGET 170 elements were applied at the bottom side of the top block and the top side of the bottom block. CONTACT 173 elements were applied on top and the bottom sides of the elastomeric bearings.

Only half of the bearing and blocks were modeled in ANSYS, exploiting the symmetry of geometry and load pattern.

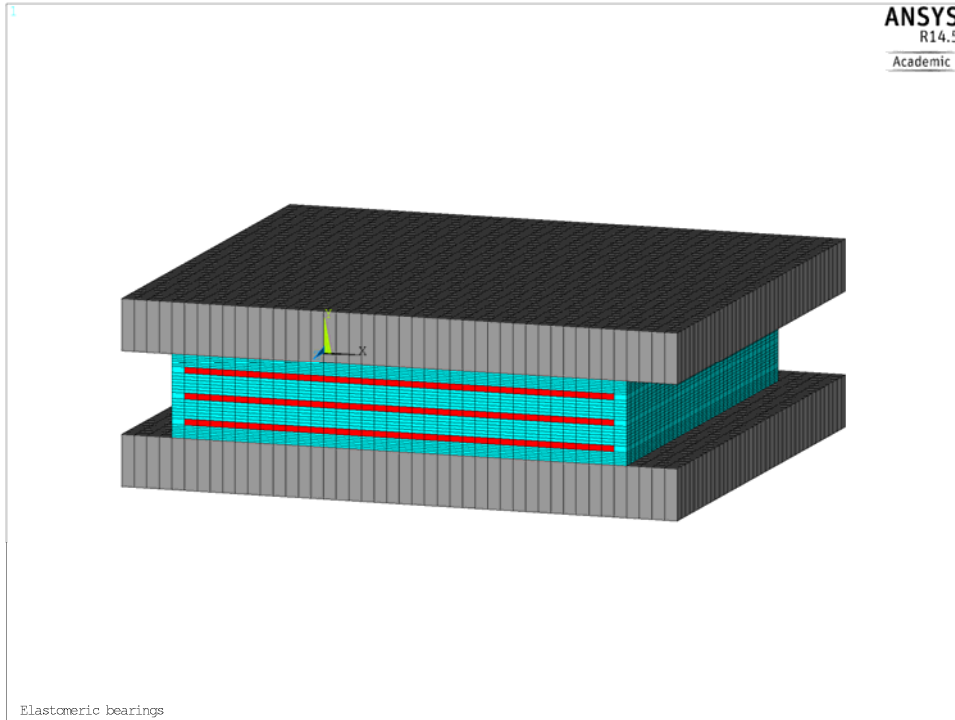


Figure 6.2: Finite element model for elastomeric bearing

Three types of modeling with different load paths were performed, in correlation to the three types of laboratory full-scale testing that were conducted: compression testing, shear testing, and rotation testing. The same bearing geometries and load patterns were used in the numerical modeling to best simulate the laboratory conditions of the full scale tests. All loads applied on the model were displacement-controlled for better convergence.

In compression modeling, as presented in Figure 6.3, the bottom rigid block was fixed at the bottom, while the top of the top block was gradually displaced with a uniform vertical deflection, U_y .

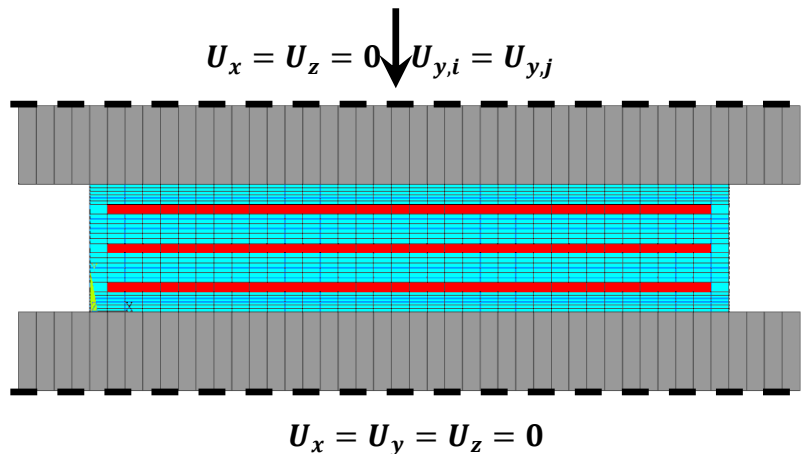


Figure 6.3: Schematic diagram for compression modeling

In shear modeling, as presented in Figure 6.4, the bottom rigid block was also fixed at the bottom, while a uniform vertical deflection U_y was first applied on the top of the bearing and maintained. The top rigid block was then sheared laterally up to a uniform displacement U_x

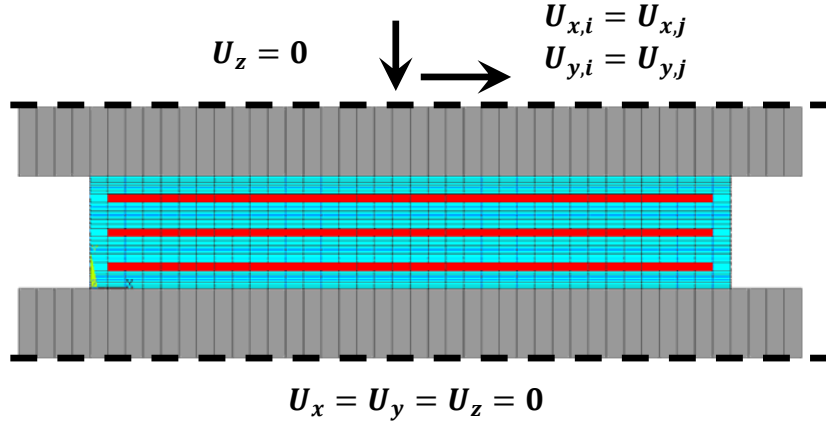


Figure 6.4: Schematic diagram for shear modeling

In the rotation modeling, as represented in Figure 6.5, the bottom rigid block was fixed at the bottom. A tapered top rigid block with a slope in longitudinal direction was mounted above the elastomeric bearing. The top block and the bearing only shared an initial contact at the bearing edge on the width side. A uniform vertical deflection U_y was applied on the top of the bearing in a gradual manner.

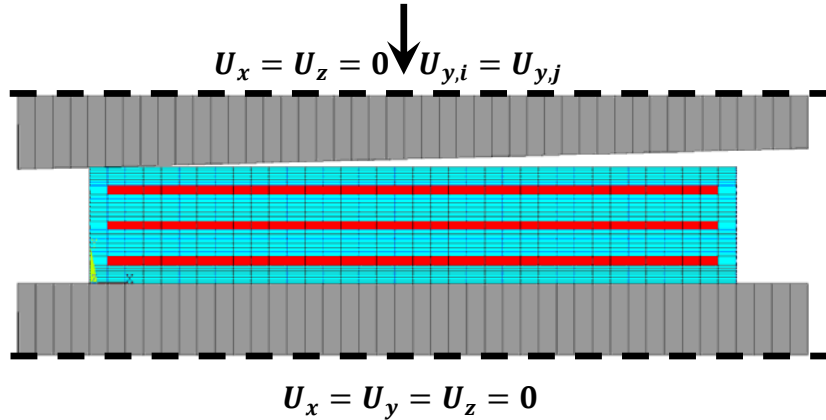


Figure 6.5: Schematic diagram for rotation modeling

A summary of loads for different analysis types is tabulated below:

Table 6.4: Summary of Loads

Modeling Type	Compression	Shear displacement	Taper angle
Compression Testing	Up to laboratory testing values	0	0
Shear Testing	1000 psi	50% of total elastomer height	0
Rotation Testing	Up to laboratory testing values	0	0.5° and 1.5 °

6.3.3 MESH

Three types of bearings that were tested in the full scale testing were investigated numerically in the finite element modeling: the small size (S), the medium size (M), and the large size (L) bearing. The bearings had the same geometry with the specimens tested in the laboratory. Their geometric specifications are presented in Table 6.5.

Table 6.5: Summary of bearing dimensions

Bearing Pad	Width (in.)	Length (in.)	No. of "t"	Layer Thickness "t" (in.)	Cover (in.)	Steel Thickness (in.)	Total Height (in.)
L	36	23	5	0.5	0.375	0.12	3.97
M	27	14	7	0.5	0.375	0.12	5.21
S	18	9	2	0.375	0.25	0.12	1.61

The numerical results of the finite element analysis are mesh size dependent. A mesh convergence study was performed, including a number of analyses on an elastomeric bearing under compression with various global mesh sizes in the direction of the length and width as well as different numbers of element layers used per elastomer layer depth wise. The results were compared in terms of the compressive stiffness to arrive at a mesh size with sufficient accuracy and reasonable computational time required.

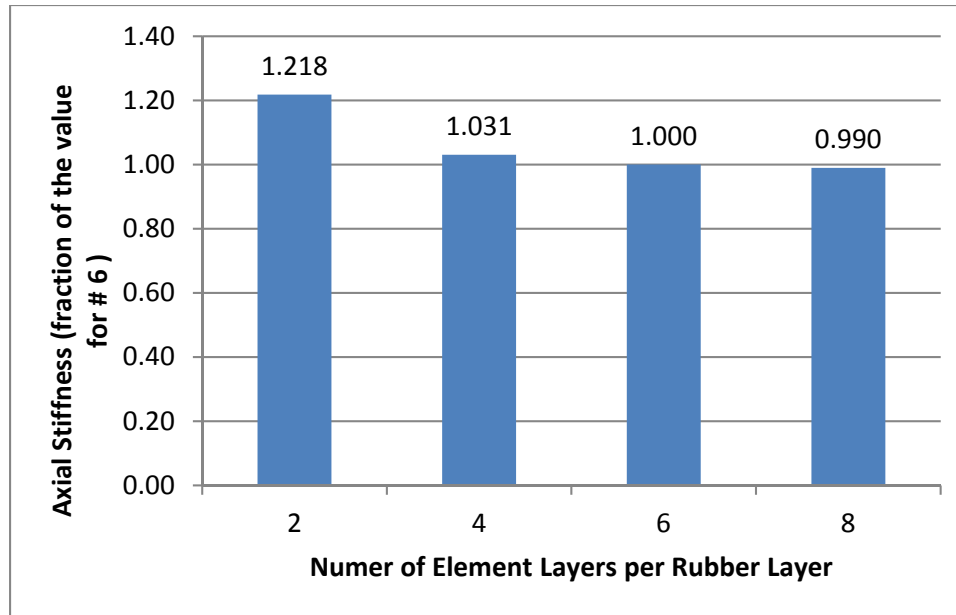


Figure 6.6: Mesh sensitivity study on number of element layers per elastomer layer

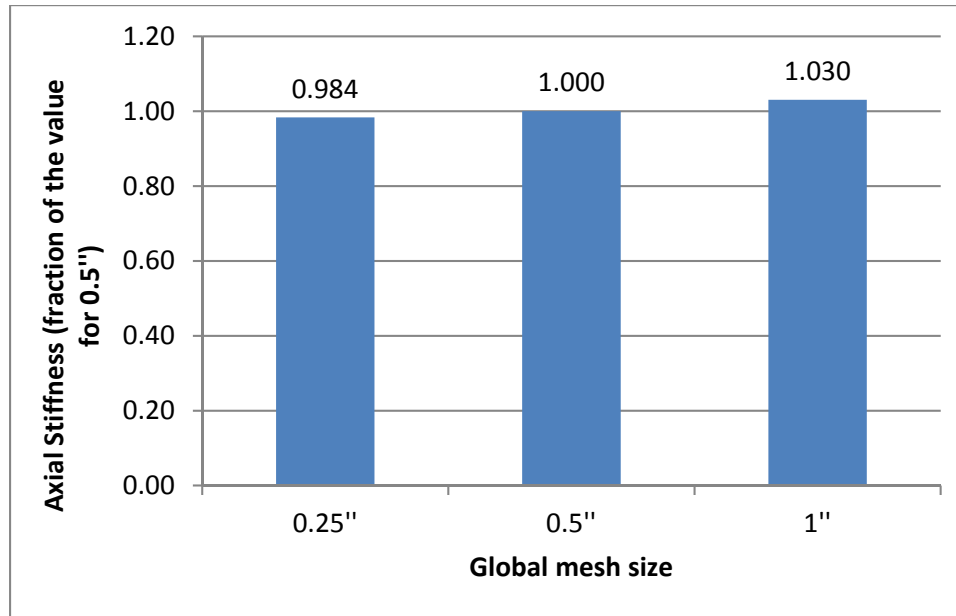


Figure 6.7: Mesh sensitivity study on global mesh size

As illustrated in Figure 6.6 and Figure 6.7 the differences between the cases were relatively small. As a result, six layers of elements were used per elastomer layer for all cases. A global mesh size (along the length and width) of 0.5" was used for medium and large size bearings, while a mesh size of 0.25" was used for the small bearing for better convergence capacity.

The three dimensional and two dimensional sectional views of meshes for all three bearings are presented below from Figure 6.8 to Figure 6.13.

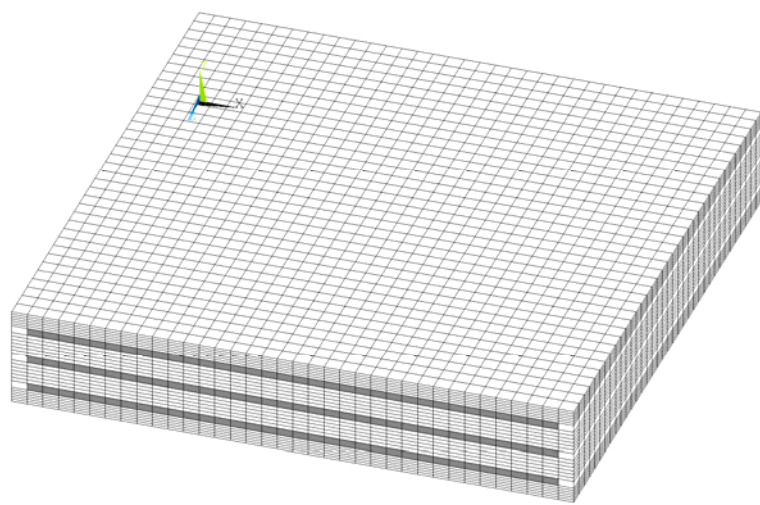


Figure 6.8: 3D view of mesh for Bearing S

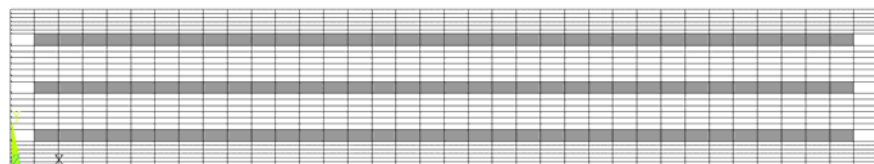


Figure 6.9: 2D sectional view of mesh for Bearing S

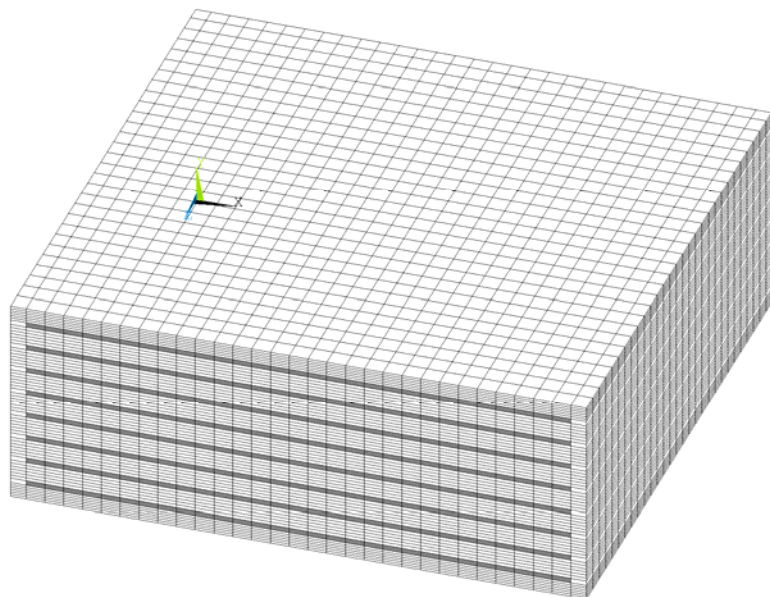


Figure 6.10: 3D view of mesh for Bearing M

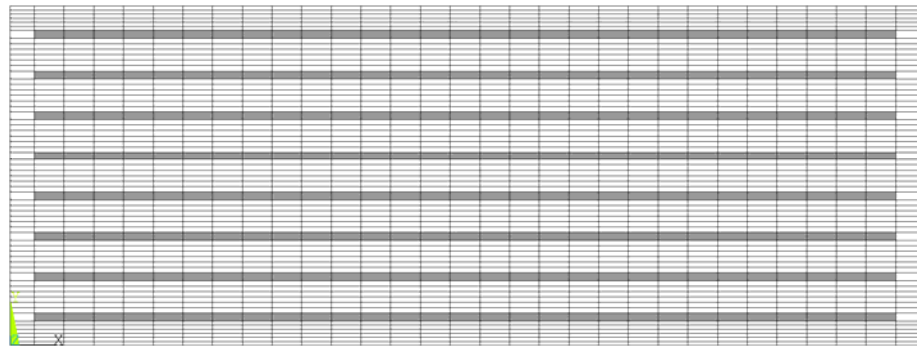


Figure 6.11: 2D sectional view of mesh for Bearing M

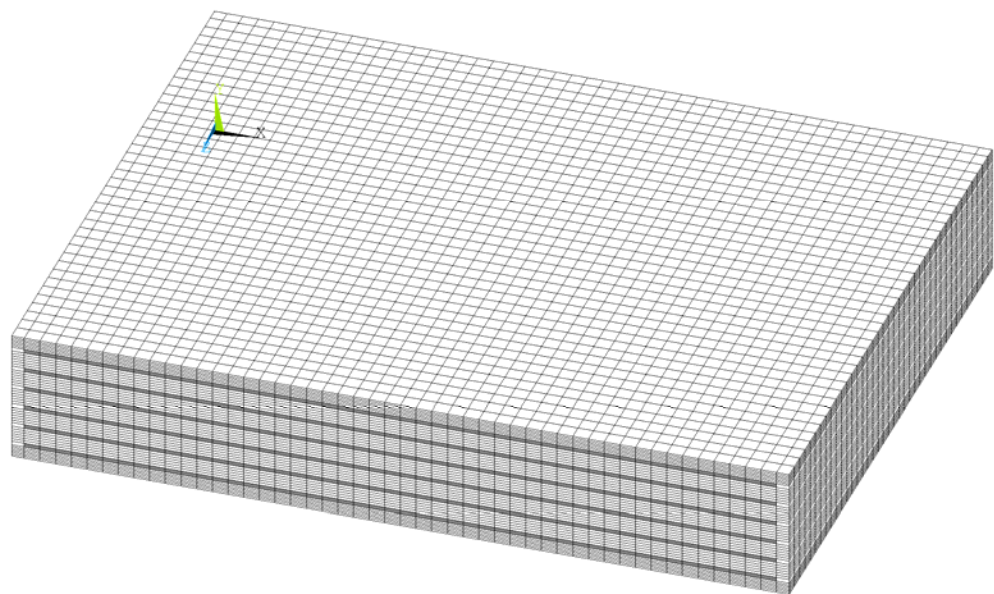


Figure 6.12: 3D view of mesh for Bearing L

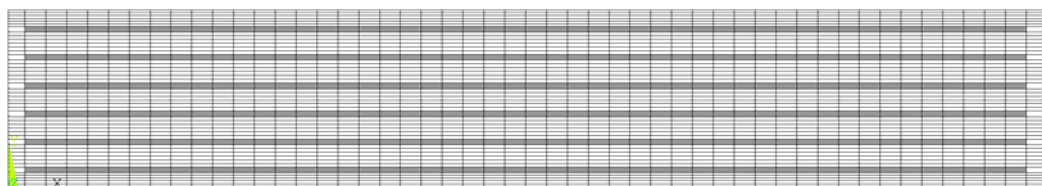


Figure 6.13: 2D sectional view of mesh for Bearing L

6.4 FEA Results

6.4.1 COMPRESSION MODELING

This section presents results from compression modeling of the elastomeric bearings as well as comparisons with the full scale testing results.

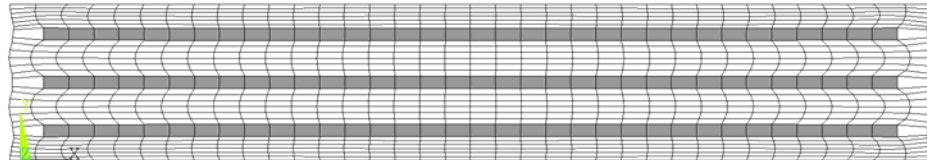


Figure 6.14: 2D sectional view of deformed mesh for Bearing S under axial load

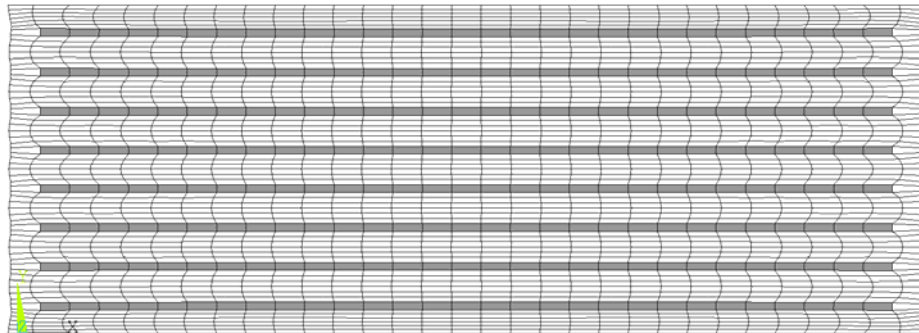


Figure 6.15: 2D sectional view of deformed mesh for Bearing M under axial load

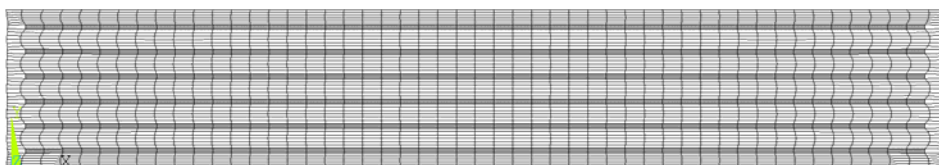


Figure 6.16: 2D sectional view of deformed mesh for Bearing L under axial load

The deformed meshes of three elastomeric bearings under the axial stress of 1ksi are illustrated from Figure 6.14 to Figure 6.16. It can be observed that the deformation profile of the elastomer layer under compression was similarly parabolic. The deformation of the elastomer was more pronounced near the exterior and insignificant at the middle of the bearing, where the deformation profile was nearly vertical. The maximum elastomer shear strain occurred at the interface of the elastomer layer and steel close to the edge of the shim.

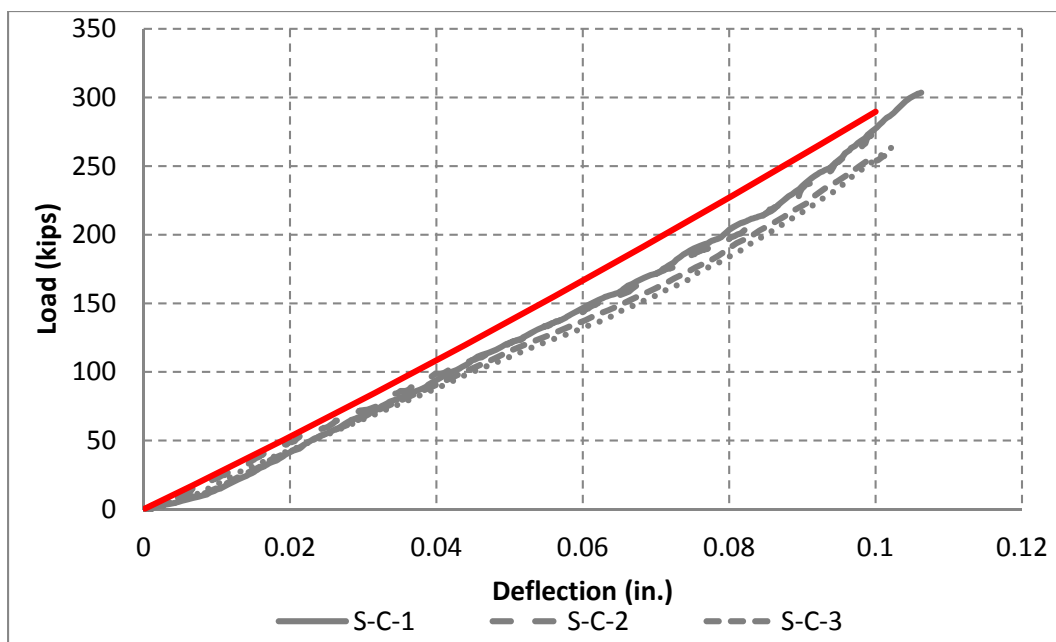


Figure 6.17: Force vs deflection curves for Bearing S under axial load

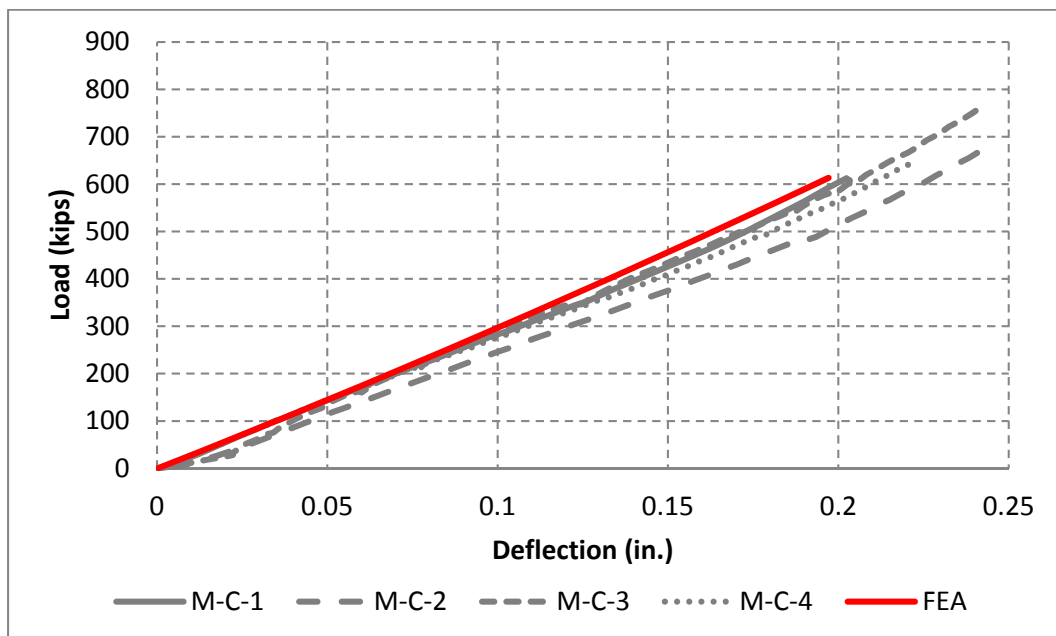


Figure 6.18: Force vs deflection curves for Bearing M under axial load

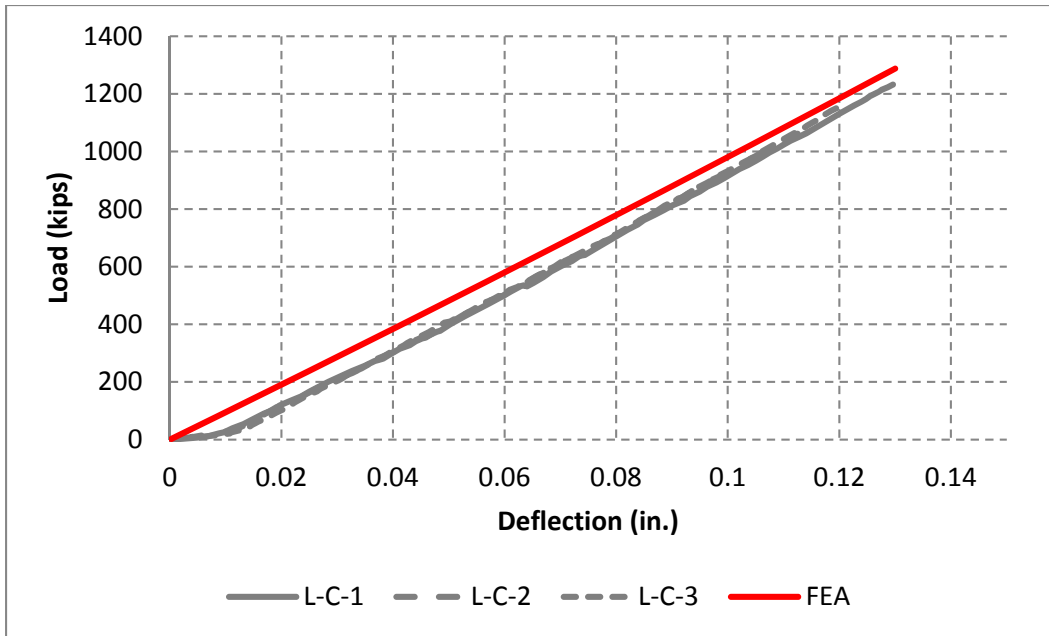


Figure 6.19: Force vs deflection curves for Bearing L under axial load

Table 6.6: Summary of numerical and experimental results

Bearing	Experimental (kips/in.)	FEA (kips/in.)	Difference (% of Experimental results)
S	2617	2892	10.5
M	2911	3096	6.4
L	9817	9883	0.7

Figure 6.17 to Figure 6.19 present the computational results of the force vs displacement curves of the three elastomeric bearings under axial deformation up to, or close to, the laboratory full scale testing loads, in correlation to the experimental results. The calculated axial stiffness values for both computational and experimental results are tabulated in Table 6.6, showing that the FEA results are in a good agreement with the experimental measurements both qualitatively and quantitatively, though the numerical model was not able to capture the initial softening behavior of elastomer that was observed in the laboratory tests.

6.4.2 SHEAR MODELING

This section presents results from shear modeling of elastomeric bearings as well as comparisons with the full scale test results. An axial stress of 1ksi was first applied on the top rigid block and bearings were then subjected to 50% lateral deformation.

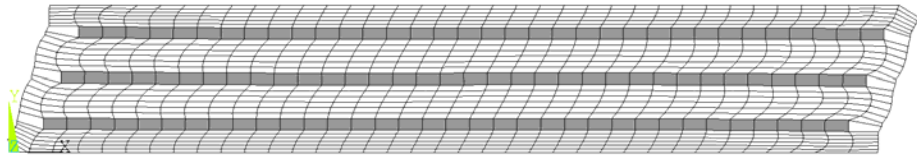


Figure 6.20: 2D sectional view of deformed mesh for Bearing S in shear

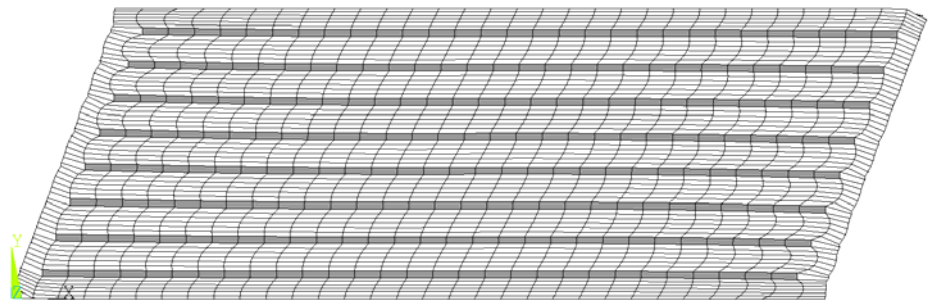


Figure 6.21: 2D sectional view of deformed mesh for Bearing M in shear

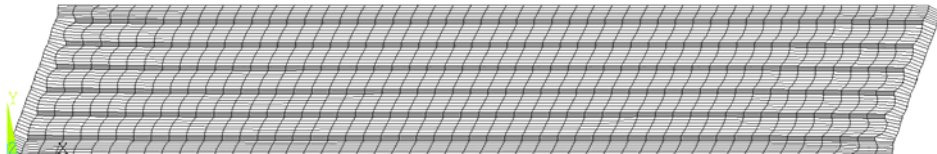


Figure 6.22: 2D sectional view of deformed mesh for Bearing L in shear

As illustrated from Figure 6.20 to Figure 6.22, the occurrence of rollover (separation of the elastomer and the superstructure) of the top elastomer cover at the “leading edge” and the diagonal edge can be readily observed because of the internal tension in diagonal direction. It can be also seen that the global lateral deformation resulted in an increase in the shear strain at the steel and the elastomer layer on one side while reduce them on the other, from the existing shear strain under compression.

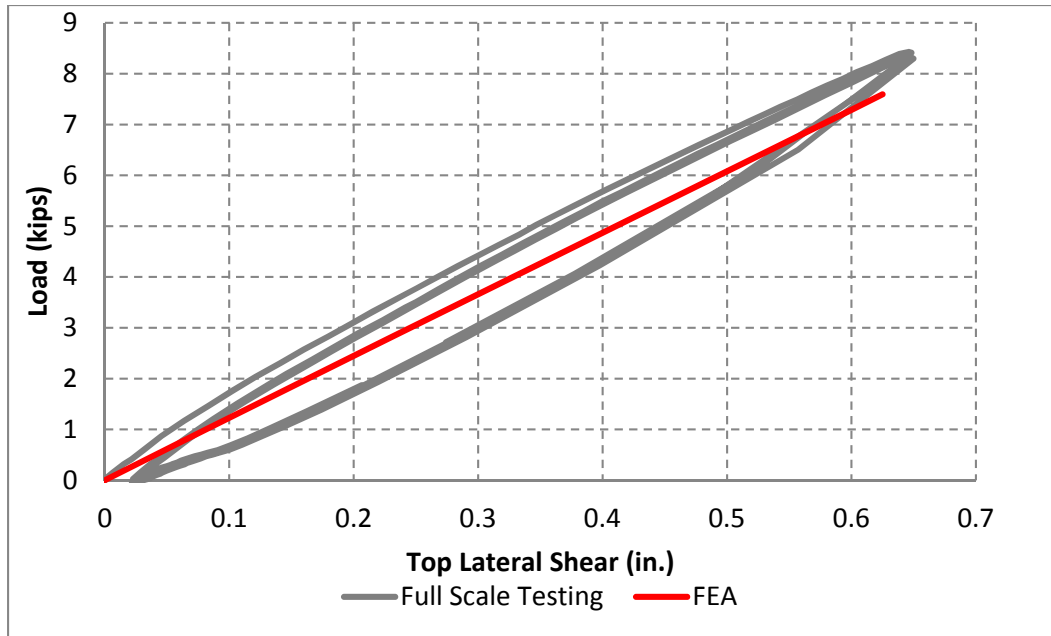


Figure 6.23: Lateral force vs displacement curves for Bearing S in shear

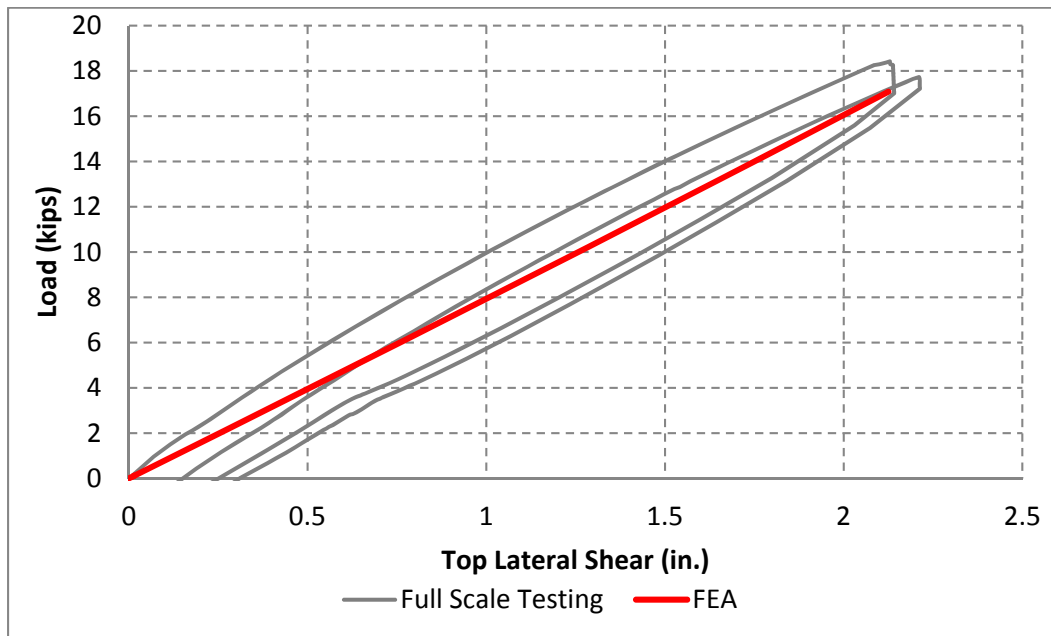


Figure 6.24: Lateral force vs displacement curves for Bearing M in shear

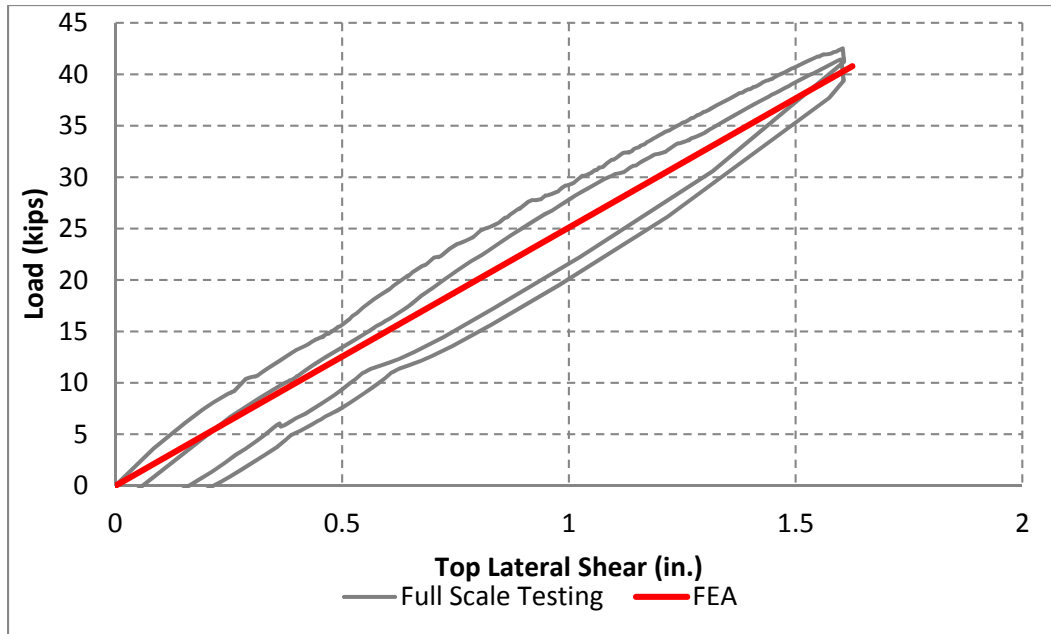


Figure 6.25: Lateral force vs displacement curves for Bearing L in shear

Table 6.7: Summary of numerical and experimental results

Bearing	Experimental (kips/in.)	FEA (kips/in.)	Difference (% of Experimental results)
S	7938.0	7594.084	4.3%
M	17811.4	17089.59	4.1%
L	41876.1	40798.91	2.6%

Figure 6.23 to Figure 6.25 presents the computational results of the lateral force vs displacement curves of three elastomeric bearings subjected to the lateral deformation of 50%. The calculated axial stiffness values for both computational and experimental results are tabulated in Table 6.7. The lateral force vs displacement curves obtained from the FEA exhibit strong linearity and the calculated lateral stiffness values agree with the experimental measurements very well with differences less than 5%.

6.4.3 ROTATION MODELING

This section presents results from rotation modeling of the elastomeric bearings as well as comparisons with the full scale test results. Only three analyses that are representative of the large size bearings used in higher demand applications were performed due to the significant computational time required to solve such complex problems. The complexity of the problems is significant due to their intrinsic nature of high non-linearity, resulting in excessive number of substeps and iterations to arrive at converged results. The details of the three analyses are tabulated below.

Table 6.8: Summary of loads for rotation modeling

Case	Bearing	Axial displacement (in)	Taper angle of top rigid block
1	M	0.35	1.5 °
2	L	0.13	0.5 °
3	L	0.345	1.5 °

Figure 6.26 and Figure 6.27 below illustrate the contact status and the deformed meshes of the medium size bearing in case 1 at various levels of axial displacement. The results presented are similar to those observed for the other modeled cases.



Figure 6.26: Contact status contour for bearing in partial contact

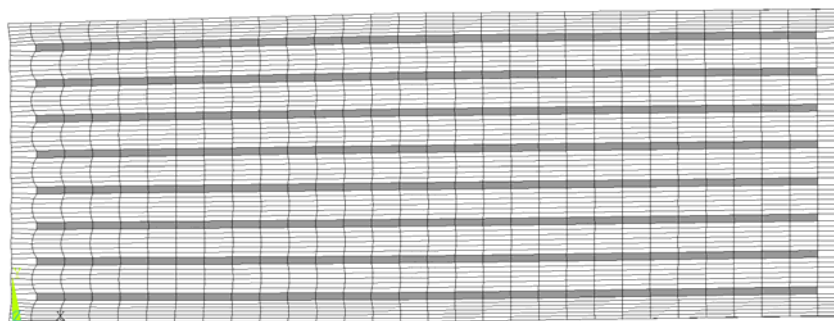


Figure 6.27: 2D sectional view of deformed mesh in partial contact in rotation modeling

Figure 6.26 and Figure 6.27 provide the contact status and deformed mesh of the medium size (M) bearing under the axial displacement of 0.15 in. of the top block. The bearing and the top block were in partial contact. The internal elastomer that was in contact with the top block was strained while the elastomer in the other areas maintained a vertical profile.

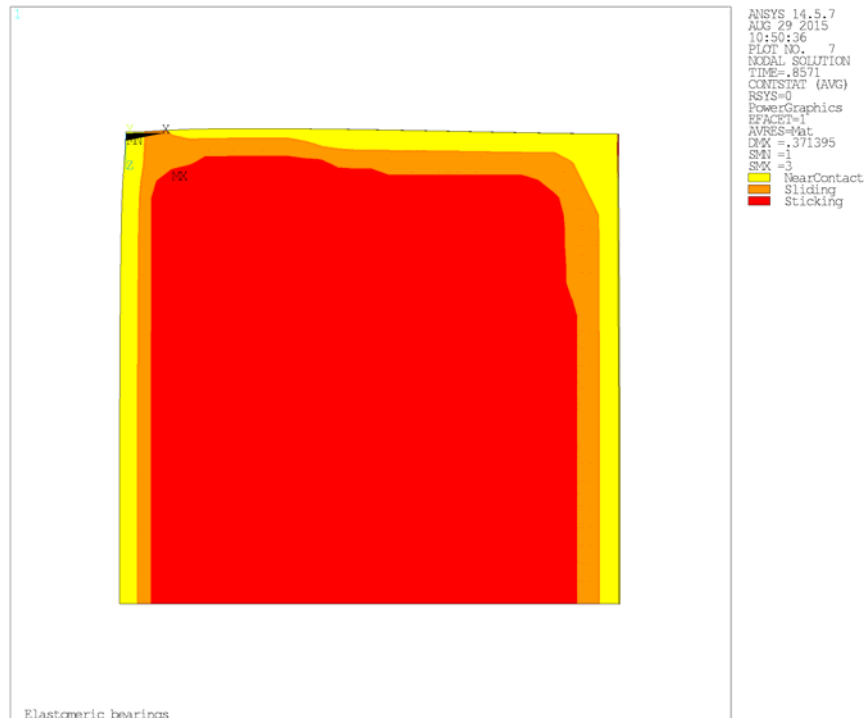


Figure 6.28: Contact status contour for bearing in complete contact

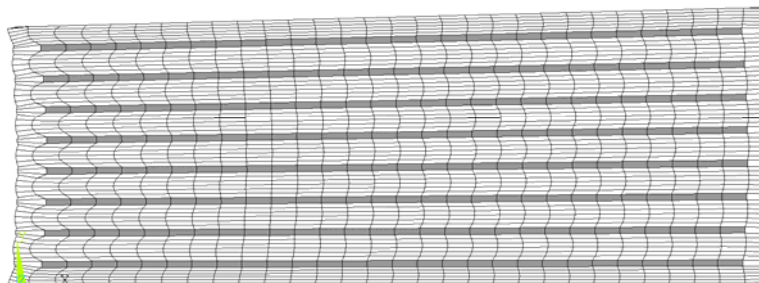


Figure 6.29: Sectional view of deformed mesh in complete contact in rotational modeling

Figure 6.30 and Figure 6.31 provide the contact status and the deformed mesh of medium size bearing under the axial displacement of 0.3 in. of the top block. At this displacement, the bearing and top tapered block were in full contact. As observed from the deformed mesh, it would be reasonable to assume that the global rotation deformation enforced on the elastomeric bearing by the tapered top rigid block was evenly distributed to each layer. It can also be seen that the elastomer was significantly more strained under the lower side of the top tapered block than the other edge.

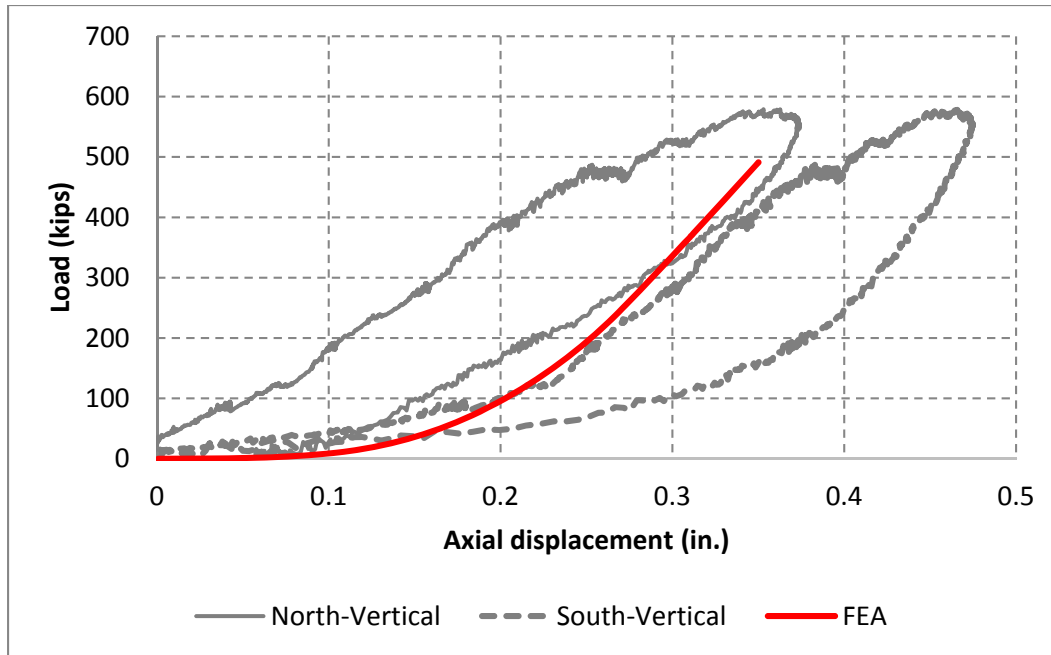


Figure 6.30: Force vs deflection curves for Bearing M in rotational modeling ($\theta=1.5^\circ$)

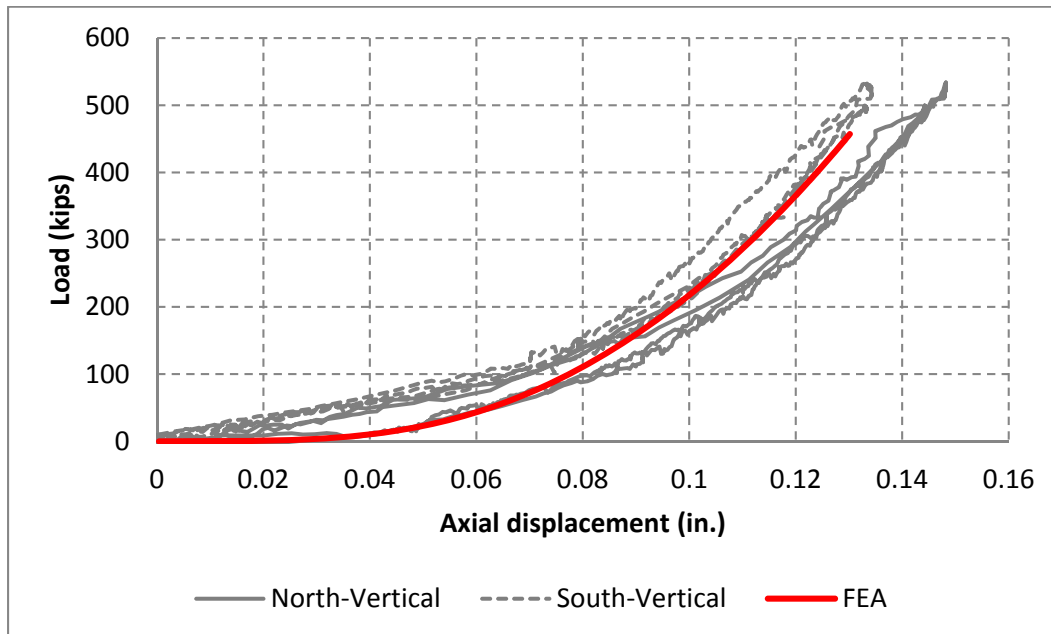


Figure 6.31: Force vs deflection curves for Bearing L in rotational modeling ($\theta=0.5^\circ$)

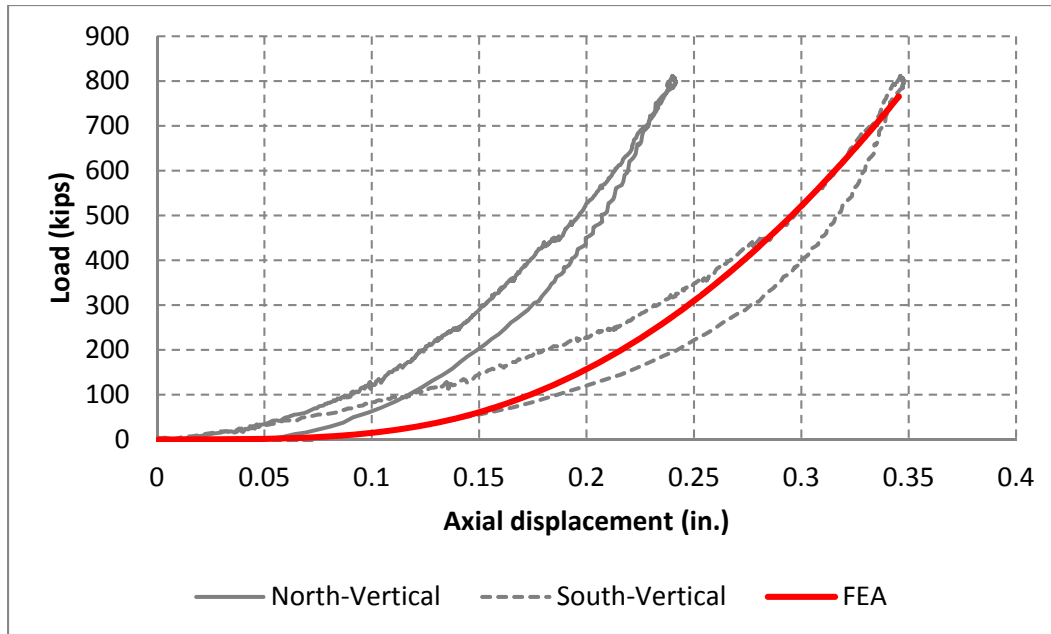


Figure 6.32: Force vs deflection curves for Bearing L in rotational modeling ($\theta=1.5^\circ$)

Figure 6.30 to Figure 6.32 presents the computational results of the axial force vs displacement curves for three the analyses that have been performed, in correlation to the experimental results. It is readily observed that bearings manufactured in the same batch experienced significant variations in their behavior, as a result of the uncertainty in the bulk compression modulus of the elastomer material. The FE model that was developed is capable of modeling the behavior of bearings under combined deformation of compression and rotation, with the numerical results being within uncertainty of the experimental measurements.

6.5 Summary

The three dimensional finite element modeling of elastomeric bearing, which serves as an indispensable approach to explore internal quantities such as stress and strain that are impractical to measure in the full scale testing, has its validity plagued by the uncertainty of bulk compression of the elastomer material, causing significant discrepancy between numerical results and experimental measurements in many cases reported by previous research studies.

An analytical method was therefore developed in this study, providing the researchers to extract material coefficients from the global force and displacement measurements of the full scale compression and shear test results.

A three dimensional finite element model was developed to simulate the behavior of the elastomeric bearings in full scale compression, shear and rotation testing, with the material coefficients obtained in the previously step. The force and displacement measurements from the full scale tests and the numerically calculated results had good agreement both qualitatively and quantitatively. This validated finite element model was used for parametric studies that are discussed in the next chapter.

CHAPTER 7: PARAMETRIC FE STUDY OF ELASTOMER LAYER

7.1 Introduction

In the previous chapter, a finite element model of elastomeric bearing was developed and validated using results from the full scale tests. When an elastomeric bearing is subjected to compression, shear, or rotational deformation, each elastomer layer acts independently similar to springs in series. A design approach is hence proposed that calculates the maximum shear strain within the elastomeric layer under various modes of deformation.

This chapter presents the results from a comprehensive parametric finite-element study of elastomer layers under axial loads and rotation, covering shape factors and bulk moduli that are likely to be encountered in practice, to validate the proposed design approach that is proposed in this study.

The total shear strain approach is proposed in this study for the design of elastomeric bearings used in higher demand applications. The total shear strain approach states the explicit summation of shear strain components induced by compression, rotation, and shear should not exceed the limit of 5.0

$$\gamma_a + \gamma_r + \gamma_s \leq 5$$

Where shear strain components induced by axial load, rotation and shear can be calculated, respectively:

$$\begin{aligned} r_a &= D_a \frac{\sigma_s}{GS} \\ \gamma_r &= D_r \left(\frac{L}{h_{ri}} \right)^2 \theta_i \\ \gamma_s &= \frac{\Delta_s}{h_{rt}} \end{aligned}$$

The empirical dimensionless coefficients D_a and D_r used to determine axial shear strain components due to the axial load and rotation in AASHTO were originally derived from two dimensional numerical studies outlined in the NCHRP 596 report. It remains unknown whether these values are sufficiently representative of actual bearing behavior without comprehensive three dimensional parametric finite element studies on the elastomer body.

As stated in the previous chapter, the bulk modulus has a profound impact on the behavior of the restrained elastomeric body, particularly those with high shape factors, under compression or rotational deformation. In these cases, the dilemma exists that numerical models provide relatively poor predictions of the axial stiffness using the bulk moduli experimentally obtained from material tests. Better results can be obtained using the measured results from laboratory full scale bearing tests. This poses significant challenges to the use of bulk modulus in design practice.

An analytical model was previously developed to determine material coefficients including the apparent bulk moduli from global measurements of the force and displacement from the full scale tests of the elastomeric bearings. Using the apparent bulk moduli obtained by this approach, finite-element analysis results were then able to provide good agreement with the experimental measurements. This not only proves the validity of the finite-element model but enables the development of a range of apparent bulk moduli that can be considered in numerical modeling and design practice.

However, it remains unclear what bulk modulus values should be used in the design and analysis of elastomeric bearings. The AASHTO LRFD specification recommends the value of 450 ksi for neoprene material, based on the experimental bulk moduli obtained from the material tests in the NCHRP 596 report, while the value of 2000 MPa (290 ksi) is suggested in the Eurocode (EN 1337-3).

In this research, the experimental bulk moduli obtained from material testing of four specimens prepared from the same rubber material, which the tested elastomeric bearings were also made from, measured 331 ksi, 335 ksi, 340 ksi and 390 ksi, while the apparent bulk moduli for the small, medium and large bearings determined from the full scale testing are 45.0 ksi, 103.9 ksi and 65.7 ksi, respectively, which are significantly lower than the values from the material tests. This demonstrates that a wide range of bulk moduli should be considered in design and analysis. It is therefore imperative to perform comprehensive numerical studies on elastomeric layers with shape factors and bulk moduli covering those normally encountered in engineering practice and to find out the appropriate use of bulk modulus in design considerations. Bulk modulus values ranging from 45 ksi to 450 ksi were used in the ensuing parametric study.

7.2 FE Model

The finite element model for the parametric numerical study only include a single layer of elastomer, and half thickness of the steel shims above and below the elastomer layer, instead of the entire elastomeric bearing, as presented in Figure 7.1

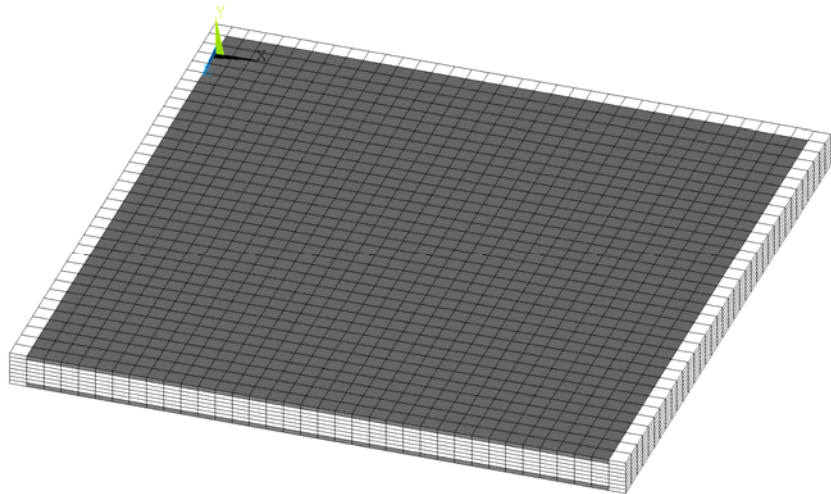


Figure 7.1: Mesh of elastomer layer S

The elastomer and steel were discretized with the ANSYS 3D 20-node solid element, SOLID 186. This element is similar to the SOLID 185 element used in the previous chapter, but features quadratic shape functions, which better characterize the profile of elastomer layer under large deformation.

The sign convention is as shown in Figure 7.2. The longitudinal axis is defined as the x direction while the transverse direction is defined as the z direction. The y axis is normal to the plane of the layer.

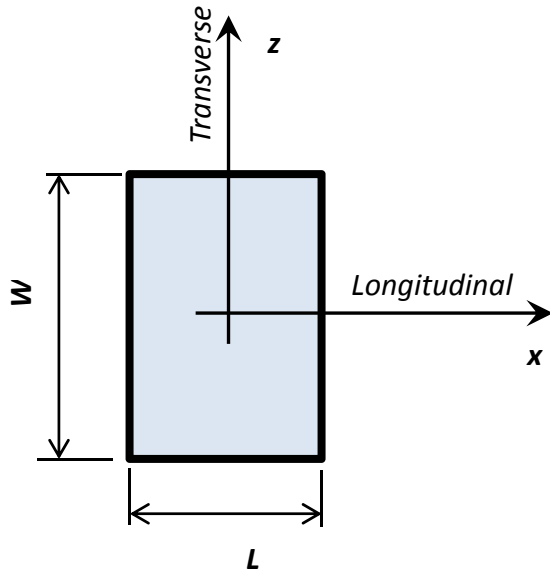


Figure 7.2: Sign convention for elastomer layer

In the finite element analysis, the elastomer layers were subjected to combinations of compression, shear, and rotation. The rotation was applied about the transverse axis of the elastomer layer and the shear deformation was enforced in the longitudinal direction. Because the layer geometries and load patterns were symmetric about the longitudinal axis for all analyses, only half of the elastomeric layer was modeled, with symmetry conditions given along the longitudinal axis.

The parametric FEA study covered elastomeric layers of four different dimensions with shape factors ranging from 8.0 to 20.6. Their geometries were the same to those from the elastomeric bearings in the full scale testing.

Table 7.1: Summary of elastomer layers

Elastomer layer	Width (in.)	Length (in.)	Layer Thickness "h _{ri} " (in.)	Cover (in.)	Shape Factor "S"	Aspect Ratio
S	18	9	0.375	0.25	8.00	2.00
M	27	14	0.5	0.375	9.22	1.93
L	36	23	0.5	0.375	14.03	1.57
XL	48	36	0.5	0.375	20.57	1.33

A fixed shear modulus $G = 100$ psi is given for all analyses, while five different values of the bulk modulus were used for each type of elastomer layer, which included 45 ksi, 70 ksi, 100 ksi, 200 ksi, and 450 ksi.

Analyses of the elastomer layers under compression and rotation were performed. All translational DOFs of the model were fixed at the bottom, and variable deformational loads were applied on the top of the model according to the displacement type.

The axial loads and rotational deformations differed for elastomer layers of different sizes. Hence, for the interest of comparison between different sized bearings, all axial loads and rotation deformation were normalized to two non-dimensional values:

$$\alpha_a = \frac{\sigma_s}{GS}$$

$$\alpha_r = \left(\frac{L}{h_{ri}} \right)^2 \theta_i$$

7.3 Compression Study

The parametric compression modeling of elastomer layer consisted of 20 analyses which considered all four layer sizes and five bulk modulus values. Uniform axial displacement loads were enforced at the top of the model to the point that an average axial stress $\sigma_a = 2GS$ ($\alpha_a = 2$) was applied.

Table 7.2: Summary of axial loads

Elastomer layer	Width (in.)	Length (in.)	Shape Factor "S"	α_a	σ_a (psi)
S	18	9	8.00	2	1600
M	27	14	9.22	2	1844
L	36	23	14.03	2	2807
XL	48	36	20.57	2	4114

A representative example of the deformed mesh of layer S with bulk modulus of 450 ksi under axial load is presented in Figure 7.3.



Figure 7.3: Deformed mesh of layer S under axial load of 1GS

For the layer S with bulk modulus of 450 ksi under axial load of 2GS, the contour of γ_{xy} , defined as shear strain in the XY plane, at the interface of the steel and the elastomer, is plotted in Figure 7.4. The longitudinal axis is along the top border of the figure and the strain contour of the other unprinted half should be symmetric about the longitudinal axis. The maximum values of γ_{xy} occur near the two ends of the longitudinal axis. Similarly, the contour of γ_{yz} , defined as shear strain in the YZ plane, at the elastomer and steel interface, is plotted in Figure 7.5. The maximum values of γ_{yz} can be found near the two ends of the transverse axis.

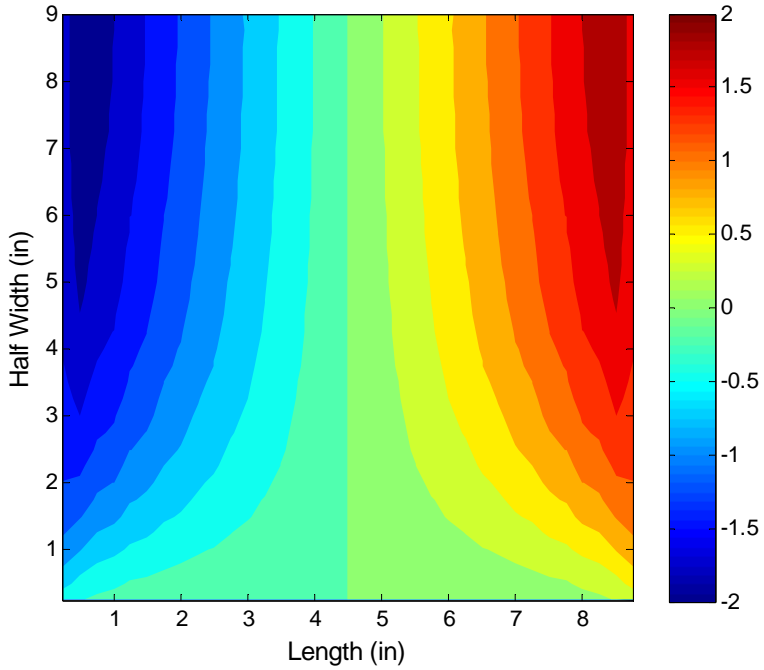


Figure 7.4: Contour of shear strain γ_{xy} for layer S under axial load of 2GS

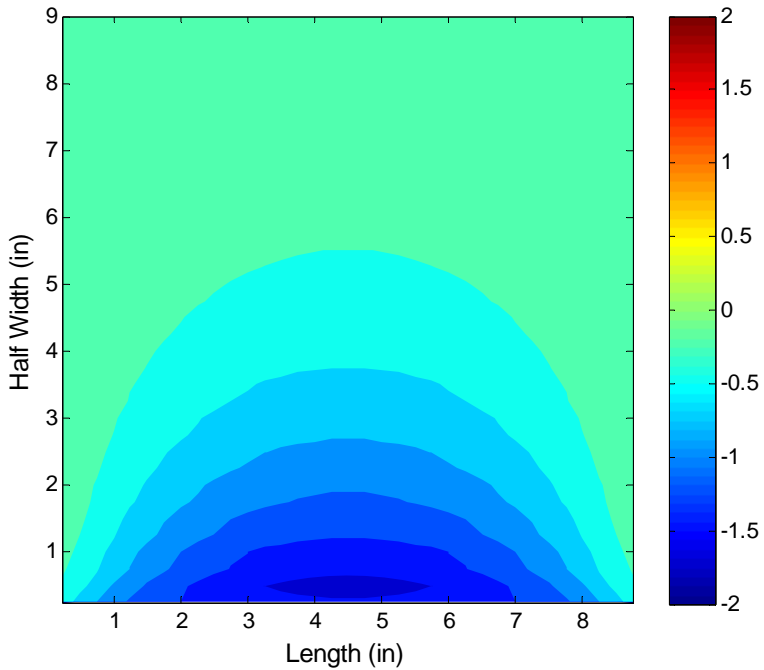


Figure 7.5: Contour of shear strain γ_{yz} for layer S under axial load of 2GS

The shear strain (γ_{xy}) profile along longitudinal axis in Figure 7.4 was extracted and is plotted in Figure 7.6. The blue markers represent FEA results and the red line represents a curve fit to the data. The FEA values near the two edges are erroneous because of the extreme mesh distortion stemming from the local stress singularity. Therefore, the numerical results within one

inch from the two edges are disregarded and replaced with the extrapolation from the interior data points. A 4th order polynomial is used for extrapolation for all analyses.

The γ_{xy} profiles along the longitudinal axis for bearing size S under various levels of axial load are presented in Figure 7.7, while γ_{yz} profiles along the transverse axis for the same analysis are given in Figure 7.8.

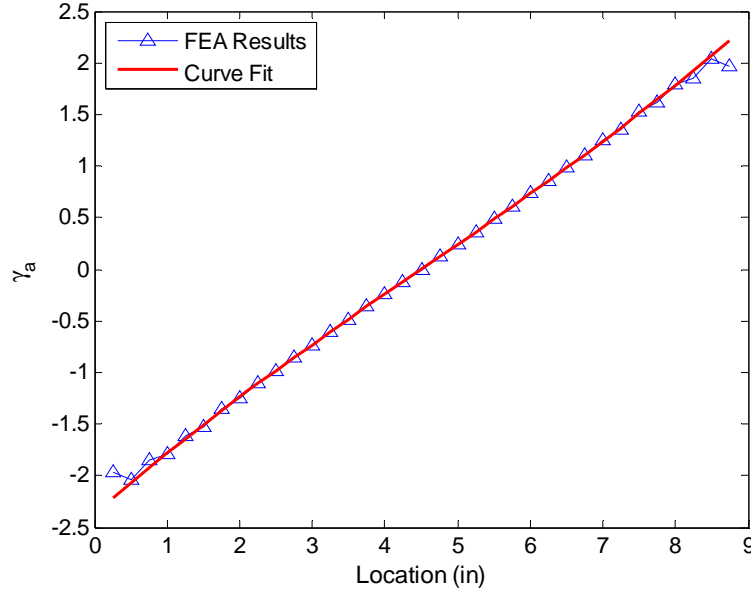


Figure 7.6: γ_{xy} profile along longitudinal axis for bearing S under axial load of 2GS

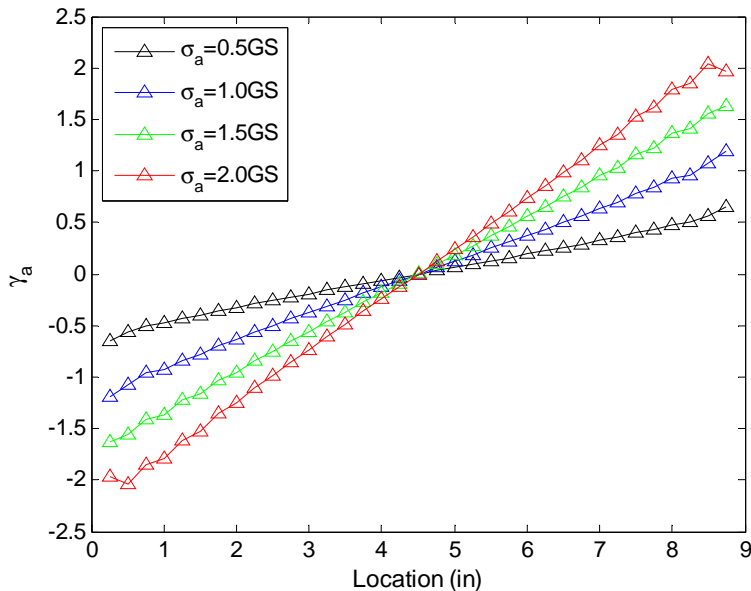


Figure 7.7: γ_{xy} profiles along longitudinal axis for bearing S under various levels of axial load

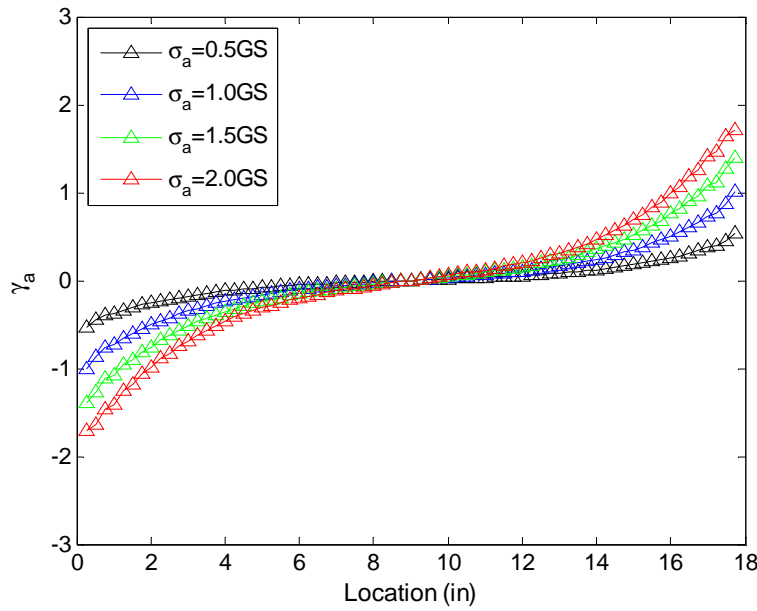


Figure 7.8: γ_{yz} profiles along transverse axis for bearing S under various levels of axial load

Figure 7.9 presents the extrapolated γ_{xy} profiles for the analyses above. Similar profiles for analyses for bearings M, L, and XL with bulk modulus of 450 ksi under axial loads of 2GS are presented in Figure 7.10, Figure 7.11 and Figure 7.12, respectively.

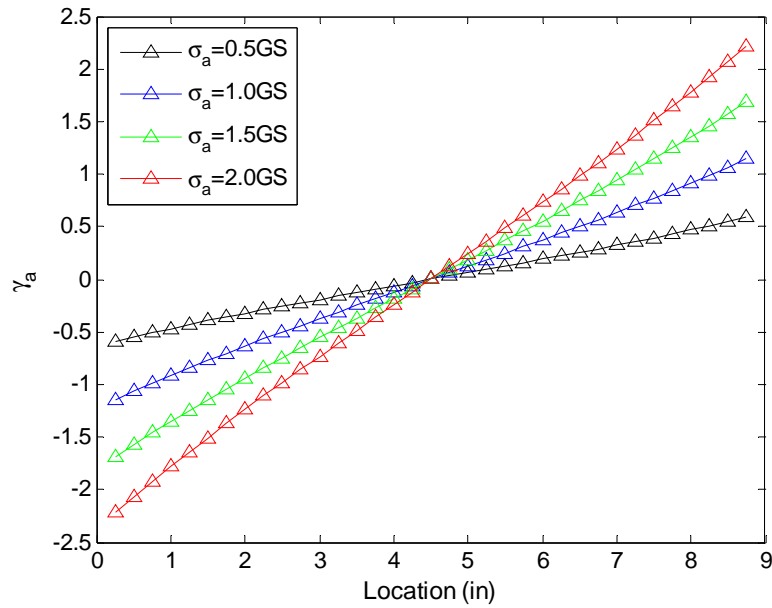


Figure 7.9: Extrapolated γ_{xy} profiles along longitudinal axis for bearing S

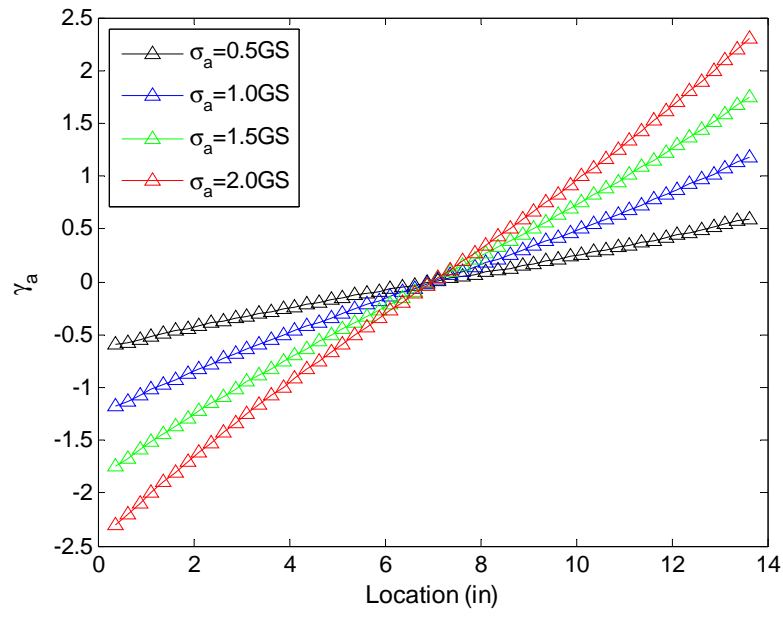


Figure 7.10: Extrapolated γ_{xy} profiles along longitudinal axis for bearing M

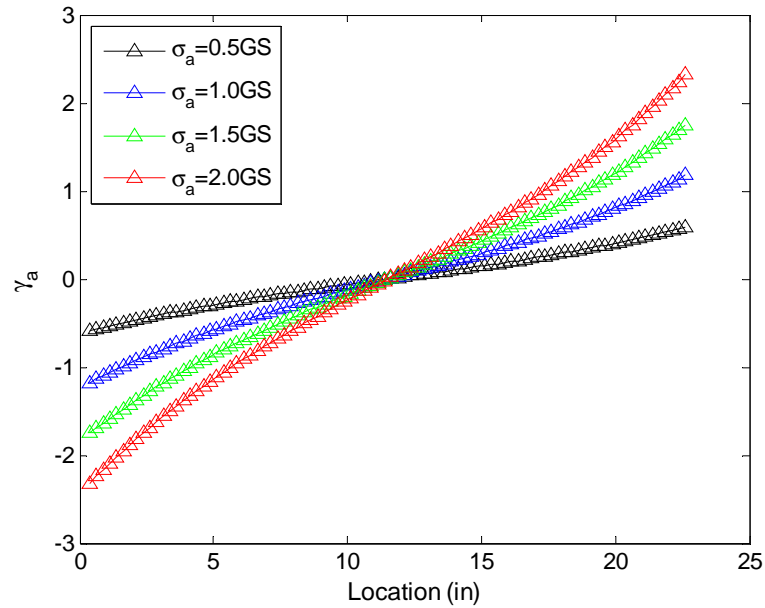


Figure 7.11: Extrapolated γ_{xy} profiles along longitudinal axis for bearing L

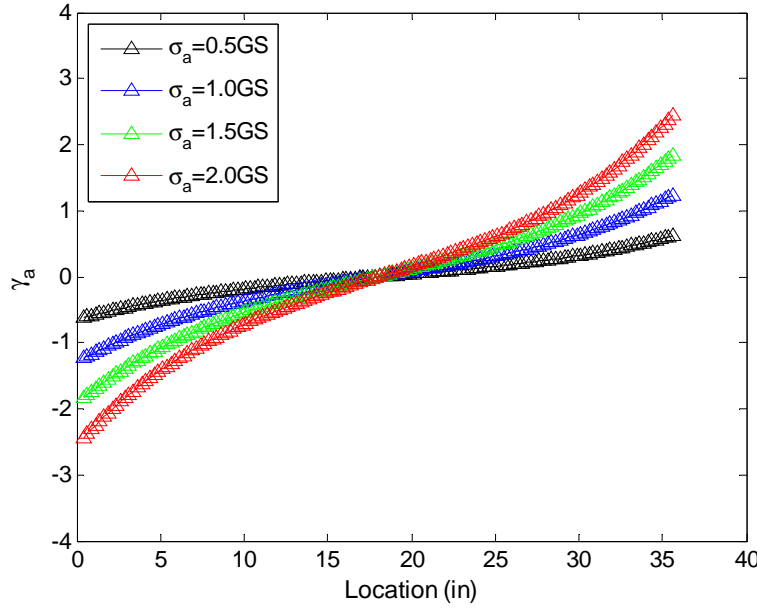


Figure 7.12: Extrapolated γ_{xy} profiles along longitudinal axis for bearing XL

According to the strain contour shown in Figure 7.4, the maximum value of γ_{xy} occurs near the end of the longitudinal axis. The shear strain γ_{xy} vs the normalized axial load α_a for the same analysis is plotted in Figure 7.13 using blue markers. It is evident from the figure that the shear strain of interest, γ_a , is related to the normalized axial load with high linearity.

Apart from the FEA results, the shear strains calculated by Method B of the AASHTO LRFD specifications are also incorporated for comparison.

$$\gamma_a = D_a \alpha_a$$

The AASHTO code specifies a constant value for D_a , which is hereinafter defined as Equation A:

$$D_a = 1.4$$

Alternatively a value that considers the bulk modulus and bearing geometry is recommended: $D_a = \max \left[d_{a1}, \left(d_{a2} + d_{a3} \times \frac{L}{W} \right) \right]$

In which

$$\begin{aligned} d_{a1} &= 1.06 + 0.210\lambda + 0.13\lambda^2 \\ d_{a2} &= 1.506 - 0.071\lambda + 0.406\lambda^2 \\ d_{a3} &= -0.315 + 0.195\lambda - 0.047\lambda^2 \end{aligned}$$

$$\lambda = S \sqrt{\frac{3G}{K}}$$

Henceforth referred to as Equation B.

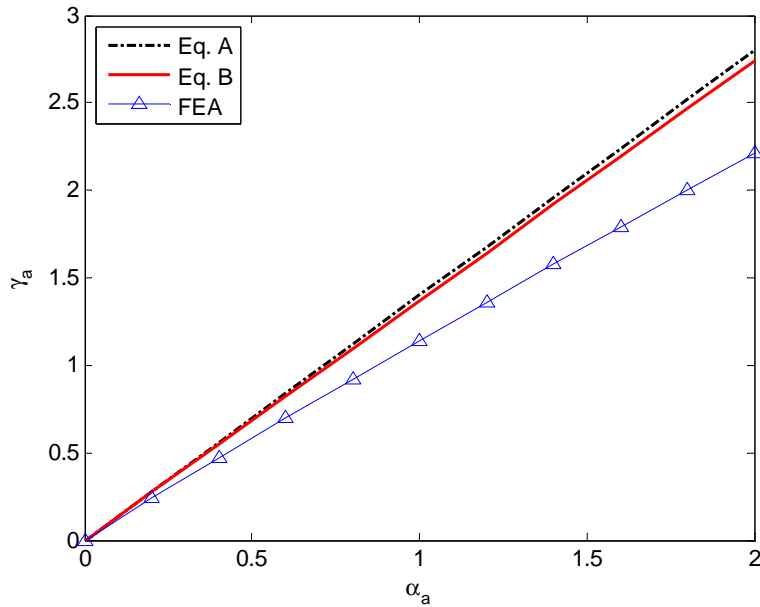


Figure 7.13: Shear strain γ_{xy} vs normalized axial load α_a for layer S with $K = 450\text{ksi}$

For comparison purposes between the FE results and design approaches, the values of D_a are also calculated using the FE results at the axial stress $\sigma_a = 2GS$ ($\alpha_a = 2$) in both longitudinal and transverse directions with the variety of layer size and bulk moduli. The comparison of D_a values between FEA results, Equation A and Equation B are presented from Figure 7.14 to Figure 7.21.

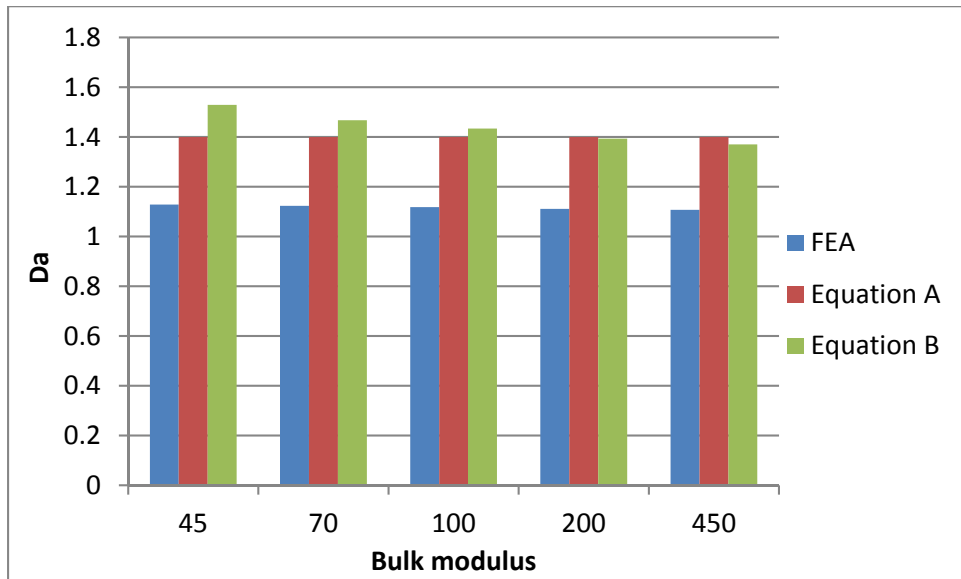


Figure 7.14: D_a values for layer S in longitudinal direction

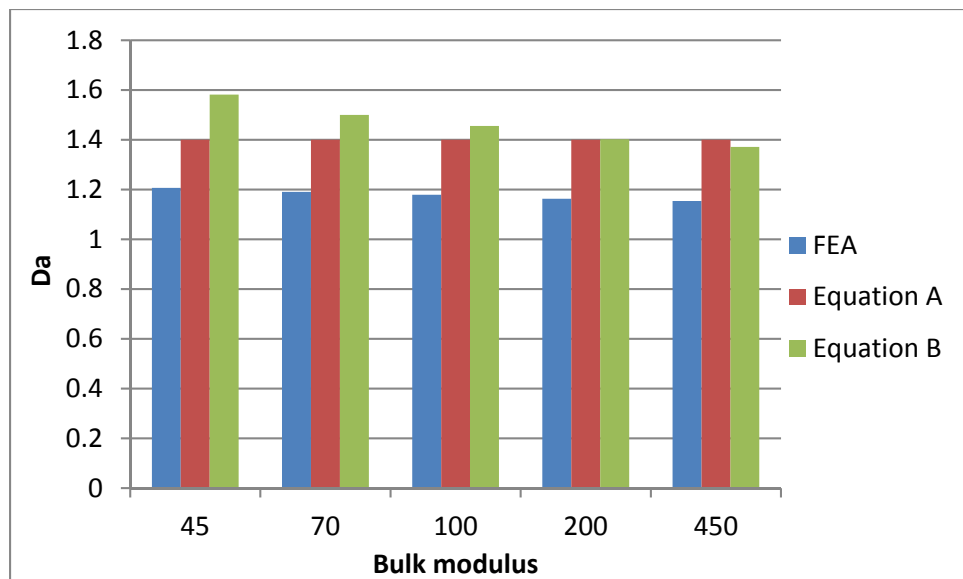


Figure 7.15: D_a values for layer M in longitudinal direction

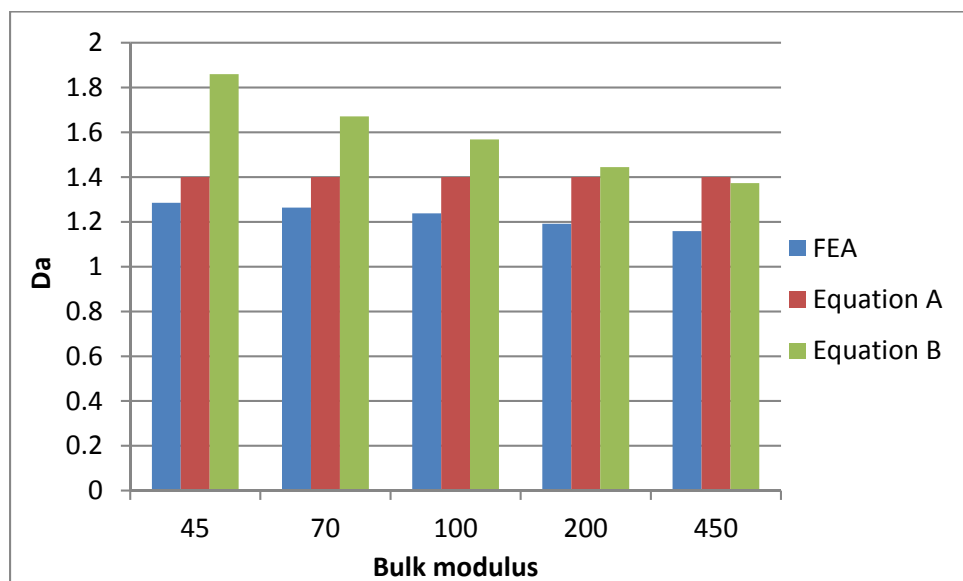


Figure 7.16: D_a values for layer L in longitudinal direction

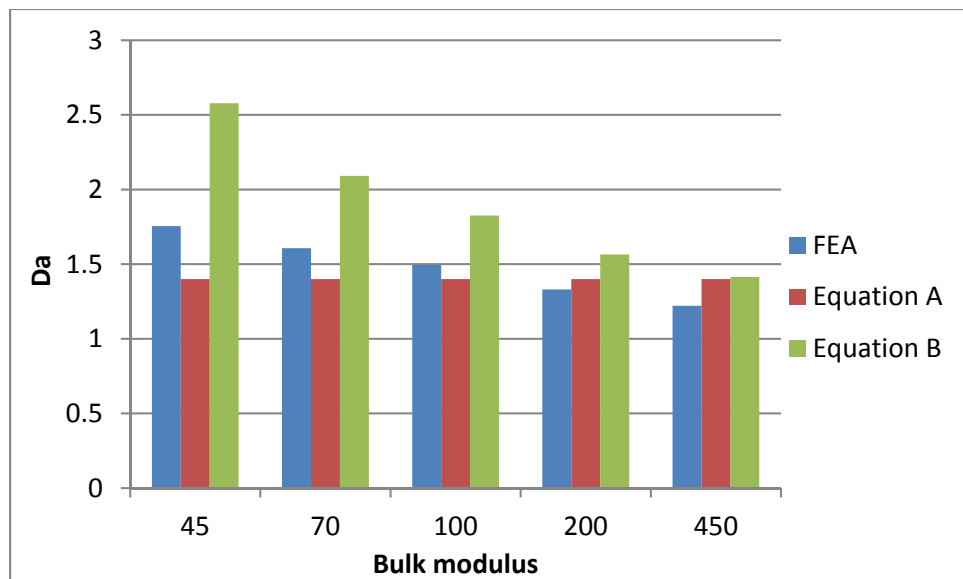


Figure 7.17: D_a values for layer XL in longitudinal direction

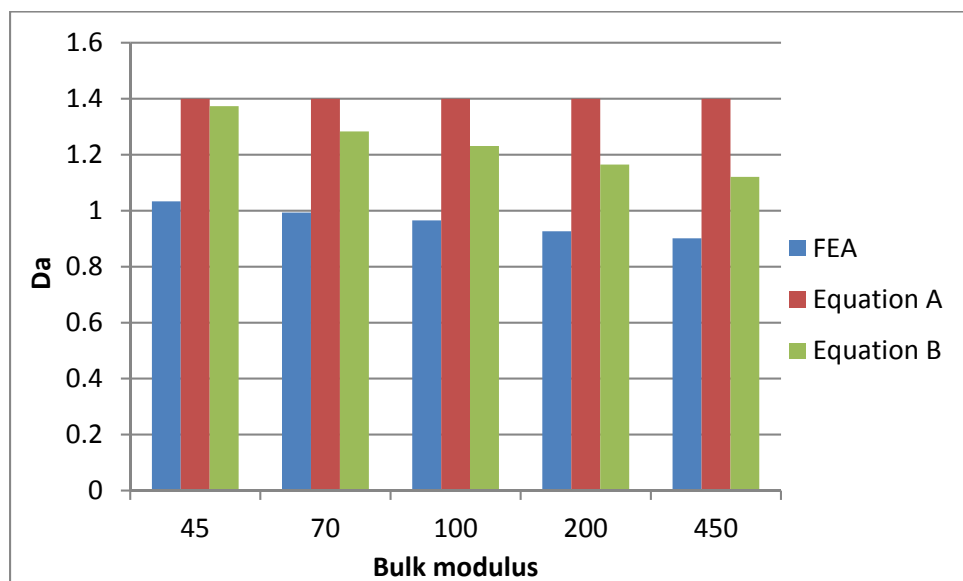


Figure 7.18: D_a values for layer S in Transverse direction

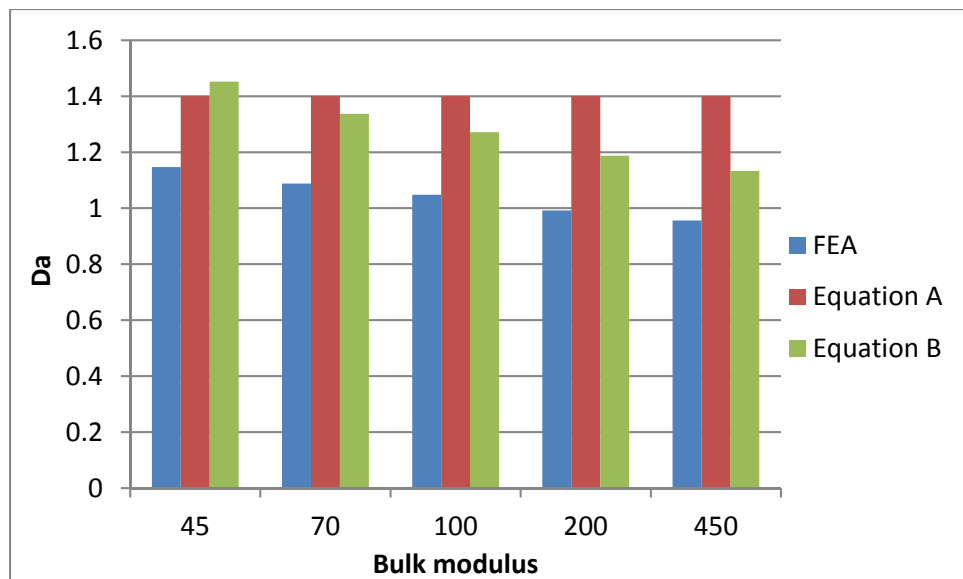


Figure 7.19: D_a values for layer M in Transverse direction

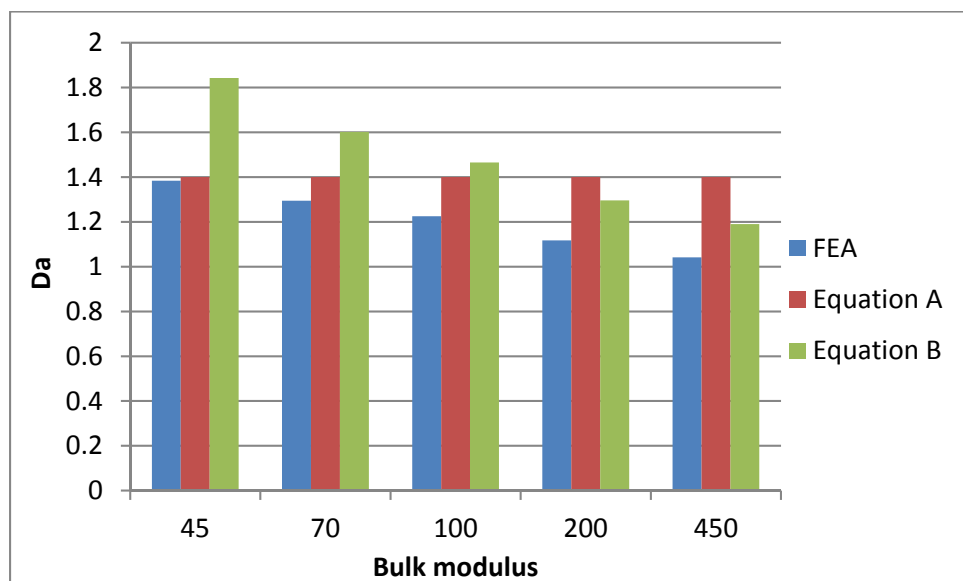


Figure 7.20: D_a values for layer L in Transverse direction

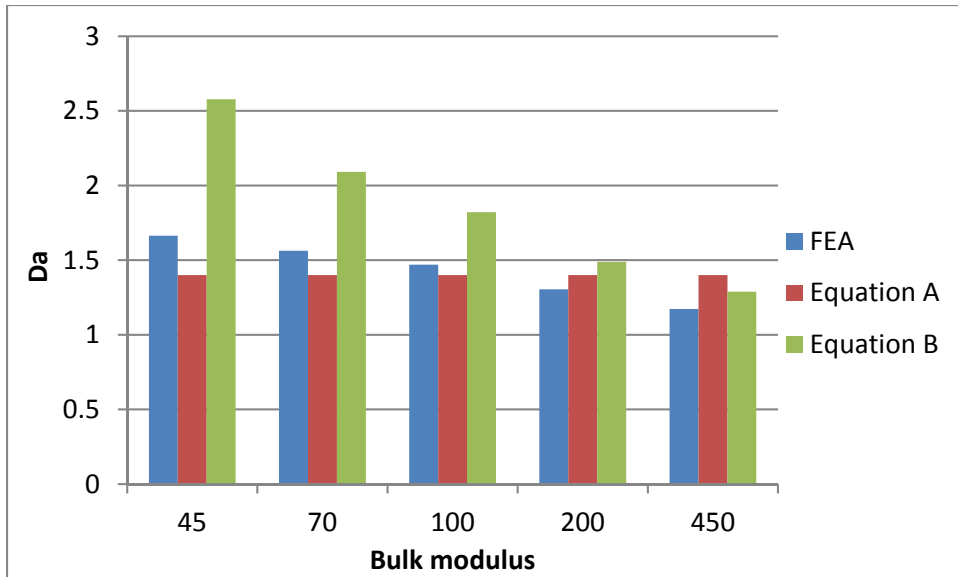


Figure 7.21: D_a values for layer XL in Transverse direction

From the comparison of D_a values above, one might observe:

- The D_a value increases with greater shape factor for a given bulk modulus.
- The D_a value decreases with greater bulk modulus for a given shape factor.
- Predictions by Eq. A and Eq. B are reasonably close in most cases. The Eq. A provides lower predictions of D_a values than Eq. B does at lower bulk modulus values, but higher values at higher modulus values.
- The predictions by Eq. A are conservative in most cases, but tend to underestimate the FEA results for the XL bearing at lower bulk moduli, while the predictions by Eq. B are conservative for all cases considered. However, this does not lead to the conclusion that Eq. B is necessarily a more conservative choice. In design practice, the available bulk modulus values are experimental values obtained either from the material testing or previous literature, which are close to the upper limit of the range of bulk moduli investigated in this study. The actual apparent bulk modulus values, unknown to the designer, could be significantly smaller, causing greater actual D_a values underestimated by Eq. B using experimental bulk modulus values. Therefore, there is no seemingly appealing cause to use the more complex Eq. B, instead of simpler but more effective Eq. A
- The constant value $D_a = 1.4$ (referred as Eq. A in this study) is suggested against the use of the more complex D_a expression in the commentary of AASHTO LRFD specification (referred as Eq. B in this study). For very large bearings, with shape factors greater than 15, a higher value $D_a = 1.8$ is recommended for use.

7.4 Rotation Study

Akin to the compression modeling, the parametric rotation modeling of elastomer layers consisted of 20 analyses which consider all four bearing sizes and five bulk modulus values. The

normalized rotation of $\alpha_r = 8$ is applied longitudinally (about transverse axis) at the top of the model as displacement loads for all analyses.

Table 7.3: Summary of normalized rotation deformation

Elastomer layer	Width (in.)	Length (in.)	Shape Factor "S"	α_r	$\theta_i (^\circ)$
S	18	9	8.00	8	0.7958
M	27	14	9.22	8	0.5847
L	36	23	14.03	8	0.2166
XL	48	36	20.57	8	0.0884

A representative example of the deformed mesh of bearing S with bulk modulus of 450 ksi under normalized rotation of $\alpha_r = 4$ is presented in Figure 7.22.



Figure 7.22: Deformed mesh of bearing S under normalized rotation of $\alpha_r = 4$

For the bearing S with bulk modulus of 450 ksi under normalized rotation of $\alpha_r = 8$, the contour of γ_{xy} at the interface of the steel and the elastomer, is plotted in Figure 7.23. The longitudinal axis is along the top border of the figure and the strain contour of the other unprinted half should be symmetric about the longitudinal axis. The maximum values of γ_{xy} occur near the two ends of the longitudinal axis.

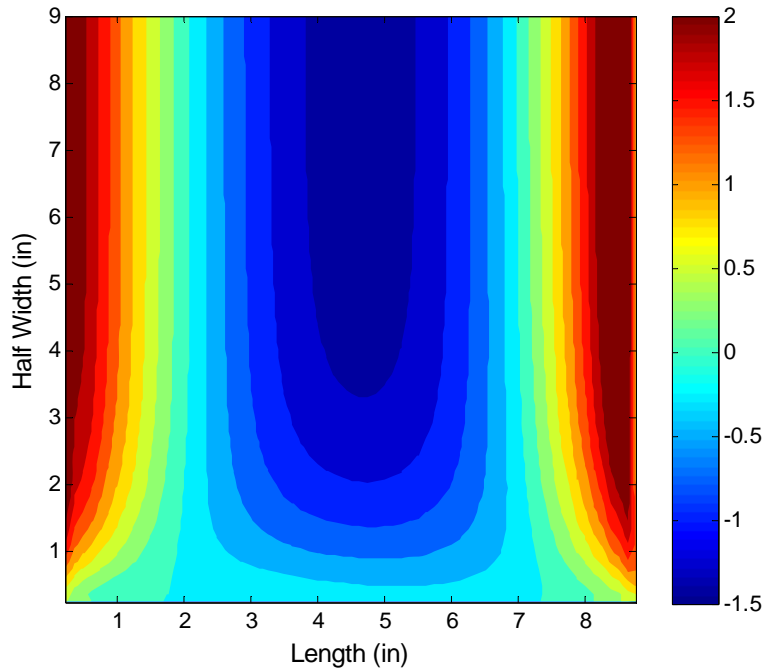


Figure 7.23: Contour of shear strain γ_{xy} for bearing S under normalized rotation of $\alpha_r = 8$

The shear strain (γ_{xy}) profile along the longitudinal axis in Figure 7.23 is extracted and plotted in Figure 7.24. The blue markers represent the FEA results and the red line represents a curve fit to the data. The same 4th-order polynomial extrapolation algorithm that was deployed in the compression modeling was also used for all rotational analyses.

The γ_{xy} profiles along the longitudinal axis for bearing S under various levels of normalized rotational deformation are presented in Figure 7.25.

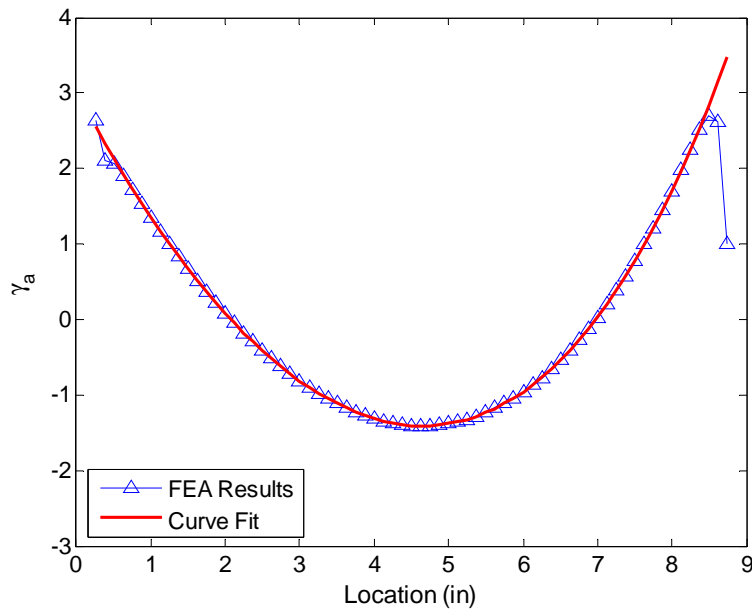


Figure 7.24: γ_{xy} profile along longitudinal axis for Bearing S under normalized rotation of $\alpha_r = 8$

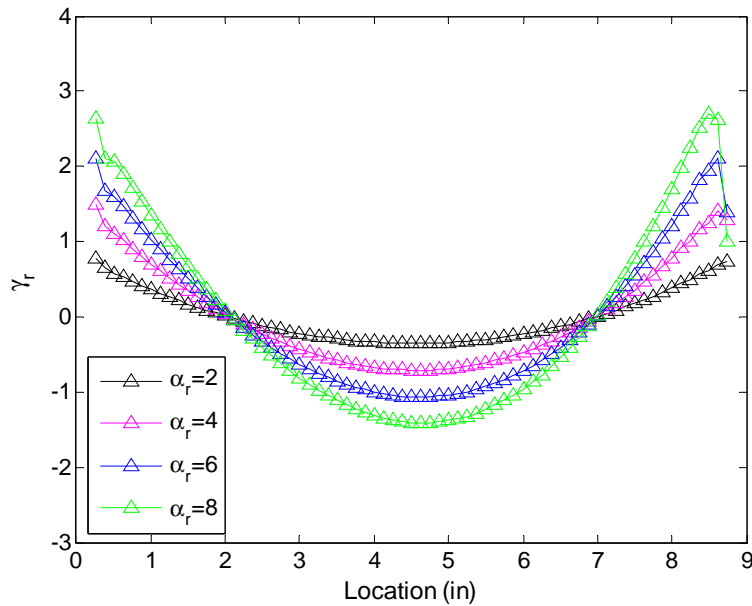


Figure 7.25: γ_{xy} profiles along longitudinal axis for Bearing S under various levels of normalized rotation

Figure 7.26 presents the extrapolated γ_{xy} profiles for the analyses above. Similar profiles for analyses for bearings M, L, and XL with bulk modulus of 450 ksi under normalized rotations up to $\alpha_r = 8$ are presented in Figure 7.27, Figure 7.28 and Figure 7.29, respectively.

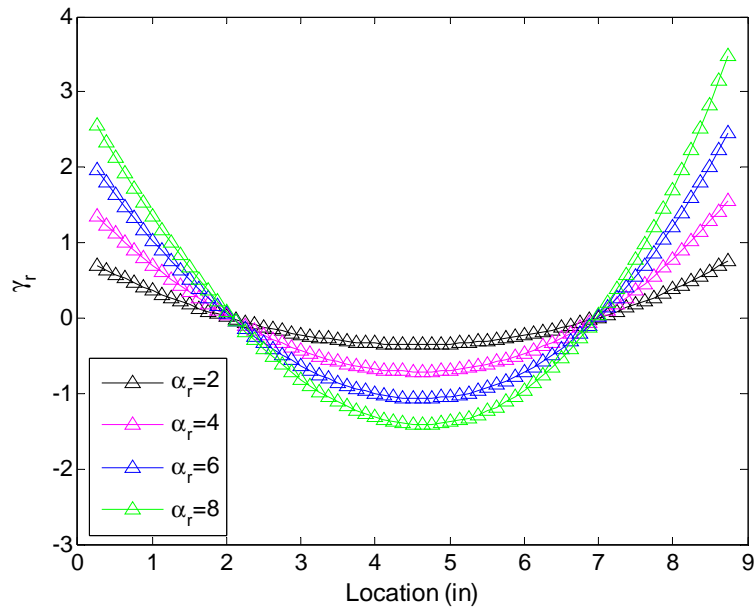


Figure 7.26: Extrapolated γ_{xy} profiles along longitudinal axis for bearing S

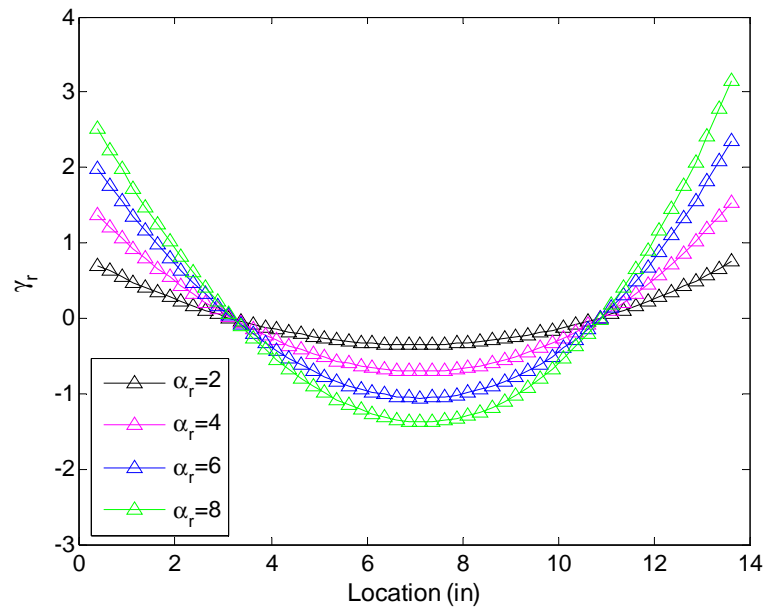


Figure 7.27: Extrapolated γ_{xy} profiles along longitudinal axis for bearing M

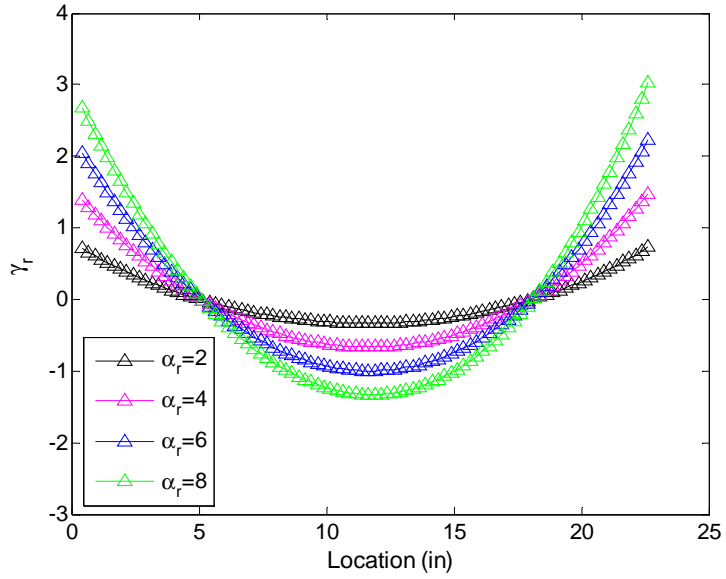


Figure 7.28: Extrapolated γ_{xy} profiles along longitudinal axis for bearing L

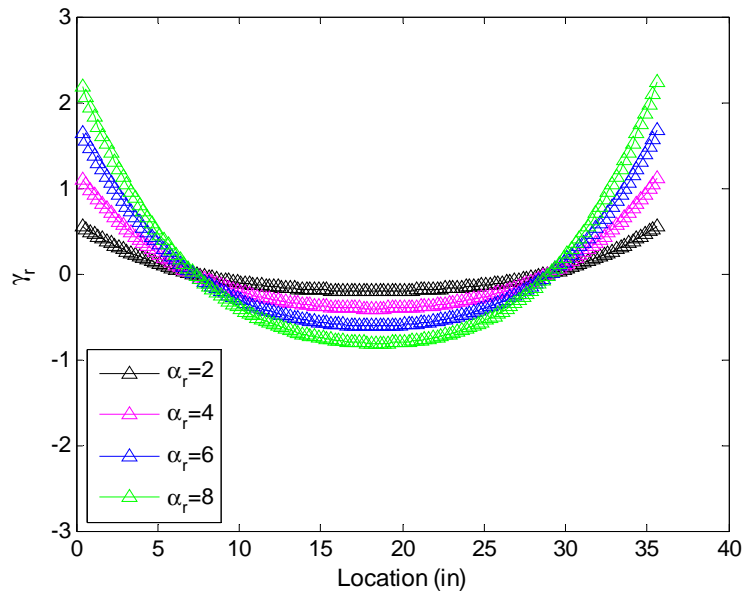


Figure 7.29: Extrapolated γ_{xy} profiles along longitudinal axis for bearing XL

As previously stated, the maximum value of γ_{xy} occurred near the end of the longitudinal axis. The shear strain γ_{xy} vs normalized rotation α_r for bearing S with bulk modulus of 450ksi under normalized rotation up to $\alpha_r = 8$, is plotted in Figure 7.30 using blue markers. It is evident from the figure that the shear strain is related to the normalized rotation with high linearity as it is in compression modeling.

Likewise, the shear strains caused by rotation were calculated by the Method B of AASHTO LRFD specification.

$$\gamma_r = D_r \alpha_r$$

A constant value for D_r is hereinafter defined as Equation A:

$$D_r = 0.5$$

Alternatively a value that considers bulk modulus and bearing geometry is recommended:

$$D_r = \frac{1.552 - 0.627\lambda}{2.233 + 0.156\lambda + \frac{L}{W}} \leq 0.5$$

In which

$$\lambda = S \sqrt{\frac{3G}{K}}$$

Henceforth is referred to as Equation B

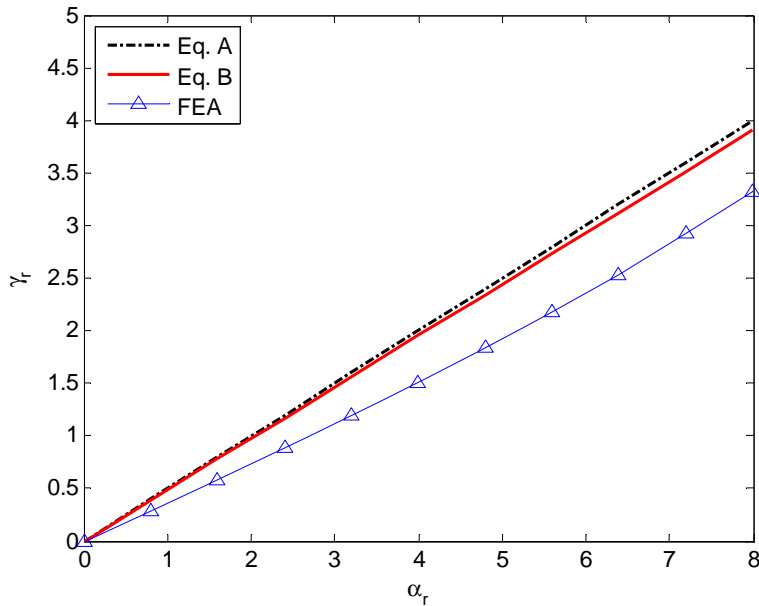


Figure 7.30: Shear strain γ_{xy} vs normalized rotation α_r for bearing S with $K = 450\text{ksi}$

Due to the high linearity of shear strain and normalized rotation, D_r can also be calculated using the FE results at the normalized rotation $\alpha_r = 8$. The comparison of D_r values between FEA results, Equation A and Equation B are presented from Figure 7.31 to Figure 7.34.

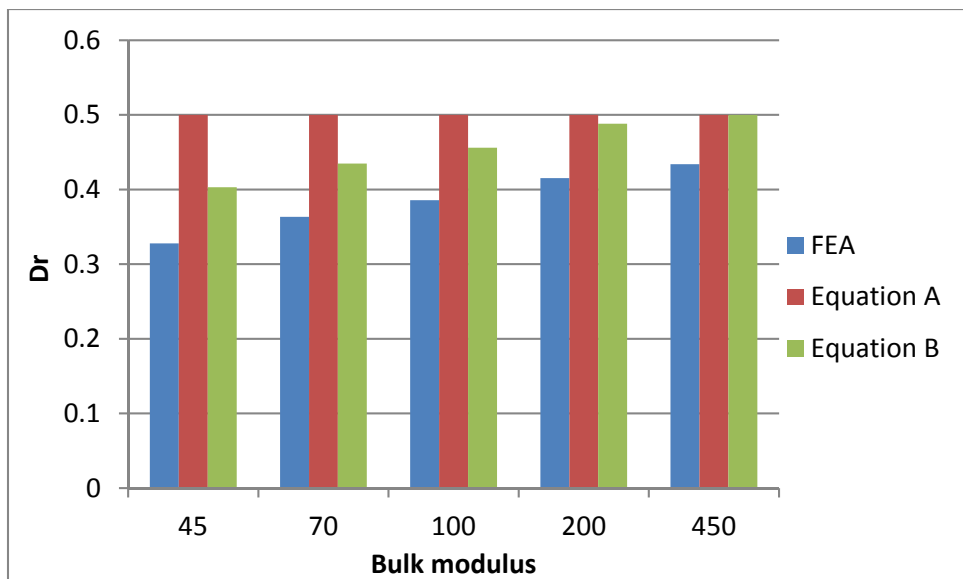


Figure 7.31: D_r values for bearing S

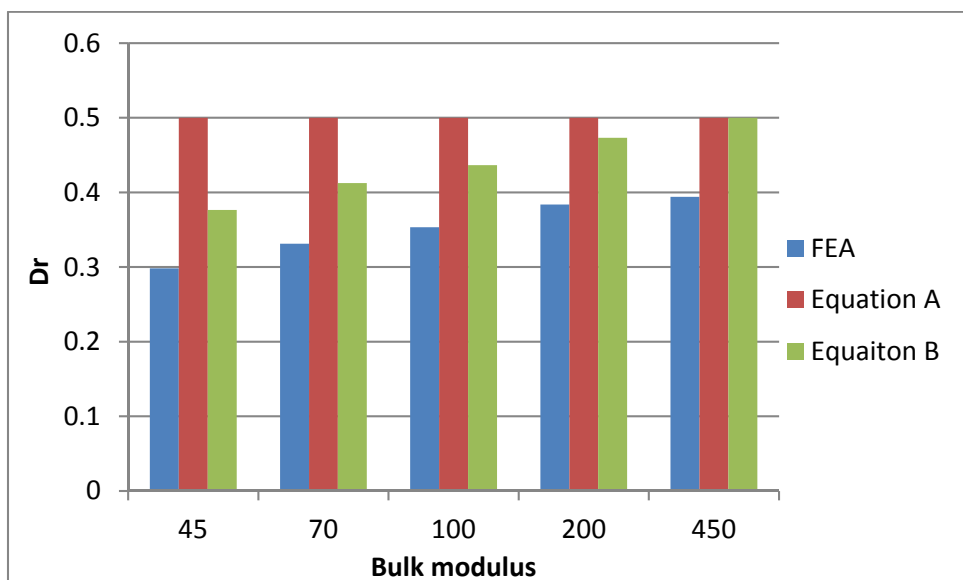


Figure 7.32: D_r values for bearing M

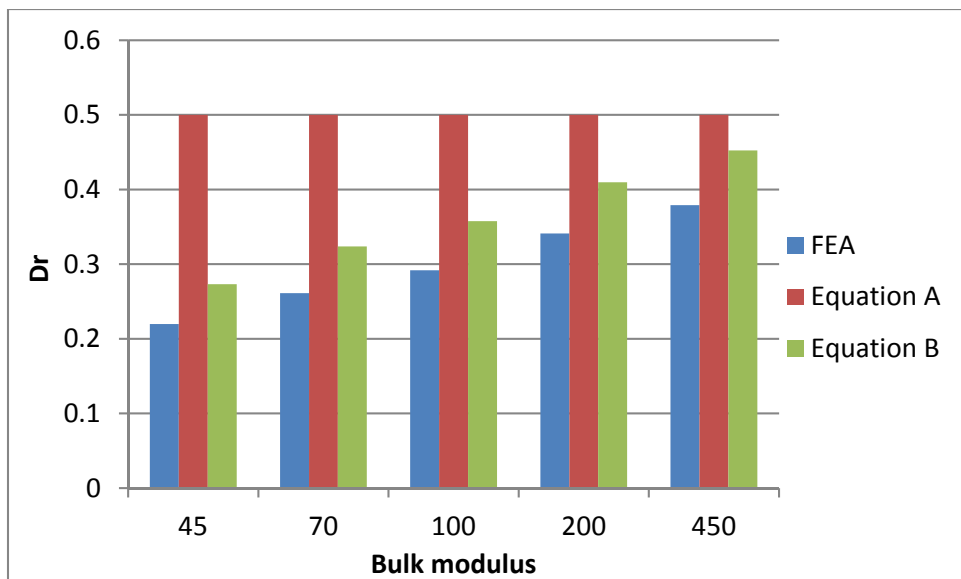


Figure 7.33: D_r values for bearing L

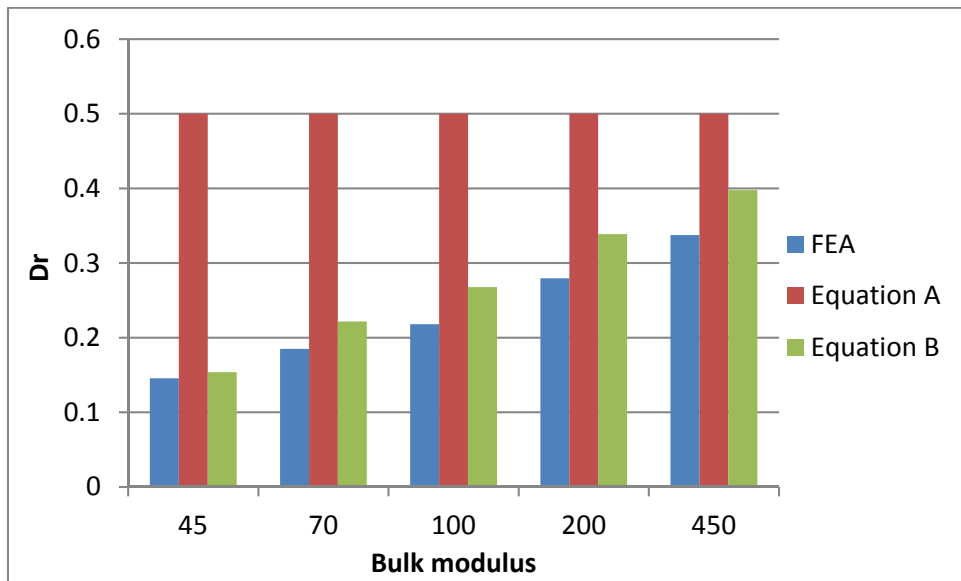


Figure 7.34: D_r values for bearing XL

From the comparison of D_r values above, one might observe:

- The D_r value decreases with greater shape factor for a given bulk modulus.
- The D_r value increases with greater bulk modulus for a given shape factor.
- The predictions by both Eq. A and Eq. B are conservative for all analyses. Eq. B appears to be in better agreement with the FEA results than Eq. A does in this study. However, this does not lead to the conclusion that Eq. B is superior to Eq. A. In design practice, the actual apparent bulk modulus values are unknown to designers. The available bulk modulus values are experimental values obtained either from the material testing or previous literature, which are close to the upper

limit of the range of bulk moduli investigated in this study, leading to very close predictions by Eq. A and Eq. B.

- The constant value $D_r = 0.5$ (referred as Eq. A in this study) is suggested for use. For very large bearings, with shape factors that are greater than 15, a lower value of $D_r = 0.4$ is recommended for use at the discretion of the designer.

7.5 Superposition Study

The proposed total shear strain design approach states that the total shear strain is the superposition of the strains caused by axial load, rotation deformation and lateral deformation based on the linear theory assumption from previous studies. In this chapter the accuracy of this superposition method is examined numerically for an elastomer body that is subjected to a variety of deformation types.

7.5.1 COMPRESSION AND SHEAR

The finite element model of bearing L was subjected to two steps of loads:

Step 1: Bearing L was subjected to a normalized axial load $\alpha_a = 2$.

Step 2: Bearing L was subjected to a uniform lateral shear deformation $\gamma_s = 0.5$.

The maximum total shears strain by steps:

Step 1: $\gamma_1 = D_a \alpha_a = 1.4 \times 2 = 2.8$

Step 2: $\gamma_2 = \gamma_1 + \gamma_s = 2.8 + 0.5 = 3.3$

The shear strain profiles of step 1 and Step 2 are plotted in Figure 7.35, from which one might find that the profile of load step 2 is nearly the same to that of step 1 by an offset of 0.5. The validity of the superposition assumption can be further examined by calculating the superposition ratio, defined as the ratio of the increase in total shear strain to the shear strain caused by the last step alone. As shown in Figure 7.36, the assumption of superposition is valid over the whole length, with the superposition ratios near unity.

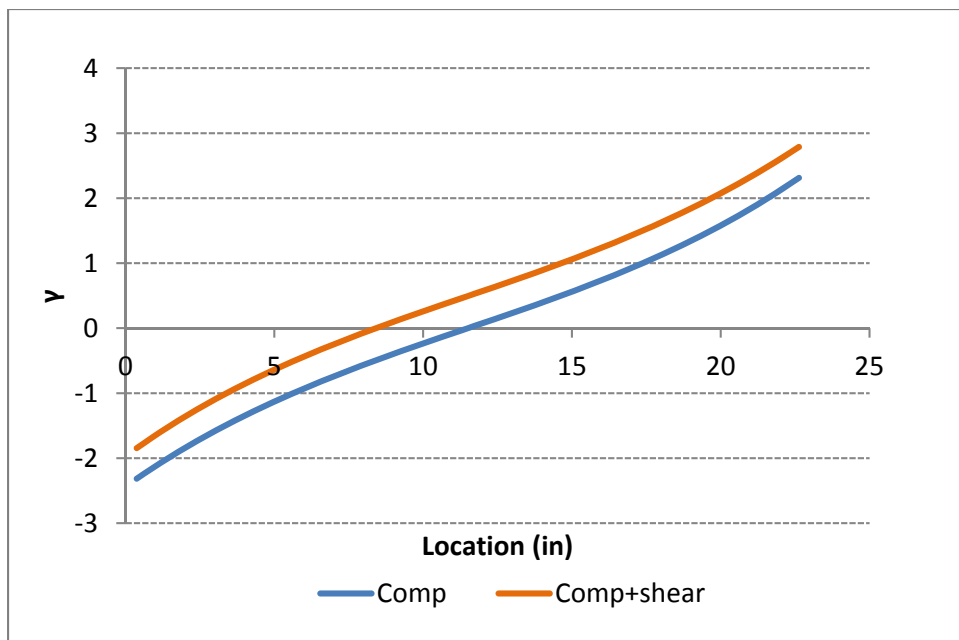


Figure 7.35: Shear strain profiles along the longitudinal axis for step 1 & step 2

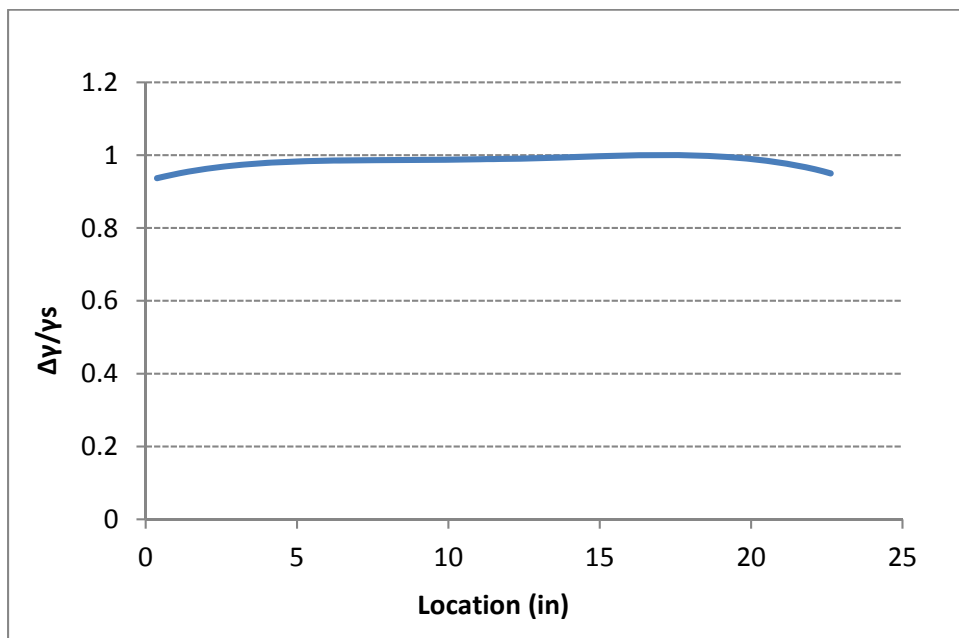


Figure 7.36: Profile of superposition ratios

7.5.2 COMPRESSION, ROTATION, AND SHEAR

The finite element model of the bearing L is subjected to three steps of loads:

Step 1: Bearing L was subjected to a normalized axial load $\alpha_a = 2$.

Step 2: Bearing L was subjected to a normalized rotation $\alpha_r = 4$.

Step 3: Bearing L was subjected to a uniform lateral shear deformation $\gamma_s = 0.5$.

The maximum total shears strain by steps:

Step 1: $\gamma_1 = D_a \alpha_a = 1.4 \times 2 = 2.8$

$$\text{Step 2: } \gamma_2 = \gamma_1 + D_r \alpha_r = 2.8 + 0.5 \times 4 = 4.8$$

$$\text{Step 2: } \gamma_3 = \gamma_2 + \gamma_s = 4.8 + 0.5 = 5.3$$

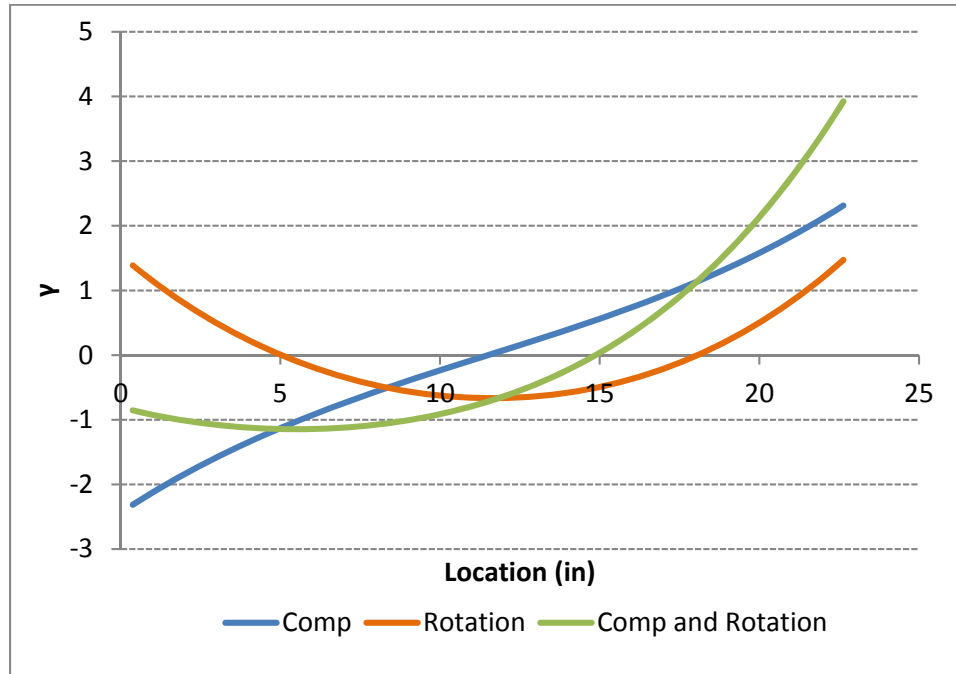


Figure 7.37: Shear strain profiles along the longitudinal axis for step 1 & step 2

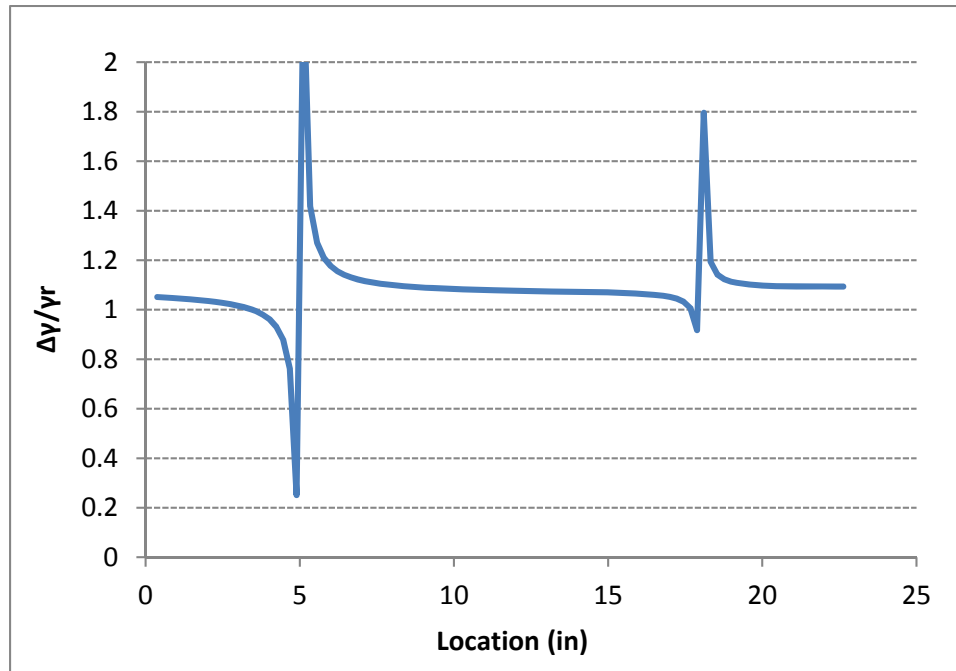


Figure 7.38: Profile of superposition ratios for step 2

The shear strain profiles of step 1 and Step 2 are plotted in Figure 7.37. It is obvious that the profile of step 2 (axial load and rotation) is nearly the linear superposition of profiles of those

of axial load and rotation alone. The validity of the superposition assumption is further examined by calculating the superposition ratio over the longitudinal axis, as provided in Figure 7.38. The calculated superposition ratios over the length are around unity except at two points where the shear strains are zero and the superposition ratios are singular.

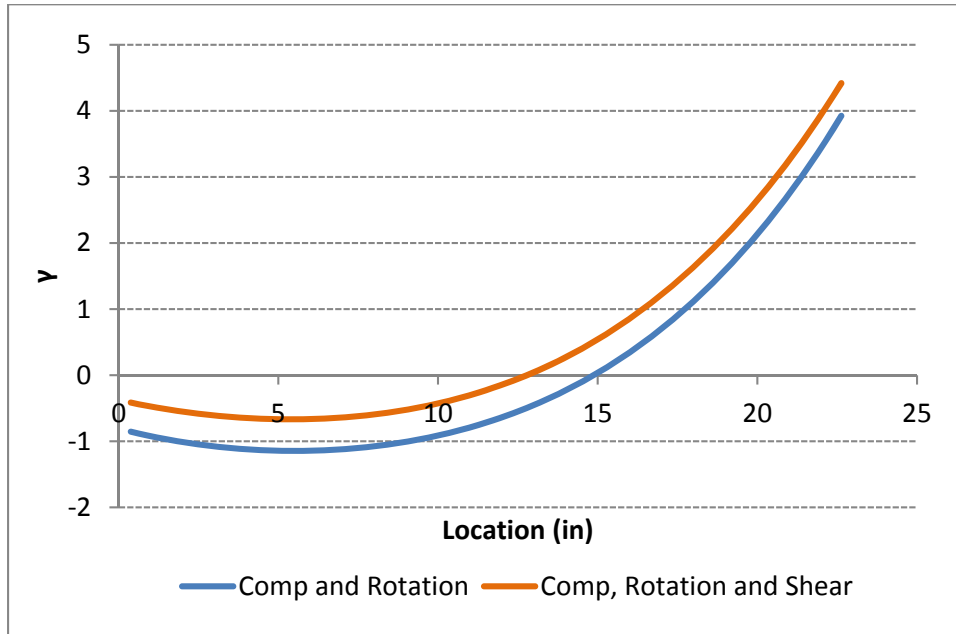


Figure 7.39: Shear strain profiles along the longitudinal axis for step 2 & step 3

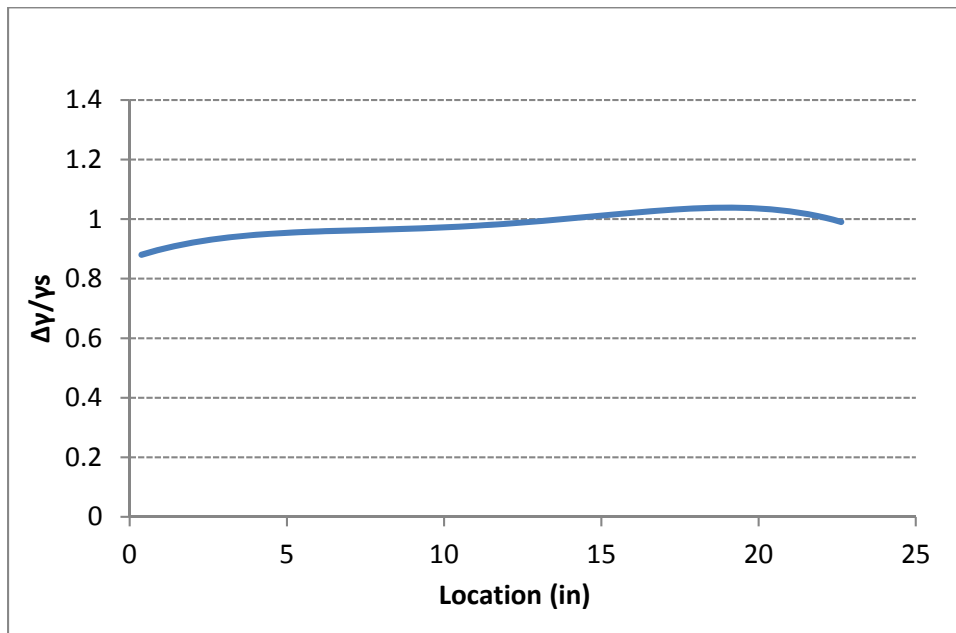


Figure 7.40: Profile of superposition ratio for step 3

Finally the shear strain profiles of step 2 and step 3 are provided in Figure 7.39, one might also tell easily, as expected, that the profile of load step 3 is no other than an offset of 0.5 from the profile of step 2, akin to the previous analysis. Similarly, the validity of the superposition assumption is further examined by calculating the superposition ratio over the longitudinal axis. Figure 7.40 presents the profile of superposition ratios for step 3 along the length, confirming the linear superposition assumption with all superposition ratios approximately at unity.

7.6 Summary

The results form a three-dimensional parametric finite element modeling of elastomer layers under axial and rotation deformation were presented in this chapter. The analyses covered a wide range of bulk moduli and shape factors (bearing sizes) that bridge the gap between limited bearing geometries studied in previous studies and bearings that are representative of higher demand applications.

The parametric finite element study showed that the total shear strain approach based upon Method B of the AASHTO LRFD specification provides adequate estimates over a wide spectrum of analyses with reasonable margins of safety.

The constant values $D_a = 1.4$ and $D_r = 0.5$ (referred as Eq. A in this study) is suggested against the use of the more complex D_a and D_r expressions in the commentary of AASHTO LRFD specification (referred as Eq. B in this study). For bearings consisting of very large and thin elastomeric layers with factors greater than 15, $D_a = 1.8$ and $D_r = 0.4$ are recommended for use. .

The linear superposition assumption upon which the total shear approach is based upon was examined. The finite element analyses confirmed that this assumption is valid on complex deformations that combine compression, rotation and shear with calculated shear strains ranging from 3.3 to 5.3.

CHAPTER 8: INVESTIGATION OF DISTRESSED BEARINGS

8.1 Problem Description

As previously discussed in chapter 3, so of the elastomeric bearings used for IH-35 NB & US-290 EB direct connector in North Austin showed significant signs of distress during periodic maintenance inspections. One of the bearings was severely distressed. To understand the cause of this damage, the research team carried out a series of measurements of all related bearings during the course of the field instrumentation.

Figure 8.1 illustrates the plan view of the IH-35 NB & US-290 EB direct connector. The bridge consists of two steel trapezoidal box girders supported on one abutment and four pier caps. Two elastomeric bearings were used at each bent.

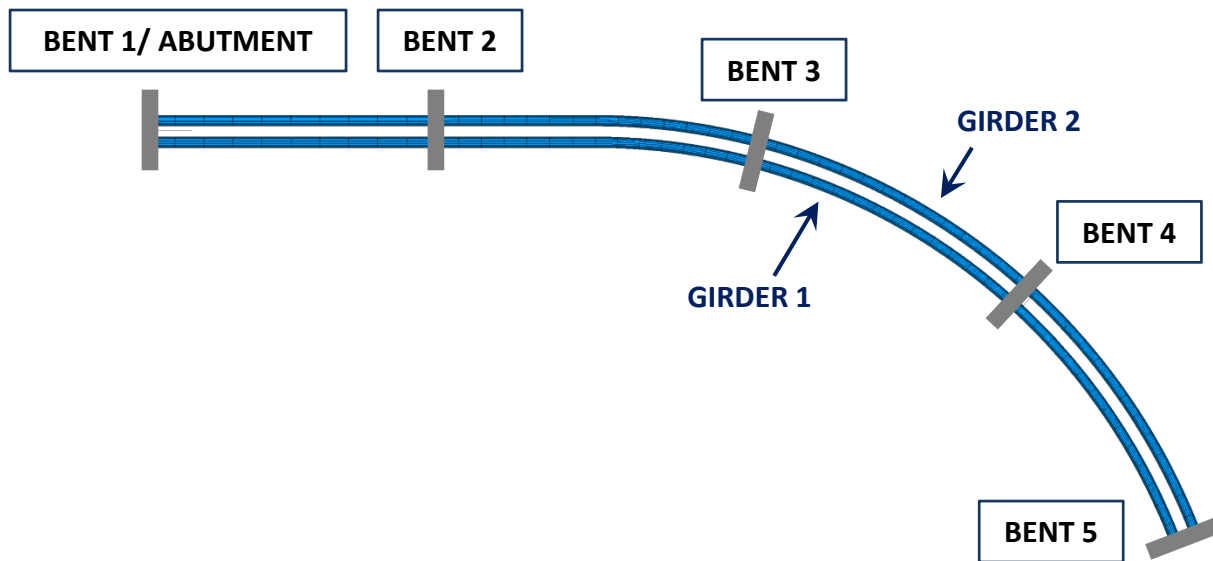


Figure 8.1: Plan of IH-35 NB & US-290 EB direct connector

The dimensions of elastomeric bearings used on this structure are provided in Table 8.1. The bearings at bent 3 consisted of rocker bearings on a steel straddle cap and are not included.

Table 8.1: Bearing dimensions per location

	L	W	t	S	n
Abutment	14	27	0.5	9.22	7
Bent 2	21	36	0.5	13.26	4
Bent 4	21	36	0.5	13.26	4
Bent 5	14	27	0.5	9.22	7

Excessive damage was observed at the bearing used for girder 1 at bent 4, as illustrated in Figure 8.2 and Figure 8.3. Slipping has taken place between the bearing and superstructure transversely. This bearing appears to be crushed on the side facing girder 2. The interior elastomer was extruded from the layer and, causing significant loss the vertical stiffness. Meanwhile, liftoff is evident on the other side of the bearing.



Figure 8.2: Distressed bearing for girder 1, bent 4



Figure 8.3: Distressed bearing for girder 1, bent 4

Another bearing for girder 1 at bent 5 was also found to be damaged, though to a lesser degree, as presented in Figure 8.4. Bearing bulging and small amount of elastomer extrusion was observed near the end that faces girder 2.



Figure 8.4: Bearing with damage for girder 1, bent 5

8.2 Methods

Measurements of the static biaxial rotations were made on each of the eight elastomeric bearings. The maximum shear strains that the bearings could undergo based on the rotational measurements were also made. Because the orientation of bearings vary over the length of the curved bridge, the sign conventions at each bearing are defined with respect to the local longitudinal axis at each location, as illustrated in Figure 8.5.

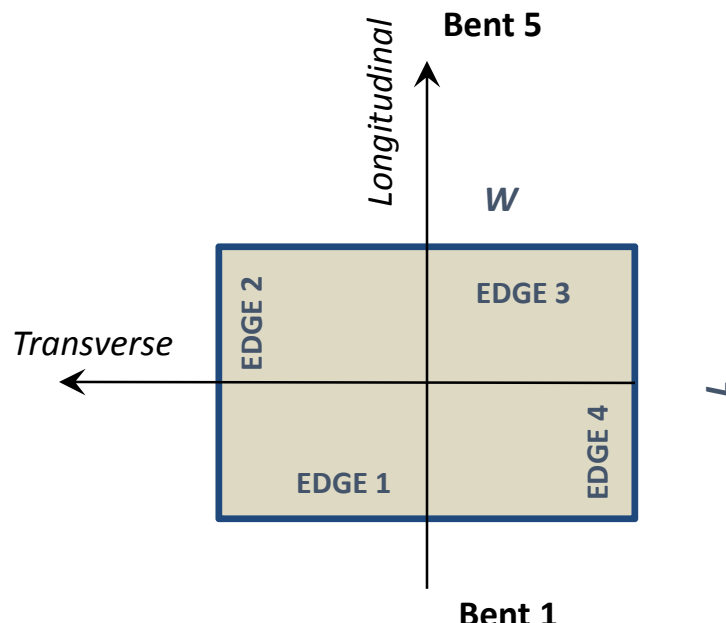


Figure 8.5: Sign conventions of a bearing

Two different methods were used to measure the angle of inclination along the longitudinal and transverse rotation at each location. The main reason for multiple measurement methods is due to the unevenness of concrete surface on which the bearings are mounted. In addition, the independence of the two methods increases the redundancy of measurements.



Figure 8.6: Digital level on the steel sole plate



Figure 8.7: Digital level on the concrete surface

Digital levels (Craftsman 48295) were used to measure the angle of inclination on the surfaces of both the concrete surface and the upper steel sole plate along the four edges of each bearing. The levels featured a digital display with a resolution of 0.1° . The bottom of the level was magnetic could therefore be attached to the steel surfaces, as shown in Figure 8.6. While measuring the angle on the concrete surface, the digital level was mounted on a long rectangular wood member that was checked for flatness at the laboratory to avoid unsteady reading due to the unevenness of surface as illustrated in Figure 8.7. The subtraction of angle on the concrete surface from that on the sole plate is the total rotational angle imposed on the elastomeric bearings.



Figure 8.8: Measuring with inside caliper

Figure 8.8 demonstrates an alternative method of measuring the rotational angle using a digital caliper (iGAGING). The resolution of this device was 0.01 inch. The vertical distance values between the upper steel sole plates and the lower concrete bearing mount at the four corners of each bearing were measured. The angle of rotation along the four edges of a bearing could then be calculated.

Both methods of measurement that were used provided valuable data for understanding the displacements and the as-constructed conditions at the bearings. As a result of surface unevenness of the concrete surface, local angle of inclination varies considerably on bearing seats. The measurements by digital level can be seen as a representation of the angle of inclination near the center of an edge, while the inside caliper provides results that are more representative of the average angle along an edge.

8.3 Measurements

The measurements of all eight bearings by the two methods are presented in Table 8.2. The unit of all measurements is in degrees.

Table 8.2: Measurements of angles

		Girder 1				Girder 2			
		Longitudinal		Transverse		Longitudinal		Transverse	
		Edge2	Edge4	Edge1	Edge3	Edge2	Edge4	Edge1	Edge3
Bent 1	$\theta_{t,L}$	0.1	0.1	N/A	0.0	0.2	0.2	N/A	0.0
	$\theta_{b,L}$	-0.5	-0.4	N/A	-0.1	-0.4	-0.4	N/A	-0.1
	$\theta_{r,L}$	0.6	0.5	N/A	0.1	0.6	0.6	N/A	0.1
	$\theta_{r,C}$	0.7	0.49	-0.09	0.02	0.57	0.57	-0.04	-0.04
Bent 2	$\theta_{t,L}$	0.2	0.3	-0.2	-0.2	0.0	0.1	-0.1	-0.1
	$\theta_{b,L}$	0.6	0.6	0.1	0.0	0.0	0.2	0.1	0.1
	$\theta_{r,L}$	-0.4	-0.3	-0.3	-0.2	0.0	-0.1	-0.2	-0.2
	$\theta_{r,C}$	-0.44	-0.33	-0.24	-0.3	-0.16	-0.06	-0.03	-0.1
Bent 4	$\theta_{t,L}$	0.0	0.1	-0.3	-0.3	-0.2	-0.1	-0.1	0.0
	$\theta_{b,L}$	0.3	-0.4	0.6	1.2	0.1	0.3	0.3	0.2
	$\theta_{r,L}$	-0.3	0.5	-0.9	-1.5	-0.3	-0.4	-0.4	-0.2
	$\theta_{r,C}$	-0.38	0.6	-0.89	-1.46	-0.22	-0.41	-0.29	-0.18
Bent 4	$\theta_{t,L}$	0.4	0.5	-0.8	N/A	0.1	0.1	-1.0	N/A
	$\theta_{b,L}$	0.2	0.9	0.3	N/A	-0.2	0.2	-0.2	N/A
	$\theta_{r,L}$	0.2	-0.4	-1.1	N/A	0.3	-0.1	-0.8	N/A
	$\theta_{r,C}$	-0.04	N/A	-0.93	N/A	0.12	N/A	-0.83	N/A

Where:

$\theta_{t,L}$: Angle of inclination on the surface of upper steel sole plate measured by digital level.

$\theta_{b,L}$: Angle of inclination on the surface of lower concrete mount measured by digital level.

$\theta_{r,L}$: Total angle of rotation by digital level ($\theta_{r,L} = \theta_{t,L} - \theta_{b,L}$).

$\theta_{r,C}$: Angle of rotation by inside caliper.

It can be seen that the measurements by the digital level and inside caliper are very close, with the majority of the differences less than 0.1° , except for a few cases approaching 0.2° . The angles of inclination on the surface of the steel sole plates by digital level are very consistent. The differences between those of two parallel edges are all within 0.1° . However, pronounced differences between the two parallel edges on the surface of the concrete are apparent. Considering the bearing for girder 1 at bent 4 for example, the angles of inclination on edge 1 and edge 3 differ by 0.6° , revealing that significant amount of surface unevenness that takes place in both global and local scales.

Figure 8.9 and Figure 8.10 summarize the maximum longitudinal and transverse angles of rotation applied on each bearing that have been determined, showing that a large amount of the angle of rotation occurs to bearings for girder 1 at bent 4 and bent 5 in the transverse direction.

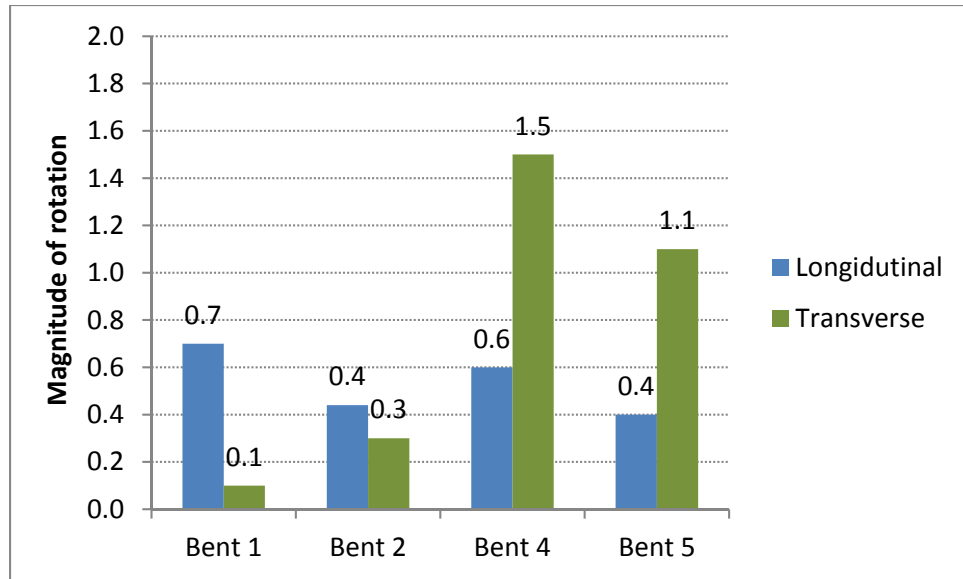


Figure 8.9: Maximum angle of rotation imposed on bearings for girder 1

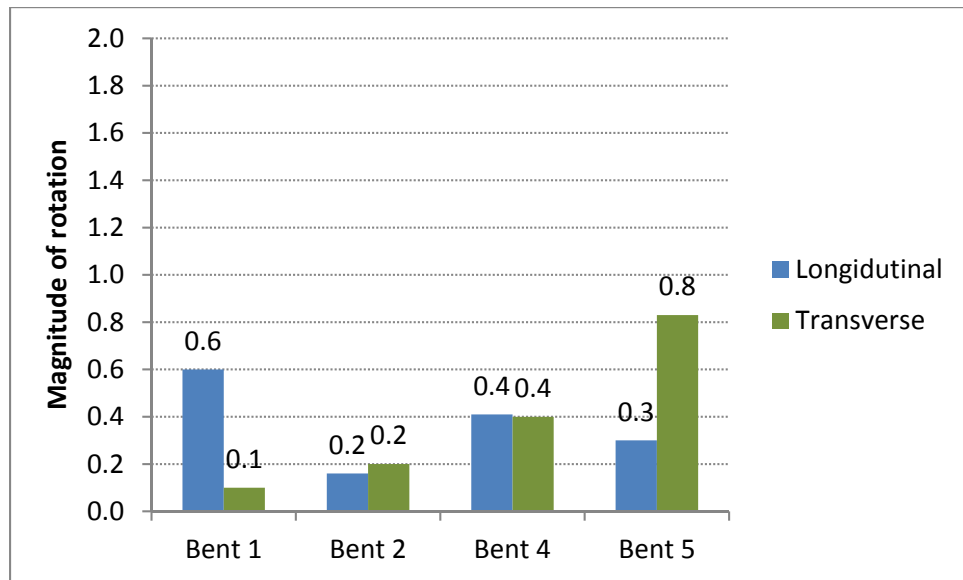


Figure 8.10: Maximum angle of rotation imposed on bearings for girder 2

The maximum shear strain γ_r due to static rotation on the edge of the interior elastomer layer of all bearings were calculated and are presented in Table 8.3 based on the maximum angles of rotations that have been measured using the proposed design methodology discussed in the previous chapter.

Table 8.3: Maximum shear strain γ_r due to static rotation

	Girder 1		Girder 2	
	Longitudinal	Transverse	Longitudinal	Transverse
Bent 1	0.60	0.32	0.51	0.32
Bent 2	-1.35	-2.71	-0.49	-1.81
Bent 4	1.85	-13.57	-1.26	-3.62
Bent 5	-0.34	-3.50	0.26	-2.64

The maximum shear strain γ_a due to static axial load on the edge of interior elastomer layer of all bearings are also calculated and presented in Table 8.4 based the maximum dead load values used for design. Two bearings used at the each bent have the same maximum dead loads.

Table 8.4: Maximum shear strain γ_a due to dead load

	Max DL (kips)	shear strain " γ_a "
Bent 1	222	0.89
Bent 2	816	1.14
Bent 4	949	1.33
Bent 5	373	1.50

Figure 8.11 and Figure 8.12 summarize the magnitude of the maximum shear strain of the bearings in both the longitudinal and transverse directions under the combined effect of imposed static rotations and maximum dead loads given in Table 8.3 and Table 8.4. A significant amount of shear strains were discovered on the bearing used for girder 1, at bent 4 and bent 5, without even including the effects of lateral deformation and dynamic effects. The severely-distressed bearing has a calculated shear strain of 14.90 transversely, which is almost three times of the allowed limit. The lightly-damaged bearing has a calculated strain of 5.0, which will certainly increase when other effects are considered. Therefore, a reasonable conclusion would be that the observed damage of the two bearings for girder 1 is the direct result of the excessive angle of inclination in the transverse direction.

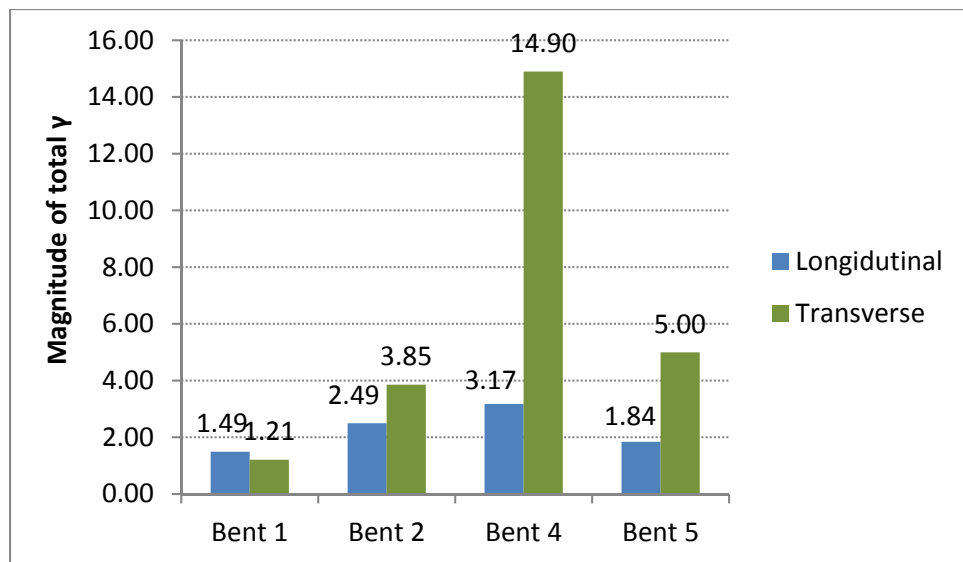


Figure 8.11: Max shear strain on bearings for girder 1 under DL and rotation

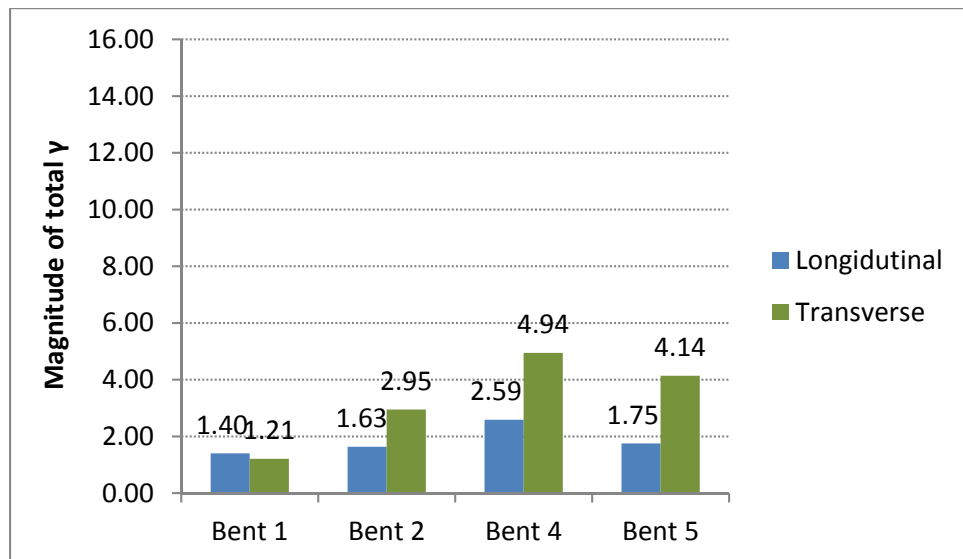


Figure 8.12: Max shear strain on bearings for girder 2 under DL and rotation

8.4 Summary

This chapter provides a discussion of results from an investigation of a number of bearings used on IH-35 NB & US-290 EB direct connector in North Austin. Two independent field measurement approaches were developed that measure the longitudinal and transverse angles of rotation that each elastomeric bearing is subjected to. The results revealed that two of the bearings that show significant amounts of distress are subjected to excessive amounts of transverse rotation. Further analyses by calculating the maximum shear strain of all bearings using the proposed design approach confirm that the observed bearing damage is the direct result of the excessive amount of transverse direction caused by a mismatch between the transverse slope of the sole plate and that of the concrete bearing seat. Due to the significant uneven nature

of the concrete surface, the error is associated with the cast-in-place concrete surface. Improved inspection of the pier caps are therefore recommended in future construction projects so as to avoid similar damage.

CHAPTER 9: CONCLUSIONS

A summary of bridge instrumentation, laboratory tests, and computational studies conducted for this research project is provided in this chapter. The conclusions and findings are presented from the standpoint of the design approach assessment and the final development of the proposed design methodology for elastomeric bearings in higher demand applications.

The IH-35 NB & US-290 EB direct connector in North Austin was selected for the field monitoring. This bridge is one of the first bridges where elastomeric bearings were used in a “higher demand application.” Although the majority of the bearings were behaving as expected, damage was found on two of the bearings. The instrumentation measurements of the thermal load and vehicular traffic induced bridge reactions that bearings are subjected to were found to be generally within the design prediction. The reason for the observed problems with two distressed bearings appears to be due to construction errors (non-level bearing seats rather than a problem with the bearing design). Improved quality control of the cast-in-place concrete is suggested in future bridges to avoid these problems.

From the material experiments conducted in this study two main results can be drawn. The first is that the magnitude of the material property variation in larger bearings, although existent and more prominent than in smaller bearing, should not be a concern for the designer and should not be a reason for disqualifying this bearing alternative. The second is that as neoprene becomes stiffer only in lower temperatures, slipping is a non-recoverable, low-temperature-driven phenomenon that should be avoided by employing appropriate design measures.

From the full-scale experiments conducted in this research project there are four major findings:

- 1) The AASHTO Method A and Method B design procedures produce safe bearing designs for what could be considered as higher demand applications, with Method A producing larger, less economical bearings.
- 2) Equations predicting the axial deflections of bearings are not accurate for bearings qualifying for higher demand applications (high shape factors, large plan areas).
- 3) Lift-off is a phenomenon associated with lower axial loads and large rotations, and the shear strains produced in that case are less than the shear strains of the fully-bonded configuration, assumed in current AASHTO design procedures, leading to conservative designs.
- 4) Buckling of elastomeric bearings for non-seismic applications can also be an issue as taller bearings are needed to accommodate bridge movements and avoid slip; however, this issue is successfully addressed by current AASHTO design approaches.

The measurements from the full scale testing also facilitated the calibration of necessary material coefficients using an analytical model developed by the researchers, leading to the successful development of a three dimensional finite element model capable of simulating the behavior of the elastomeric bearings in full scale compression, shear, and rotation testing. The finite element analysis and experimental results are in good agreement both qualitatively and quantitatively. The validated finite element model was used to perform a more comprehensive parametric finite element study.

Three-dimensional parametric finite element modeling of elastomer layers under axial and rotational deformation were performed, covering a wide range of bulk moduli and bearing

dimensions with shape factors varying from 8 to 20. The results demonstrate that the total shear strain approach based upon Method B of the AASHTO LRFD specification provides adequate estimates for the overwhelming majority of the analyses with reasonable margins of safety. Based on the results of the parametric finite element modeling and previous full scale testing, a higher compressive stress limit of 2 GS is hence recommended.

Parametric finite element modeling also indicates that AASHTO Method B might under-predict the shear strain caused by axial load in some cases, if the bulk modulus experimentally obtained from material testing is used for calculation. Therefore the constant dimensionless coefficients $D_a = 1.4$ and $D_r = 0.5$ for calculating the shear strains caused by axial load and rotation are recommended for use against the more complex alternative values that adopt bulk modulus in AASHTO LRFD specification. For very large sized bearings, with shape factors greater than 15, $D_a = 1.8$ and $D_r = 0.4$ is recommended for use in design.

The linear superposition assumption upon which the total shear strain approach is based was examined in the finite element analyses, revealing that this assumption is valid on complex deformations that combine compression, rotation and shear with calculated shear strains ranging from 3.3 to 5.3.

As a result of laboratory and analytical studies in this research project, a design methodology, that qualifies the application of elastomeric bearings to the higher demand application, is proposed based upon the AASHTO Method B with necessary alternations. The details of the design methodology and examples are presented in Chapter 10.

During the removal of the field instrumentation, measurements of the static angle of rotations in both the longitudinal and transverse directions were taken. The results show that the two damaged bearings are subjected to excessive transverse rotations. Further analyses by calculating the maximum shear strain of all bearings using the proposed design approach confirmed that the observed bearing damage is the direct result of the excessive amount of transverse rotation. This as well serves as compelling proof of the validity of the proposed design methodology in this study. It is advised that necessary measures and caution should be exercised during construction to ensure that bearing seats are cast level.

CHAPTER 10: DESIGN METHODOLOGY AND EXAMPLES

10.1 Rubber Design Properties and Bearing Design Parameters

10.1.1 RUBBER STIFFNESS/STRENGTH

In the design of steel-laminated elastomeric bearings, the limiting factor in most of the cases is the maximum expected shear strain due to expected deformations at the steel to rubber interface. Although typical values of shear strain at failure range between 350 and 400%, as seen in Figure 10.1, the limit set in codes is 500% accounting for the non-uniformity of the stress state, conservatism in the demands calculation, and size effects.

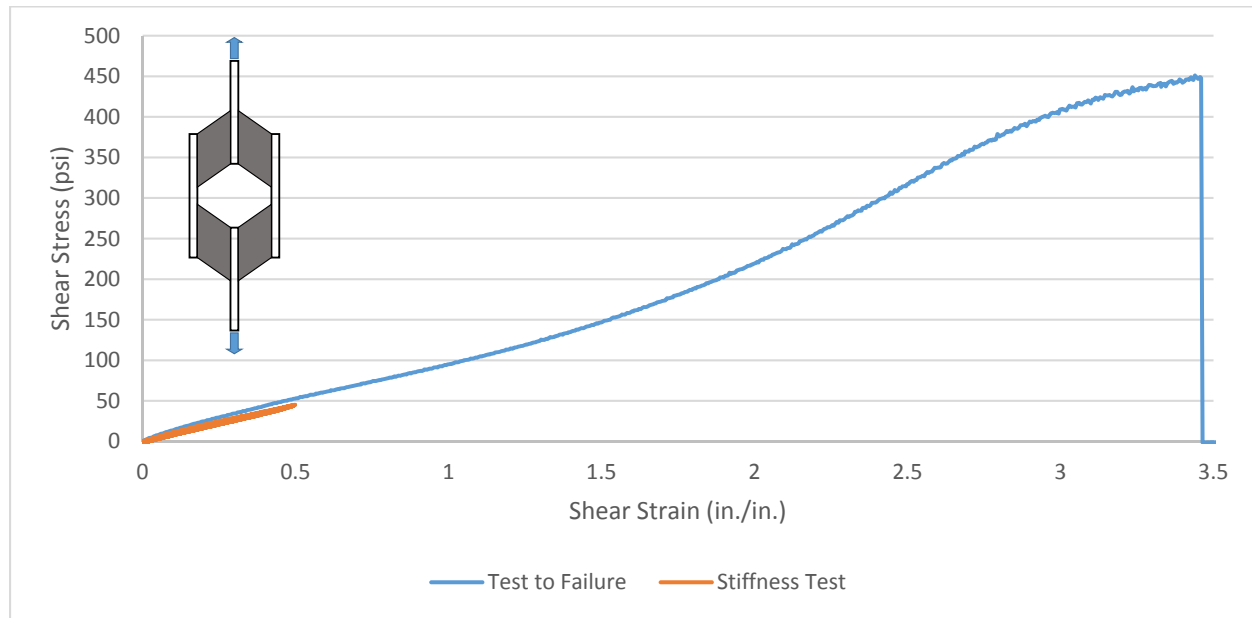


Figure 10.1: Typical shear stress-strain curves for service shear deformations (orange) and failure (blue)

10.1.2 TEMPERATURE DEPENDENT STIFFNESS

Slip between the steel girders and elastomer can be the cause of abrasion and deterioration of the cover layer, leading to serviceability concerns. Due to the relatively low shear stiffness of steel-laminated elastomeric bearings compared to other types of bearings, slip is less likely to occur. However, for larger plan area bearings and lower compressive loads the slip potential is present. The potential is further increased accounting for the fact that the elastomer stiffness is elevated at lower temperatures, as can be seen in Figure 10.2. As a result slip is a cold-temperature-driven, non-recoverable phenomenon and the design should carefully consider the stiffening effect of the elastomer.

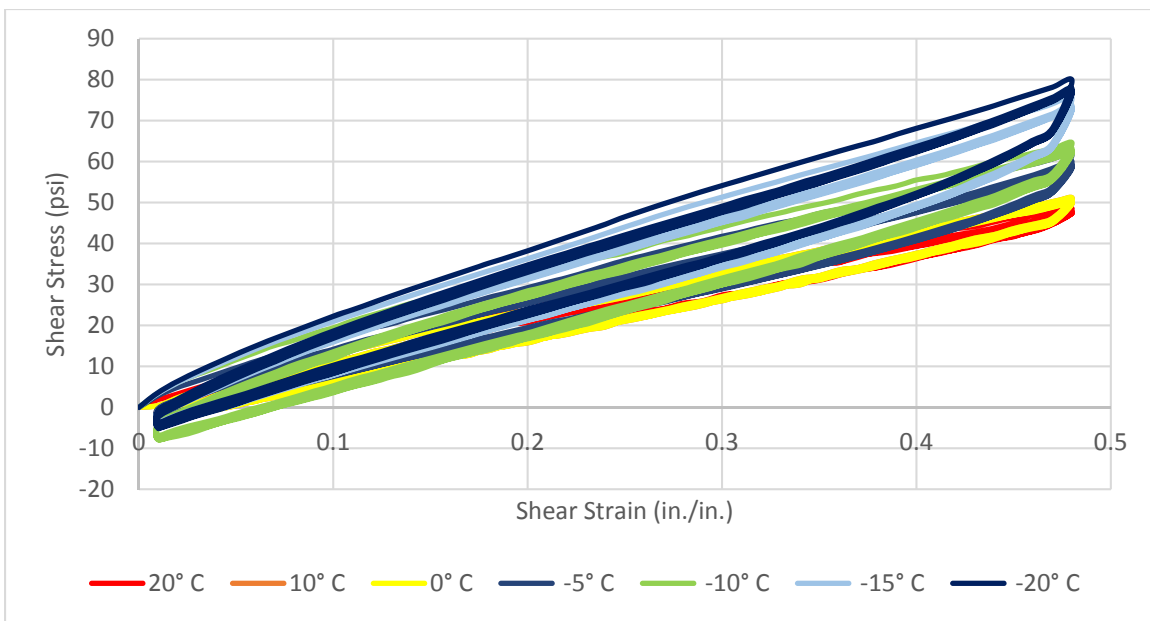


Figure 10.2: Stress-strain curves for rubber at various temperatures

10.1.3 DESIGN PARAMETERS

- L = plan dimension of the bearing perpendicular to the axis of rotation under consideration (generally parallel to the global longitudinal bridge axis) (in.)
- W = plan dimension of the bearing parallel to the axis of rotation under consideration (generally perpendicular to the global longitudinal bridge axis) (in.)
- h_{ri} = thickness of the i^{th} elastomeric layer (in.)
- h_{rt} = total elastomer thickness (in.)
- n = number of interior layers of elastomer, where interior layers are defined as those layers which are bonded on each face.
- G = shear modulus of the elastomer at room temperature (ksi)
- G_{cold} = shear modulus of the elastomer at lowest temperature expected (ksi)
- μ = coefficient of friction between rubber and steel (recommended value = 0.3)

10.2 Design Approach

10.2.1 LIMITATIONS OF CURRENT (TxDOT) DESIGN METHODOLOGY

The current TxDOT elastomeric bearing design methodology employs a stress-based approach for the axial load limit, combining an absolute limit for the axial stress with a shape-factor-dependent axial stress limit. Tests have shown that such limits are conservative. In addition to the axial stress limits, the rotational limits are set as a function of the calculated axial deflection of the bearing. Tests have shown a tendency to underestimate the vertical deflection of the bearing under axial load, leading to inherent conservatism for the rotational limits.

Another limit that the current TxDOT procedure employs is a stability limit based on the geometrical characteristics of the bearing, not taking into account the level of axial stress/load.

All sources of conservatism mentioned above will result in unnecessarily large bearings with increased potential to slip, thus promoting other types of bearings as more economical and reliable alternatives.

It should be noted that the previous bearings on the instrumented bridge that were designed for higher demand applications following the TxDOT procedure produced bearings that could safely meet their demands. It was in fact the first step into extending the use of elastomeric bearings for higher demand applications, after combining TxDOT sponsored research results with AASHTO LRFD Bridge Design Specifications existing at that time (1999), prior to the introduction of the total shear strain approach. It is the opinion of the research team that despite slipping, these bearings would have performed very well had the bridge piers been constructed within established tolerances.

10.2.2 AASHTO/ EN-1337 DESIGN METHODOLOGY

Current codes and design procedures use a total shear strain approach as a limit for the bearing design. This approach calculates the shear strains at the steel-to-elastomer interface due to the imposed modes of deformation. As a result, the approach limits the sum of the shear strains produced by all expected deformation modes to be less than the shear strain at failure of the elastomer. This subsequently results in a more efficient design, decreasing the size and cost of the bearing, making it a viable alternative for higher demand applications.

10.2.3 ALTERATION PROPOSAL OF CURRENT AASHTO LRFD DESIGN PROVISION AND TxDOT DESIGN PRACTICE

As two of the objectives of this research project are to assess the AASHTO LRFD and TxDOT design methodologies and propose design recommendations, this section provides a discussion of recommended changes to these provisions and practices. The proposed methodology adopts the current AASHTO LRFD method B total shear strain approach with the following alterations:

a. Relaxation of compressive stress provision

The current AASHTO limits the dead load compressive stress to the smaller of 1.20 ksi and 1.2 GS, and a total compressive stress to the smaller of 1.5 ksi and 1.5 GS. This limit, albeit reasonable for the design of smaller bearings, are unnecessarily conservative for larger bearings, and even counterproductive for safety concerns in some cases. Over-conservative compressive stress limit lead to excessive bearing dimensions in design, which severely undermines the rotation performance of bearings and exacerbates their susceptibility to slipping in cold weather. A higher compressive stress limit of 2 GS is recommended.

b. Design for “no-slip” condition

It has been found from the field instrumentation portion of this study that slipping is a cumulative, cold-weather-driven phenomenon. As a result, slip tends to accumulate towards the contraction side of the bridge leading to potential hazards such as the girder movement relative to the bearing. As a result, the research team proposes to design for no-slip except if a restoring mechanism is included.

c. Appropriate values for bulk modulus

It is observed from full-scale testing and previous studies that equations that are used to predict the compressive stiffness of the bearing tend to overestimate the values of bearings with high shape factors using the bulk modulus experimentally obtained from material testing, for uncertain reasons. As the parametric finite element study revealed, the use of bulk modulus experimentally obtained from material testing for AASHTO Method B might lead to the underprediction of shear strain caused by axial load. Therefore the constant dimensionless coefficients for calculating the shear strains caused by axial load and rotation are recommended for use in the proposed design procedure against the values that yield from more complex expressions that use bulk modulus in AASHTO specification. On the other hand, a range of apparent moduli (45 ksi – 450 ksi) that are lower than the experimentally obtained bulk modulus, if any, is recommended for calculating the compressive deflection for bearings with higher shape factors for the least favorable consideration at the discretion of designers.

d. Construction tolerances

It has been found from the field instrumentation portion of this study, at the locations of distressed bearings, that the potential for construction tolerances to be exceeded is large. That is the most probable reason according to the research team that led to the damage of the bearings in the bridge that was monitored. Caution needs to be shown for meeting the tolerances specified, as the impact of not meeting them tends to be more severe for larger bearings.

e. Rotation directivity

Bearings that can qualify for the *higher demand application* characterization are often used in curved or skewed girder systems, leading to rotational demands about their two major axes. Current design practice was observed to be the check of the bearing rotation capacity about its weak axis versus the square root of the sum of the squares of the rotational demands plus the tolerance value. This check, after being proven unconservative for bearings with larger aspect ratios, is suggested to be altered to check against the rotational capacity about each axis of the bearing separately.

10.3 Design Procedure (Code Language)

Steel-laminated elastomeric bearings should consist of alternate bonded layers of elastomer and internal steel reinforcement. No external steel load plate should be bonded to the upper or the lower elastomer layer.

The shape factor for a rectangular bearing without holes may be taken as:

$$S_i = \frac{LW}{2h_{ri}(L + W)} \quad \text{Equation 1}$$

The shear strain caused by axial load may be taken as:

$$\gamma_a = \frac{D_a \sigma_s}{G S_i} \quad \text{Equation 2}$$

where:

D_a = dimensionless coefficient used to determine shear strain due to axial load (recommended value = 1.4)

σ_s = average compressive stress due to total static or cyclic load from applicable service load combinations in AASHTO-Table 3.4.1-1 (ksi)

The shear strain caused by rotation may be taken as:

$$\gamma_r = D_r \left(\frac{L}{h_{rt}} \right)^2 \left(\frac{\theta_s + 0.005}{n} \right) \quad \text{Equation 3}$$

where:

D_r = dimensionless coefficient used to determine shear strain due to rotation (recommended value = 0.5)

θ_s = static or cyclic design rotation angle from applicable service load combinations in AASHTO-Table 3.4.1-1 (rad). Rotations in both directions shall be taken into consideration.

For bearings with shape factors ≥ 15 , following alternative dimensionless coefficients used to determine shears caused by axial load and rotation are advised at the discretion of designers:

$$D_a = 1.8$$

$$D_r = 0.4$$

The shear strain caused by shear displacement may be taken as:

$$\gamma_s = \frac{\Delta_s}{h_{rt}} \quad \text{Equation 4}$$

where:

Δ_s = maximum total static or cyclic shear displacement of the elastomer from applicable service load combinations in AASHTO-Table 3.4.1-1 (in.)

To check against stability, the following parameters should be used:

$$A = \frac{1.92 \frac{h_{rt}}{L}}{\sqrt{1 + \frac{2.0L}{W}}} \quad \text{Equation 5}$$

$$B = \frac{2.67}{(S_i + 2.0) \left(1 + \frac{L}{4.0W} \right)} \quad \text{Equation 6}$$

All the above parameters are used for the bearing design checks. The total rubber thickness shall satisfy:

$$h_{rt} \geq 2\Delta_s \quad \text{Equation 7}$$

The static and cyclic components of the shear strain shall be calculated separately. Combinations of axial load, rotation, and shear displacements at the service limit state shall satisfy:

$$(\gamma_{a,st} + \gamma_{r,st} + \gamma_{s,st}) + 1.75(\gamma_{a,cy} + \gamma_{r,cy} + \gamma_{s,cy}) \leq 5.0 \quad \text{Equation 8}$$

The static component of the average compressive stress shall satisfy:

$$\sigma_{s,st} \leq 2.0GS_i$$

Equation 9

To check against stability the bearing shall satisfy:

$$2A \leq B$$

Equation 10

In case Equation 10 is not satisfied, the stress due to total load shall satisfy:

$$\sigma_{s,max} \leq \frac{GS_i}{2A - B}$$

Equation 11

To check against slipping the bearing should satisfy:

$$\sigma_{s,min} \geq \frac{G_{cold}\Delta_s}{\mu h_{rt}}$$

Equation 12

10.4 Design Flowchart

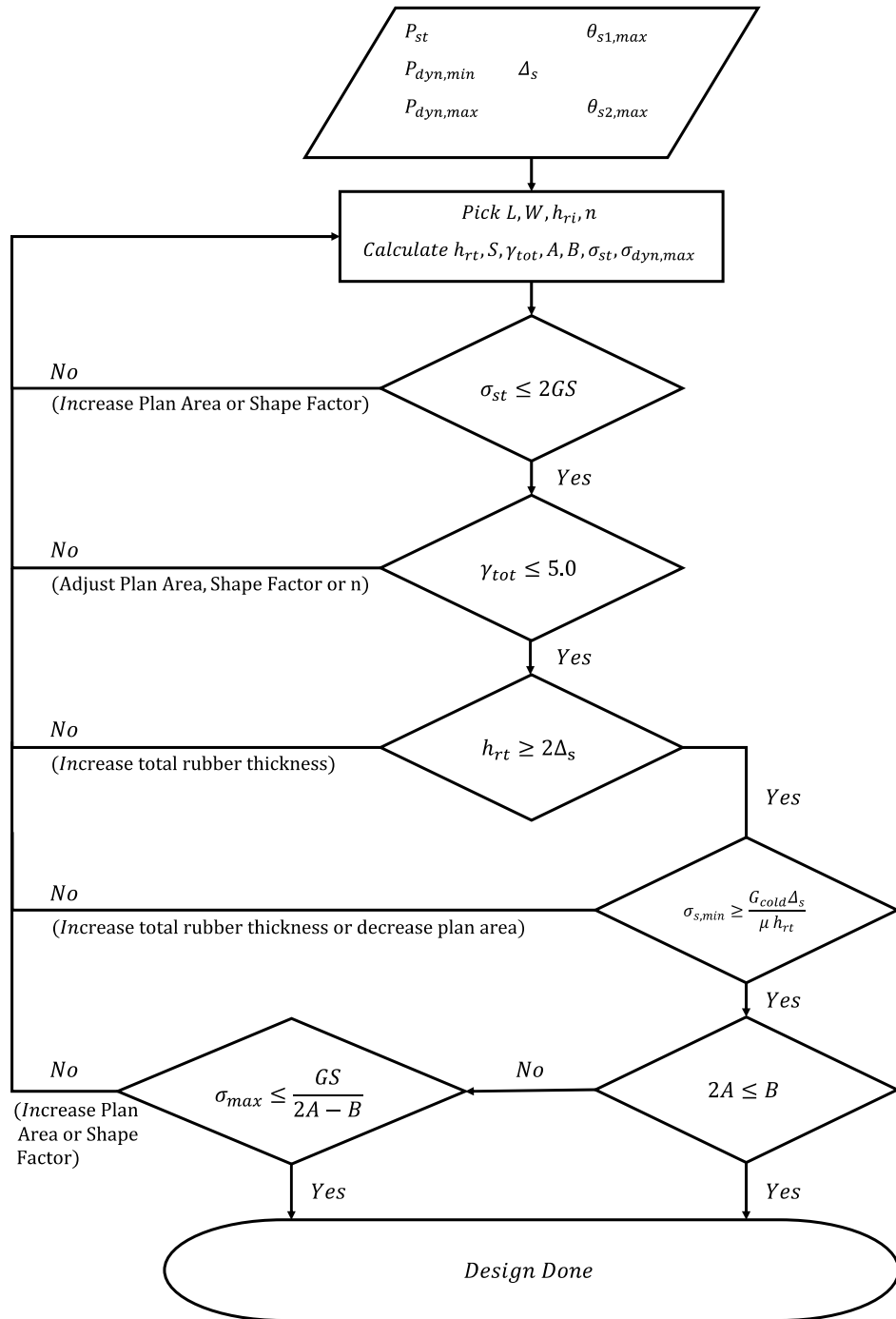


Figure 10.3: Proposed bearing design flowchart

10.5 Design Examples

In this section, three bearing designs are presented. The first is a slip critical bearing according to current design procedures, the second design would be classified as a normal

application, and the third a bearing with high axial and rotational demands. The design values corresponding to each bearing are summarized in Table 10.1.

Table 10.1: Summary of design values

Bearing	P _{max} (kips)	P _{st} (kips)	P _{min} (kips)	Δ _{s,st} (in.)	Δ _{s,cy} (in.)	θ _{1,st} (rad.)	θ _{1,cy} (rad)	θ _{2,st} (rad.)	θ _{2,cy} (rad.)
1	540	373	54	2.48	0	0.01466	0.00361	0.00367	0.0009
2	317	177	75	2.49	0	0.00528	0.00281	0.0001	0.00005
3	1177	945	604	1.9	0	0.00602	0.00541	0.0002	0.00018

10.5.1 BEARING 1

The thickness of the cover layer needs to be less than 70% of the thickness of the internal layers. The shear stiffness of the elastomer is assumed to be 0.1 ksi. This makes the solution of thicknesses of 0.25 in. and 0.375 in. for respective cover and internal layers more attractive. If a bearing is selected with 15 internal layers and plan dimensions of W=25 in. and L=20 in. the resulting shape factor of the bearing is as follows:

$$S_i = \frac{25 \cdot 20}{2 \cdot 0.375(20 + 25)} = 14.81$$

Static and cyclic shear strain components can then be calculated. For the cyclic portion of the axial load the difference between P_{max} and P_{st} is determined. The maximum total shear deformation Δ_s is taken as 65% of the total ΔL due to thermal loads. Angles of rotation θ₁ and θ₂ correspond to rotations about the transverse and longitudinal axis respectively. As a result, the shear strains are calculated as follows:

$$\begin{aligned} \gamma_{a,st} &= \frac{D_a \sigma_{s,st}}{GS_i} = \frac{1.5 \cdot 0.746}{0.1 \cdot 14.81} = 0.705 \\ \gamma_{a,cy} &= \frac{D_a \sigma_{s,cy}}{GS_i} = \frac{1.5 \cdot (1.08 - 0.746)}{0.1 \cdot 14.81} = 0.316 \\ \gamma_{s,st} &= \frac{\Delta_{s,st}}{h_{rt}} = \frac{2.48}{6.125} = 0.405 \\ \gamma_{s,st} &= \frac{0}{5} = 0 \end{aligned}$$

For calculating shear strains due to rotation, the construction tolerance is suggested to be applied to each component of the rotation. As a result the corresponding shear strains are:

$$\begin{aligned} \gamma_{r1,st} &= D_r \left(\frac{L}{h_{ri}} \right)^2 \left(\frac{\theta_{1,st} + 0.005}{n} \right) = 0.5 \cdot \left(\frac{20}{0.375} \right)^2 \cdot \frac{0.01466 + 0.005}{15} = 1.864 \\ \gamma_{r1,cy} &= D_r \left(\frac{L}{h_{ri}} \right)^2 \left(\frac{\theta_{1,cy} + 0.005}{n} \right) = 0.5 \cdot \left(\frac{20}{0.375} \right)^2 \cdot \frac{0.00361 + 0.005}{15} = 0.816 \\ \gamma_{r2,st} &= D_r \left(\frac{W}{h_{ri}} \right)^2 \left(\frac{\theta_{2,st} + 0.005}{n} \right) = 0.5 \cdot \left(\frac{25}{0.375} \right)^2 \cdot \frac{0.00367 + 0.005}{15} = 1.284 \\ \gamma_{r2,cy} &= D_r \left(\frac{W}{h_{ri}} \right)^2 \left(\frac{\theta_{2,cy} + 0.005}{n} \right) = 0.5 \cdot \left(\frac{25}{0.375} \right)^2 \cdot \frac{0.0009 + 0.005}{15} = 0.874 \end{aligned}$$

Now applying the total shear strain approach for direction 1:

$$(\gamma_{a,st} + \gamma_{r1,st} + \gamma_{s,st}) + 1.75(\gamma_{a,cy} + \gamma_{r1,cy} + \gamma_{s,cy}) \leq 5.0$$

$$(0.705 + 0.405 + 1.864) + 1.75(0.316 + 0 + 0.816) \leq 5.0$$

$$4.955 \leq 5.0 \quad \text{OK}$$

For direction 2:

$$(0.705 + 0.405 + 1.284) + 1.75(0.316 + 0 + 0.874) \leq 5.0$$

$$4.476 \leq 5.0 \quad \text{OK}$$

Checking for total rubber thickness:

$$h_{rt} \geq 2\Delta_s$$

$$6.123 \geq 4.96 \quad \text{OK}$$

Checking for static axial stress component:

$$\sigma_{s,st} \leq 2.0GS_i$$

$$0.746 \leq 2.96 \quad \text{OK}$$

Checking for stability:

$$A = \frac{1.92 \frac{h_{rt}}{L}}{\sqrt{1 + \frac{2.0L}{W}}} = 0.251$$

$$B = \frac{2.67}{(S_i + 2.0) \left(1 + \frac{L}{4.0W}\right)} = 0.121$$

$$2A \leq B$$

$$0.502 \leq 0.121 \quad \text{NOT OK}$$

$$\sigma_{s,max} \leq \frac{GS_i}{2A - B}$$

$$1.08 \leq 3.879 \quad \text{OK}$$

To check against slipping and to facilitate the design of steel laminated elastomeric bearings the minimum pressure at the bearing is taken as the average between the pressure due to dead load and the minimum pressure. This accounts for the fact that the likelihood of minimum load to happen at the coldest time is low.

Checking for slipping:

$$\sigma_{s,min} \geq \frac{G_{cold}\Delta_s}{\mu h_{rt}}$$

$$\frac{0.746 + 0.108}{2} \geq \frac{1.5 \cdot 2.48}{0.3 \cdot 6.125}$$

$$0.427 \geq 0.135 \quad \text{OK}$$

As a result, the selected bearing satisfies all design criteria and is suitable to accommodate the design loads.

10.5.2 BEARING 2

This bearing has similar shear demands with bearing 1; however, 12 internal layers of 0.375 in., 0.1 ksi neoprene elastomer are selected due to the decreased potential of slip. Plan dimensions L and W are selected 14 in. and 17 in. respectively. For the bearing the resulting shape factor is as follows:

$$S_i = \frac{17 \cdot 14}{2 \cdot 0.375(17 + 14)} = 10.24$$

The shear strains are:

$$\begin{aligned}\gamma_{a,st} &= \frac{D_a \sigma_{s,st}}{GS_i} = \frac{1.5 \cdot 0.74}{0.1 \cdot 10.24} = 1.017 \\ \gamma_{a,cy} &= \frac{D_a \sigma_{s,cy}}{GS_i} = \frac{1.5 \cdot (1.822 - 0.74)}{0.1 \cdot 10.24} = 0.804 \\ \gamma_{s,st} &= \frac{\Delta_{s,st}}{h_{rt}} = \frac{2.49}{5} = 0.498 \\ \gamma_{s,st} &= \frac{0}{5} = 0\end{aligned}$$

For calculating shear strains due to rotation, the construction tolerance is suggested to be applied to each component of the rotation. As a result the corresponding shear strains are:

$$\begin{aligned}\gamma_{r1,st} &= D_r \left(\frac{L}{h_{ri}} \right)^2 \left(\frac{\theta_{1,st} + 0.005}{n} \right) = 0.5 \cdot \left(\frac{14}{0.375} \right)^2 \cdot \frac{0.00528 + 0.005}{12} = 0.597 \\ \gamma_{r1,cy} &= D_r \left(\frac{L}{h_{ri}} \right)^2 \left(\frac{\theta_{1,cy} + 0.005}{n} \right) = 0.5 \cdot \left(\frac{14}{0.375} \right)^2 \cdot \frac{0.00281 + 0.005}{12} = 0.453 \\ \gamma_{r2,st} &= D_r \left(\frac{W}{h_{ri}} \right)^2 \left(\frac{\theta_{2,st} + 0.005}{n} \right) = 0.5 \cdot \left(\frac{17}{0.375} \right)^2 \cdot \frac{0.0001 + 0.005}{12} = 0.436 \\ \gamma_{r2,cy} &= D_r \left(\frac{W}{h_{ri}} \right)^2 \left(\frac{\theta_{2,cy} + 0.005}{n} \right) = 0.5 \cdot \left(\frac{17}{0.375} \right)^2 \cdot \frac{0.00005 + 0.005}{12} = 0.432\end{aligned}$$

Now applying the total shear strain approach for direction 1:

$$\begin{aligned}(\gamma_{a,st} + \gamma_{r1,st} + \gamma_{s,st}) + 1.75(\gamma_{a,cy} + \gamma_{r1,cy} + \gamma_{s,cy}) &\leq 5.0 \\ (1.017 + 0.498 + 0.597) + 1.75(0.804 + 0 + 0.453) &\leq 5.0 \\ 4.313 &\leq 5.0 \quad \text{OK}\end{aligned}$$

For direction 2:

$$(1.017 + 0.498 + 0.436) + 1.75(0.505 + 0 + 0.432) \leq 5.0 \\ 4.116 \leq 5.0 \quad \text{OK}$$

Checking for total rubber thickness:

$$\begin{aligned}h_{rt} &\geq 2\Delta_s \\ 5 &\geq 4.96 \quad \text{OK}\end{aligned}$$

Checking for static axial stress component:

$$\begin{aligned}\sigma_{s,st} &\leq 2.0GS_i \\ 0.74 &\leq 2.047 \quad \text{OK}\end{aligned}$$

Checking for stability:

$$\begin{aligned}A &= \frac{1.92 \frac{h_{rt}}{L}}{\sqrt{1 + \frac{2.0L}{W}}} = 0.305 \\ B &= \frac{2.67}{(S_i + 2.0) \left(1 + \frac{L}{4.0W} \right)} = 0.167 \\ 2A &\leq B \\ 0.71 &\leq 0.167 \quad \text{NOT OK} \\ \sigma_{s,max} &\leq \frac{GS_i}{2A - B} \\ 1.332 &\leq 2.313 \quad \text{OK}\end{aligned}$$

Checking for slipping:

$$\frac{\sigma_{s,min} \geq \frac{G_{cold} A_s}{\mu h_{rt}}}{\frac{0.744 + 0.315}{2} \geq \frac{1.5 \cdot 2.49}{0.3 \cdot 5}} = \frac{0.529 \geq 0.166}{0.529 \geq 0.166} \quad \text{OK}$$

As a result, the selected bearing satisfies all design criteria and is suitable to accommodate the design loads.

10.5.3 BEARING 3

Due to the higher rotational demand in only one direction 10 internal layers of 0.5 in., 0.1 ksi neoprene elastomer are selected. The cover layers remain 0.25 in. The respective plan dimensions L and W are selected at 22 in. and 32 in... The resulting shape factor for the bearing is as follows:

$$S_i = \frac{32 \cdot 22}{2 \cdot 0.5(32 + 22)} = 13.04$$

The shear strains are:

$$\begin{aligned}\gamma_{a,st} &= \frac{D_a \sigma_{s,st}}{GS_i} = \frac{1.5 \cdot 1.441}{0.1 \cdot 13.04} = 1.441 \\ \gamma_{a,cy} &= \frac{D_a \sigma_{s,cy}}{GS_i} = \frac{1.5 \cdot (1.795 - 1.441)}{0.1 \cdot 13.04} = 0.354 \\ \gamma_{s,st} &= \frac{A_{s,st}}{h_{rt}} = \frac{1.9}{5.5} = 0.345 \\ \gamma_{s,st} &= \frac{0}{5} = 0\end{aligned}$$

For calculating shear strains due to rotation, the construction tolerance is suggested to be applied to each component of the rotation. As a result the corresponding shear strains are:

$$\begin{aligned}\gamma_{r1,st} &= D_r \left(\frac{L}{h_{ri}} \right)^2 \left(\frac{\theta_{1,st} + 0.005}{n} \right) = 0.5 \cdot \left(\frac{22}{0.5} \right)^2 \cdot \frac{0.00602 + 0.005}{10} = 1.067 \\ \gamma_{r1,cy} &= D_r \left(\frac{L}{h_{ri}} \right)^2 \left(\frac{\theta_{1,cy} + 0.005}{n} \right) = 0.5 \cdot \left(\frac{22}{0.5} \right)^2 \cdot \frac{0.00541 + 0.005}{10} = 1.008 \\ \gamma_{r2,st} &= D_r \left(\frac{W}{h_{ri}} \right)^2 \left(\frac{\theta_{2,st} + 0.005}{n} \right) = 0.5 \cdot \left(\frac{32}{0.5} \right)^2 \cdot \frac{0.0002 + 0.005}{10} = 1.065 \\ \gamma_{r2,cy} &= D_r \left(\frac{W}{h_{ri}} \right)^2 \left(\frac{\theta_{2,cy} + 0.005}{n} \right) = 0.5 \cdot \left(\frac{32}{0.5} \right)^2 \cdot \frac{0.00018 + 0.005}{10} = 1.061\end{aligned}$$

Now applying the total shear strain approach for direction 1:

$$\begin{aligned}(\gamma_{a,st} + \gamma_{r1,st} + \gamma_{s,st}) + 1.75(\gamma_{a,cy} + \gamma_{r1,cy} + \gamma_{s,cy}) &\leq 5.0 \\ (1.441 + 0.345 + 1.067) + 1.75(0.354 + 0 + 1.008) &\leq 5.0 \\ 4.891 &\leq 5.0 \quad \text{OK}\end{aligned}$$

For direction 2:

$$\begin{aligned}(1.441 + 0.345 + 1.065) + 1.75(0.354 + 0 + 1.061) &\leq 5.0 \\ 4.982 &\leq 5.0 \quad \text{OK}\end{aligned}$$

Checking for total rubber thickness:

$$h_{rt} \geq 2A_s$$

$$5.5 \geq 3.8 \quad \text{OK}$$

Checking for static axial stress component:

$$\begin{aligned}\sigma_{s,st} &\leq 2.0GS_i \\ 1.34 &\leq 2.607 \quad \text{OK}\end{aligned}$$

Checking for stability:

$$\begin{aligned}A &= \frac{1.92 \frac{h_{rt}}{L}}{\sqrt{1 + \frac{2.0L}{W}}} = 0.167 \\ B &= \frac{2.67}{(S_i + 2.0) \left(1 + \frac{L}{4.0W}\right)} = 0.130 \\ 2A &\leq B \\ 0.334 &\leq 0.130 \quad \text{NOT OK} \\ \sigma_{s,max} &\leq \frac{GS_i}{2A - B} \\ 1.67 &\leq 6.403 \quad \text{OK}\end{aligned}$$

Checking for slipping:

$$\begin{aligned}\sigma_{s,min} &\geq \frac{G_{cold} A_s}{\mu h_{rt}} \\ \frac{1.342 + 0.858}{2} &\geq \frac{1.5 \cdot 1.9}{0.3 \cdot 5.5} \\ 1.1 &\geq 0.115 \quad \text{OK}\end{aligned}$$

As a result, the selected bearing satisfies all design criteria and is suitable to accommodate the design loads.

REFERENCES

- AASHTO (2012). Load and Resistance Factor Design Specification for Highway Bridges, 6th Edition. A. A. o. S. H. a. T. Officials. Washington, D.C.
- Anderson, M., P. Mott and C. Roland (2004). "The compression of bonded rubber disks." Rubber chemistry and technology **77**(2): 293-302.
- Bakirzis, E. and P. B. Lindley (1970). "Slipping at Contact Surfaces of Plain Rubber Pads in Compression." Civil Eng & Public Works Review/UK/.
- Bradberry, T. E., J. C. Cotham and R. D. Medlock (2005). "Elastomeric bearings for steel trapezoidal box girder bridges." Transportation Research Record: Journal of the Transportation Research Board **1928**(1): 27-38.
- Buckle, I., S. Nagarajaiah and K. Ferrell (2002). "Stability of Elastomeric Isolation Bearings: Experimental Study." Journal of Structural Engineering **128**(1): 3-11.
- Chen, Q. (2008). Effects of thermal loads on Texas steel bridges, The University of Texas at Austin.
- Chen, Q., Helwig, T.A., Herman, R.S., Grisham, G., and Arikan, Y., "Effects of Thermal Loads on Texas Steel Bridges," Research Report 5040-1, January 2009.
- EN1337-3 (2005). Structural bearings - Part 3: Elastomeric bearings. The European Committee of Standardization, Berlin.
- English, B., R. Klingner and J. Yura (1994). "Elastomeric Bearings: Background Information and Field Study."
- Gent, A. and P. Lindley (1959). "The compression of bonded rubber blocks." Proceedings of the Institution of Mechanical Engineers **173**(1): 111-122.
- Gent, A. N. (1964). "Elastic stability of rubber compression springs." Journal of Mechanical Engineering Science **6**(4): 318-326.
- Gent, A. N. and E. A. Meinecke (1970). "Compression, bending, and shear of bonded rubber blocks." Polymer Engineering & Science **10**(1): 48-53.
- Heymsfield, E., J. McDonald and R. Avent (2001). "Neoprene Bearing Pad Slippage at Louisiana Bridges." Journal of Bridge Engineering **6**(1): 30-36.
- Holownia, B. (1980). "Effect of different types of carbon black on elastic constants of elastomers." Plast. and Rubb.: Mats. and Applics. **5**: 129-132.
- Koh, C. and H. Lim (2001). "Analytical solution for compression stiffness of bonded rectangular layers." International Journal of Solids and Structures **38**(3): 445-455.
- McDonald, J., E. Heymsfield and R. R. Avent (2000). "Slippage of neoprene bridge bearings." Journal of Bridge Engineering **5**(3): 216-223.

Muhr, A. and A. Thomas (1989). "Allowing for non-linear stress-strain relationships of rubber force-deformation calculations. Pt. 1: compression stiffness of bonded rubber blocks." NR Technology **20**: 8-14.

Muscarella, J. V. and J. Yura (1995). An experimental study of elastomeric bridge bearings with design recommendations, University of Texas at Austin.

Nguyen, H. and J. Tassoulas (2010). "Directional Effects of Shear Combined with Compression on Bridge Elastomeric Bearings." Journal of Bridge Engineering **15**(1): 73-80.

Nims, D. K. and A. Parvin (2000). Instrumented Elastomeric Bridge Bearings, University of Toledo, Department of Civil Engineering.

Peng, S. H., T. Shimbori and A. Naderi (1994). "Measurement of elastomer's bulk modulus by means of a confined compression test." Rubber chemistry and technology **67**(5): 871-879.

Qiao, S. and N. Lu (2014). "Closed-Form Solutions for Bonded Elastically Compressible Layers." International Journal of Solids and Structures.

Roeder, C. W. and J. F. Stanton (1996). Steel bridge bearing selection and design guide.

Roeder, C. W., J. F. Stanton and T. Feller (1989). Low temperature behavior and acceptance criteria for elastomeric bridge bearings.

Roeder, C. W., J. F. Stanton and A. W. Taylor (1987). Performance of elastomeric bearings.

Stanton, J., G. Scroggins, A. Taylor and C. Roeder (1990). "Stability of Laminated Elastomeric Bearings." Journal of Engineering Mechanics **116**(6): 1351-1371.

Stanton, J. F., C. W. Roeder, P. Mackenzie-Helnwein, C. White, C. Kuester and B. Craig (2008). NCHRP Report 596 - Rotation Limits for Elastomeric Bearings. Washington, D.C., Transportation Research Board.

Weisman, J. and G. Warn (2012). "Stability of Elastomeric and Lead-Rubber Seismic Isolation Bearings." Journal of Structural Engineering **138**(2): 215-223.

Yeoh, O., G. Pinter and H. Banks (2002). "Compression of bonded rubber blocks." Rubber chemistry and technology **75**(3): 549-562.

Yura, A. Y. J. A. (2002). "Parameters Influencing Performance of Elastomeric Bearings at Low Temperatures." Journal of Structural Engineering **128**(8): 986-994.

Yura, J., A. Kumar, A. Yakut, C. Topkaya, E. Becker and J. Collingwood (2001). NCHRP Report 449: Elastomeric Bridge Bearings: Recommended Test Methods.